

Review

Studies on the Quality of Joints and Phenomena Therein for Welded Automotive Components Made of Aluminum Alloy—A Review

Bogdan Derbiszewski ^{1,*}, Andrzej Obraniak ², Adam Rylski ^{3,*}, Krzysztof Siczek ⁴  and Marek Wozniak ⁴ ¹ Polytechnic Faculty, Calisia University, 62-800 Kalisz, Poland² Faculty of Process and Environmental Engineering, Lodz University of Technology, 90-924 Lodz, Poland; andrzej.obraniak@p.lodz.pl³ Institute of Material Engineering, Lodz University of Technology, 90-924 Lodz, Poland⁴ Department of Vehicles and Fundamentals of Machine Design, Lodz University of Technology, 90-537 Lodz, Poland; ks670907@p.lodz.pl (K.S.); marek.wozniak.1@p.lodz.pl (M.W.)

* Correspondence: b.derbiszewski@uniwersytetkaliski.edu.pl (B.D.); adam.rylski@p.lodz.pl (A.R.)

Abstract: To fulfill the need to limit automotive emissions, reducing vehicle weight is widely recommended and achieved in many ways, both by the construction of individual elements of the vehicle and by the selection of light materials, including Al alloys. Connecting these elements with each other and with elements made of iron alloys can be realized, inter alia, by welding or stir welding. However, the quality of the welds obtained varies widely and depends on many design, operational, and environmental factors. The present study focused on a review of various welding techniques used to join both similar and dissimilar Al alloys utilized in the automotive industry, the effect of various process parameters on weld quality, and the phenomena observed in such welds. The research methodology was based on the analysis of the content of articles from main databases. Apart from capturing the current state of the art, this review evaluates reaching the possible highest joint quality and welding process disadvantages such as porosity, poor surface quality, a tendency toward hot cracking, and low ductility for the Al alloys applied in the automotive industry.

Keywords: welding process; vehicle components; aluminum alloy



Citation: Derbiszewski, B.; Obraniak, A.; Rylski, A.; Siczek, K.; Wozniak, M. Studies on the Quality of Joints and Phenomena Therein for Welded Automotive Components Made of Aluminum Alloy—A Review.

Coatings **2024**, *14*, 601. <https://doi.org/10.3390/coatings14050601>

Academic Editors: Hector R. Siller and Emmanuel Segura-Cárdenas

Received: 21 March 2024

Revised: 27 April 2024

Accepted: 5 May 2024

Published: 10 May 2024



Copyright: © 2024 by the authors. Licensee MDPI, Basel, Switzerland. This article is an open access article distributed under the terms and conditions of the Creative Commons Attribution (CC BY) license (<https://creativecommons.org/licenses/by/4.0/>).

1. Introduction

The necessity to limit emissions from vehicles [1–3] imposed by the applicable regulations might be fulfilled, inter alia, via a reduction in their weight [4,5]. For example, the utilization of lighter and equally durable components for suspension elements and frames helps to accomplish such an aim [6].

However, the vehicles' weight reduction achieved by changing their material composition is limited by the extent of material substitution and by material choice [5]. Although composite materials, such as carbon fiber-reinforced plastics (CFRPs) [7,8] offer excellent mechanical properties for lightweight applications, their production is sometimes more energy- and emission-intensive than that of conventional metals, and their recycling methods are limited. Interestingly, some low-energy consumption processes to produce polymer matrix composites for automotive applications (e.g., pultrusion, liquid composite molding, and filament winding) have appeared on the market. Therefore, the traditional mild steel and cast iron utilized in vehicle manufacturing can be partially replaced by high-strength steel HSS, magnesium alloys, wrought Al, and cast Al [5]. For example, a B-pillar outer panel can also be made of high-strength 7075 alloy [9].

Many important structural components of the vehicle made from Al alloys are welded structures [10,11]. For the automobile body, Al alloys from the 5xxx and 6xxx groups are commonly used; however, welding problems occur [12,13]. Particularly, 6082 Al alloy can be applied to vehicle components [14].

The goal of the present paper was to review various welding techniques used to join both similar and dissimilar Al alloys utilized in the automotive industry, the effect of various process parameters on weld quality, and the phenomena in such welds. Additionally, several recommendations regarding the selection of the welding method for specific Al alloy combinations are presented.

If there are welded joints in a structural element, the strength of the element differs from the strength of the base material (BM) of this element. This difference is considered during design calculations using the so-called joint quality factor, joint efficiency factor, weld joint factor, or strength reduction coefficient depending on the calculation method or code [15]. Joint quality factor values range from 0.0 to 1.0, depending on the material, the type of weld, and the level of accuracy of joint testing [16]. When there are two or more welds in a component, the worst-case weld is evaluated to determine the joint quality factor value. The joint efficiency can be expressed in terms of the ultimate tensile strength (the ratio of the UTS of the welded joint and that of the BM—usually the softer one of dissimilar alloys) [17–19] or, less frequently, in terms of elongation (the ratio of the elongation of welded joints and that of the BM—usually the softer one of dissimilar alloys) [18].

This review includes considerations on the concept of weldability and the techniques for joining vehicle components made of Al alloy with various welding types, such as conventional welding, friction stir welding (FSW), resistance spot welding (RSW), gas metal arc welding (GMAW), cold metal transfer (CMT) welding, magnetic pulse welding (MPW), and collision welding and laser welding. Various Al alloys used for the welding process and problems occurring during such a process are considered. Features of Al welded joints and phenomena that occurred therein are widely discussed in this review.

2. Weldability

The welding process is closely related to the concept of weldability. The latter subject encompasses a wide range of definitions and interpretations considering various aspects of design, fabrication, fitness for service, and repair. This is reflected in the definitions for weldability provided by both the American Welding Society and the ISO Standard 581:1980 [20].

In this review, as in [20], weldability was considered from the standpoint of materials' resistance or susceptibility to failure. From a fabrication standpoint, this is characterized by the ability to produce defect-free welded joints. The different weld defects generated during fabrication belong to two groups:

One group is related to the welding process and procedures. This comprises the lack of fusion, undercut, and slag inclusions avoidable by changes in process conditions.

The other group is associated with the material. This comprises solidification cracks and hydrogen-induced cracks, which are usually difficult to eliminate by changes in process conditions alone.

Weldability also characterizes the behavior of welded structures after putting them into service. Failures in such structures sometimes have a time-delay nature. Such failure modes include corrosion [21], fatigue [22–24], stress rupture (creep) [25–27], or complex combinations of these and other failure mechanisms [28], which could be unexpected and catastrophic.

Particularly, using the cold metal transfer (CMT) arc welding method for lap and butt joints of components made of EN AW-7075 alloy, the authors of [21] found much lower corrosion resistance in the transition zone between the heat-affected zone (HAZ) and the BM in the medium salinity environment, corresponding to the sea conditions according to ASTM G85.

As for the fatigue, using rotary bending fatigue tests, the authors of [22] evaluated the fatigue properties of 4000A-based Al alloys in both forged and non-forged forms. All the aluminum alloys studied possessed surface and inclusion-oriented fatigue failures; however, the deterioration in fatigue life occurred only in non-forged alloys. The fatigue failure in the high-cycle fatigue region was mainly induced by internal inclusions or defects.

The forging process enhanced the fatigue strength and reduced the scatter of the fatigue life of Al alloys. Li et al. [23] reviewed the fatigue mechanism, influencing factors, the crack growth rate, and fatigue life for the friction stir welding (FSW) process. They found that the fatigue performance of the FSW joints depended on welding process parameters, test environment, stress ratio, residual stress, and weld defect. They also reported that the optimized process parameters can provide high-quality welds and enhance the weld fatigue life. Laser peening is an effective post-weld treatment to lower the fatigue crack growth rate and increase the material fatigue life. Bahaideen et al. [24] reported that the fatigue strength of 2024-T4 Al alloy at an elevated temperature (180 °C) was reduced by a factor of 1.2–1.4 in comparison to the dry fatigue strength at room temperature.

In relation to the issue of creep, Azadi and Aroo [25] studied the creep properties and failure mechanisms of two materials under working conditions in engine pistons made of the AlSi12CuNiMg piston Al alloy and an Al matrix silicon oxide nanocomposite made by stir-casting the Al alloy and 2 wt.% of nanoparticles. The creep standard specimens that were studied under 100 MPa of applied stress and at a temperature of 250 °C exhibited similar microstructure features. Nanoparticles had an insignificant effect on the microstructure of the Al alloy. The lifetime of the creep specimens decreased when nanoparticles were added to the Al alloy. Local agglomerations of 2 wt.% nanoparticles reduced the creep properties of the Al alloy. Both materials exhibited brittle fracture behavior. The cleavage and quasi-cleavage marks on the fracture surfaces indicated failure mechanisms. Chen et al. [26] studied the compression creep behavior of samples made of 8030 Al alloys under a deformation temperature of 200~250 °C and compression stress ranging from 20 to 40 MPa. They reported that the dislocation viscous glide controlled by lattice self-diffusion was the dominant creep mechanism for the samples at 200 °C under 20 MPa compression stress. The studied sub-grain contours were ambiguous, and the dislocations with long curved morphologies were homogeneously distributed within grain inners after creep for 100 h. Using a creep-testing machine in 300 h tests, Li et al. [27] studied the room-temperature tensile and compressive creep properties of 2219-T87 Al alloy welds obtained by friction stir welding (FSW) or tungsten inert gas welding (TIG) arc welding. They found that the creep strain of the samples in the compressive test was lower than that in the tensile state under the same stress level. Compared to TIG arc welding, the FSW process provided joints with a higher yield strength (YS), a fine homogenous, and no pores defect microstructure, and thus a better creep resistance. In addition, when the creep stress was lower than the YS, the creep values of the welds obtained by FSW and TIG after 1×10^5 h were below 1%.

Fourmeau et al. [28] studied the effect of stress state and plastic anisotropy on the fracture behavior of a rolled AA7075-T651 Al plate under quasi-static loading conditions, both experimentally and numerically. They reported that the strain to failure and the failure modes strongly varied with the stress state and the loading direction due to the complex microstructure of the alloy. The numerical simulations they conducted showed that the heterogeneous stress and strain fields in the specimens highly impeded the accurate location of the point where fracture initiation was difficult, thus determining the local fracture strain as a function of stress state and loading direction.

3. Techniques for Joining Vehicle Components Made of Al Alloy

Joining vehicle components made of Al alloys can be difficult, especially if components are made of dissimilar Al alloys. Al alloys are difficult to weld due to their specific thermophysical properties and intricate physical metallurgy. Work-hardened alloys often exhibit strength loss in the HAZ. The strength of precipitation-hardened alloys is highly reduced in both the HAZ and the weld metal due to coarsening or full [29]. There are some techniques allowing for the proper joining of such different components, especially adhesive bonding [30–33], pointwise mechanical fastening (by clinching or riveting, or with fasteners) [34,35], resistance spot welding (RSW) [36], electron-beam welding (EBW) [37], and cold metal transfer (CMT) welding [38], to name a few.

3.1. Various Kinds of Welding Processes

3.1.1. Conventional Welding

Conventional welding of Al alloys has limited technological or executive difficulties [39]. No problems were reported when producing good-quality Al joints using conventional, less efficient slag-free welding processes [40]. Welding with a coated electrode does not provide acceptable weld quality, as porous structures with a tendency to crack are formed. Therefore, welding with coated electrodes is rarely used and only for irrelevant structural components [14]. The most popular non-slag welding processes used on an industrial scale are tungsten inert gas (TIG) and metal inert gas (MIG) methods [14,41]. Gas tungsten arc welding (GTAW) is also known as tungsten inert gas (TIG) welding [42].

The TIG welding process is characterized by the fact that an electric arc appears between an infusible tungsten electrode and a bonded Al alloy in an inert gas shield. No additional material is needed; however, an extra binder material in the form of a wire can be introduced into the weld pool manually. Usually, shielding gas in the form of argon, helium, or Ar-He mixtures is fed via the nozzle of the welding torch to limit the oxidation and nitrification of both the weld and the electrode.

The MIG welding process is characterized by the fact that an electric arc exists between a fusible electrode and a bonded Al alloy under an inert gas shield. The electrode wire becomes the fusible electrode fed in an automatic and continuous way. The wire is selected according to technological guidelines for a specific welded Al alloy.

The pros and cons of both MIG and TIG processes [14] are presented in Table 1.

Table 1. Pros and cons of both MIG and TIG processes.

Welding Process	Pros	Cons
MIG	<ul style="list-style-type: none"> - Allows for welding several types of alloys in all positions - High welding efficiency higher from coated electrodes and the TIG method - Relatively low cost of welding consumables - High-quality welds - Enables automation 	<ul style="list-style-type: none"> - The quality of produced welds is affected by the skill and experience of a welder - High purchase costs of equipment and accessories - The necessity of using an additional binder
TIG	<ul style="list-style-type: none"> - Enables welding several types of alloys in all positions - Allows for welding thin metal sheets - High-quality welds - Easy control and handling of the welding process - Lack of liquid metal splashing - No need to use an additional binder - Allows for automation without applying an additional binder 	<ul style="list-style-type: none"> - Low welding speed and low efficiency, especially in the case of thicker components, - The quality of produced welds is affected by the skills of a welder - Impossible to automate the process with the application of an additional binder

However, despite the prevalence of advantages, welding Al alloys using MIG and TIG processes still results in either poor functional properties of the joint or low relative efficiency [43,44].

3.1.2. Friction Stir Welding

Friction stir welding (FSW) involves the use of a non-consumable rotating cylindrical tool comprising a cylindrical threaded pin at one end, and a shoulder at the other end, which moves along the contacting surfaces of two rigidly butt-clamped plates placed on rigid backing support. At the same time, the shoulder is forced to the top surface of the workpiece. During the motion of such a tool along the butting surfaces, heat is generated from frictional energy dissipation at the shoulder/workpiece and, to a lesser extent, at the pin/workpiece contact surfaces. This enhances the temperature and causes the softening of the material adjacent to such contacting surfaces. During the motion of the tool along

the butting surfaces, thermally softened material in front of the tool is highly deformed, extruded around the tool to the region behind the tool, and compacted/forged to form a joint/weld [45]. Due to tool rotation and forward translation, FSW is an inherently asymmetric process relative to the workpiece, and material flow and temperature distribution during such a process are also asymmetric. For dissimilar Al alloys, the asymmetric characteristic of the process is compounded by the discontinuity in material properties across the weld zone. Therefore, the placement of the alloys on either the advancing or retreating sides significantly influences the final weld properties [46]. The material around the tool is joined due to both the stirring and extrusion of the material. The shapes of the final joint in FSW include onion ring nuggets, zigzag shapes, and void defect nuggets, which depend on welding conditions. The shape of the final joint strongly affects its mechanical properties [47]. In comparison to conventional welding methods, FSW needs much less energy, no coverage gas or flux, and no filler metal; thus, joining any Al alloy is independent of the compatibility of the composition, which is an issue in fusion welding [48].

The FSW process is well recognized in the literature [49–52] and is also discussed in the case of dissimilar alloys [53–55].

The FSW process enables the joining of both similar Al alloys [56,57] and dissimilar alloys [58,59]. The FSW process is applied in the fabrication of Al alloy wheels and fuel tanks [60]. Friction stir lap welding (FSLW), being a form of FSW, involves plunging a rotational tool into two overlapped sheets and retracting it after passing a determined distance [61].

Parameters like tool geometry and joint configuration strongly affect the material flow and temperature evolution, and the same is true regarding the microstructure of joints. Due to the combination of frictional heat and the mechanical intermixing of materials, typical microstructural zones appear after FSW such as (a) the BM; (b) the HAZ containing grains similar to the BM; (c) the thermomechanically affected zone (TMAZ), comprising plastically deformed grains; and (d) the stir zone (SZ), also known as the nugget zone (NZ), consisting of fine and recrystallized grains (Figure 1). The fine-grain structure of the SZ is a result of severe plastic deformation caused by the stirring action of the tool. The region next to the SZ is less plastically deformed and is subjected to partial dynamical recrystallization, and this zone is named the TMAZ. However, no plastic deformation is seen in the HAZ, and it only experiences a thermal effect [62].

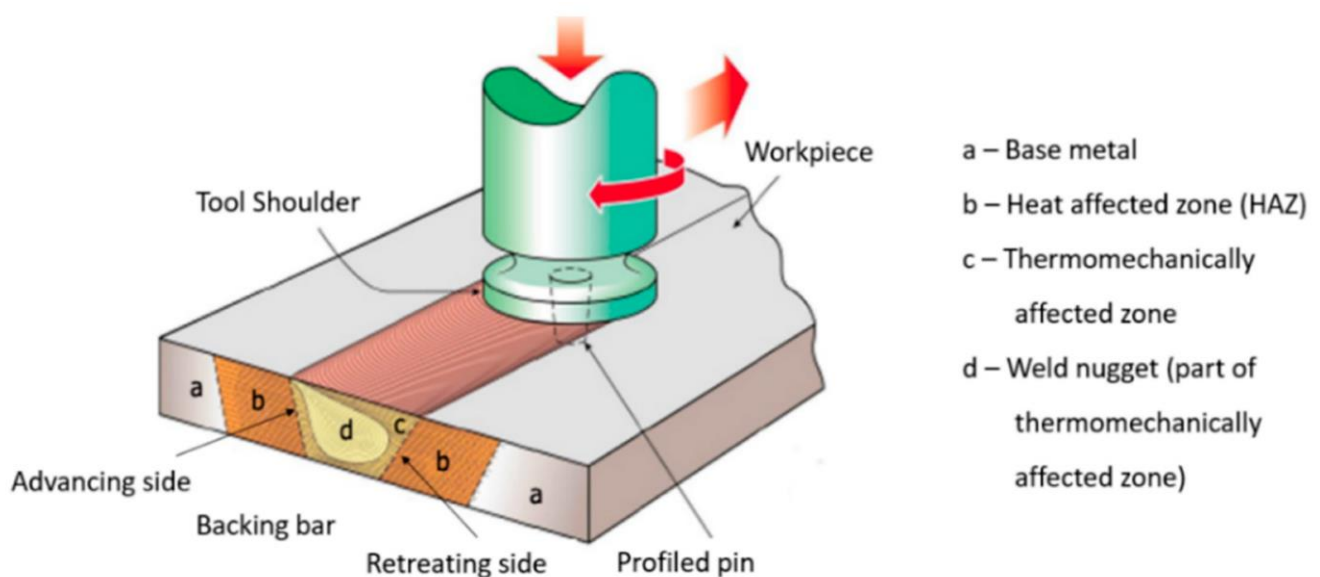


Figure 1. Weld zones in the butt joint obtained using the FSW process [63].

An FSW lap weld also comprises a few zones [64] (Figure 2), which include the following:

- Parent material (PM)—including the material portion positioned farthest away from the center of the weld, without any deformation or change in mechanical and structural characteristics;
- HAZ—including the material portion of the neighboring weld where the material is subjected to heat causing a change in structure and mechanical properties. This zone does not undergo plastic deformation;
- Thermoplastic deformation zone—including the material portion affected by the tool resulting in mechanical and heat reactions. Al alloys can undergo intensive plastic deformation in this zone without material recrystallization. This zone covers the border between the non-crystallized material and the weld core;
- Weld core—including the material portion undergoing full recrystallization. This zone is characterized by a small, axially distributed grain with a size of a few micrometers large (Al alloys). Through this zone, the FSW tool pin travels during the welding process.

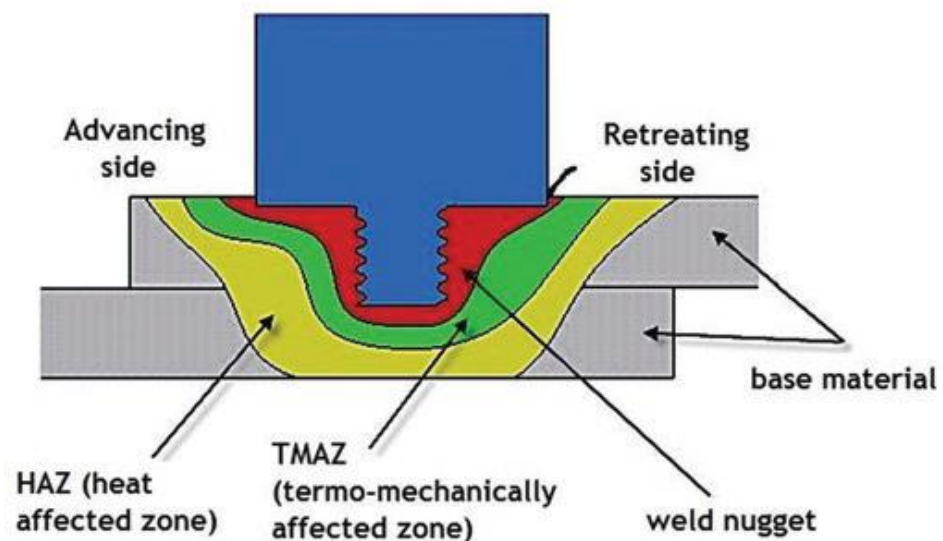


Figure 2. Weld zones in a lap joint obtained using the FSW process [64]. Reproduced under open access agreement and Creative Commons License CC-BY 4.0 [<https://ein.org.pl/Information-for-Authors,3806.html> (accessed on 15 April 2024)].

3.1.3. Resistance Spot Welding

Resistance spot welding (RSW) is a welding process in which sheet metal pieces are joined together by applying pressure and passing a large current through a localized area while the sheets are fixed together. The power supply type in resistance spot welding is divided into silicon-controlled rectifiers (SCRs) and inverter DC types [65]. Kim et al. [36] reported that during the resistance spot welding of the 5J32Al alloy sheet for the car body, the range of the optimal welding condition of inverter-type resistance spot welding was larger than that of SCR-type resistance welding. The nugget size obtained using inverter-type resistance spot welding was larger than that obtained with SCR-type RSW under the same welding conditions.

3.1.4. Gas Metal Arc Welding (GMAW)

Gas metal arc welding (GMAW) is an arc welding process using a metal wire as a combined electrode and a filler metal in a plasma arc and inert shielding gas. GMAW provides high productivity and penetration and has no need for flux, little spatter, and the ability to weld in all positions. A typical weld bead resulting from the GMAW of Al alloys comprises three zones. At the beginning of the weld under a quasi-steady state, a cold weld is formed. The BM is heated up from room temperature, and the electrode material starts to drop onto the welding coupon, initiating the weld bead formation. The weld pool

temperature, fluid flow, and weld bead shape vary continuously. In the middle of the weld, the welding process is at a quasi-steady state. Near its end, arc termination prevents the energy and material transfer into the weld pool. The molten pool solidifies, forming a crater-shaped weld end. Ripples are formed on the surface of the weld bead [66].

3.1.5. Cold Metal Transfer Welding

Cold metal transfer (CMT) welding is a modified MIG welding process based on a short-circuiting transfer process, which differs from the classical MIG method in the type of mechanical droplet cutting method [67].

According to [68], the CMT welding process is an advanced type of gas metal arc welding (GMAW) with less heat input in which the welding wire is retracted during the short circuit, providing sufficient time for the weld to cool before placing each drop.

The CMT process allows the control of material deposition and low thermal input by the application of a dedicated wire feed system coupled with high-speed digital control [69]. The control of the wire feed rate and the cycle arcing phase allow sufficient energy to be generated to melt both the BM and a globule of filler wire [70]. The CMT process is mainly characterized by the following features:

The point of the short circuit with low current corresponds to low heat input, and the short circuit occurs in a stable controlled manner [31].

Kah et al. [71] described the short-circuiting transfer process, the so-called “mechanically assisted droplet deposition”, utilized in controlling short circuits by retracting the wire from short-circuiting.

Contrary to the conventional MIG process, the droplet detachment mode of the CMT process involves no electromagnetic forces, which leads to less spatter [72].

Although there are some excellent reviews related to various methods of joining components made of Al alloys and other materials [38,73], several dissimilar welding technologies, based on either fusion welding or solid-state welding, are reviewed here, focusing on similar joining among Al alloys.

The retraction of the wire during the short-circuiting phase of the CMT welding process prevents spatter generation and produces better weld bead aesthetics. CMT welding was found to be more stable, and the root produced showed a better finish, both on the surface and back of the joint, than that obtained using MIG welding [74].

3.1.6. Collision Welding

According to [75], for firmly bonded metals, the solid-state joining of similar as well as almost unweldable dissimilar metals (e.g., steel and Al alloys) can be achieved through high-velocity forming, also referred to as collision welding. The advantage of such a welding technique is having fewer problems associated with a heat-affected zone (HAZ), such as the formation of brittle intermetallic phases or cracking, which are observed in fusion welding. The strength of collision welds can reach or even exceed that of the weakest parent material.

Known collision welding methods are [75] explosive welding (EXW) (possible work-piece dimensions are in the order of meters); laser impact welding (LIW) (dimensions of the order of millimeters); and magnetic pulse welding (MPW) (dimensions of the order of centimeters). Bellmann et al. [76] explained that collision welding was accompanied by the ejection of a metal jet, a cloud of particles (CoP), or both phenomena. The CoP formed during the collision of the joining components was compressed by the closure of the joining gap. At small collision angles, it reached temperatures that enabled the melting of the joined surfaces. The formation of the CoP decreased with the enhancement of the material YS, and the escape of the CoP was inhibited by enhancing surface roughness. Both effects impede welding with low-impact velocities. Weld formation was easier with smooth surfaces and under vacuum-like conditions. The temperature in the joining gap exceeded 5600 K under normal ambient pressure. Niessen et al. [77] stated that collision welding is a high-speed joining method resulting from the plastic deformation of at least

one of the joining components. During the process, the formation of the so-called jet and the emergence of a cloud of particles enable bond formation.

The collision kinetics affects both the cloud of particle (CoP) formation and its temperature, governing the bond mechanism and the achievable size of the welded area. The latter also depends on the initial collision angle, its progression, and the rolling movement.

The width of the weld interface can be enhanced by a smaller gradient of the collision angle when the weldable area of the welding window is achieved.

3.1.7. Magnetic Pulse Welding

Magnetic pulse welding (MPW) is based on an oblique collision process between two joining partners (a movable flyer and a stationary target) at high relative velocities under a collision angle [78].

During the MPW process, the collision between the flyer and target materials occurs under a powerful Lorentz force that is produced by interrelating two counteracting magnetic fields [68]. The flyer is accelerated by an induced electromagnetic pressure that is generated by an electrical circuit comprising a charged capacitor bank and a coil actuator [78].

Affected by a collision angle, a point of collision (PoC) moves along the colliding surfaces. When the dynamic elastic limit of the material is exceeded, material flow results from the plastic deformation of the contact surfaces, and a stream of material is pushed ahead of the PoC [79,80]. This so-called jetting removes brittle oxide layers and surface contaminations from the surfaces, which are ejected either as a compact stream or as a dispersed cloud of particles (CoP) [81]. Depending on the collision conditions, a CoP results from a dispersed material stream, spalled surface contamination through oxide layer formation, or both phenomena, whereas the CoP can partly or completely hide the cumulative jet [76,81].

During such a process, the hyper-plastic deformation needed for interfacial bonding is generated because of the high strain rates related to the high-velocity impact between the two metals. This high plastic deformation subsequently causes local heating and high-strain hardening in the welding interface [82]. Thus, increasing the local temperature causes local fusion and the formation of a thin continuous layer at the interface of the two metals [83], which is wavy in some cases.

MPW provides high bond strengths, no heat-affected zones, and low electrical resistance, even between metals with differing thermomechanical and chemical properties [84,85].

According to [86], the MPW process can be applied to several Al alloys, including 1050, 2017, 3004, 5182, 5052, 6016, and 7075. Niessen et al. [77] studied the MPWed Al sheets (EN AW-1050A Hx4, a YS of 99 MPa, a TS of 105 MPa), with an initial thickness of 2 mm for the target as well as the flyer. The thickness of the latter changed in the range of 1–2 mm. They found that during a single magnetic pulse welding process using aluminum, both fusion-like and solid-state welding can occur. Using a flyer with proper geometry, which affects its rolling movement on the top of the target during MPW, can improve the weld interface formation.

3.1.8. Laser Welding

According to [87], for thicker weldments, penetration requires a higher welding heat input. The significant difference in temperature between the front and back of the weldment causes significant welding distortion. The laser mirror welding process involving the use of symmetrical double-laser heat sources that act on a flat-plate butt-joint structure allows for the deformation-free and high-efficiency welding of thick plates. Complex interactions of double keyholes and double-sided joint pools occur during the welding process.

3.2. Problems during the Welding Process

The welding process of Al alloys is accompanied by many problems, including porosities, the loss of alloying elements, poor bead geometry, and the softening of the HAZ. Laser

welding is widely used for Al alloys due to its advantages such as low heat input, high welding speed (WS), formability, and a high production rate [88].

The degradation of electrode life is the main barrier in the application of resistance spot welding (RSW) for Al vehicles [89–91]. The use of the RSW cladding technique for different Al alloys improves the sheet weldability while maintaining the structural performance. This cladding technique combines a highly conductive, electrically stable Al alloy, used as the covering sheet, with a high-strength alloy, used as the core sheet [92].

3.3. Al Alloys for Welding

Al alloys from the 5xxx and 6xxx groups are welded using TIG and MIG, and the best parameters and methods of welding these alloys are still being investigated [11–13,93].

According to [14], the 6082 alloy can be welded with TIG and MIG processes. MIG welding exerts better effects than the TIG process regarding the TS and fatigue strength. TIG welding can be advantageous owing to the obtained weld strength parameters, but on an industrial scale, it has technological issues and low WS. The most favorable effect of welding this Al alloy is obtained with the MIG process using a 4043 wire under a WS of about 500 mm/min.

According to [94], to achieve the required end-use properties, components made of various Al alloys usually need heat treatment. Heat treatment processes are specified by the AMS2770 (Heat Treatment of Wrought Aluminum Alloy Parts) and AMS2771 (Heat Treatment of Aluminum Alloy Castings) standards, detailing heat treatment processes such as aging, annealing, and solution heat treatment in addition to parameters such as times, temperatures, and quenchants.

Wrought Al alloys can be divided into two categories: non-heat-treatable and heat-treatable alloys. Non-heat-treatable alloys, which include the 1xxx, 3xxx, 4xxx, and 5xxx series alloys, derive their strength from the preparation of solid solutions and are further strengthened by strain hardening or, in a few cases, aging. Heat-treatable alloys include the 2xxx, 6xxx, and 7xxx series and are strengthened by solution heat treatment followed by precipitation hardening (aging).

Various Al series possess different chemical, physical, and mechanical properties: The 1000 series presents high electric conductivity and lower mechanical strength, the 2000 series presents high strength, the 3000 series presents high conductivity with better mechanical strength and formability, the 4000 series has good corrosion resistance, 5000 and 6000 series provide good mechanical properties and formability, and the 7000 series is known as the ultra-high-strength aluminum [92].

Automobile body structures are commonly made from Al alloys belonging to the following groups: 2XXX, 5XXX, 6XXX, and 7XXX. The general information regarding their composition, strength, and weldability is presented in Table 2 [14].

Table 2. Al alloys applied in the automotive industry.

Group of Aluminum Alloys	Main Alloy Components	Durability	Weldability
2XXX	Al-Cu	High	Low
5XXX	Al-Mg	Increased	High
6XXX	Al-Si-Mg	Increased	High
7XXX	Al-Zn	High	Low

The 1100 Al alloy comprises almost 99% pure Al, which provides 1100 alloy sheets with extremely high malleability and corrosion resistance. This alloy is used for heat insulators [95].

The 2xxx series comprises Al alloyed with Cu. The 2024 alloy is applied for pistons, brake components, rotors, cylinders, wheels, and gears due to its high strength and fatigue resistance [95].

The 3xxx series comprising Al alloyed with Mg provides high formability. The 3003 alloy exhibits high strength, good formability, workability, and drawing capabilities. It is applied for automotive piping, paneling, and power castings for hybrids and EVs. The 3004 alloy shares similar characteristics as the 3003 alloy and can also be used for cowl grille panels and radiators. The 3105 alloy possesses high corrosion resistance, formability, and welding characteristics. It is applied in auto body sheets for fenders, doors, and floor paneling [95].

The 4xxx series comprises Al alloyed with Si. The 4032 alloy is applied for pistons, compressor scrolls, and engine components. It exhibits high weldability and abrasion resistance [95].

The 5xxx series comprises Al alloyed with Mg; thus, it possesses enhanced strength. The 5005 alloy is applied for body paneling, fuel tanks, steering plates, and piping. The 5052 alloy is used for fuel tanks, truck trailers, suspension plates, display paneling, bracketry, disk and drum breaks, and many other non-critical auto parts. The 5083 alloy is used in complex automotive components such as engine bases and body paneling. The 5182 alloy is applied for structural bracketry, doors, hoods, and front wing end plates. The 5251 alloy is used for auto paneling [95].

The 6xxx series comprising Al alloyed with Mg and Si provides the best extrusion and casting capabilities, as well as ideal surface finishing. The 6016 and 6022 alloys are used for auto body covering, doors, trunks, roofs, fenders, and outer plates needing dent resistance. The 6061 alloy exhibits particularly good surface finishing characteristics, corrosion resistance, and high strength. It is applied for cross members, brakes, wheels propeller shafts, truck and bus bodies, airbags, and receiver tanks. The 6082 alloy, which possesses extremely high impact resistance, is used for the load-bearing framework. The 6181 alloy is applied for exterior body paneling [95].

The 7xxx comprising Al alloyed with Zn and Mg is immensely powerful and possesses extremely high strength. The 7003 alloy is an extrusion alloy often used for welded shapes in manufacturing impact beams, seat sliders, bumper reinforcement, motorbike frames, and rims. The 7046 alloy possesses hollow extrusion capabilities and good welding characteristics. It is applied similarly to 7003 [95].

Alloys from the 2XXX and 7XXX groups exhibit the most favorable mechanical properties (extremely high ultimate). However, for technological reasons, the susceptibility to welding is best for materials from 5XXX and 6XXX groups [14].

Cast Al alloys cannot undergo work hardening, so they are used in either as-cast or heat-treated conditions. Common heat treatments include homogenization, annealing, solution treatment, aging, and stress relief. Typical mechanical properties for commonly used casting alloys comprise a UTS ranging from 138 to 345 MPa and a YS ranging from 103 to 276 MPa with an elongation of up to 20% [96]. The 7075 alloy possesses extremely limited weldability and therefore cannot be used in conventional welding methods [97].

Some Al alloys (i.e., 1000, 3000, and 4000 series) have low mechanical performance, despite good electric and chemical properties, while heat-treatable Al-Mg-Si alloys (6000 series) present process robustness issues, a narrow welding lobe, and/or short electrode life, despite good mechanical properties [92].

The 7000 series Al alloys are beneficial for automotive structures, as they allow for obtaining improved mechanical and safety properties. However, they are prone to hot cracking and welding embrittlement, and therefore the joining of 7000 series sheets is expected to involve mechanical methods such as the use of self-piercing rivets [98].

3.3.1. Similar Al Alloys

CMT welding provides the efficient welding of similar alloys including the 7075 [99] and 6061 alloys [100]. Laser-CMT hybrid welding can join thin sheets made of the 6061 alloy [101]. Laser-CMT hybrid welding produces welded joints with better mechanical properties and aesthetics than laser welding and laser-MIG hybrid welding. The post-weld heat treatment (PWHT) improved the welded joints of 6061 alloys obtained

using the CMT gas metal arc welding (CMT GMAW) via the production of uniformly distributed fine precipitates [102]. The CMTW process can be used for the cladding of the 6061 alloy [103]; for the additive manufacturing of, for example, Al-6.3% Cu alloys [104]; and for repair welding, including an Al-Si-Mn alloy coating on a commercially pure Al plate [105].

3.3.2. Dissimilar Al Alloys

Luijendijk [106] reported that gas tungsten arc welding (GTAW) can be applied to dissimilar Al alloys of the 5xxx and 6xxx series, including 5083 (AlMg4.5Mn)-O, 5754 (AlMg3)-H32, 6082 (AlMgSi1)-T6, 6060 (AlMgSi0.5)-T6, and 6061 (AlMgSi1)-T4.

Kaba et al. [107] reported that dissimilar 2024-T3 and 7075-T6 structural hardening Al alloys can be joined by the TIG twine electrode arc welding process.

Jweeg et al. [108] found that the friction method involves stir welding and provides fine grains. Two new methods, namely friction stir processing (FSP) and the reverse of the rotation of stir processing (RRSP), were applied for joining 3 mm thick components made of dissimilar 5052 and 7075-T6 alloys. The FSW process included a one-pass process of the welded sample, whereas FSP involved two passes of welding in the same rotational direction, and RFSP was performed using two passes of welding, with the first pass using a tool with rotational speed (TRS) set counterclockwise and the second set clockwise.

Dissimilar Al alloys can be joined using laser welding, nonvacuum electron-beam (NVEB) welding, or gas tungsten arc welding (GTAW), as the high electrical and thermal conductivity of Al does not allow for the use of mash-seam welding for such alloys [109–112].

Bamberg et al. [92] evaluated the increased weldability of an AW-6111 (core sheet) clad with a 4040 alloy (cover sheet) through an RSW process, by establishing a proper welding lobe (affected by the nominal and maximum welding current levels and weld spot diameters). They also analyzed the electrode erosion behavior and the formed microstructure of joints. Compared to a pure 6111 Al sheet, the clad sheets exhibited improved weldability characteristics and prolonged electrode service life.

Studying the CMT welding joints of components made of 5083-H111 and 6082-T651 alloys, Gungor et al. [113] found that the microhardness of the welded joints was like characteristic hardness traverse across weldments [114], while decreases in hardness were slightly close to the BM.

Hardness decreases were maximum at the 18% level. For the 5083 similar alloy weld joint, microhardness values varied in the range of 77–92 HV0.2 and the hardness reached its minimum value in the weld zone. For the 6082 similar alloy weld joint, microhardness varied in the range of 79–96 HV0.2, hardness enhanced in the weld zone to around 96 HV0.2, while hardness decreased at the HAZ to 79 HV0.2. For the 6082 BM, hardness reached a value of around 82 HV0.2. For the weld joint using the 5083 and 6082 dissimilar alloys, microhardness varied in the range 76–96 HV0.2. Microhardness in the HAZ of this joint was similar to that of the 6082 similar alloy weld joint and that of the dissimilar 5083/6082 alloy weld joint. Differently, the weld zone of the dissimilar 5083/6082 alloy weld joint exhibited a slightly higher hardness value. The increase in microhardness close to the HAZ of the 6082 alloy occurred due to the partially solution-treated zone where some precipitates were dissolved, causing some post-weld hardening, but those not dissolved were coarsened. Microhardness degradation in precipitation-hardened 6082 alloy in the far HAZ of the dissimilar 5083/6082 alloy weld joint and the similar 6082 alloy weld joint resulted from the overaged zone where precipitate hardening occurred [115].

The weld joints and BM had adequate TS values. The average YS and TS were 244 and 272.3 MPa for the similar 5083 alloy weld joint, 216 and 230 MPa for the dissimilar 5083/6082 alloy weld joint, and 216.3 and 22.3 MPa for the similar 6082 alloy weld joint, respectively [113]. The CMT welding features were closer to FSW (higher WS and extremely low heat input) and had higher YS values than any other welding methods reported in the literature.

The 5083 similar welded joint exhibited the best fatigue performance along with porosity and YS values, followed by the 6082 similar weld joint and the 5083/6082 dissimilar weld joint [113].

Elrefaey and Ross [116] studied the welding joints of components made of 5182-O and 6082-T4 alloy sheets obtained in the CMT welding process. Such joints exhibited mechanical properties not worse than those for 5182/5182 and 6082/6082 joints. In the 5182 sheets, the HAZ exhibited microstructure comprising fine precipitates of the second phase and the coarsening of the Mg_2Al_3 precipitates in the Al matrix.

Boşneag et al. [117] experimentally studied the FSW process of three dissimilar alloys, with different properties, namely 2024, 6061, and 7075 alloys. They found that the rotation speed strongly affected the temperature of the process, which could differ by up to 50 °C with a twofold increase in the rotation speed. The higher value for the rotation speed reduced the vertical force required. The roughness values enhanced with an increase in the rotation speed and decreased with the progress of the welding process. Better microhardness properties and better mixing of metals in the joint were observed with higher values of the rotation speed.

Sharma and Upadhyay [118] studied the butt FSW process of 5086 and 7039 dissimilar alloys. Single-pass, dissimilar butt welds were obtained under optimized process parameters, a threaded cylindrical tool, and a 5086 plate on RS. They observed a heterogeneous microstructure in the stir zone. The transition boundary comprised much more strengthening precipitates than regions rich in Zn or Mg.

Some variations of collision welding are also applicable to dissimilar aluminum alloys. Pourabbas et al. [119] reported the use of the MPW for joining 4014/7075 alloys. Meng et al. [120] used vaporizing foil actuator welding (VFAW) for joining 2024-T3/7075-T6 sheets.

The applicability of these three welding methods for various Al alloys and the weldability of the latter are presented in Table 3.

Table 3. Pros and cons of both MIG and TIG processes. The applicability of three welding methods for various Al alloys and the weldability of such alloys.

Welding Method	Al Alloys Group	1xxx	2xxx	3xxx	4xxx	5xxx	6xxx	7xxx	Ref.
	Main Alloy Elements	Al	Al, Cu	Al, Mn	Al, Si	Al, Mg	Al, Si, Mg	Al, Zn	
	Thermally Strengthened	No	Yes	No	No	No	Yes	Yes	
Fusion welding		weldable	nonweldable	weldable	weldable	weldable	weldable	Non-weldable	[121]
FSW		weldable	weldable	weldable	weldable	weldable	weldable	weldable	[121]
Laser welding		Partially weldable	Partially weldable	NA	NA	weldable	weldable	Partially weldable	[122]

4. Features of Welded Al Joints and the Phenomena Occurring Therein

Most Al alloys are susceptible to liquation cracking during conventional fusion welding due to their large partially melted zone (PMZ), significant solidification shrinkage, high thermal contraction, and residual intermetallic compounds [123–126]. If liquation cracking occurs during the FSW of specific Al alloys, it must be controlled by choosing appropriate welding parameters, including tool dimension, backing material, cooling device, tool rotation speed, and peak temperature, to limit its incidence [127].

Cornacchia and Cecchel [128] studied the influence of various welding techniques including metal inert gas (MIG), cold metal transfer (CMT), and fiber laser–MIG hybrid method, on the microstructural and mechanical properties of joints between extruded 6181/6082-T6. They reported higher quality of CMT and fiber laser–MIG hybrid welding techniques than traditional MIG.

During the FSW process of the 2024 and 7010 alloys, liquation or melted film formation other than liquation cracking occurred [129,130].

4.1. TIG and MIG Welding Methods

In the case of TIG and MIG methods used for the welding of components made of 6082 alloys, an enhancement in the TS and YS values was observed in the weld area. During tensile tests of samples taken from the welded parts of this alloy, cracking occurred outside of the weld area, while the exact location indicated the propagation of the neck under tension in the HAZ area [14].

Wang et al. [131] studied the features of the various welded joint zones of the 7003 alloy welded by TIG welding using a 5356 welding wire. They found that the HAZ, occurring about 30 mm away from the center of the welding seam, was the softened zone due to η' (MgZn₂) coarsening. The corrosion resistance rates of the TIG-welded joint zones were in the order of the welded zone > the overaging zone > the BM > the quenching zone. Continuous precipitates from grain in the quenching zone formed a continuous anode corrosion channel, which intensified stress corrosion cracking and exfoliation corrosion and thus decreased the corrosion resistance of the quenching zone. Discontinuous precipitates from the grain in the overaging zone and the BM increased the corrosion resistance of these zones.

Alisibramulisi et al. [132] studied the butt-welded joints of plates made of the 6060 and 7046 alloys with two tempers, T4 and T6, prior to welding. The joints were obtained through a pulsed MIG-welding process in one single pass using a stainless-steel backing and the 5183 filler wire. The authors studied the subsequent effects of natural aging (NA) and post-weld heat treatment (PWHT) on the joints' properties. Post-weld heat treatment (PWHT) or an alternative natural aging (NA) significantly affected the resulting HAZ hardness distribution as well as the cross-weld tensile properties for the 6060 and 7046 alloys. Conversely, the initial temper condition was less important for the same properties. However, the initial temper condition influenced the resulting BM's hardness and the elongation to fracture for the 6xxx alloy.

Haryadi and Kim [133] studied the effect of PWHT on FCG behavior and the tensile properties of TIG butt-welded 6013-T4 sheets. The T82 heat treatment varied using three artificial aging times (soaking). They reported that the various aging in T82 heat treatment affected the mechanical properties of the joints. PWHT-T82 with aging for 18 h yielded the highest fatigue resistance, while 18 h aging provided the highest TS.

Hou et al. [134] studied the weldability of a 5052 alloy sheet using MIG and an Al-Mg-In welding wire. They reported that the joint strength of Al5.4Mg0.13In welding wire was close to that of the ER5356 welding wire. Under the welding conditions of 90 A and 40 mm/min, the TS of the welded joint of Al5.4Mg0.13In welding wire and ER5356 welding wire reached 86.9% and 86.1% of the BM's TS, respectively. The spreading areas of the Al5.4Mg0.13In welding wire were better than that of the ER5356 welding wire, causing good wettability.

Shanavas and Raja Dhas [135] studied the mechanical properties of the joints obtained by TIG welding and FSW with the 5052-H32 alloy. They found that the joints fabricated by the FSW process exhibited better metallographic and mechanical properties than those fabricated using the TIG welding process. The welding current and the inert gas flow rate strongly affected the quality of the TIG-welded joint. The best quality was achieved with a welding current of 180 A, an inert gas flow rate of 11 lpm, a WS of 100 mm/min, and an arc voltage of 20 V. Shetty et al. [136] reported that the selection of appropriate age-hardening parameters comprising the use of solutions and artificial aging with various elevated temperature–time conditioning with suitable welding parameters like current, voltage, WS, and inert gas allowed for the sound joining of the TIG-welded 6061 and 5154 alloys.

Zhu et al. [137] studied the effect of the post-weld treatment of the 5154 alloy by means of cleaning using a Nd:YAG laser after welding with different cleaning speeds. They found

that a Nd:YAG laser effectively removed the welding slag and eliminated the pores in the weld under a certain cleaning speed. For the cleaning speed in the range of 5.2–20.7 mm/s, laser cleaning eliminated the residual stress of the welded joint and improved the welding joint's strength.

Studying the GTAW-obtained welded joints of dissimilar alloys of the 5xxx and 6xxx series, including 5083-O, 5754-H32, 6082-T6, 6060-T6, 6061-T4, with the plate thickness in the range of 1.5–5 mm, Lujendijk [106] reported that the welds appeared asymmetric. The welding reduced the strength of the material in the HAZ to a smaller extent in solution-hardened and strain-hardened alloys compared to precipitation-hardened alloys. For the latter, the post-welding strength was less reduced in the naturally aged condition than in the artificially aged case. The reduction in strength for strain-hardened alloys was independent of material thickness for its specified range.

Kaba et al. [107] reported that the welding joints of 2024-T3 and 7075-T6 dissimilar structural hardening Al alloys obtained by a TIG twin-electrode arc welding process provided a stable arc and a good bead appearance. Several zones were generated, namely the molten zone WZ, the bonding zones LZ, and HAZs with various microstructures. The HAZs were fewer than those resulting from the conventional TIG welding process. Precipitates of θ (Al_2Cu), S (Al_2CuMg), and η (MgZn_2) types were formed in the HAZs of 2024 and 7075 BMs, respectively. The microhardness was lower in the molten zone and higher in the HAZ of the 7075-T6 alloy. The embrittlement of tensed samples was accompanied by a 44% and 37% drop in the TS of 7075-T6 and 2024-T3 BMs, respectively. The use of GTAW for various dissimilar combinations of 5182-H16, 5754-O, 6022-T4, and 6111-T4 alloys provided various cracking resistance during welding. It was the highest for the 5182/5754 alloy pair, while combinations of the 6022 alloy with either 5754 or 5182 alloys exhibited the lowest cracking resistance [138].

The Al 7xxx series alloys are weldable if the amount of Cu used as an alloying additive is below 1 wt.%. Cu causes hot cracks in welds or HAZs due to melting the metal and mixing it with the filler metal during the welding process, using MIG or TIG processes [139]. Such methods are conducted with high linear energy, which leads to a high degree of mixing of metals, thus increasing the risk of hot cracks. The high-energy course of the process leads to the formation of a dendritic structure in the HAZ, significantly weakening the mechanical properties and the corrosion resistance of these alloys [140].

The use of laser beam welding or hybrid laser/gas metal arc GMA welding is also limited for Al 7xxx series alloys. This is due to the high-power density of the integrated laser beam, compared to arc welding methods, which increases the risk of hot cracks and induces intense metal evaporation, generating many gas pores in turn [141].

Niu et al. [142] studied the butt-welded joints of components made of 2219-T87 alloys obtained by a double-pass tungsten inert gas arc welding process. They found that the two fusion zones (FZs) were the weakest regions in the joint, with microhardness values of 76 and 78 HV. The microhardness of the heat-affected zone (HAZ) increased with the increase in distance from the fusion line except for a valley value at a distance of about 4.5 mm. The mean grain size of the two FZs was 74.4 and 79.2 μm , whereas it was 41.5, 44.9, and 43.4 μm for the two HAZs and the BM, respectively. The coarse whitish particles of FZs containing about 60.4% and 54.2% Cu had a small strengthening effect, while the percentage was about 24.6% for the BM zone, which was close to that of the HAZ. A high number of θ' strengthening phases dispersed in the BM zone, whereas hardly any precipitates occurred in the FZ and the HAZ adjacent to the FZ. So, the coarsening of grain size, the lowering and segregation of the alloying element content, and precipitate evolution caused softening in the FZ, while precipitate evolution caused softening in the HAZ.

Kwon and Weckman [143] studied the welded joints of 1.2 mm thick sheets made of the 5182 alloy obtained using a plasma arc welding–TIG (PAW-TIG) double-sided process. They found that the structure of all joints mainly comprised tiny equiaxed crystals, and the proportion increased with the increase in WS. In this process, welding heat was concentrated, the cathode cleaning effect was high, and the welding seam was large.

Nyrkova et al. [144] studied the properties of the welded joint of components made of the 2219 alloy obtained by single-pass welding with a non-fusible electrode along and across the rolled product and heat-treated to the T62 state in liquid amyl and its vapors at a temperature of 50 °C for 45 days. They reported that, in the longitudinal direction, the welded joints exhibited a YS varying in the range of 301–317 MPa compared to that of the BM in the range 295–297 MPa, a strength limit in the range of 409–415 MPa compared to that of the BM in range of 422–425 MPa, and elongation in ranges of 4.0%–5.8% and of 17.6%–19.1%, respectively. In the transverse (P) direction, such joints showed a TS varying in the range of 309–331 MPa compared to that of the BM in range of 304–307 MPa, a YS varying in range of 392–414 MPa compared to that of the BM in range of 428–433 MPa, and elongation in ranges of 2.1%–3.3% and of 12.6%–15.0%, respectively. The strength coefficient of the welded joints in the longitudinal direction was 0.96, while in the transverse direction, it was 0.94. The joints in the above environment were resistant to corrosion cracking and intergranular corrosion, and resistance against exfoliating corrosion was in grade 2. Aging in amyl and amyl vapors did not change the strength grades of the BM samples and the welded joints in both directions, while the plasticity parameters varied: The YS of the BM enhanced by ~5%–6%, whereas the YS of the welded joints decreased by ~6%–7%, and the relative elongation of the BM decreased by ~5%–16%, whereas that of the welded joints decreased by about ~20%. All samples were fractured in a viscous manner. After the exposure to amyl, the coefficient of the strength of the welded joints in the longitudinal and transverse directions was equal to 0.91, and after using amyl vapors, it was 0.95 in the longitudinal direction and 0.96 in the transverse direction.

According to Su et al. [145], 5083 Al plates can be welded using 5356 alloy filler metals comprising various amounts of Sc and Zr. Significant grain refinement occurred in the fusion zone (FZ) of the welded joints after the addition of Sc and Zr. The filler metal comprising 0.2 wt.% Zr + 0.1 wt.% Sc yielded the smallest grain size with 29 µm, and the filler metal with 0.2 wt.% Sc + 0.1 wt.% Zr addition resulted in a close grain size value of 30 µm. The 0.2 wt.% Sc addition effectively modified the microstructure of filler metal and enhanced the mechanical properties. The grain size of the fusion zone using 5356 + 0.2 wt.% Sc + 0.1 wt.% Zr filler metal decreased by 75.8%, and the highest UTS was increased by 15% in comparison to that of the unmodified alloy joints. However, the individual addition of 0.2 wt.% Zr could not clearly modify the filler metal. The improvement in mechanical properties resulted from the occurrence of refined grains.

According to Palanivel et al. [146], the fusion welding joints of Al alloys can comprise various defects, including hot cracking, porosity, slag inclusion, etc., which worsen the mechanical and metallurgical properties. These defects very seldom occur in friction stir-welded joints due to a lack of melting during the welding process. During this process, metals are joined in the solid state because of the heat generated by the friction and flow of metal resulting from the stirring action.

Kumar and Sundarrajjan [13] optimized the pulsed TIG welding parameters for the butt joints of 2.14 mm thick sheets made of the 5456 alloy obtained using a 5356 filler material. Before welding, the BM sheets were pickled with a solution of NaOH and HNO₃, wire-brushed, degreased in acetone, and finally preheated to 100 °C. After planishing, the mechanical properties of the joints were enhanced by up to 15% due to the release and redistribution of internal stresses in the weld region. The behavior of the welded joints at the optimum conditions, including a peak current of 80 A, a base current of 40 A, a WS of 230 mm/min, and a pulse frequency of 4 Hz, resulted from the increase in the amount of Mg₂Al₃ precipitates formed in the Al matrix.

The selection of appropriate TIG welding parameters, including current, torch speed, arc voltage, arc gap, electrode diameter, electrode tip angle, shielding gas, and flux, improves penetration as well as weld quality. TIG welding disadvantages such as low weld penetration can be limited, and TIG weld quality can be enhanced using various methods, including ATIG (activated-flux TIG), FBTIG (flux-bounded TIG), and PCTIG (pulsed

current tungsten inert gas) welding. In particular, the use of flux or fluxes and the pulsed current method improved both the weld penetration and weld quality [147].

Chen et al. [148] studied the effects of ultrasound on grain fragmentation in the TIG weld of pure Al. They found that the use of ultrasound can break the grain of the TIG weld of pure Al. The microstructure transformed from a plane crystal, columnar crystal, and uniform equiaxed crystal into a plane crystal, deformed columnar crystal, and nonuniform equiaxed crystal after the application of ultrasound. The ultrasonic amplitude and welding current highly affected grain fragmentation. The degree of fragmentation first increased and then decreased with an increase in ultrasonic amplitude, and it increased with an increase in the welding current. The higher intensity of acoustic nonlinearity increased the degree of grain fragmentation. The acoustic pressure in the weld pool exceeded the cavitation threshold, and cavitation bubbles appeared. The use of ultrasound did not change the flow velocity in the weld pool. The high-pressure conditions under cavitation led to grain fragmentation in a pure Al TIG weld at an ultrasonic-assisted TIG welding process.

Gupta et al. [149] compared TIG and MIG welding techniques applied to the 6062 alloy. They found that the impact strength of the MIG joints exceeded that of the TIG joints. However, the hardness in the weld metal region was lower than that of the BM. The hardness pattern in the MIG-based weld region exhibited higher values compared to that in the TIG-based weld region. In the case of MIG, the microstructure was exceptionally fine and equiaxed, exhibiting uniformly distributed grains with strengthening precipitates, while after TIG welding, dendritic grain structures were observed. Due to a fine-grain structure, the MIG-based joint exhibited better tensile and mechanical properties compared to those of the TIG-based joint. The joint efficiency reached up to 40.5% in the case of TIG, while it was up to 91.8% in the case of MIG. Therefore, MIG is more suitable than TIG welding for joining the 6062 alloy.

Zhang et al. [150] studied a 6061 alloy joint obtained using a double-sided double TIG welding process with a single power supply. The structure of this joint was equiaxed, with fewer columnar crystals, and a lower number of thermal cracks in the weld. Additionally, the pore size of such joints was smaller, and the distribution was diffused in comparison to the joints obtained by plasma arc welding with variable polarity values.

Squillace et al. [151] compared the features of the welded butt joints of the 2024-T3 alloy obtained with TIG and FSW techniques. They noticed general degradation of the mechanical properties of the TIG joints, due to elevated temperatures experienced by material. For the FSW joint, lower process temperatures and high plastic deformations due to tool motion resulted in a complex situation because slightly worsened mechanical properties appeared in the nugget zone, including the flow arm zone and TMAZ, while in the HAZ, due to the initiation of the heat treatment of the alloy, a slight improvement in such properties appeared. In the nugget zone, the light recovery of hardness relative to the TMAZ occurred, due to the recrystallization of an exceptionally fine-grain structure. In both kinds of joints, the parent alloy exhibited a clear pitting tendency, while the weld bead and the HAZ showed passive behavior. In the case of the FSW joint, such differences were fewer. The nobler behavior occurred on the RS of the FSW bead compared to its AS.

Comparing the fatigue properties of 5052 alloy joints obtained by FSW and TIG techniques, Wang et al. [152] reported that the fatigue properties of FSW-based joints were better than those of the TIG-based ones.

Comparing microstructural and mechanical characteristics of welds of the Al–4.5 Mg–0.26 Sc heat-treatable alloy obtained with TIG and FSW techniques, Cabello et al. [153] found that hardening precipitates were more affected by the TIG process than by the FSW process. This highly reduced the mechanical properties of the TIG welds.

Investigating the influence of welding processes on the mechanical and metallurgical properties of Al–Mg–Sc alloy plates welded using FSW and TIG techniques, Zhao et al. [154] reported that the mechanical properties of the FSW-based joint were much better compared to those of the TIG-based joint. The TS and the YS of the FSW-based joint were 19% and 31% higher than those of the TIG-based joint, respectively. Due to the low welding temperature

of the FSW process and the high thermal stability of $\text{Al}_3(\text{Sc}, \text{Zr})$ particles, cold-working microstructures were well preserved.

Comparing the fatigue crack growth behavior of square butt joints of the 2219 alloy, obtained with the GTAW, EBW, and FSW techniques, Malarvizhi and Balasubramanian [155] reported that the FSW joints exhibited superior fatigue crack growth resistance compared to EBW and GTAW joints. This was due to the formation of exceptionally fine grains.

Investigating the mechanical and metallurgical properties of Al-Mg-Mn-Sc-Zr alloy joints obtained with FSW and TIG techniques, Zhen et al. [156] found that the strength of FSW and TIG joints decreased in comparison to that of the BM, but the strength of FSW joints was higher than that of the TIG ones. The loss of substructure strengthening and an insignificant loss of precipitation strengthening of $\text{Al}_3(\text{Sc}, \text{Zr})$ reduced the strength of the FSW joint. In the case of the TIG welded joint, the lack of both strain hardening and a significant precipitation strengthening effect of $\text{Al}_3(\text{Sc}, \text{Zr})$ particles contributed to its softening. Simultaneously, the grains in the nugget zone of FSW joints were finer than those in the molten zone of TIG joints.

Anjaneya Prasad et al. [157] studied 6061 alloy joints obtained by MIG and FSW techniques. The MIG welding process was realized with a WS of 110 mm/min. The FSW provided 10–100 times smaller grains than MIG in the microstructure of the joints. The MIG process produced a lower TS than FSW. The amount of heat input influenced the weld material hardness, and the width of hardness was influenced by the shoulder diameter and heat input. The FSW process enhanced the weld quality.

Jannet et al. [158] compared the mechanical properties of the joints of 6061-T6/5083-O alloys obtained using FSW under four rotation speeds (450, 560, 710, and 900 rpm) and fusion welding (MIG and TIG). They reported that the PWHT process provided better tensile properties in all joints; however, a better TS was observed in FSW joints. The latter exhibited grain refinement with a fine distribution of precipitates. Microhardness in the HAZ and the BM was lower than that in the weld region. The width of the HAZ of FSW joints was narrower than for fusion-welded joints.

Sasidharan et al. [159] compared the tensile and microstructural properties of the joints of the AA2219 alloy obtained with DCSP (direct-current straight polarity) TIG and the FSW technique. They found that the UTS of the DCSP TIG joint was 257.5 MPa, while that of the FSW joint was 287.9 MPa, providing WE values of 58.5% and 65.4%, respectively. The percentage elongation for FSW was also higher than that of the BM. The FSW joints exhibited much fewer microporosities than DCSP TIG joints.

Kumar et al. [160] performed TIG, MIG, and FSW using the AA6061 alloy. FSW was performed under 60 mm/min WS, 0.69 kJ/mm heat input, 635 rpm of TRS, 16mm tool shoulder diameter, 7 mm pin diameter, 4.7 mm pin length, and 20-degree tool tilt angle. The heat input in the case of the FSW process was less than that of the TIG and MIG welding processes. In FSW, the heat input was 38% less than that in TIG and 51.2% less than that in MIG. FSW joint efficiency was 19.4% higher than that of TIG and 35.5% higher than that of MIG. Compared to the TIG and MIG techniques, the FSW method provided sound welds with higher joint efficiency and less heat input.

Navyashree and Sivaramakrishna [161] compared the properties of plates made of the 6082 alloy joined using TIG and FSW techniques. They found that the microstructure of the FSW joint differed from that of the TIG joint. The TS and hardness of the FSW joint were better than those of the TIG joint. The FSW method with a tool having a smooth pin provided a smooth surface finish. The HAZ of the FSW joint was well fused and free from nonmetallic defects.

Work-hardened (non-heat-treatable) Al alloys including the 5xxx series exhibit much less strength in the HAZ in the case of arc welding due to the annihilation of dislocations. In the fusion welding of Al alloys, a wide HAZ is formed due to high heat conduction. However, in the case of laser welding providing less heat input and more concentrated energy, the HAZ is narrower, leading to less strength loss [30].

Interestingly, the use of nanoparticles coated on BMs and electrodes in fusion welding (GMAW and GTAW) provides joints with improved mechanical properties and microstructural formations by grain refinement [162].

To summarize, the mechanical and metallurgical properties of welded joints are affected by welding process parameters. Fusion welding reduces the mechanical properties due to softening in the HAZ and weld metal [29]. FSW joints exhibited better mechanical and metallurgical properties in comparison to TIG and MIG joints, similar to the findings in [163]. According to [164], MIG welding provides a high WS and versatility. During MIG welding, porosity is a major problem affecting the weld strength. Also, residual tensile stress sometimes occurs, affecting the mechanical properties of the welds. Due to faster cooling rates, cracks and deformation occasionally occur in MIG-welded joints. In particular, the changing values of welding current and WS can strongly affect the weld quality, its microstructure, hardness, TS, and impact strength. Lower welding voltage and gas flow rate and a higher WS and wire feed rate result in the maximum UTS of the weldment. During the MIG process, the weld metal can fail to fuse properly with the BM under an improper WS or welding angle. MIG welding is not suitable for vertical or overhead weld positions due to the high heat input and fluidity of molten metal. During the welding of the BM, two zones, namely the HAZ and weld pool (melted zone), are generated, and their microstructure is strongly affected by input parameters. In particular, the input current changes the grain size and structure of the HAZ by producing the heating effect.

Conventional MIG welding is characterized by an unstable arc, insufficient heat input, and small penetration depth [5]. These problems can be resolved with the pulsed MIG welding technique based on a pulsed current waveform, allowing for the precise control of the metal transfer rate [165], which is applicable to 6061/A356 or 5083 alloy joints [166].

The arc of MIG welding can also be stabilized using the plasma MIG welding technique [167].

The microstructural and mechanical behavior of MIG weldments can be improved using an alternating magnetic field and ultrasonic vibration. The metal transfer rate and stability of ultrasonic MIG welding are much better than that of conventional MIG [168,169].

The main disadvantage of TIG welding, namely its low weld penetration, can be limited, and TIG weld quality can be enhanced using various methods, including ATIG (activated flux TIG), FBTIG (flux-bounded TIG), and PCTIG (pulsed-current tungsten inert gas) welding. In particular, the use of flux or fluxes and pulsed current methods improved both the weld penetration and weld quality [147].

It can also be noted that comparative studies focused on the use of various welding techniques for Al alloys of the 5xxx series have only been conducted by very few researchers.

4.2. Cold Metal Transfer (CMT) Welding Method

Al alloys can be joined using low-energy welding methods, such as cold metal transfer (CMT) [38,170,171], which is a modification of the GMA welding process, limiting the amount of heat input to the welding zone. This is due to metal transfer in a short arc using the reciprocating wire feeding (RWF) technology [172,173]. During CMT welding, temperature variations in welds and parent metals strongly affect the material characteristics, residual stresses, and thus dimensional and shape accuracy of the welded products [174]. Feng et al. [175] pointed out that the CMT process is especially suitable for welding thin Al alloy sheets due to the low heat input and slight deformation.

The welded joints of parts made of a 7075 alloy using the CMT method exhibited no spatter or cracks and extremely low porosity. The joints had minimum microhardness in the weld zone (WZ) and slight hardness weakening in the HAZ compared to the BM. The joints had mechanical property coefficients of 77%, 60%, and 69% for the YS, UTS, and elongation, respectively. CMT welding produced joints with mechanical characteristics better than MIG and TIG processes and comparable to FSW and LBW processes [99].

During the CMT welding of thin sheets made of a 6061 alloy using a filler material with the same composition as the BM, the welded joints possessed a quasi-binary composition.

These joints were less susceptible to solidification cracking and exhibited a controlled fusion line, a narrower HAZ, and a weakened intermetallic phase area. The welded joints revealed fine recrystallization. A uniform distribution of grains and their size in the HAZ and the BM occurred [100].

Dutra et al. [176] studied the welded joints obtained using two different wire electrodes 5183 and 5087. The weld using the 5087 electrode exhibited higher mechanical performance during tensile tests. Microhardness was similar in both the WZ and the HAZ. The welded joints obtained with both wire electrodes showed the same toughness. The crack tip opening displacement toughness test showed that the applied combinations of the base and feed material yielded good cracking resistance characteristics. A higher incidence of pores was observed in the case of the 5183 wire electrode.

Shu et al. [177] studied the most vulnerable zones in three-pass cold metal transfer (CMT)-welded joints. They found that the highest principal stress made the joint symmetric, becoming overly sensitive to tensile cracks. The boundaries between the weld seam and the base plates were sensitive to cracks as the equivalent von Mises stress was the highest when the first inter-pass cooling was finished. The third weld pass and the inter-pass remelted zones showed low mechanical performance resulting from the coarse grain and the coarse grain boundary, respectively.

During studies on the CMT welding of parts made of the AA7A52 alloy, Shu et al. [178] found that intergranular segregation, providing the coarse grain boundary between weld passes, resulted in inferior mechanical performance. A tri-axial stress distribution in the fusion zone pointed to the tendency to tensile failure under service conditions. The softened zone was much wider inside the base plates than close to the flat surfaces. The strip-shaped quenched zone was narrower than the averaging zone of the internal plates. The control of heat input amount via the selection of appropriate welding parameters led to the absence of hot cracks in the welded joints of the 7075 alloy [170].

One of the phenomena occurring in various Al-welded joints is the so-called 'weld unzipping'. Under dynamic loading, such joints can fail due to this mechanism, which is characterized by unstable crack growth along the HAZ–weld metal interface [179,180]

Gay et al. [181] stated that the fracture mechanics approaches allow for understanding weld unzipping. The failure along weld lines is quantified via the difference between stable and unstable fractures. When a structure is subjected to certain load types, the propagation of a crack is driven by the stress field developing ahead of the crack tip. The stress and strain fields are characterized by the stress intensity factor (KI) under elastic conditions or the J integral (JI) or crack opening displacement under conditions with significant plasticity. Such parameters describe the mechanics of the crack affected by the applied load and the length of the crack. The resistance of a particular material to fracture is the fracture toughness described by a single value of KI or JI at which fracture occurs in that material. However, in thin sections of tough metals, a fracture is a clearly long-lasting process of the material deforming and tearing ahead of the crack tip. This is characterized by a tearing resistance curve, which is determined as the function of the crack growth resistance (R) in a material against KI or JI, known as a K–R or J–R curve, and captures the relationship between the crack tip stress and strain fields and the process of fracture for a particular metal. The balance between no fracture, stable fracture, and unstable fracture is driven by the relative magnitudes of the stresses and strains ahead of the crack tip and the ability of the material to resist those stresses and strains. This is represented by a comparison of the stress intensity factor, or the J integral, for the cracked and loaded structure and the tearing resistance curve for the metal under consideration. No fracture occurs if the applied KI or JI is less than the K_{material} or J_{material} ; then, the crack does not extend. An unstable fracture occurs when the applied KI or JI is higher than the K_{material} or J_{material} , and the crack therefore extends. A stable fracture occurs when the applied KI or JI is initially greater than the K_{material} or J_{material} and then becomes less than the K_{material} or J_{material} as the crack extends and then stops. It does not extend until the applied KI or JI is sufficiently increased to again overcome material resistance to fracture.

Chinnasamy et al. [68] studied the welded joints of components made of 2014-T6 alloys obtained by the pulsed CMT welding process. They reported that a defect-free weld was obtained under a constant WS of 450 mm/min, a welding current of 110 A, and an electrode feed rate of 5550 mm/min. The joint exhibited a maximum strength of 303 MPa, extending joint efficiency up to 67%. This was due to welding wire pulsing and dip and retreat motion refining the dendritic grains in the weld metal and enhancing the strength of the joints.

The CMT welding of the 2A14 alloy in 3 mm thickness using ER2319 filler metal allowed for obtaining joints with excellent quality under a welding current of 105 A and a WS of 8 mm/s. The weld width and porosity gradually enhanced with the constant increase in the welding heat input. The center of the welded joint consisted of many fine equiaxed dendrites, and the gray matrix was uniformly distributed accompanied by many dots and blocks as a white second phase, corresponding to the composition of the Al₂Cu phase. The microhardness of welded joints under various welding heat inputs was stable and exhibited a certain softening degree; the BM was the highest, followed by the HAZ [182].

In the case of the 7475-T7351 alloy, CMT welds exhibited better mechanical properties as compared to those obtained with GMAW [183].

Tian et al. [184] reported that, during CMT welding for aluminum alloy cladding fabrication, the enhancement of heat input caused a higher weld depth and contact angle and a reduced overlap length.

To summarize, the lower volume of heat input makes CMT welding an expected method for joining thin sheets and plates made of Al alloys [175,185] or from Al/steel [186].

CMT technology is expected to be used not only for welding thin Al alloys but also for welding dissimilar metals such as Al alloy/steel and Al alloy/Mg alloy [186–189].

The use of the CMT welding technique limits spatter and the distortion of joints and requires limited cleanup. CMT requires less current for the same amount of material deposition in comparison with conventional pulsed MIG welding [175].

In this technique, the length of the arc can be monitored and easily controlled through mechanical means. Therefore, the stability of the arc is perfect, irrespective of the surface to be joined and a faster rate of joining, thereby making it possible to employ the CMT welding technique in all positions and for any application [186].

There are several recently developed types of CMT welding techniques, namely pulsed advanced CMT [68], advanced CMT, CMT + P, and dynamic CMT [190]. Conventional CMT, pulsed CMT (CMT-P), advanced CMT (CMT-ADV), and pulsed advanced CMT (CMT-PADV) are suitable processes for depositing Al alloy due to excellent performance in controlling porosity. Such depositing methods are applicable in modern additive manufacturing of Al alloys and are also used in the automotive industry [104,191].

According to [38], laser–CMT hybrid welding provides welds with better mechanical properties and aesthetics than laser welding and laser–MIG hybrid welding.

4.3. Laser Welding

Bunaziv et al. [29] performed an excellent review on laser beam and laser–arc hybrid welding of various Al alloys. They studied the solidification cracking and evaporation of alloying elements, porosity and keyhole stability, and the weldability of such alloys in detail.

Bergman et al. [192] noticed that the low absorption of laser radiation at a wavelength of 1064 nm and the high thermal conductivity hindered the effective laser welding of 5754 and 6016 Al alloys.

According to Park and Rhee [193], in Al laser welding, the strength of the weld is typically reduced by porosity, underfill, and Mg loss. To overcome these problems, laser welding with a filler wire is utilized.

Schempp et al. [194] noticed that the refinement of the weld metal grain structure improved the mechanical properties of the weld and limited its susceptibility to solidification cracking. Using AlTi5B1 for the refining of the grain microstructure of laser beam (LB) and gas tungsten arc (GTA) Al welds by inoculation, it was found that these methods limited

the mean grain size of the weld metal, and through a transition from columnar to equiaxed grain structure, CET occurred. The development of both grain size and shape was affected by the BM (alloys 1050A, 5083, and 6082) and the welding process. The GTA welding process allowed for better refinement than LB. The solidification of LB welds occurred faster than that of GTA welds.

Zhao and DebRoy [195] elaborated on a numerical model for the prediction of the keyhole geometry and the temperature profile, particularly macroporosity formation, during the laser welding of Al alloys. Based on the knowledge that the weld metal had large pores when the welding mode changed from conduction to a keyhole mode or vice versa, the model enabled the prediction of macroporosity formation when the welding mode was caused by an alteration in the process parameters.

Pastor et al. [196] investigated the porosity during the laser welding of Al alloys. They found that the macroporosity in the welds was caused by the instability of the keyhole. They explained that the too-quick collapse of the keyhole prevented the molten metal from flowing into the center of the keyhole before the realization of solidification. The instability of the keyhole and pore formation could be limited by controlling laser beam defocusing and the WS. With respect to underfill, a recurrent defect occurred at the root of full-penetration welds.

Sheikhi et al. [197] studied the mechanism of the hot cracking phenomenon occurring during the pulsed laser welding of the 2024 alloy. The author explained that most forms of cracking were caused by shrinkage strains that occurred during the cooling down of the weld metal. The racing development was controlled by two opposing forces: the stresses generated by the shrinkage of the metal, and the surrounding rigidity of the BM. Shrinkage stresses increased with the increase in the shrinking metal volume. The solidification rate affected the vulnerable zone length, which controlled the susceptibility to solidification cracking. A greater solidification rate caused a higher volume change rate and a weakening vulnerable zone length, enhancing the liquid flow rate. Therefore, for the removal of solidification cracks under a high solidification rate, a higher liquid flow rate or a smaller vulnerable zone length is needed.

Yi et al. [198] studied the microstructure and texture of the joints of plates made of 6016 and 5182 alloys obtained by laser welding with a wire used in the same welding process. They reported that the weld seams of 6016 and 5182 alloys comprised columnar dendrites and equiaxed dendrites, and strong texture along the crystallographic direction $\langle 100 \rangle$ appeared in the columnar dendrite area. Constitutional supercooling together with heterogeneous nucleation affected the welded joints. As heterogeneous nucleation strongly affected the 6016 alloy joint, the ratio of the equiaxed dendrites in the 6016 alloy was high, the grain orientation was randomly distributed, and the main texture of the columnar dendrites was a cubic one ($\langle 100 \rangle \{001\}$). In contrast, heterogeneous nucleation slightly affected the 5182 alloy joint, the texture of the equiaxed dendrites was distributed along the $\langle 100 \rangle$ direction, the 5182 alloy joint mainly contained columnar dendrites, and the textures of the columnar dendrites were fiber $\langle 100 \rangle \parallel \text{RD}$, cubic ($\langle 100 \rangle \{001\}$), and Goss ($\langle 100 \rangle \{011\}$).

Sánchez-Amaya et al. [199] studied the effect of laser power and the linear welding rate on the sizes and properties of butt weld beads made of the 5083-T0 and 6082-T6 alloys using a high-power diode laser. Maximum penetration values of 3 and 2.3 mm were obtained for 5083 and 6082, respectively. This is related to the dependency of thermal properties on the total amount of alloying elements. The microstructure of the different beads was similar for both alloys and for all the studied conditions. The fusion zone had two zones, an external zone with dendritic growth and an inner part with the fine precipitation of the second phases in a solid solution matrix of Al. In both alloys, the microhardness of the fusion zone was a little higher than that of the BM surrounding the bead. The weld beads exhibited good corrosion resistance.

In the case of Al alloys in the 2xxx series, during one-sided laser welding, the welding piece is heated on one side, causing large deformation, sizeable residual stress, low penetration depth, and poor joint performance [87].

Zhu et al. [200] fabricated a joint of 2 mm thick components made of similar AA2219-O alloys using fiber laser welding, after which a combination of PWHT and electromagnetic (EM) pulse treatment was applied. This post-welded treatment provided joint efficiency exceeding 100%. Such a treatment reduced the occurrence of eutectic phases and promoted precipitation strengthening via dispersoid formation, i.e., the G.P(II) zone and metastable θ'' phase (Al₂Cu). The joint hardness was higher than that in the BM. A TS of 393 MPa after PWHT was reached, while that in the BM was 153 MPa, indicating an increase of 258%. After EM treatment, it further increased to 303%. The ductility (a decrease in area after tensile testing) decreased from 33% in the BM to 10% under an as-welded condition. Such ductility was restored to 18% after PWHT but dropped down to 9%–11% after EM treatment.

Wang et al. [201] obtained a joint of components made of 8 mm thick similar 5A06-H112 alloys using fiber LBW. The WE reached up to 90%. Infinity-shaped oscillations (∞) with fiber LBW reduced the porosity from 40% down to 2%. Simultaneously, weld elongation reached 90% of that in the BM. The oscillations significantly reduced the penetration depth with a change from the keyhole to the transition mode.

Peng et al. [202] developed a joint of components made of 35 mm thick similar 5A06 alloys using fiber LBW under subatmospheric pressure. The WE at 10 Pa ambient pressure reached up to 90%, while at 1 atm, it was up to 73%. The use of a subatmospheric pressure allowed for enhancing the mechanical properties of deep welds because of higher retained hardness in the fusion zone, lower porosity, lower evaporation of Mg, and more uniform grain distribution.

Braun [203] developed a butt joint of components made of similar 6013-T4/T6 alloys using the Nd:YAG LBW process with an Al₁₂Si wire and various atomized powders as filler material. The WE reached up to 75%. The welded joint underwent PWHT, which allowed for enhancing the WE by up to 90%. No cracking occurred at the macro level. In the as-welded condition for WM independent of the tempering condition, similar hardness was obtained with softening (T6 for the BM had 140 HV) except for the weld obtained using AlSi₁₂Mg₅ powder. Hardness enhanced with the increase in Si with Mg content. The PWHT applied to T6 restored low hardness in the FZ, but for WM, low hardness persisted. Post-PWHT restoration in the WM resulted from precipitation strengthening in α -Al dendrite cores comprising needle-shaped β'' and Q' phases, which were aligned along the <100> direction as a result of Mg and Si enrichment from filler powder. The residual elements (Fe and Cu) that had a deleterious effect on mechanical properties appeared in the inter-dendritic area. Al₁₂Si was an optimum filler material compared to filler powders comprising Si with Zr, Mn, and Cr.

Zhang et al. [204] obtained a butt joint of 2 mm thick components made of similar Al-Zn-Mg-Cu (0.23 wt.% Zr and 0.14 wt.% Er)-T6 alloys using fiber LBW. The welded joint was subjected to PWHT (7–60 days), providing significant softening in the WM and HAZ closer to the BM. The post-PWHT WE reached up to 70%. Small grains appeared near the fusion line, while the WM center comprised equiaxed dendrites with higher grain sizes like the BM. Strong segregation of alloying elements along grain boundaries was observed, leading to the formation of brittle T phases comprising Al₂Mg₃Zn₃. The matrix in the WM exhibited the absence of Zn and Mg, inducing softening. There should be a careful balance between heat input and the response of alloying elements, which makes such alloys hard to weld.

Enz et al. [205] fabricated a T joint of 2 mm thick components made of dissimilar 7050/2023 alloys via fiber laser welding using a 4047 wire. Helium was used as a shielding gas, which allowed for porosity suppression by reducing the melt viscosity with improved degassing. The WE reached up to 90%, which was achieved due to softening in the welded zone and the HAZ.

Viscusi et al. [206] obtained a T joint of components made of dissimilar 3 mm thick and 6156/2.7 mm thick 2139 alloys with Nd:YAG laser welding using a 4047 wire. The WE

reached even above 100%. Slight softening was observed in the HAZ. The joint exhibited favorable strain distribution after welding in the BM but not in the softer HAZ.

Enz et al. [207] developed a butt joint of 2 mm thick components made of dissimilar 7075-T6/5182-O alloys using Nd:YAG. LBW. A larger beam diameter (0.8 mm as focused) caused a larger weld pool with improved degassing and low hydrogen (2 ppm). The 7075-T6 alloy exhibited softening, while the AA5182-O alloy possessed similar hardness as that of the BM in both the WM and the HAZ. PWHT applied to T6 significantly restored the hardness to the level of the BM. The WE reached up to 118%. A fracture appeared in the BM of the 5181 alloy; in other cases, the fracture existed in the fusion zone resulting from discontinuities (undercut/underfills).

Bunaziv et al. [29] stated that the high thermal conductivity and reflectivity of Al alloys induce lower laser beam absorptivity with lower processing efficiency. Weld porosity, humping, and underfills often result from a low melting point and density, which promotes high liquidity with low surface tension. Porosity is the most persistent, and it worsens mechanical properties. Laser beam welding (LBW) significantly enhances productivity due to high penetration depths. The deep penetration keyhole mode may enhance productivity >10–20 times compared to conventional arc welding. However, welds are susceptible to cracking and porosity.

Bunaziv et al. [29] pointed out that both process productivity and quality can be further improved using laser–arc hybrid welding (LAHW). Porosity can be minimized by optimizing process parameters, which is complex, especially for LAHW, as many adjustable parameters sometimes interact with each other and need time to adjust. LAHW may be beneficial due to the use of a filler wire and a wider process window through the manipulation of heat input. The development of novel filler materials can provide enhanced strength and corrosion resistance. The use of novel technologies such as laser beam oscillations, electromagnetic backing, shorter wavelength diode laser sources, grain refiners, and the use of nanoparticles in filler wires may further improve the quality of welds. The use of a vacuum, although expensive, can solve most processing problems, thus significantly enhancing productivity.

To summarize, laser welding technology is often used for joining Al alloys due to its adjustable heat input, high energy density, high accuracy, small deformation after welding, and slight changes in structure, as was confirmed in [87].

It should also be noted that the WE obtained using the laser welding process can exceed 100%.

4.4. Laser–MIG Hybrid Welding

Laser–MIG hybrid welding combines the advantages of both laser and MIG welding by reducing residual stress and enhancing mechanical properties and efficiency. However, laser–MIG hybrid welding also results in cracks, porosity, and coarse grains, which strongly affect the mechanical properties of welded joints [29,208–211].

Yan et al. [212] fabricated a defect-free joint of 8 mm thick components made of similar 2A12 alloys (an Al–Cu–Mg alloy of 2xxx series, used in truck wheels) with CO₂ laser–MIG hybrid welding using a 2319 (Cu~6 wt.%) wire. The joint efficiency reached up to 78%. They observed the segregation of Cu/Si-rich precipitates on grain boundaries and in inter-dendritic areas, causing intergranular fracture. The wire providing more Cu for the precipitates' formation allowed for obtaining higher strength. They suggested that the finer distribution of precipitates can be obtained by controlling the welding parameters together with the Cu-alloyed filler wire.

Ahn et al. [213–215] obtained a butt joint of 3 mm thick components made of similar 2024-T3 alloys in fiber laser–MIG hybrid welding with different He–Ar shielding gas combinations and a 4043 wire. The joint efficiency reached up to 86%. They reported that He-rich shielding gas allowed for obtaining wider welds with a lower undercut and underfill. HAZ softened up to 20% because of the coarsening and dissolution of secondary phases under a low cooling rate. The weld metal strength decreased by 30% because

of Mg evaporation and a higher grain size. Some porosity and cracking occurred. The use of 4043 filler wire led to a slight enhancement of the strength by reducing the crack sensitivity. The elongation with and without filler was 24% and 14.9% for the BM, and 3.7% for the weld, respectively. Further optimization of process parameters resulted in a further reduction in crack sensitivity and higher stability through a combined application of a slightly defocused laser and the lowering of both WS and heat input from the laser beam.

Yan et al. [216] fabricated a joint of components made of 4 mm thick similar 5083-H111 alloys using fiber laser–MIG hybrid welding with an ER5356 wire. The joint efficiency reached up to 85%. They observed less softening in the HAZ and WM compared to those of MIG. The HAZ width was 100% narrower. The TS was slightly higher than that of MIG. Fatigue was improved, but failure occurred because of porosity.

Similarly, Huang et al. [217] obtained a joint of components made of 10 mm thick similar 5083-H111 alloys using fiber laser–MIG hybrid welding with an ER5356 wire. They also found softening in the WM and HAZ. The applied laser setup provided uniformly dispersed Al₆(Mn, Fe) secondary phases with a higher density of dislocations.

Leo et al. [218] fabricated a joint of components made of 3 mm thick similar 5754 alloys using fiber laser–MIG hybrid welding with an ER5356 wire. The WE reached up to 82%. The obtained weld underwent PWHT at 35 °C for 50 min, which allowed for an increase in the WE of up to 98%, close to that of the BM with a UTS of 244 MPa. This is due to the elimination of softening through a reduction in the segregation and restoration of the Mg solution's strengthening mechanism.

Yan et al. [219] produced a joint of components made of 5 mm thick components made of similar 6005-T5 alloys using fiber laser–MIG welding with a 5356 wire. The WE reached up to 74%. They found that the fiber laser–MIG process provided better results than MIG. The reduced joint efficiency resulted from WM and HAZ softening (hardness reduced by 15%), porosity, a larger grain size than the BM, and losses of alloying elements (Mg and Mn) caused by the keyhole regime, causing their concentrations to be lower than those obtained in MIG. LAHW provided a 100% narrower HAZ with a lower decrease in hardness compared to MIG.

Zhang et al. [220] obtained a butt joint of components made of 8 mm thick components made of similar 6082-T6 alloys with fiber laser–MIG welding using a 5087 wire. They found equiaxed dendrites in the center of the WM, which were twice smaller than those obtained from pure MIG, with 96 µm and 50 µm, respectively. Mg₂Si phases were reprecipitated due to a higher cooling rate during LBW. The strength decreased due to large pores in the WM and coarsened precipitates with a size of 0.5–1.0 µm.

Yan et al. [221] produced butt joints of components made of 4 mm thick components made of similar 6061-T6 alloys using fiber laser–MIG welding with an ER4043 wire. The WE reached up to 80%. They reported that LAHW using the ER4043 filler wire provided higher weld strength, which resulted from a smaller grain size with reprecipitation but lower fatigue due to microporosity compared to when using an ER5356 filler wire.

Wang et al. [222] obtained a butt joint of components made of 3 mm thick components made of similar 6061-T6 alloys using fiber laser–TIG with an ER5365 wire. The weld was subjected to PWHT at 520 °C for 1 h, which led to the WE reaching up to 87%. The weld's high strength resulted from the fine (nanolevel) reprecipitation of the β'' phase with uniform distribution.

Hu and Richardson [223] produced a joint of 2 mm thick components made of similar 7075-T6 alloys using Nd:YAG laser–MIG hybrid welding with a 2319 wire. The weld joint was artificially aged at 120 °C for 24 h, which provided a strength level comparable to that of the BM. The post-aging WE reached up to 85%. Intensive softening was obtained in the as-welded condition. Natural aging (3 weeks) compared to 10-day artificial aging only slightly improved the strength. Alloying elements were redistributed in the dendritic structure along grain boundaries with depletion inside dendrite branches occurring independent of the PWHT type.

Ola and Doern [224] developed a joint of 6.3 mm thick components made of similar 7075-T665 alloys using Yb:YAG laser-MIG hybrid welding with an ER4043 wire. The laser-MIG method provided much less HAZ cracking than LBW using a cold wire due to higher heat input, thus inducing less tensile stresses on cooling. High crack susceptibility was observed in the HAZ. Post-welding natural aging (5 weeks) restored hardness and provided a WE of up to 85%.

Allen et al. [225] fabricated I-groove butt joints of 12.7 mm thick components made of similar AA7xxx alloys using fiber laser-MIG with a 5556 wire. The WE reached up to 60%. LAHW provided level B quality, with 0.3% porosity resulting from cleaning the parent material and applying a low-moisture shielding gas. The used filler wire provided exceptionally fine grains and enhanced mechanical properties. The TS and elongation of the hybrid weld metal were slightly less than the welds made by autogenous LBW. The weld metal was the least ductile zone, resulting from the unfavorable microstructure comprising intensive microsegregation and the formation of inter-dendritic eutectic films.

According to [226], during the laser-MIG hybrid welding of Al alloys, the intensity of the evaporation of individual elements from the BM and electrode wire, as well as the composition of the protective gas medium, highly influenced the passage of laser radiation to the metal welded. The use of Ar and high welding currents caused the shielding of radiation and a reduction in the penetration depth. This effect can be limited by using Ar/He mixtures or pure He to protect the weld pool and the pulse modulation of laser radiation. For speeds in the range of 30–60 m/h, compared to MIG, hybrid welding allows for the enhancement of the WS of 6 mm thick metal by 80%–160%, a reduction in heat input in the welded metal by 30%–60% times, and a significant reduction in the deformation of the joints with a thickness of 4 mm. In the hybrid welding of metal with a thickness of 6 mm or more using laser radiation with a power in the range of 1–4 kW, the MIG method plays a leading role. Typical defects in the hybrid welding of Al alloys, including Al-Mg-Mn, Al-Cu-Mg, and Al-Mg-Li, are in the forms of porosity and holes, which can be limited by the better protection of the weld pool and the optimization of welding modes.

Hybrid laser beam welding (HLBW) technology linking the advantages of laser welding with TIG was used for joining Al alloys. The use of hybrid laser beam welding enhanced the weld speed and improved the weld penetration, thus enhancing productivity and weld quality. Porosity formation is unavoidable in actual HLBW but controllable by adding a shielding gas unit, which is only accepted for in cases in which extremely high weld quality is required due to excessive costs. The HLBW of Al alloys has high reflectivity, which can be minimized by tilting the laser head to the needed degree of deviation, but this influences weld penetration [227].

Laser-MIG hybrid welding seems to be particularly useful for some Al alloys of the 5xxx series. This technique is under continuous development.

4.5. Laser Mirror Imagewelding and Laser Impact Welding

During the laser mirror welding process, symmetrical double-laser heat sources act on the flat-plate butt-joint structure. LMIW can realize the deformation-free and high-efficiency welding of thick plates. There are complex interactions of double keyholes and double-sided joint pools during the LMW process [72].

Daehn and Lippold [228] explained that, during LIW, a focused laser beam ablated a sacrificial layer placed on the surface of a metal flyer foil. The rapid vaporization of this layer generated a high-pressure plasma. By using a transparent overlay, the plasma was confined, thus increasing its pressure further. The plasma produced shock waves and accelerated the flyer toward the target metal. Due to collision, the jetting and interlocking of the foils occurred along a weld interface. High-velocity gradients appeared amongst regions of the flyer foil upon laser incidence, which was affected by the spatial profiles of the laser beam and the associated pressure pulse. The temporal profiles of the laser pulse and the corresponding pressure load determined the nature of and time to impact during LIW.

Zhao et al. [229] studied the microstructure and mechanical properties of the welding joints of components made of the 5A06 alloy obtained using double-sided double-arc welding (DSAW) and laser-TIG double-sided welding (LADSW) joints. They found that the energy efficiency of LADSW exceeded that of DSAW. With the enhancement of laser power, the ratio of the energy efficiency of LADSW to DSAW gradually increased. The TS of the LADSW joints reached 365.1 MPa, and elongation after breaking was 9.0%. The TS and elongation at the break of DSAW joints were 327.8 MPa and 5.5%, respectively.

Qi et al. [87] studied the relationship between process parameters and weld bead formation for welded joints of components made of the 2219 alloy obtained using laser mirror welding. They reported that when the molten pool was formed, the stability of the keyhole was the worst, and the tensile performance was low. The joints obtained using LMIW were more uniform and symmetrical compared to those obtained with laser double-sided asynchronous welding. Columnar crystals were formed at the interfaces of the two ends of the weld and the BM. From the fusion line at the waist of the weld to the center of the weld, the size of the fine equiaxed dendrites gradually varied, reaching the size of coarse equiaxed ones. The tensile properties of LMIW joints were affected by process parameters. Such properties were first enhanced and then declined with an increase in the laser heat input. The LMIW joint reached the highest TS of 213 MPa under a laser power of 2.5 kW and a WS of 2.0 m/min. Many pits appeared in the tensile joint fracture with a ductile nature. In addition, pore defects occurred in the tensile fracture morphology of the joints, induced by the instability of the keyhole during the welding process.

Generally, LMIW provides better joint quality compared to one-side laser welding [230,231].

Laser mirror welding is expected to be used in flat-plate butt structures. It provides a high penetration depth, a small HAZ, good efficiency, small welding deformation, and slight post-welding residual stress. However, due to the unique structure of flat butt joints, gravity affects the molten pool during welding, which impedes the stability control of welding, thus promoting defects such as welding pores, cracks, undercuts, etc. [72].

Sadeh et al. [232] experimentally characterized the spatial and temporal profiles of Nd-YAG laser beam pressure pulse by focusing on laser impact welding (LIW) simulation. LIW tests were conducted using standoff distances of 0.12, 0.26, 0.40, and 0.54 mm, as well as laser fluence values of 31.08 and 37.30 J/cm². Independent of the laser fluence value, sound welds were obtained only at standoff distances of 0.26 and 0.40 mm. The proper welds were obtained without spring-back in the central region. The strongest weld was obtained using a standoff distance of 0.26 mm and a laser fluence of 37.30 J/cm². In all the tests, failure occurred on the flyer (Al) side of the weld.

Wang and Gu [233] studied the effect of laser fluence on the weld interface morphology during the oblique LIW of 0.1 mm thick aluminum flyer foils to aluminum base foils of 0.1 mm thickness. For similar metal couples (Al/Al), some uniform wavy structures were observed. The wavy morphology enhanced the direct contact area and facilitated interlocking between two metal surfaces, thus providing strong bonding. The shock welding interface exhibited much higher hardness than the BMs. The tensed weldments exhibited limited shear strength after laser shock welding.

Laser-induced effects heavily depend on the laser spot size, laser wavelength, pulse duration, and the irradiated material [234].

Using the same laser pulse energy, the laser impact generated ultrasounds or shock waves affected by the laser spot size, pulse duration, etc. In particular, good weld properties (for laser spot size of 6 mm and impact angle of 20 degrees) were obtained at laser fluences of 13.44, 14.15, and 14.85 J/cm² when they welded 0.05 mm thick sheets of aluminum and copper flyers to 0.1 mm thick sheets of aluminum base foils [235]. It was found that doubling and tripling the standoff distance between the foils increased the weld diameter by 50% and 83%, respectively.

To summarize, the LMIW method is more effective than one-side laser welding. Laser shock welding is a process predestined for producing metallurgical bonds between both similar and dissimilar metal pairs.

4.6. Electron-Beam Welding

Cam et al. [236] studied welded joints of plates made of different Al alloys (2024, 5005, and 6061) obtained via the electron-beam (EB) welding of plates with a thickness of 5 mm except for alloy 5005, which had a thickness of 3 mm, to find the local microstructure–property relationships that would satisfy the service requirements for an electron-beam-welded Al alloy component with weld zone strength undermatching. Autogenous electron-beam (EB) welding allowed for obtaining defect-free welds of 5005, 2024, and 6061 alloys. However, a low level of porosity occurred in most cases, which was acceptable for Al alloy weldments. An extremely low level of porosity was obtained in all EB welds owing to surface cleaning before welding and the vacuum environment of the EB welding process.

Mg loss occurred in the fusion zone of all the joints during welding. No distinct heat-affected zone (HAZ) existed in the 5005 alloy joint, although a clear minimum hardness value was found in the HAZ region. The 6061 alloy joint exhibited an overaged HAZ region. In the 2024 alloy joint, a narrow HAZ region with particle coarsening (overaged region) was also observed. The fusion zone of the 2024 alloy joint exhibited columnar dendritic grain formation with uniformly dispersed particles, whereas the fusion zones of the 5005 and 6061 alloys showed a dendritic solidification microstructure with isolated particles along the grain boundaries, as well as within the grains [236].

The EB-welded joints possessed minimum hardness in the fusion zones (strength undermatching) due to the loss of strengthening elements and/or phases (dissolution). Although the minimum hardness was in the HAZ region of the 5005 alloy joint, the decrease in hardness in the fusion zone was not as significant as that in the other two joints. The coarsening of strengthening phases reduced the hardness in the HAZ regions. After a transverse tensile test of the autogenous EB-welded joints, their strength slightly decreased, and losses in ductility occurred in 2024 and 6061 alloys, owing to the strain value in the narrow, lower-strength fusion zone (~2 mm in width), although the 5005 alloy joint had a relatively high ductility level, compared to the respective baseplate [236].

The fusion zone of the 5005 alloy joint and both the fusion zone and HAZ of the 6061 alloy joint showed higher fracture toughness than that of the BM and thus displayed higher resistance to stable crack growth. The fusion zone of the 2024 alloy joint showed similar or slightly lower fracture toughness values than those of the respective baseplate, whereas the HAZ region showed the lowest R curve behavior [236].

Kim et al. [19] studied the EB joint of 4.5 mm thick AA6061-T6 plates obtained at a traveling speed of 1200 mm/min under the beam current of 35 mA and an accelerating voltage of 60 kV in a vacuum of 10^{-3} Pa. They found that relative to the rolling directions of the tested specimens, the TS exhibited no difference between the longitudinal and transverse welds. The tensile fracture of the transverse welded specimens appeared in the BM zone far from the weld. The ductile fractured zone comprised only dimples with a microvoid coalescence. The joint efficiency of a longitudinal welded joint was 85%, while that of a transverse welded joint was 74%. The hardness distributions of the weld center line for a square butt-welded zone were in the range of 61 to 70 VHN, whereas those for the HAZ were in the range of 75 to 87 VHN. This resulted from the welding heat cycle and the use of the AWS 4047 filler material (Al-10%Si). The addition of filler caused higher hardness compared to the fusion welding joint due to the shear stresses induced by tool motion, leading to a fine-grain structure.

Fujii et al. [237] explained the mechanism of bubble generation during the welding of the 2219 Al alloy using electron-beam (EB) welding and gas tungsten arc (GTA) welding in both terrestrial and microgravity environments. While hydrogen is the main source of porosity in Al alloys, bubbles are formed via a reaction between the molten Al and Al_2O_3 , forming Al_2O . Pores are formed only in a vacuum, as during electron-beam welding, and they are distributed only in the upper part, while the pores formed due to hydrogen are widely distributed in the upper half. The pores are formed due to a chemical reaction at the highest temperature, not due to the reduced solute species. The number of pores was significantly reduced under microgravity during EB welding, but it increased in GTA

welding using a shielding gas containing hydrogen. The number of pores increased with the enhanced thickness of the oxide film.

Elseddig et al. [238] studied the effects of beam current, sweep size, WS, and focus position on the UTS when welding an AA1350 aluminum alloy with an electron beam. They predicted the optimal arrangements of the welding parameters focused on maximizing the UTS of the weld joint.

According to [239], electron-beam welding (EBW) is advantageous compared to other traditional fusion welding methods due to its high energy density, deep penetration, large depth-to-width ratio, and exceedingly small HAZ. Using the Taguchi method with gray relational analysis, the authors optimized the EB-welded joint of the 2219 alloy in terms of its YS, hardness, and bead geometry.

Using EBW, Sobih et al. [240] obtained an acceptable joint of the 2219 alloy. They reported that the EB cosmetic pass enables eliminating the undesired surface undercutting of the weld bead. The small beam diameter provided a distinguished weld zone with a full penetration depth and a small bead width (3.51 mm), while the high heating and cooling rate during electron-beam welding induced a small HAZ; thus, a UTS of 295 MPa associated with a WE of 62% was obtained.

4.7. Resistance Spot Welding (RSW)

Al alloys possessing high electrical and thermal conductivity need higher current (2.5 to 3 times) and shorter weld time than steel. The resistance spot welding (RSW) of Al alloys requires consistency in terms of uniform pressure and current. During Al RSW, the deterioration of electrodes may occur due to nonuniform pressure and current. Electrode erosion can also occur, causing the formation of undersized welds, which are avoidable by using proper surface coatings and treatments on electrodes [241].

Al easily reacts with oxygen in the atmosphere, forming surface oxide films of high resistivity and corrosion protection ability, thus preventing the formation of weld nuggets in RSW [150].

Auhl and Patrick et al. [242] reported that the breaking down of oxide film and proper weld nugget formation usually need high electrode pressure. Additionally, a surface cleaned with chemicals allows us to obtain the thinnest oxide layer, thus elongating the electrode life [242–246].

The use of hybrid processes, such as the combination of ultrasonic waves or magnetic excitation, can improve the weld nugget quality of RSW-welded Al alloys. These allow for obtaining defect-free joints with good mechanical properties [247,248]. Resistance welding should be utilized for components made of the 7178 alloy [249].

Resistance to the general corrosion of copper-free wrought 7xxx alloys is good, approaching that of the wrought 3xxx, 5xxx, and 6xxx alloys. Copper-containing alloys of the 7xx.x series, such as 7049, 7050, 7075, and 7178, have lower resistance to general corrosion than those of the same series that do not contain copper. All 7xxx alloys are more resistant to general corrosion than 2xxx alloys but less resistant than wrought alloys of other groups [250].

Fracchia et al. [251] studied the welded joints of two sheets made of the 5454 alloy obtained through a resistance welding process. After the mechanical lamination process, they observed the presence of defects. They reported the good mechanical properties of the joints, while in the defects, oxide inclusions occurred. The authors noted that the mechanical properties of the welded joints of Al and its alloys can be worsened due to gas porosity, oxide inclusions and oxide filming, solidification (hot) cracking or hot tearing, reduced strength in the weld and HAZ, the lack of fusion, reduced corrosion resistance, and reduced electrical resistance.

Matokhnyuk et al. [252] studied the fatigue behavior of the welded joints of 40 mm plates made of the 2219 alloy obtained using resistance butt welding and argon-arc welding, under symmetric and pulsating loading cycles. They found that at stresses exceeding the endurance limit, the fracture of specimens was of a multi-site nature and began from their

surface. At stresses close to the endurance limit, the fatigue crack in the specimens fractured at a lower number of loading cycles and initiated from their surfaces and at longer lives, from subsurface fracture initiation sites. Under zero-to-tension loading cycles and the same heat treatment conditions, the endurance limit value of specimens made by resistance butt welding was close to that of specimens without welding and significantly exceeded that of specimens with argon-arc welding. For both types of welding, fatigue cracks propagated via pores in the weld or the heat-affected zone.

Bamberg et al. [92] reported that the cladding of various Al alloys is commonly used to improve sheet weldability while simultaneously maintaining structural performance. For cladding, a combination of a highly conductive, electrically stable Al alloy is used as the covering sheet, with a high-strength alloy used as the core sheet. They evaluated the improved weldability of an AW-6111 alloy (core sheet) clad with an AW-4040 alloy (cover sheet), which was affected by a proper welding lobe, electrode erosion behavior, and the formed microstructure. Compared with a pure AW-6111 aluminum sheet, clad sheets exhibited weldability characteristics and enhanced electrode service life.

Bamberg et al. [98] realized the RSW process of AW-7075 free of welding discontinuities, providing a proper weld lobe, electrode cap durability, and better microstructure characteristics. Welding was conducted using an upslope welding current, CuAg0.1 electrode caps, and a higher electrode force. This reduced the temperature at the contact surface, limiting electrode erosion and a tendency for Cu–Al alloying. The quality of welding and mechanical properties was high.

To summarize, the cladding of various Al alloys is beneficial due to providing better sheet weldability while maintaining structural performance. According to [253], the high contact resistance caused by the oxide layer on the surface of Al alloys and the required high welding current during the RSW of Al alloys caused rapid electrode-tip wear and inconsistency in weld quality. The cleaning of the oxide layer, the sliding of a few microns between sheets, increasing the electrode force, and using low-current preheating significantly decreased the contact resistance and increased joint quality.

4.8. Friction Welding

Ochi et al. [254] studied the effect of heat input on the performance of friction-welded joints of the 5056 alloy. The heat input for welding solid materials was classified into six categories, namely the friction heat input and deformation input during the friction stage, upset stage, and total stage. The authors found that the deformation heat input during the upset stage affected the joint performance, and the sound joints were obtained with a deformation heat input of over 100 J/s. Sound joints were obtained with upset burn-off lengths of over 2 mm.

Studying the weld joints of dissimilar 5052 and 7075-T6 alloys obtained by FSW, FSP, and RFSP, Jweeg et al. [108] found that the TS values of samples using FSP and RFSP were higher than those of FSW for all the TRS of welding. The microhardness values for all samples at the stir zone exceeded that of the BM of 7075-T6 and were lower than that of the BM of 5052; the hardness of FSP and RFSP samples using a speed range of 710–1500 rpm was about 50% higher than that of the base metal of the 7075 alloy.

Interestingly, FSW is an expected heat exchange method for application in the automotive industry, where porous cast components are often used. This process is also recommended for cast or extruded battery trays.

4.8.1. Friction Stir Welding

The main advantages of FSW, due to being primarily a phase operation, are extremely low distortion, the absence of alloy related to deformation, and high fabrication durability. This process is applicable for the fabrication of various joint types, including butt, lap, T, spot, and fillet joints, and facilitates the further welding of hollow parts like tanks, tubes, pipes, and stocks with different thicknesses. It is also utilized for welding tapered hollow sections and parts of three-dimensional shapes [255].

According to Patel et al. [256], the quality of FSW using dissimilar Al alloy combinations was strongly affected by welding parameters, including BM placement, the TRS, and WS. The placement of the BM drives material flow, while rotational speed and WS affect heat input on both sides of the joint during welding. The welding parameters also affect mechanical properties, including hardness and joint strength. Some studies related to the effect of the placement of the BM (i.e., whether a particular material is placed on the AS or the RS) on the material flow, the resulting microstructure in the SZ, and the mechanical properties of the weld have been performed. Other researchers investigated the influence of tool geometry, including shoulder-diameter-to-pin-diameter ratio and pin profile (cylindrical, conical, or polygonal) on the microstructure and mechanical features of the weld.

However, Di Bella et al. [257] pointed out that the joint quality obtained in the FSW process depends on not only the process parameters but also the features of the Al alloys involved, including their heat treatment and the thickness of the welded sheets.

The effect of heat treatment of welded alloys

Heat-treatable Al alloys from the 2xxx, 6xxx, and 7xxx series obtain their strength from a precipitation hardening process [257]. The high temperatures generated during FSW to various extents dissolve the strengthening precipitates (Cu, Mg, and Zn) in the HAZ of heat-treatable alloys. The high heat treatment applied locally softened alloys, thus decreasing the overall joint strength in this zone. The heat also induced a redistribution of precipitates in the zone affected by alloy composition, welding parameters, and cooling rate, thus influencing the mechanical properties. To restore the required post-welding mechanical properties, such alloys need subsequent post-weld heat treatment involving a specific temperature and time cycle to reprecipitate the strengthening phases, thereby regaining the needed strength [258]. FSW also influences the microstructure and electrochemical behavior of the various FSW zones (HAZ, TMAZ, and SZ) [259].

Non-heat-treatable Al alloys from the 1xxx, 3xxx, and 5xxx series are insensitive to precipitation hardening [257]. They gain strength via cold working or strain hardening. Such alloys showed minimal material softening in the HAZ during FSW. Due to possessing cold working-based strength, these alloys have mechanical properties that are only slightly affected by localized heating in FSW. The latter causes grain refinement resulting from the high plastic deformation caused by the rotating tool, increasing joint TS and fatigue resistance. Such alloys usually do not need post-weld heat treatment. The joint mechanical properties are firmly retained with less additional heat treatment [260].

The behavior of FSW joints between a heat-treatable Al alloy and a non-heat-treatable one depends on various factors. Both alloys possess different mechanical properties. The heat-treatable alloy has higher strength, while the non-heat-treatable alloy exhibits lower strength but better formability. Such a difference influences the overall joint strength and performance due to different changes in hardness considering precipitation-hardened and solid-solution-hardened Al alloys [261]. The joint shows variations in strength, ductility, and toughness, mainly at the alloys' interface. Frictional heat generation during FSW and the mechanical mixing of the materials facilitate the formation of intermetallic compounds at the interface. Such intermetallics possess different mechanical properties than the BMs, further affecting the joint behavior. This phenomenon always occurs during the FSW of dissimilar alloys. The type, volume, and distribution of intermetallics vary depending on the alloy set and the process parameters used [262–266].

FSW causes various microstructural changes in both the HAZ and the weld zone, depending on the alloy set, process parameters, and the cooling rate. Differences in grain size, phase distribution, and precipitate formation between heat-treatable and non-heat-treatable alloys influence the joint's strength, hardness, and corrosion resistance [258,267,268]. In heat-treatable Al alloys, material softening is strongly affected by the dissolution of strengthening precipitates and grain size growth when subjected to process-induced thermal cycles. The weakening of mechanical properties in such alloys can be partially compensated for by utilizing subsequent aging treatments, whether natural or artificial [269–276]. On the

other hand, in non-heat-treatable Al alloys, the softened zone highly compromises the joint tensile properties, hardness, and fatigue resistance. The principal mechanisms controlling such a softening include recovery and recrystallization [277–279].

Investigating the FSW-obtained joint between 2024/7075 alloys, Beygi et al. [280] found that tensed welded samples exhibited fracture surfaces with large dimples and precipitates within them, confirming the coarsening of the precipitates inside the (RS) 2024 alloy. This coarsening in the weld region meaningfully softened the material due to the concentrated plastic strain generated therein. For (AS) 7075 alloy, coarsening is prevented by the initial artificially heat-treated state (T6) of the 7075 alloy, accompanied by an initial solution-treated state (T3) of the 2024 one. Coarsening is also impeded by the lower maximum temperature reached with the 2024 alloy during the FSW process compared to that with the 7075 alloy. The FSW method induces joint residual stresses resulting from thermal expansion and plastic deformation. The welded joint of dissimilar Al alloys exhibits differential thermal expansion and contraction, causing residual stress concentrations. Residual stresses affect the joint's distortion, crack susceptibility, and overall mechanical behavior [281,282].

Additionally, the post-weld heat treatment of dissimilar Al alloys changes their behavior. Heat-treatable alloys often need specific heat treatment cycles to ensure the necessary mechanical properties. However, non-heat-treatable alloys are limited to traditional heat treatments [283]. Consequently, FSW joints between dissimilar Al alloys need careful selection and the optimization of such processes.

The effect of the welded sheet thickness

Also, the FSW sheet thickness significantly affects the welding process and the joint quality [284,285].

Thicker sheets need increased heat input to increase their temperature to the required range for FSW. The higher thickness induces a greater heated material volume, thus needing more time and energy. Consequently, thicker sheets need adjusted welding parameters, including the enhanced TRS and AF, for sufficient heat generation to ensure effective material stirring and plasticization. Thicker sheets also provide better heat dissipation due to their larger volume, causing a higher temperature gradient across the thickness during FSW. This nonuniform temperature distribution influences the formation of defects such as voids, cracks, or incomplete bonding. The proper control of FSW parameters, including the TRS, WS, and dwell time, provides adequate heat input and minimal thermal gradients [257].

Thicker sheets possess enhanced levels of residual stresses resulting from higher thermal gradients and the related thermal expansion and contraction effects. These residual stresses usually influence the joint structural integrity and need post-weld heat treatment or other stress relief techniques to weaken their effect [286].

The sheets' thickness affects the material flow and mixing characteristics. Thicker sheets show lower material flow, which results from their higher thermal mass and enhanced resistance to deformation. This varies the material mixing between the joint AS and RS. To compensate for this, optimized tool geometry and process parameters provide better material mixing and achieve a homogeneous joint [257].

Thicker sheets enhance the FSW joint strength caused by the larger bonded area and higher material volume involved in the welding process. This is because a higher thickness ensures more material undergoes the stirring action of the rotating tool, inducing enhanced mixing and bonding between the adjacent sheets. The larger bonded area and higher material volume improve the overall joint strength [287–289].

However, the higher thickness also often causes inadequate heat input, insufficient mixing, or defects if not properly addressed. Optimization is necessary for process parameters, tool design, and post-weld inspections focused on the specific characteristics of thicker sheet materials to provide high-quality joints [257].

The specific adjustments for FWS parameters such as the TRS, WS, and AF as a function of sheet thickness often vary depending on the welded alloy set and other factors [290,291].

Modeling of the FSW process

A separate issue related to the FSW process is its modeling. Di Bella et al. [257] reviewed, inter alia, the main tools to design and predict the mechanical behavior of dissimilar aluminum joints. There are some cases of using mathematical modeling to optimize the FSW process for similar Al alloys. For example, Thete and Kadlag [292] optimized the FSW process parameters, including the TRS, WS, and AF, to obtain the highest TS of a similar 6082-T6 (H30) alloy joint using an L9 orthogonal array with the Taguchi method.

Statistical methods like the design of experiment (DoE) approach can be used to systematically vary process parameters such as the TRS, WS, and applied force to study their effects on the weld quality and mechanical properties. The use of statistical techniques such as the response surface methodology (RSM) allows for the determination of optimal process parameter settings, leading to required weld characteristics such as defect-free joints, high strength, and improved fatigue resistance [257].

Statistical analysis can be applied to study the relationship between process parameters, microstructure evolution, and the resulting mechanical properties. Statistical approaches can also be useful in the evaluation of the reliability and fatigue life of FSW joints. Using probabilistic models or techniques like the Weibull analysis, the probability of failure or the fatigue life of welds can be estimated under different loading conditions, which is necessary for ensuring the long-term performance and durability of FSW structures. The obtained information can be expanded when solving complex problems using heuristic techniques such as neural networks and genetic algorithms, both lessening the need for experiments and allowing for the real-time monitoring and control of the welding process [257].

Numerical modeling like finite element analysis and computational fluid dynamics allows us to study/analyze/predict the characteristics of the joint at all varying process parameters. They are particularly useful for describing/designing/optimizing very complex thermal/mechanical and metallurgical phenomena involved in the FSW process [257].

Also, Khalafe et al. [293] revealed in their review that various artificial intelligence (AI) techniques, including fuzzy logic, artificial neural fuzzy interfacing system (ANFIS), heuristic methods, heuristic algorithms, wavelet methods, machine learning, hybrid systems, and artificial neural networks, facilitate the enhancement of the rate of production with better accuracy for both similar and dissimilar alloys, also including Al ones.

Positioning of Alloy

The direction of the welding tool motion affects the FSW joint microstructure and mechanical properties, i.e., material stirring and mixing strongly depend on the placement of the alloy affecting material flow [256]. The FSW process shows inherent asymmetry in the material flow between the AS and the RS of the SZ. Therefore, the position of the BM in the AS or the RS highly affects the temperature distribution, material composition within the SZ, and the metal's plastic flow. These factors, in turn, highly affect the mechanical properties of FSW joints [294,295]. In particular, when considering the AS and the RS in the FSW joint, the following effects can be observed [257]:

Heat Input: The AS experiences a higher heat input than the RS. A welding tool moving forward generates more frictional heat, enhancing plastic deformation and temperature in the AS. This can cause different thermal cycle gradients on both sides of the joint.

Grain Structure: Different heat inputs on the AS and the RS can induce variations in the weld grain structure. The AS experiences more severe deformation and recrystallization, inducing finer grain sizes than in the RS. The grain structure influences the strength and toughness of the joint.

Composition Variation: various Al alloys may have various compositions and mechanical properties. The AS, experiencing higher heat and deformation, can induce the localized diffusion of alloying elements between the BMs. Such diffusion can affect the composition and resulting features of the joint.

Residual Stresses: The differences in heat input and the resulting microstructure can induce variations in residual stresses along the joint. Residual stresses can influence the structural integrity and distortion of the welded components.

The material flow in FSW has a complex nature, and thus the placement of materials significantly affects the welding procedure, similar to the TRS and WS, as it can highly affect the outcome of the welding process [296]. The optimization of the FSW process for Al alloys needs careful consideration regarding the effects of the AS and the RS. Process parameters, including the TRS, WS, and tool design, can be adjusted to provide the required joint features. Also, post-weld heat treatment or other techniques may be applied to further refine the microstructure and features of the weld.

The placement of the alloy strongly affects material stirring and mixing. Material behavior on the AS and the RS can significantly differ (Figure 3). In particular, it can determine the final microstructure of the joints made between Al alloys with significantly different mechanical properties [297,298]. The higher hot-strength material should be placed on the advancing side to enhance the mechanical properties of a dissimilar joint [299–301]. Local weld temperatures were highest on the AS, where the highest shear rates were observed.

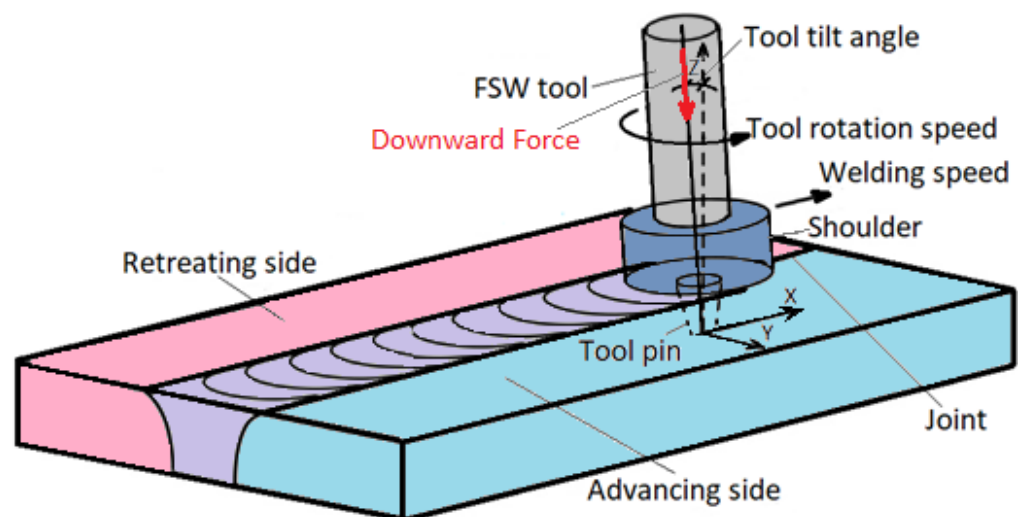


Figure 3. The advanced side and retreating side in the butt joint obtained through the FSW process.

Some researchers have stated that a BM with lower solution temperatures and thus easily softenable at higher temperatures should be positioned on the RS, where a lower temperature is used [302].

Investigating similar and dissimilar FSW joints between 2017-T6 and 6005A-T6 alloys, Simar et al. [303] found that better-quality joints were obtained when a softer BM was placed on the RS.

However, studying the FSW joints of 5052/A5J32 alloys obtained with the TRS varying from 1000 rpm to 1500 rpm and the WS varying from 100 mm/min to 400 mm/min, as well as using a tilt angle of 3° with a tool with shoulder diameter of 8 mm, a threaded cylindrical pin diameter of 3 mm, and a length of 1.45 mm, Kim et al. [304] found that setting the high-strength Al alloy on the AS induced excessive agglomerations and defects caused by limited material flow. Consequently, high-strength Al should be placed at the RS to minimize this effect.

Studying the FSW joints between (AS) 5083-O/(RS) 6082-T6 alloys obtained under a WS of 400 mm/min or 300 mm/min, a constant TRS of 400 rpm, and a tilt angle of 0 degrees, using a two-part MX-triflute tool with a probe diameter-to-length ratio of 1:0.8 (i.e., a 7.0 mm tip diameter with a cone angle of 5°) and a scroll shoulder diameter of 25 mm, Donatus et al. [305] found that in the joints, material primarily flew from the AS to the RS without significant mixing. However, opposite material flow was mainly observed within the tool shoulder region, with the highest level of material displacement present

at the transition area between the tool shoulder and the tool pin regions. Additionally, material extrusion predominantly occurred in the TMAZ of the RS, which depended on the rotational motion of both the tool shoulder and the tool pin. Regarding the grain structure, the finest grains occurred in the regions nearest the tool edge within the RS.

Investigating the FSW joint between 5052-H32/6061-T6 alloys, Park et al. [306] found that the material mixing patterns in the joints differed depending on the placements of BMs, the 5052 alloy set on the AS improved the mixing of BMs in the SZ, whereas the placement of BMs did not affect the location of fracture as the welds failed in the AS of the weak HAZ [307].

The welded joints of components made from 2024-T351/5083-H112 alloys in one sample and from 7075-T651/2024-T351 alloys in a second sample (Table 4) were studied by Niu et al. [308]. The 2024 and 7075 alloys were placed on the AS, while the 5083 and 2024 alloys were placed on the RS, respectively. The sole effect of the alloys' position on the joint properties was not examined.

Niu et al. [309] studied the effect of BM locations on the corrosion behavior of the 2024-T351/7075-T651 joint obtained with a tool possessing a threaded pin with 5.9 mm in diameter and 6.0 mm in length, a concave shoulder of 15 mm in diameter, and a tilt angle of 2.5°, at a TRS of 600 rpm and WS of 200 mm/min. They found that the top section of the SZ was composed of the BM of the RS, whereas the middle and bottom sections were composed of the BM of the AS. The SZs exhibited corrosion resistance close to that of the BM placed on the AS, with dominating intergranular corrosion. In particular, the finely recrystallized grains within the SZs showed more clearly visible intergranular corrosion compared to the BM. However, the appearance of grain boundary precipitates and precipitate-free zones, which were intermittently distributed within the SZ of the 2024 alloy, successfully weakened the damage induced by intergranular corrosion in the SZ.

Studying the FSW joints between 7075-T651/2024-T351 alloys (Table 4), Hasan et al. [310] found that materials' fixed location on the AS and the RS of the weld influenced the quality of joint, which was better in the case when a softer BM was positioned on the AS.

The proper FSW joints between 7075-T6/2024-T3 alloys were studied by Ge et al. [61] for which 7075 and 2024 sheets were used as an upper sheet on the RS and a lower sheet on the AS, respectively. The sole effect of the alloys' position on the joint properties was not studied.

Studying the FSW joints of components made of 7075-T651/5083-H111 alloys (Table 4), Kalembe-Rec et al. [311] reported that a higher TRS in the configuration with 5083 on the AS and 7075 on the RS was accompanied by the occurrence of porosity, voids, or wormholes in the stir zone. The highest TS of the defect-free joint was obtained with 5083 on the AS, 7075 on the RS, a TRS of 280 rpm, and using the triflute pin. Then, the WE reached above 100%. However, the effect of alloys' location on the WE was small.

The proper FSW joints between 2024-T4/7075-T6 alloys were studied by Safarwali et al. [312] for which the 2024 alloy was placed on the AS, and the 7075 alloy was placed on the RS of the joint. The sole effect of the alloys' position on the joint properties was not studied.

For the study of the FSW joints of plates comprising dissimilar 6351-T6/5083-H111 alloys, Palanivel et al. [313] placed the 6351 alloy on the AS and the 5083 alloy on the RS. They observed that the tool shoulder increased the material transport at the top surface from the RS to the AS, pushing it downward within the tool pin diameter.

During the study of the FSW joints of components made of dissimilar 2017A-T451 and 7075-T651 alloys, Hamilton et al. [314] found that the 7075 alloy exhibited longer positron lifetimes than the 2017 A alloy. The positron lifetime profiles across the weld comprised many local maxima and minima on the AS and the RS, corresponding to the hardness behavior. Weld temperatures on the advancing side were greater compared to those on the retreating side, thus promoting more precipitation on the AS away from the weld center. This behavior is related to the higher positron lifetime on the advancing side compared to the retreating side, at the same distance from the weld center.

Studying the FSW joints of dissimilar 5052/Al-Mg₂Si alloys (Table 4), Huang et al. [315] utilized the 5052 alloy on the RS and Al-Mg₂Si one on the AS. They observed that on the top of the RS and at the bottom of the AS, the weld nugget (WN) comprised no banded structure. Contrarily, on the top of the AS, at the bottom of the RS, and at the center of the WN, a banded structure was observed. This band structure partly covered the weld width extending from the AS toward the RS. A rich Al-Mg₂Si layer was also formed at the weld's top surface on the RS. The interface between the 5052 alloy and the rich Al-Mg₂Si region at the bottom of the RS appeared as a transitional layer with a thickness of 50 µm. The interface began from the top surface of the RS because the materials on the RS were not driven to the AS. With an increase in distance from the top surface, the interface location changed to the AS because the materials on the RS were dragged to the AS.

For the FSW joints of components made of dissimilar 2024/6061 alloys (Table 4), Moradi et al. [316] found that the fraction of precipitates in the SZ on the RS exceeded that on the AS. The extent of continuous dynamic recrystallization in the TMAZ on the AS was less than that on the RS, and recrystallized grains seldom occurred on the AS. The initial texture components became asymmetric after the FSW process. The overall texture intensity was weaker on the AS and stronger on the RS compared to the starting materials. Discontinuous static recrystallization and/or meta-dynamic recrystallization occurred on the AS. The microhardness profile on the AS was almost identical, while it comprised three distinguishable regions on the RS.

The FSW joints of 6061-T6/6351-T6 alloys (Table 4), studied by Prasanth and Raj [317], were obtained for cases where each of the dissimilar 6061-T6 and 6351-T6 alloys was placed separately on the AS and the on the RS of joints. The sole effect of the alloys' position on the joint properties was not examined.

Studying double-sided FSW joints of components made of dissimilar 6082-T6/7075-T6 alloys (Table 4), Azeez and Akinlabi [318] reported that slight abnormalities on the RS were caused by the preheating of the plates during the initial welding process.

In the case of single-sided FSW joints of components made of the same alloys, Azeez and Akinlabi [318] reported that some microstructure imperfection occurred at the weld nugget when 6082 Al plates were clamped on the RS to the backing plate. However, deviation in the positioning of the Al plates prevented the fabrication of good bonding and quality welds despite the material flow and mixing occurrence.

The proper FSW joints of rolled plates made of dissimilar 6061-T651/5A06-H112 alloys (Table 4), studied by Peng et al. [319], were obtained when the 6061 alloy was placed on AS, while the 5A06 alloy was placed on the RS of joint. The sole effect of the alloys' position on the joint properties was not studied.

The correct FSW joints of dissimilar 6101-T6/6351 alloys (Table 4), studied by Das and Toppo [320], were obtained when the 6101 alloy was placed on the AS, while the 6351 alloy was placed on the RS of the joint. The sole effect of the alloys' position on the joint properties was not examined.

The proper FSW joints of dissimilar 2024-T3/6063-T6 alloys (Table 4), studied by Sarilmaz [321], were obtained when the 2024 alloy was placed on the AS, while the 6063 alloy was placed on the RS of the joint. The sole effect of the alloys' position on the joint properties was not studied.

Studying the FSW joints of components made of dissimilar 2219-T87/2195-T8 alloys (Table 4), No et al. [322] found that the best-joining properties were obtained for conditions including a TRS of 600 rpm and a WS ranging from 180 to 240 mm/min when the 2219-T8 alloy was on the RS.

During the study of the FSW joints of components made of dissimilar wrought 2017A/cast AlSi9Mg alloys (Table 4), Kopyscianski et al. [323] reported that the AlSi9Mg alloy on the AS dominated the weld center. The local maximum on the AS was on the nugget side with a high density of the bands of the 2017A alloy.

The proper FSW joints of dissimilar 5083-H12/6061-T6 alloys, studied by Ghaffarpour et al. [324], were obtained when the 6061 alloy was placed on the AS, while the 5083 alloy

was placed on the RS of the joints. The sole effect of the alloys' position on joint properties was not studied. The FSW joints possessed a much higher quality and improved mechanical properties than those obtained with TIG welding.

Studying the UFSW joints of dissimilar 6061 and 7075 alloys, Bijanrostrami et al. [325] placed the 6061 alloy on the AS and the 7075 alloy on the RS on top of a steel backing plate.

The FSW joints of dissimilar 6082-T6/5083-H111 alloys (Table 4), studied by Kasman et al. [326], were obtained when the 6082 alloy was positioned on the AS, while the 5083 alloy was positioned on the RS of joints. The small cavity- and tunnel-type defects occurred at the nugget zone and were located on the advancing side of the pin. These defects reduced the strength and elongation of the weld joint.

The FSW joints of 6 mm thick sheets made of dissimilar 5083-H111/6351-T6 alloys (Table 4), studied by Palanivel et al. [144], were obtained when the 6351-T6 alloy was placed on the AS, while the 5083-H111 alloy was placed on the RS of the joint. Similarly, In studies presented in [182,186], the 6351 alloy was placed on the AS, while the 5083-H111 alloy was placed on the RS of the joint. The grain size within the friction stir-processed (FSPed) region was much smaller than that in the parent material due to the higher temperature and extensive plastic deformation. The grain size in the TMAZ clearly differed from that in the FSPed region.

The FSW joints of dissimilar 5052-H32/6061-T6 alloys (Table 4), studied by Doley and Kore [327], were obtained when the 5052 alloy was placed on the RS, while the 6061 alloy was placed on the AS of the joints. The microhardness values of dissimilar welds were lower at heat-affected zones (HAZs) on both sides of the weld line, whereas the lowest value was found for the HAZ of the 5052 alloy.

For studying the effect of shoulder-diameter-to-pin-diameter ratio on the microstructure and mechanical properties of the FSW joints of dissimilar 2024-T6/7075-T6 alloys (Table 4), Saravanan et al. [328] placed the 2024-T6 alloy on the AS and the 7075-T6 alloy on the RS. They reported that the joints fabricated with ratios of 2 and 2.5 fractured in the heat-affected zone (HAZ) of the advancing side, while the joints fabricated with ratios of 3, 3.5, and 4 fractured at the SZ. For all D/d ratios, the minimum hardness was seen at the HAZ on the advancing side and was maximum in the SZ and again decreased in the HAZ of the retreating side.

Studying the FSW joints of sheets made of dissimilar Al-Mg-Si/Al-Zn-Mg alloys (Table 4), Yan et al. [296,329] found that for the Al-Zn-Mg alloy positioned at the advancing side (AS), the joints exhibited better fatigue properties caused by the bridging effect of the large second-phase particles. For the Al-Zn-Mg alloy placed at the AS, there was limited movement of the Al-Mg-Si alloy material to the AS due to its easier flow. For the Al-Mg-Si placed at the RS, there was no RS material (Al-Zn-Mg) flow to the AS due to the high resistance to the flow of this material.

The proper FSW joints of dissimilar 2024-T3/6061-T6 alloys (Table 4), studied by Zapata et al. [330], were obtained when the 2024 alloy was placed on the AS, while the 6061 alloy was positioned on the RS of the joints. The sole effect of the alloys' position on the joint properties was not studied.

Studying the FSW joints of the dissimilar UFGed 1050/6061-T6 alloys (Table 4), Sun et al. [331] reported that sound welds were performed at wide revolutionary pitches ranging from 0.5 to 1.25 mm/min, only when the 6061-T6 alloy was placed on the AS. Otherwise, the welds exhibited large defects, which were formed in the softened 1050 RS.

The proper FSW joints of dissimilar 2024-T3/2198-T3 alloys (Table 4), studied by Texier et al. [332], were obtained when the 2024-T3 and 2198-T3 sheets were on the RS and the AS of joints, respectively. The sole effect of the alloys' position on the joint properties was not examined.

The correct FSW joints of dissimilar 6061/7050 alloys (Table 4), studied by Rodriguez et al. [333,334], were obtained when the 7050 alloy was positioned on the AS, while the 6061 alloy was positioned on the RS of the joints. The sole effect of the alloys' position on the joint properties was not determined.

The proper lap FSW joints of dissimilar 6111-T4/5023-T4 alloys (Table 4) were studied by Yoon et al. [47]. Two different joints, one with 6111 as the top plate on the RS and the other with 5023 as the top plate, were used. The sole effect of the alloys' position on the joint properties was not studied.

Studying the FSW joints of the dissimilar 6061/5086 alloys (Table 4), Ilangovan et al. [335] placed the 6061 alloy on the AS and the 5086 alloy on the RS. They found that the AS of the thermomechanically affected zone (AS-TMAZ) was the softest region considering the microhardness plot for both pin profiles, including the straight cylindrical (STC) one, the threaded cylindrical (THC) one, and the tapered cylindrical (TAC) one. This is due to the dissolution of precipitates in the AS-TMAZ region, which occurs as a result of the prevalence of heating and cooling cycles during welding. Under tensile loading, the strain localization occurred in such a region, thus causing failure. Only slight hardness variations were found at the RS.

During studies on the butt FSW joints of components made of dissimilar 2050/6061 alloys (Table 4), Reza-E-Rabby et al. [336] found that joint quality, process parameters, and welding temperature depended on material orientation in FSW. Defect-free welded joints with effective material transportation in the weld nugget zone were formed when using the 2050 alloy on the advancing side. In the latter case, the tool was also less loaded by in-plane reaction force.

The proper FSW joints of dissimilar 5083-O/6082-T6 alloys (Table 4), studied by Donatus et al. [337], were obtained when the 5083 alloy was positioned on the AS, while the 6082 alloy was positioned on the RS of the joints. The sole effect of the alloys' position on the joint properties was not studied.

Studying the FSW joints of components made of dissimilar cast Al-Si alloys A319/A413 (Table 4), Karam et al. [338] obtained sound joints between A319 and A413 plates when the A413 alloy was placed on the AS, while the A319 alloy was placed on the RS of the joints. Each tensed welded specimen was fractured outside the welded regions in the A413 BM placed on the AS.

The proper butt FSW joints of dissimilar 7075-O/6061-O and 7075-T6/6061-T6 alloys (Table 4), studied by Ipekoglu and Cam [339], were obtained when the 6061 alloy was placed on the AS, while the 7075 alloy was positioned on the RS of the joints. The sole effect of the alloys' position on the joint properties was not studied.

Studying the FSW joints of dissimilar 6061-T6/7075-T6 alloys (Table 4), Cole et al. [295] reported that the quality of welds was sensitive to alloy placement, tool offset, and tool-workpiece interface temperature. Under tensile loading, welds failed in the heat-affected zone of 6061 on the AS of the weld. Weld tool offsets into the 7075 alloy used on the retreating side enhanced the TS of the joint. The weld AS was hotter than the RS at both the tool shoulder and pin. There was a 20 °C enhancement in the advancing-side shoulder interface temperature when offsetting from -2 to +2 mm, while a lesser enhancement appeared at the pin interface (~3 °C). The strongest welds (-2 mm offset) corresponded to the lowest temperatures on the AS.

During studies of the lap FSW joints of 5 mm thick sheets made of dissimilar 2024-T3/7075-T6 alloys (Table 4), Song et al. [340] found that the WS and joint combination affected the hook geometry, which in turn affected the lap shear strength. In all 2024/7075 joints, voids occurred, and the joints fractured from the tip of the hook on the AS along the SZ/TMAZ interface during the lap shear test, inducing the tensile fracture mode. In 7075/2024 joints, the hook on the RS horizontally extended a long distance into the bottom stir zone at a higher WS. The 7075/2024 joints exhibited greater failure load than the 2024/7075 joints at lower WS values, while the opposite trend occurred at higher WS values.

The proper FSW joints of dissimilar 6061-T6/5083 alloys (Table 4), studied by Jannet and Mathews [341], were obtained when the 6061 alloy was placed on the AS, while the 5083 alloy was placed on the RS of the joints. The sole effect of the alloys' position on the joint properties was not studied.

For studying the correct FSW joints of dissimilar 5083-H111/6351-T6 alloys (Table 4), Palanivel et al. [342,343] placed the 6351 alloy on the AS, while the 5083 alloy was placed on the RS of the joint.

During studies of the butt FSW joints of plates made of dissimilar 2014-T6/6061-T6 alloys (Table 4), Jonckheere et al. [344] found that alloy placement and the tool's lateral shift affect weld hardness, as they influence the precipitate radius and volume fraction. The 2014 alloy was successively placed on the RS and AS. More 2014 alloys were observed in the nugget zone if the tool was shifted toward the 2014 alloy on the AS.

Similarly, Jonckheere et al. [345] reported that material flow and joint quality, regardless of material placement, are affected by welding conditions and their influences on heat input and weld nugget temperatures. If the 2014 alloy is placed on the AS of the weld, an abrupt transition between the weld nugget and the 6061 alloy occurs, leading to premature fracture in tension.

The FSW joints of dissimilar A356/6061-T6 alloys (Table 4), studied by Ghosh et al. [346,347], were obtained when the 6061 alloy was placed on the AS, while the A356 alloy was placed on the RS of the joints. According to [346], the low hardness of the A356 alloy was observed at the retreating side. The increase in hardness at the AS was correlated to the higher strength of 6061 with respect to the A356 alloy. This was due to the composite microstructure where both alloys were observed near the weld line. As reported in [347], during welding, in front of the tool, the material is plasticized and transported from the RS to the AS.

Studying the FSW joints of dissimilar Al alloys, Koilraj et al. [348] found that the microstructures of the weld's TMAZ on the AS exhibited highly deformed grains, with clearly discernible SZ/TMAZ and TMAZ/HAZ boundaries. On the RS, these boundaries were diffused, especially the latter. On the AS, there was a significant drop in hardness from the 2219 BM to the weld nugget boundary. On the RS, only a slight drop in hardness from the 5083 BM to the weld nugget boundary was observed.

For the FSW of dissimilar cast and wrought 6061 alloys (Table 4), Dinaharan et al. [349] reported that the material location strongly affected the material flow behavior. The material on the advancing side occupied the major portion of the weld zone under enhanced TRS. The joint exhibited the maximum TS when the cast Al alloy was positioned on the AS.

During the study of the FSW joints of dissimilar 5083-H111/6351-T6 alloys (Table 4), Palanivel et al. [350] found that the transportation of plasticized material from the AS to the RS was uniform from the top to the bottom of the joint when a tool with a straight pin profile was utilized.

The proper FSW joints of dissimilar 5052-H34/5023-T4 alloys (Table 4), studied by Song et al. [125], were obtained when the 5052 alloy was placed on the AS, while the 5053 alloy was placed on the RS of the joints. The sole effect of the alloys' position on the joint properties was not studied.

Studying the FSW joints of dissimilar 5052/A5J32 alloy sheets (Table 4), Kim et al. [304] obtained defect-free welds under all welding conditions by fixing the A5J32 alloy on the retreating side. However, for fixing the 5052 alloy on the retreating side, some welding defects occurred at the joint under certain welding conditions with weakened heat input. Placing the high-strengthened Al alloy on the AS led to excessive agglomerations and defects due to limited material flow. Therefore, this kind of Al alloy should be placed at the RS to limit the resistance to material flow.

The proper FSW butt joints of dissimilar 7050-T7451/2024-T351 alloys (Table 4), studied by Prime et al. [351], were obtained when the 2024 alloy was placed on the AS, while the 7050 alloy was placed on the RS of the joints. The sole effect of the alloys' position on the joint properties was not studied.

Gérard and Ehrström [299] suggested that the material with a higher solidus temperature should be on the AS to improve joint quality and eliminate internal defects/porosity.

For the study of the butt FSW joints of dissimilar 2024-T351/6056-T4 alloys (Table 4), Amancio-Filho et al. [300] placed the 2024-T351 alloy, considered the stronger one of the joined alloys, on the AS.

In the case of the FSW joints of wrought 6061/Al and A356 Al alloys (Table 4), Lee et al. [301] found that joint properties are strongly affected by the alloy on the RS. The mechanical properties of the SZ were greater when 6061 Al alloys were fixed at the retreating side. The WE was 80% for similar A356 joints, and for cases of dissimilar alloys, it was 83% for A356 on the AS and 87% for A356 on the RS.

Liu et al. [57] studied the relationship between the welding parameters and tensile properties of the FSW joints of components made of the 2017-T351 alloy (Table 4). The void-less joints fractured near or at the interface between the weld nugget and the thermo-mechanically affected zone (TMAZ) on the AS.

Studying the FSW joints of components made of 1050-H24 alloy (Table 4), Liu et al. [277] found that the location of the maximum strain gradually moved to the RS from the AS of the joint. Therefore, the fracture location of the joint gradually changed to the RS from the AS of the joint as the WS gradually increased.

The FSW joints of dissimilar cast AlSi9Mg (hypoeutectic silumin)/2017A alloys (Table 4), studied by Mroczka [352], were obtained when the 2017A alloy was positioned on the AS, while the AlSi9Mg alloy was positioned on the RS of the joints. During the process, the welding line was offset toward the AS, and an additional heat source was applied from the root side.

Studying the FSW joints of components made of 2017A alloy (Table 4), Mroczka et al. [353] found that microhardness tended to grow on the AS of the joint.

The FSW joints of dissimilar 7003/7046 alloys (Table 4), studied by Yang et al. [354], were obtained when the 7003 alloy was placed on the AS, while the 7046 alloy was placed on the RS of the joints. The hardness was much higher on the RS than on the AS, and the average hardness difference between the two sides was about 30 HV. After artificial aging, the hardness enhanced significantly, while the hardness difference increased to about 50 HV for the two sides.

Kasman and Ozan [355] studied butt FSW joints of 6013 Al plates (Table 4) obtained via the pin-offset technique. The highest TS, equal to 206 MPa, was obtained under the 1.5 mm pin offset toward the AS and a TRS of 500 rpm.

Zhao et al. [356] studied the influence of exchanging the AS and the RS material on the microstructure, mechanical properties, and electrochemical corrosion resistance for the FSW joints of components made of dissimilar 6013-T4/7003 alloys (Table 4). The joint with 6013-T4 placed at the AS was called the A6R7 joint. Accordingly, A7R6 referred to the joint with Al7003 placed at the AS. The authors reported that various joint cross-sections were obtained when exchanging the AS and RS materials. The material on the AS was more deformed during the welding process. When Al6013 was positioned on the AS, the plastic flow of the weld was enough. Independent of the AS or the RS, the Al6013-T4 side was the weak region in terms of both the TS and hardness. The fracture location matched the point of minimum hardness, confirming a correlation between fracture and the lower BM strength.

In lap FSW, when the rotation speed was low and the WS was high, void-type defects appeared on the AS or center of the nugget [357].

Studying the FSW joints of the 6061-T6 alloy (Table 4), Juarez et al. [358] reported that considering the surfaces of tensile specimens during welding without heat treatment (BMW) and solubilized heat treatment and partial aging before welding (HTBW), most of the fractures occurred on the AS of the tool and in the heat-affected zone. Fractures appeared on the unaffected material zone (UFM) and the RS for the case with solubilized heat treatment and aging after welding (HTAW).

Godhani et al. [359] obtained proper butt joints of dissimilar 6061-T6/7075-T6 alloys (Table 4) when the 6061 alloy was placed on the AS, while 7075 was used on the RS of the joint. The sole effect of the alloys' position on the joint properties was not studied.

Investigating the FSW joints of components made of dissimilar 5052/and 6061 alloys obtained with various pin-eccentric stir tools (the pin eccentricities of 0, 0.4, and 0.8 mm),

Chen et al. [360] obtained sound joints using the 6061 alloy on the AS. The sole effect of the alloys' position on the joint properties was not studied.

Zhang et al. [361] studied the FSW joints of 5 mm thick similar and dissimilar 7075AA7075-T651/2024 and AA2024-T351 alloys obtained using a tool with a cylindrical taper threaded pin, a shoulder diameter of 15 mm, a pin diameter 3.76 mm on the insertion side and 6.66 mm on the shoulder side, a pin length of 5 mm under TRS values of 600, 950, 1300 and 1650 rpm, a WS of 100 mm/min, and a tilt angle of 2.5 degrees. They found that the width of the TMAZ on the RS was greater than that of the AS.

Material flow under specific welding conditions is the common thread among the different studies, with material placement closely behind but distinguishably secondary. Various configurations of FSW joints of various Al alloys were presented by Patel et al. [254].

Table 4. Configurations of FSW joints of various Al alloys.

Refs.	Configuration	Alloy Combinations	Thick (mm)	Alloy Positioning	
				AS	RS
[308]	Butt	2024-T351/5083-H112	6.35	2024	5083
[308]	Butt	7075-T651/2024-T351	6.35	7075	2024
[310]	Butt	7075-T651/2024-T351	6	Both	Both
[311]	Butt	7075-T651/5083-H111	6	Both	Both
[311]	Butt	5052/AlMg ₂ Si	8	AlMg ₂ Si	5052
[316]	Butt	2024-T351/6061-T6	6	2024	6061
[317]	Butt	6061-T6/6351T6	6.35	Both	Both
[318,362]	Butt	6082-T6/7075-T6	10	7075	6082
[319]	Butt	6061-T651and 5A06-H112	5	6061	5A06
[320]	Butt	6101-T6/6351-T6	12	6101	6351
[321]	Butt	2024-T3/6063-T6	8	2024	6063
[322]	Butt	2219-T87/2195-T8	7.2	Both	Both
[323]	Butt	2017A-T451/cast AlSi9Mg	6	2017A	AlSi9Mg
[326]	Butt	5083-H111/6082-T6	5	6082NR	5083NR
[144]	Butt	5083-H111/6351-T6	6	6351	5083
[328]	Butt	2024-T6/7075-T6	5	2024	7075
[296,329]	Butt	Al-Mg-Si/Al-Zn-Mg	15	Both	Both
[331]	Butt	UFG 1050/6061-T6	2	Both	Both
[332]	Butt	2024-T3/2198-T3	3.18	2198	2024
[333,334]	Butt	6061-T6/7050-T7451	5	7050	6061
[335]	Butt	5086-O/6061-T6	6	6061	5086
[336]	Butt	2050-T4/6061-T651	20	Both	Both
[337]	Butt	5083-O/6082-T6	NR(~7)	5083	6082
[338]	Butt	A319/A413 cast	10	A413	A319
[339]	Butt	7075-O/6061-O 7075-T6/6061-T6	3.17	6061	7075
[295]	Butt	6061-T6/7075-T6	4.6	Both	Both

Table 4. Cont.

Refs.	Configuration	Alloy Combinations	Thick (mm)	Alloy Positioning	
				AS	RS
[341]	Butt	5083-O/6061-T6	6	6061	5083
[346,347]	Butt	A356/6061-T6	3	6061	A356
[348]	Butt	2219-T87/5083-H321	6	2219	5083
[349]	Butt	6061 cast/6061 rolled	6	Both	Both
[350]	Butt	6351-T6/5083-H111	6	6351	5083
[127]	Butt	5052-H34/5023-T4	~1.5	5052	5023
[304]	Butt	5052-H34/5023-T4	1.5 & 1.6	Both	Both
[351]	Butt	7050-T7451/2024-T351	25.4	2024	7050
[300]	Butt	2024-T351/6056-T4	4	2024	6056
[301]	Butt	cast A 356/6061	4	Both	Both
[57]	Butt	2017-T351	5	Both	Both
[277]	Butt	1050-H24	5	Both	Both
[352]	Butt	2017A-T451/AlSi9Mg	6	2017A	AlSi9Mg
[353]	Butt	2017A	6	Both	Both
[354]	Butt	7003-T4/7046-T4	3	7003	7046
[356]	Butt	6013-T4/7003	2.8	Both	Both
[355]	Butt	6013-T6	5	Both	Both
[358]	Butt	6061-T6	9.5	Both	Both
[359]	Butt	6061-T6/7075-T6	6	6061	7075
[325]	Underwater Butt	6061-T6/7075-T6	5	6061	7075
[46,314,363]	Butt NA Butt	2017A-T451/7075-T651	6	Both	Both
[342,343]	NA Butt	6351-T6/5083-H111	6	6351	5083
[344,345]	NA Butt	2014-T6/6061-T6	4.7	Both	Both
[324]	NA	5083-H12/6061-T6	1.5	6061	5083
[330]	NA	2024-T3/6061-T6	4.8	2024	6061
[327]	NA	5052/6061	1, 1.5	6061	5052
[312]	NA	2024-T4/7075-T6	4	2024	7075
[313]	NA	6351-T6/5083-H111	6	6351	5083
[357]	Lap	6111-T4/5023-T4	1	Both	Both
[340]	Lap	2024-T3/7075-T6	5	Both	Both
[47]	Lap	6111-T4/5023-T4	1	Both	Both
[61]	Lap	7075-T6/2024-T3 7075-upper; 2024-lower	3	2024	7075

It can be noticed that the material position (AS/RS) plays a significant role in the FSW process, particularly in the case of dissimilar Al alloys. The placement of harder material in the AS, for both butt configuration and to a lesser extent lap configuration, provides better joint quality. This agrees with observations in [364]. It can be inferred that higher mechanical properties in the weld zone were often obtained when a harder material was placed on the RS. Some authors did not study the effect of the Al alloys' position on the

joint properties, probably based on recommendations from the literature for a given pair of Al alloys. Some valuable findings related to the effect of alloy placement on the FSW joint properties are presented in Table 5 (some of the data were published earlier in an excellent review by Di Bella et al. [257]).

Table 5. Effect of position of sheets.

Ref.	Alloys Position	Pin Profile	Tilt Angle (°)	TRS [rpm]	WS [mm/min]	AF [kN]	Main Results
[296]	(AS/RS) 2017-T6/(RS/AS) 6005A-T6	NA	NA	NA	NA	NA	Better performance joints are obtained when the BM with lower mechanical properties, is positioned on the RS.
[309]	(AS/RS) 2024-T351/(RS/AS) 7075-T651	Threaded	2.5	600	200	NA	The SZs show corrosion resistance close to that of the BM on the AS, with dominating intergranular corrosion.
[304]	(AS/RS) 5052/(RS/AS) 5J32	Threaded cylindrical	3	1000; 1500	100; 200; 300; 400;	NA	Positioning the high-strength alloy on the AS promotes excessive agglomerations and the creation of defects due to limited material flow.
[306]	(AS/RS) 5052-H32/(RS/AS) 6061-T6	NA	NA	NA	NA	NA	The position of 5052 on the AS ameliorates the mixing of the BMs in the SZ, whereas the placement of base metals does not affect the location of the fracture.
[305]	(AS) 5083-O/(RS) 6082-T6	Triflute	0	400	300; 400	NA	Material primarily flows from the AS to the RS with insignificant mixing inside the tool shoulder region. Material extrusion predominantly occurs in the TMAZ on the RS. The finest grains appear in the regions closest to the tool edge inside the RS.
[356]	(AS/RS) 6013-T4/(RS/AS) 7003	Conical	2.5	800	400	NA	The material on the AS undergoes higher deformations during the FSW. Regardless of the 6013-T4 placement, it is the weaker region in both tensile specimens and hardness samples.
[310]	(AS/RS) 7075-T651/(RS/AS) 2024-T351	Conical threaded and with flute radius (0, 2, 3, 6, and ∞ mm)	NA	900	150	NA	Material placement on the AS and the RS of the weld influenced the weld quality, which was better in the case when a softer BM was positioned on AS.
[311]	(AS/RS) 7075-T651/(RS/AS) 5083-H111	Triflute, tapered with a thread	NA	280; 355; 450; 560	140	26.4	The (AS) 5083/(RS) 7075 alloy placement was accompanied by the occurrence of porosity, voids, or wormholes in the SZ at higher TRS values. The highest TS of the defect-free joint was obtained at TRS of 280 rpm, and the triflute pin.

Table 5. Cont.

Ref.	Alloys Position	Pin Profile	Tilt Angle (°)	TRS [rpm]	WS [mm/min]	AF [kN]	Main Results
[316]	(AS) 2024/ (RS) 6061	Square frustum	2	800	31.5	NA	The fraction of precipitates in the SZ on the RS exceeded that on the AS. The extent of continuous dynamic recrystallization in the TMAZ on the AS was less than that on the RS and the recrystallized grains seldom occurred on the AS. The overall texture intensity was weaker on the AS and stronger on the RS than that of the BMs. Discontinuous static recrystallization and/or meta-dynamic recrystallization occurred on the AS. The microhardness profile on the AS was uniform while comprising three different regions on the RS.

Tool Rotation Speed, Welding Speed, and Axial Force

The tool rotation speed influenced the intensity of plastic deformation and thus material mixing. Kalembe-Rec et al. [311] found that material mixing was proportional to the TRS for a dissimilar 7075–5083 joint. Under high TRS values, numerous imperfections, including poor surface (flash), voids, porosity, tunneling, or the formation of wormholes, occurred due to excessive heat input [365,366]. Low WS values enhance the heat input and are often accompanied by defects such as tunneling [341,346,367–369].

Obtaining a defect-free joint with a good metallurgical bond and mechanical properties needs the selection of an appropriate/optimized combination of the TRS and the WS, particularly for combinations of dissimilar Al alloys [317,322,324,325,327,330,331,338,341,342,346–348].

Tool Rotational Speed

During the FSW process, the rotating tool generates heat and friction, softening the welded component material and forming a plasticized region around the tool. The rotating tool moving along the joint presses the softened material behind it, forming a solid-state weld. The TRS affects the welding process [370,371] through the following factors:

- Heat generation: As the rotating tool generates frictional heat in the contact zone between the tool and the welded components, it controls the material plastic flow depending on heat generation or input [256]. Higher TRS values allow for generating more heat, which induces material softening and facilitates material mixing and bonding between the welded components.
- The size of the plasticized zone around the tool: This influences the intensity of material plastic deformation and consequently its mixing [256,355]. A higher TRS increases the plasticized zone, providing a better bond between the two welded components [365–367].
- Weld quality: A too-low TRS causes incomplete weld formation and poor bonding between the welded components. A too-high TRS induces weld defects, including poor surface (flash), voids, porosity, and tunneling or the formation of wormholes due to excessive heat input.
- Tool wear: A higher TRS often increases wear on the tool, thus decreasing its lifespan.
- Axial force (pushing the tool through the welded components): The TRS also influences AF magnitude, as a higher TRS needs higher AF, constraining the tool's position and averting its slippage out of the joint.

Additionally, the TRS influences the joint behavior as a function of the sheet Al alloy in various manners [372]. Modifying the TRS affects the size and macrostructure of the NZ

of the FSW joint between components made of the 2524-T351 alloy. The width of such a zone increases with an increase in the TRS. Under a high TRS, the area of the recrystallized zone expands with an increase in temperature, which causes this phenomenon [373]. The insufficient energy yielded for dynamic recrystallization at lower TRS values causes incomplete dynamic recrystallization and ineffective grain refinement strengthening. At a higher TRS, the higher strength in the NZ resulted from a smaller grain size [374]. In the joint between components made of the 5086-H32 alloy, a lower TRS induces various defects resulting from inadequate heat, which causes improper material softening [375]. The excessive heating and deformation induced by the TRS in the 5052-O alloy enhanced b-phase (Mg_2Al_3) particles via Mg atom diffusion toward grain boundaries. The dissolution of such intermetallic particles within the NZ subsequently reduced the joint strength [376]. With an increase in the TRS of the 6082-T6 alloy, the weld temperature first increased and then decreased, thus facilitating the creation of smaller equiaxed recrystallized grains in the NZ. The hardness in the NZ zone increased with the TRS increasing to 1200 rpm due to the increased dislocation density. This increase in dislocations resulted from the precipitation and dissolution of the second phase, together with the refinement of the Al matrix grain size in the microstructure of the zone [377]. For the 7075-T6 alloy, the TRS strongly affects weld properties, i.e., by increasing the TRS from 600 to 1550 rpm, the average nugget grain size increased from 6.8 to 8.9 μm . Also, at a medium TRS, optimum mechanical properties are achievable [378].

Several studies have been performed related to the FSW of dissimilar Al alloys [254,379].

Studying the FSW joint between (RS) 5083-H12/(AS) 6061-T6 alloys obtained under various TRS (700, 1600, and 2500 rpm) and WS (25, 212.5, 400 mm/min) values using a tool with various pin diameters (2, 3, and 4 mm) and shoulder diameters (10, 12, and 14 mm), Ghaffarpour et al. [380] found that the effect of the pin diameter was less clear than that of the TRS. With an increase in both the TRS and the pin diameter, the heat input increased, enhancing the TS. The effect of the TRS was greater than that of the WS and the shoulder diameter. Thermocouple measurements, tool torque, the extent of material mixing, and macrostructural images confirmed that the temperature under the tool was more strongly affected by the TRS compared to the WS, as also reported for 5083/6082 joints [381]. The enhancement in the TS with greater friction heat resulted from the better mixing of dissimilar alloys due to proper stirring caused by higher heat input. Additionally, the plasticization effect during FSW increased with higher heat input. Consequently, softer materials were easier to mix and stir. The strength reached a maximum value by increasing the heat input, and then its values decreased beyond a certain optimum heat level. The lowest hardness occurred in the HAZ of the 6061-T6 sheet. When the TRS increased, the hardness of the mixing zone decreased. This was because the higher TRS generated more heat, leading to local annealing in both sheets. Additionally, the frictional heat increased the temperature over the aging temperature of the 6061-T6 sheet. Consequently, the fine Mg_2Si precipitates, due to undergoing the hardening phase in the 6061 alloy, either dissolved or grew, thus decreasing the hardness. The same phenomenon can occur in the case of 5083-H12 alloy. Excessive heat often induced grain growth in both alloys, thereby lowering strength and hardness. Consequently, the optimal TRS had intermediate values [382].

The welded joints of components made of 2024-T351/5083-H112 alloys in one sample and 7075-T651/2024-T351 alloys in another sample (Table 6), studied by Niu et al. [308], were obtained under a TRS of 600 rpm and WS of 150 mm/min, respectively.

The proper FSW joints of 7075-T651/2024-T351 alloys (Table 6), studied by Hasan et al. [310], were obtained under TRS of 900 rpm and WS of 150 mm/min.

Ge et al. [61] studied how EST affects the shear failure load of lap joints. The shear fracture mode occurred in lap joints obtained with a small (3 mm) pin at all WS values. A higher TRS, lower WS, and greater plunge depth improved the diffusion bonding strength of the lap joint. The lap shear failure load decreased with the increase in the WS, due to

worsened diffusion bonding induced by lower heat input. The highest lap shear failure load with a small pin was obtained at a WS of 60 mm/min.

Studying the FSW joints of components made of 7075-T651/5083-H111 alloys (Table 6), Kalemba-Rec et al. [311] reported that, at higher TRS values, the placement of 5083 on the AS and 7075 on the RS was accompanied by the occurrence of porosity, voids, or wormholes in the stir zone. The highest TS of the defect-free joint was obtained at a TRS of 280 rpm. A higher TRS at a constant WS caused a lower WE.

Saeidi et al. [368] found that an enhancement in the TRS from 450 to 800 rpm at a selected WS (30, 41.5, or 50 mm/min) initially reduced and then enhanced the joint efficiency.

The proper FSW joints of 2024-T4/7075-T6 alloys (Table 6), studied by Safarjali et al. [312], were obtained under a TRS of 1140 rpm and a WS of 32 mm/min. The effect of the TRS and the WS on the joint properties was not investigated.

Palanivel et al. [313] conducted studies on the FSW joints of components made of dissimilar 6351-T6/5083-H111 alloys (Table 6), focusing on the optimization of, inter alia, TRS and WS. They found that the weld quality related to its UTS was affected by the tool shoulder profile, the TRS, and the WS. The WE reached up to 78.7% for the full impeller shoulder tool, with a WS of 60 mm/min and a TRS of 1000 rpm.

For studying FSW sheets made of dissimilar 2017A-T451 and 7075-T651 alloys, Hamilton et al. [363] obtained the best welds using a tool positioned with a tool tilt angle of 1.5°. The TRS and WS were 355 rpm and 112 mm/min, respectively, and the applied force during processing was 32.8 kN.

Gupta et al. [383] conducted studies on the FSW joints of components made of dissimilar 5083-O and 6063-T6 alloys by focusing on the optimization of tool geometry, TRS, and WS. Multi-optimal weld properties comprising the TS, the average hardness at the NZ, the set of process parameters, and the average grain size at the NZ were obtained for a TRS of 900 rpm and a WS of 60 mm/min. The WE reached up to 76.4%.

Huang et al. [315] revealed that, for Al metal matrix composites (MMCs), the material flow depended on the TRS and the reinforcing phases. The welding of Al-Mg/Al-Mg₂Si alloys (Table 6) also depended on the hard and brittle intermetallic compounds of the primary Mg₂Si phases in Al-Mg₂Si alloys.

The proper FSW joints of dissimilar 2024/6061 alloys (Table 6), studied by Moradi et al. [316], were obtained under a TRS of 800 rpm and a WS of 31.5 mm/min. The effect of the TRS and WS on joint properties was studied neither solely nor in combination.

The FSW joints of dissimilar 6351-T6/6061-T6 alloys (Table 6), studied by Prasanth and Raj [317], were obtained under TRS values of 600, 900, and 1200 rpm and WS values of 30, 60, and 90 mm/min. The authors determined the relationship between the TRS, the WS, and the AF versus the UTS, the YS, and elongation. The highest WE was obtained for a TRS of 900 rpm, a WS of 60 mm/min, and an AF of 6 kN.

The proper FSW joints of dissimilar 6082-T6/7075-T6 alloys (Table 6), studied by Azeez et al. [318,362], were obtained under TRS values of 950 and 1000 rpm and WS values of 80 and 100 mm/min. The increase in the TRS with the same WS slightly increased the hardness of the joint, whereas the increase in the WS with the same TRS slightly decreased the hardness.

Peng et al. [319] studied the FSW joints of rolled plates made of dissimilar 6061-T651 and 5A06-H112 alloys (Table 6), obtained for various TRS and WS values. With the increase in the TRS, more heat was generated during FSW. The increase in heat input could enlarge the size of the HAZ and reduce the slant angle of the HAZ, thus causing the fracture angle to decrease and the dimples to change from inclined ones to normal ones.

During Charpy impact tests on the FSW joint between (AS) 6101-T6/(RS) 6351-T6 alloys obtained at three TRS values (900, 1100, and 1300 rpm), a WS of 16 mm/min, and a tilt angle of 2° and using a high-C high-Cr steel tool comprising a shoulder with a diameter of 25 mm and a pin with a large diameter of 8 mm, small diameter of 6 mm and a length of 11.7 mm, as well as a taper cylindrical thread profile, Das and Toppo [320] reported that the minimum energy was found at a TRS of 900 rpm due to low friction pressure and insufficient

friction time, causing the inadequate generation of frictional heat and insufficient time for the formation of a strong bond between the welded components. However, with the TRS increasing to 1100 rpm, the impact energy of the joint also increased. Subsequently, as the TRS further increased to 1300 rpm, the impact energy decreased. This decrease in impact energy resulted from grain refinement occurring in the weld zone due to the high friction heat generated. The impact test samples exhibited a ductile fibrous fracture.

Studying the FSW joint of 6101-T6/6351-T6 obtained for a TRS ranging from 900 rpm to 1500 rpm, a WS of 60 mm/min, a tilt angle of 2°, and various AFs (4, 5, 6, and 8 kN) and using an EN32 steel tool comprising a flat-faced shoulder with diameter of 18 mm, a pin with diameter of 6 mm and length of 5.85 mm, and a cylindrical threaded profile, Das et al. [384] found that the TRS of 1300 rpm provided better mechanical and metallurgical properties of joints. At lower TRS values, the TS started to worsen mainly due to inadequate tool stirring, which generated minimal frictional heat at TRS values of 900 rpm and 1100 rpm. Consequently, compromising the material flow decreased the TS. However, an enhanced TRS (1300 rpm) increased the UTS due to the sufficient heat input at this TRS, promoting better joint quality. The weld region comprised equiaxed fine grains, further increasing the TS. For the TRS exceeding a certain threshold (1500 rpm), excessive heat input occurred, inducing reprecipitation and reducing the dislocation density of strengthening precipitates such as Mg₂Si, which resulted in a weakened TS. During bending tests under a TRS of 900 rpm, the joints exhibited lower ductility. Additionally, microcracks occurred on the outer surface of the weld joint. Such issues resulted from improper material mixing and insufficient AF applied during FSW. At a TRS of 1100 rpm, heat generation enhanced the improvement in the flow of the softened mixture of the two alloys. Consequently, the ductility of the joints improved. At a high TRS of 1500 rpm, the material flow became excessive due to the intense heat generated between the tool shoulder and the welded components' interface. This excessive flow induced the breakage of the intermetallic Mg₂Si compound, decreasing the bending strength. However, at a TRS of 1300 rpm, the joint exhibited enough ductility due to the uniform interdiffusion of the intermetallic Mg₂Si compound in the NZ, thus enhancing the bending strength. Microhardness varied at the NZ due to differences in the heat input during the FSW, also affecting the BM microstructures. At a TRS of 900 rpm, the hardness was lower than those of the BMs and other joints due to a softening effect at the weld joints. The hardness was affected by the distribution of the intermetallic Mg₂Si compound and the grain microstructure within the NZ. At a TRS of 1300 rpm, the rate of the heat input increased, causing the formation of fine equiaxed grains and a well-spaced microstructure within the NZ, thus exhibiting an optimum microhardness value. Therefore, the hardness at the NZ was affected by the grain size. However, with a further increase in the TRS to 1500 rpm, the hardness decreased, mainly because the high heat input caused material softening in the NZ. Consequently, the grain size and the dissolution of strengthening precipitates, such as Mg₂Si, decreased, further reducing the hardness.

Investigating the FSW joints of components made of dissimilar 2024-T3/6063-T6 alloys (Table 6), Sarsilmaz [321] found that microstructural and mechanical properties were strongly affected by variations in welding parameters within the chosen range of welding conditions. Under lower rotational and higher traverse speed in all welding conditions, the Wohler curves exhibited maximum fatigue strength.

Studying the FSW joints of components made of dissimilar 2219-T87/2195-T8 alloys (Table 6), No et al. [322] found that the WS only slightly affected the properties of the joint, but the latter strongly depended on the TRS.

Kopyscianski et al. [323] obtained high weld quality for process parameters including a WS equal to 112 mm/min, a TRS equal to 355 rpm, and a vertical force equal to 32.8 kN (Table 6). The effect of the TRS and the WS on joint properties was studied neither solely nor in combination.

The proper FSW joints of 5083-H12/6061-T6 alloys (Table 6), studied by Ghaffarpour et al. [324], were obtained under TRS values in the range of 700–2500 rpm and WS values in the range of 25–400 mm/min.

For the underwater FSW joints of dissimilar 6061/7075 alloys (Table 6), Bijanrostami et al. [325] found that the maximum TS of 237.3 MPa and elongation rate of 41.2% were reached at a TRS of 1853 rpm and a WS of 50 mm/min. Thus, the WE reached up to 76.5%.

Studying the effect of the TRS-to-WS ratio (v ratio) on the strength of the FSW joints of dissimilar 6082-T6/5083-H111 alloys (Table 6), Kasman et al. [326] found that an NZ profile containing onion rings of the shape depended on the value of the TRS and the WS. These speeds also caused variations in the effect of a constant v ratio on the profile and the structure of the NZ. At a lower TRS and WS, lower UTS values were observed.

Studying the FSW joints of dissimilar 5083-H111/6351-T6 alloys (Table 6), Palanivel et al. [144] reported that a low WS and high TRS enhanced the frictional heat because of the enhanced residing time of the tool. The TRS caused the stirring and mixing of the material surrounding the rotating pin, which in turn enhanced the temperature of the metal. Thus, the TRS strongly affected the WS. A low TRS providing a low heat input led to a lack of stirring and yielded defects. Contrarily, during FSW, the enhancement in the TRS caused an increase in the heat input. More heat input destroyed the regular flow of plasticized material, and an enhanced TRS induced the excessive release of stirred materials to the upper surface, which left voids in the weld zone. The lowest and highest WS produced defects due to the increased frictional heat and insufficient frictional heat generated, respectively. The FSW at higher WS values caused a short exposure time in the weld area with insufficient heat and poor plastic flow of the metal and produced defects in the joints. Higher WS values causing low heat inputs provided faster cooling rates of the welded joint and hence resulted in defects.

Studying the FSW joints of components made of 5052-H32/6061-T6 blanks (Table 6), Doley and Kore [327] found that, for all thicknesses, the weld produced at 63 mm/min speed exhibited more ductility compared to that produced at 98 mm/min.

Saravanan et al. [328] reported that the maximum TS of 356 MPa was obtained with a D/d ratio of 3, a TRS of 1200 rpm, a WS of 12 mm/min, and an AF of 8 kN (Table 6).

Yan et al. [296,329] obtained the proper FSW joints of sheets made of dissimilar Al-Mg-Si/Al-Zn-Mg alloys (Table 6) under a TRS equal to 800 rpm and a WS equal to 180 mm/min.

Studying the FSW joints of components made of dissimilar 2024-T3/6061-T6 alloys (Table 6), Zapata et al. [330] found that the enhancement of the TRS decreased the magnitude of the longitudinal residual stresses. This was due to the increase in the heat input and the weakening of thermal mismatch between the different zones of the weld. The effect of the WS on the residual stress was small in comparison to the effect of the TRS, generating only a small increase in the profile of the retreating side when it was enhanced.

For the butt FSW joints of 2 mm thick plates including one rolled from ultrafine-grained UFGed 1050 alloy and the other made of the 6061-T6 alloy (Table 6), Sun et al. [331] found that at various WS values, two fracture modes occurred for the tensed specimens depending on their revolutionary pitches. The FSW joints were obtained under a TRS of 800 rpm and WS values of 400, 600, 800, and 1000 mm/min.

From a second source of information, studying the butt FSW joints of the ultrafine-grained UFGed 1050 Al plates with a thickness of 2 mm and 2 mm thick 6061-T6 alloy plates (Table 6), Sun et al. [331] reported that after welding under a revolutionary pitch varying in range from 0.5 to 1.25 mm/rev, in the joint stir zone, the initial nanosized lamellar structure of the UFGed 1050 Al alloy plate changed into an equiaxial grain structure with greater average grain size as a result of dynamic recrystallization and the subsequent grain growth. An equiaxial grain structure with a lower grain size simultaneously appeared in the 6061 alloy plates, together with the coarsening of the precipitates.

The proper FSW joints of 2024-T6/6061-T6 alloys (Table 6), studied by Sun et al. [327], were obtained under a TRS of 1000 rpm and a WS of 500 mm/min.

During studies on the butt FSW joints of components made of dissimilar 6061 and 7050 alloys, Rodriguez et al. [334] found that in the joint microstructure, distinct lamellar bands occurred, and various degrees of intermixing affected by the TRS were observed. The joints consistently fractured on the 6061-alloy side. Two modes of failure existed, one in the stir zone and the other in the heat-affected zone. The inadequate material intermixing produced at low TRS values induced low mechanical strength and failure in the stir zone. The failure in the heat-affected zone at high TRS values occurred due to material softening. Studying the FSW joints of components made of dissimilar 6061 and 7050 high-strength Al alloys, Rodriguez et al. [333] found that the cyclic strain hardening and the number of cycles to failure enhanced with an increase in the TRS.

The proper butt FSW joints of dissimilar 6061/7050 alloys (Table 6), studied by Rodriguez et al. [333,334], were obtained under TRS values of 270, 340, and 310 rpm and a WS of 114 mm/min.

The lap FSW joints of plates made of dissimilar 6111-T4/5023-T4 alloys (Table 6), studied by Yoon et al. [47], were obtained with a revolutionary pitch of 0.067 mm/rev, an onion ring nugget with a rotation speed of 1500 rpm and a WS of 100 mm/min, and a revolutionary pitch of 0.7 mm/rev with a void-defect nugget with a TRS of 1000 rpm and a WS of 700 mm/min.

Ilangovan et al. [335] reported that all three pin profiles yielded defect-free surface joints with a TRS of 1100 rpm and a WS of 22 mm/min (Table 6) because heat generation was the same for those tool pin profiles.

During studies on the butt FSW joints of components made of dissimilar 2050/6061 alloys (Table 6), Reza-E-Rabby et al. [336] found that quality welds can be produced at low rotational and travel speeds. Flats could not produce defect-free welds at the highest WS.

The proper FSW joints of dissimilar 5083-O and 6082-T6 alloys (Table 6), studied by Donatus et al. [337], were obtained under a TRS of 400 rpm and a WS of 400 mm/min.

The FSW joints of dissimilar cast Al-Si alloys A319 and A413 (Table 6), studied by Karam et al. [338], were obtained under rotational values of 630, 800, and 1000 rpm and WS values of 20, 40, and 63 mm/min. The average size of the Si particles and α -Al grains enhanced with an increase in the TRS and/or a decrease in the WS. At the center of the stirred zone, Si particles were more uniformly distributed at low welding or high TRS values compared to the case with higher welding or lower TRS. The average hardness of the welded regions enhanced with the increase in the WS and/or a decrease in the TRS.

The butt FSW joints of dissimilar 7075-O/6061-O and 7075-T6/6061-T6 alloys (Table 6), studied by Ipekoglu and Cam [339], were obtained under TRS values of 1000 and 1500 rpm and WS values of 150 and 400 mm/min. The enhancing rotational rate increased the amount of the (RS) BM in the DXZ microstructure.

Cole et al. [295] found that the highest joint strength was achieved at 700 rev/min spindle speed and 100 mm/min weld speed with 7075-T6 on the retreating side (Table 6). The highest value of weld interface temperatures was obtained for a low tool travel speed value equal to 100 mm/mm.

During studies on the lap FSW joints of 5 mm thick sheets made of dissimilar 2024-T3/7075-T6 alloys (Table 6), Song et al. [340] found that the hook deflects significantly upwards into the stir zone (SZ) at lower WS values in both combinations. The WS and joint combination affected the hook geometry, which in turn affected the lap shear strength. In both joint combinations, the lap shear strength increased with the enhancement of WS. The 7075/2024 joints exhibited a greater failure load than the 2024/7075 joints at lower WS values, while the opposite trend occurred at higher WS values. In the case of 2024/7075 joints, the WE varied in the range of 15%–39% depending on the WS in the range of 30–300 mm/min. The WE reached up to 57% under a WS of 150 mm/min in the case of the 7075/2024 joint.

The proper FSW joints of dissimilar 6061-T6/5083-O alloys (Table 6), studied by Jannet and Mathews [341], were obtained under TRS values of 600, 750, and 900 and a WS of 60 mm/min.

The FSW joints of 5083-H111 and 6351-T6 alloys, studied by Palanivel et al. [342], were obtained considering a TRS of 950 rpm and three values of the WS (36, 63, and 90 mm/min). The WS of 63 mm/min provided the best quality of welds.

The butt FSW joints of the dissimilar 2014-T6 and 6061-T6 alloys, studied by Jonckheere et al. [344], were obtained under TRS values of 500 and 1500 rpm and a WS of 90 mm/min. The welds obtained at the TRS of 500 rpm containing more 2014 alloy in their SZ or in contact with the tool shoulder were cooler and presented a narrower softened zone. The welds obtained at a TRS of 1500 rpm exhibited no effect of the tool shift or alloy placement on their hardness profile.

Palantivel et al. [343] reported that the joints exhibited a higher TS using a straight square pin profile tool at a TRS of 950 rpm, a WS of 63 mm/min, and an AFe of 14.7 kN (Table 6). The AF acting on the tool most contributed to the UTS, followed by the tool pin profile, the WS, and the TRS for the range considered. The WE reached up to 88.6%.

Studying the FSW joints of components made of dissimilar A356/6061 alloys (Table 6), Ghosh et al. [346] reported that with an increase in the WS, the matrix grain size became finer, without the incessant limitation of Si-rich particles' size being affected by interaction time between the tool and the substrate. The maximum WE of 116% with respect to that of the 6061 alloy occurred at an intermediate tool-traversing speed, providing a fine matrix grain size and a small size of Si-rich particles.

The lap FSW joints of 7075-T6/2198-T351 alloys (Table 6), studied by Velotti et al. [385], were obtained under a TRS of 830 rpm and a WS of 40 mm/min. The WE was quite low in comparison to that obtained using the butt FSW joints of the same alloy pair.

Studying the FSW joints of plates made of dissimilar 2219-T87/5083-H321 alloys (Table 6), Koilraj et al. [348] found that the WS strongly affected the joint soundness. The welds were obtained under a TRS ranging from 400 to 800 rpm, and WS ranged from 15 to 60 mm/min. The WE reached up to about 90%.

For the FSW dissimilar cast and wrought 6061 alloys (Table 6), Dinaharan et al. [349] reported that the material location prior to welding and the TRS strongly affected the material flow behavior. The material on the advancing side occupied the major portion of the weld zone under enhanced TRS. The joint exhibited the maximum TS when cast Al alloy was positioned on the AS at all TRS values.

Studying of FSW joints of components made of dissimilar 5083-H111/6351-T6 alloys (Table 6), obtained under three TRS values (600 rpm, 950 rpm, and 1300 rpm), a WS of 60 mm/min, an AF of 8 kN, and a tilt angle of 0° and using high-carbon high-chromium steel tools with a shoulder diameter of 18 mm, pins with a diameter of 6 mm and a length of 5.7 mm, and five various profiles (i.e., straight square, straight hexagon, straight octagon, tapered square, and tapered octagon), Palanivel et al. [350] reported that the TRS and the pin profile influenced the joint strength because of varying material flow, loss of cold work in the HAZ in the 5083 side, the dissolution and overaging of precipitates in the 6351 side, and the formation of macroscopic defects in the weld zone. They found that an increase in TRS (from 600 to 1300 rpm) at a constant traverse speed of 60 mm/s for various pin geometries initially enhanced and then decreased the weld effectiveness. The weld fabricated using a TRS of 950 rpm and straight square pin profile reached an efficiency of up to 88.6%.

For the FSW joints between (RS) 2219-T6/(AS) 5083 alloys obtained under five various TRSs (400, 800, 1200, 1600, and 2000 rpm), WEs (30, 210, 390, 570, and 750 mm/min), and tool offsets (−2, −1, 0, +1, and +2 mm), and a tilt angle of 2° and using an H13-grade steel tool with a 15 mm diameter shoulder, a frustum-shaped threaded pin of a 6 mm top diameter and a 4 mm bottom diameter, Mastanaiah et al. [367] reported that defect-free welds were achievable under a wide range of conditions. However, at the lowest TRS, highest WS, and with a tool offset toward the 2219 alloy, welds could comprise defects. The degree of intermixing was strongly affected by the TRS and WS. At higher TRS and lower WS values, a more intensive intimate mixing between dissimilar alloys occurred. Under

the conditions of high heat input (TRS varying from 400 to 2000 rpm) and the lowest WS of 30 mm/min, extensive intermixing occurred in the NZ.

Laska et al. [379] studied dissimilar butt joints between (AS) 5083/(RS) 6060 alloys, which were obtained under a TRS ranging from 800 to 1200 rpm, a WS of 100 m/min, and a tilt angle of 2°. The joints were obtained using a composite tool comprising X210Cr12 steel shoulder with a flat surface and a diameter of 18 mm together with a 73MoV52 steel pin with a length of 2.5 mm and a hexagonal shape with a distance of 6 mm across the flats. The authors found that increasing the TRS enhanced the hardness within the NZ due to the greater heat input and a more efficient recrystallization process. At a TRS of 1200 rpm, the increase in the heat input reduced the hardness of the HAZ possessing no recrystallization. In the HAZ on the 6060 side, the lowest density of dislocations with the highest mobility occurred, decreasing strength within this zone.

During comparative studies on TIG welding and FSW, Goriparthi et al. [386] studied, inter alia, the FSW joint of 5083-O/7075-T651 alloys obtained at various TRSs (i.e., 800, 1000, 1100, 1200, and 1400 rpm) and a WS of 40 mm/min, using a tool with a straight square pin profile. They found that at lower TRSs, the generated heat was insufficient, and at higher TRSs, excessive heat induced the overflow of solidified materials and defect formation.

Devaraju et al. [387] investigated the FSW joint of 2024/6061 alloys obtained at three TRSs (i.e., 900, 1120, and 1400 rpm), a WS of 40 mm/min, an AF of 5 kN, and a tilt angle of 1.5° and using a tool comprising a shoulder diameter of 24 mm, a pin with a diameter of 8 mm and a length of 5.8 mm. They reported that the occurrence of a well-defined grain boundary region distinguished the recrystallized area of the SZ from the distorted regions within the TMAZ. Improved tensile features were observed at a TRS of 900 rpm.

Investigating the FSW joints between (AS) 6082-T6/(RS) 7075-T6 alloys obtained under various TRSs (i.e., 800, 1000, 1200, and 1400 rpm), various WS values (i.e., 90, 120, and 150 mm/min), and a tilt angle of 2° and using an H13 steel tool with a shoulder diameter of 23 mm and a triangular frustum pin, Aval [388] reported that only the joints obtained at TRSs of 1000 and 1200 rpm with WSs of 90 and 120 mm/min exhibited satisfactory properties. The enhancement of the TRS (from 1000 to 1200 rpm) and lowering of the WS (from 120 to 90 mm/min) facilitated enhanced heat generation, higher peak temperatures, and reduced the maximum tensile residual stress. However, such findings contradicted the results of Giorgi et al. [389].

To explain such contradictory findings, Richards et al. [390] suggested that the stress profile appearing in the joint resulted from the mismatch in plastic strains caused by steep temperature gradients occurring during the FSW process. Temperature gradients, particularly the material cooling rate and its uniformity, more significantly affected the joint maximum tensile residual stress than the peak temperatures alone.

Investigating the FSW joints between (AS) 2014/(RS) 7075 alloys obtained under various TRSs (i.e., 1000, 1200, and 1400 rpm), WS values (i.e., 30, 45, and 60 mm/min), AFs (i.e., 3, 6, and 9 kN), and tilt angles (i.e., 0, 1, and 2°) and using high-carbon steel H13 tools with a shoulder diameter of 20 mm and pins with a diameter of 6 mm and three different profiles (i.e., straight cylinder, tapered, and threaded one), Haribalaji et al. [391] found that the TRS and AF significantly affected the joint TS and microhardness. An improper set of TRS and AF prevents the formation of defect-free welds. The best welding parameters for achieving the maximum TS were achieved at a TRS of 1000 rpm, a WS of 45 mm/min, an AF of 6 kN, and a tilt angle of 2°. However, the maximum hardness was reached at a TRS of 1000 rpm, a WS of 60 mm/min, an AF of 6 kN, and a tilt angle of 2°. Such optimal parameters were obtained using a threaded tool pin profile.

Zuiko et al. [392] studied the FSW joints between 5182/2519 alloys placed on the RS and the AS, obtained under two combinations of TRS and WS (500 rpm/380 mm/min and 1000 rpm/760 mm/min) using a tool with a shoulder of 12.5 mm in diameter and a M5 cylindrical pin of 2.7 mm in length. Both combinations allowed for obtaining defect-free joints. The first combination provided a slightly higher joint UTS.

Investigating the FSW joint between 1100/5052 alloys, obtained under various TRSs (i.e., 1750, 2230, and 3500 rpm) and a WS of 22 mm/min, Tarkono et al. [393] reported that a TRS of 1750 rpm caused the defect of the hole, a rough surface, and no stable welding, whereas a TRS of 2230 rpm yielded a rough surface but more stable welding, and a TRS of 3500 rpm resulted in a smooth surface and stable welding.

Studying the FSW joints between 6061/5083 alloys, obtained under various TRSs (i.e., 1100, 1300, and 1500 rpm) and various WSs (i.e., 30, 45, and 60 mm/min), Sivaselvan et al. [394] found that an increase in the TRS speed caused poor wear performance, whereas the increase in the WS provided better wear performance.

Investigating the FSW joints between 6061-T6/5052-H32 alloys, obtained under various TRSs (i.e., 900, 1100, and 1400 rpm), WSs (i.e., 40, 50, and 60 mm/min), and tool pin profiles (cylindrical, conical, and square), Heramo and Workneh [395] reported that, in particular, the square tool pin profile, the TRS of 1400 rpm, and the WS of 40 mm/min were the optimal process parameters.

Studying the FSW joint between 2219-T8/2195-T8 alloys placed on the AS and on the RS, obtained under a TRS ranging from 800 rpm to 1200 rpm, two WSs (i.e., 200 mm/min and 800 mm/min), and using an H13 steel tool with a concave shoulder of 21 mm in diameter and a threaded cylindrical pin of 8 mm in diameter and 5.8 mm in length, Wang et al. [396] obtained sound joints under all the welding conditions. With the enhancement of the sheet thickness, the TRS required adjustment to accommodate the additional material volume and provide adequate heat generation. Thicker sheets needed higher heat input, so higher TRSs facilitated the generation of more frictional heat at the interface between the tool and the welded components. However, the TRS can be enhanced only up to a certain level, as an excessive TRS causes overheating or material defects. Therefore, a balance is necessary to provide the needed heat input without compromising joint quality.

Investigating the butt FSW joint of 6mm thick components made of dissimilar 5383/7075 alloys, obtained under a TRS ranging from 700 to 900 rpm, a WS ranging from 40 to 80 mm/min, an AF of 10 kN, and a tilt angle of 0°, and using a tool with a shoulder diameter of 24 mm, a square pin with a diameter of 8 mm and a length of 5.7 mm, Sivachidambaram et al. [397] found that varying WS values affected the YS, and a lower WS caused the maximum YS. A TRS of 700 rpm and WS of 40 mm/min provided remarkably high TS and hardness. The authors reported three relationships between the TRS and the WE for various WSs (i.e., 40, 60, and 80 mm/min).

The FSW joints of dissimilar 5052-H34/5023-T4 alloys (Table 6), studied by Song et al. [125], were obtained under a TRS of 1500 rpm and WS values in the range of 100–700 mm/min. At a TRS of 1500 rpm and all WSs studied, cracks occurred beneath the tool shoulder on the RS 5023. Many protuberances like dendrites confirmed the presence of liquid among the grain boundaries and resolidified material indicative of liquation cracking during FSW. At a TRS of 1500 rpm and a WS of 400 mm/min, the peak temperature of 490 C was measured close to the edge of the tool shoulder, where liquation cracking occurred, and this was much below the melting points of the 5052 and 5023 alloys but high enough to induce eutectic or peritectic reactions between precipitates and the Al matrix.

Ghosh et al. [347] reported that tool rotation and traversing speed significantly affected the microstructure of welds. Welding at low a TRS and WS caused the generation of fine grain size in the 6061 alloy near the interface, limited residual thermal stress, a reduction in the extent of recovery–recrystallization, enhanced defect density, the promotion of finer distribution of Si-rich particles, and the increased consolidation of transported material at the back of the tool to eliminate discontinuities within weld nuggets. The welds fabricated at the lowest tool rotational and traversing speed exhibited the best mechanical properties. The 80 mm/min tool-traversing speed was optimal to achieve a joint efficiency of ~116% with respect to that of 6061 Al alloy.

The FSW joints of dissimilar 5052/A5J32 alloys (Table 6), studied by Kim et al. [304], were obtained at two TRSs (1000 and 1500 rpm), and four WSs (100, 200, 300, and 400 mm/min). In the case where A5J32 was fixed on the RS, the highest strength of

the welded joints appeared under a TRS of 1000 rpm and a WS of 300 mm/min. The WE reached up to about 94%.

The proper FSW butt joints of 7050-T7451/2024-T351 alloys (Table 6), studied by Prime et al. [351], were obtained under a WS of 50.8 mm/min.

The correct FSW joints of dissimilar 5182-O, 5754-O, and 6022-T4 alloys (Table 6), studied by Miles et al. [398], were obtained at a TRS ranging from 500 to 1500 rpm and a WS ranging from 130 to 400 mm/min.

The proper butt FSW joints of 6061-Al used alone and with dissimilar 6061-T6/2024-T3 alloys (Table 6), studied by Ouyang and Kovacevic [399], were obtained under TRS values in the range of 151–914 rpm and WS values in the range of 57–330 mm/min.

The butt FSW joints of dissimilar 2024-T351/6056-T4 alloys (Table 6), studied by Amancio-Filho et al. [300], were obtained under a TRS ranging from 500 to 1200 rpm and a WS ranging from 150 to 400 mm/min. Sound joints were obtained at a TRS of 800 rpm and WS of 150 mm/min.

The proper FSW joints of cast A356/wrought 6061 alloys (Table 6), studied by Lee et al. [301], were obtained under a TRS of 1600 rpm, and the WS ranged from 87 to 267 mm/min. The area of the SZ slightly decreased with the increase in the WS due to the different cooling rates.

The correct FSW joints of dissimilar 7003/7046 alloys (Table 6), studied by Yang et al. [354], were obtained under a TRS of 2000 rpm and WS of 400 mm/min.

Studying the FSW joints of rolled sheets made of dissimilar 2024/5056 alloys, Ivanov et al. [400] obtained proper joints using lower linear WSs and high TRSs.

For the butt FSW joints of components made of 6063 and 5083 alloys, obtained for various TRSs in the range of 600–1200 rpm, 4 kN axial load, and WS of 40 mm/min (Table 6), Kumar et al. [401] reported that the joints with a higher TS, lower flexural strength and lower impact strength with maximum hardness were fabricated at a TRS of 1000 rpm with a cylindrical profile. The flexural strength and impact strength decreased, whereas the TS and hardness increased with an increase in the TRS.

Studying the FSW joints of 2618-T87/5086-H321 alloys (Table 6), Sasikala et al. [402] reported that achieving sound joints was affected, inter alia, by the WS. The best joint quality was consecutively affected by tool pin geometry, the TRS, the WS, and the D/d ratio. The WE reached up to 90%.

For the FSW joints of components made of 3003-H12 alloy (Table 6), Aydin et al. [403] found that the tensile weld strength enhanced with an increase in the WS or a decrease in the rotation speed. The tensile fractures of the joints were in the BM under welding parameter combinations including (TRS = 1070 rpm)/(WS = 40 mm/min) and (TRS = 2140 rpm)/(WS = 224 mm/min). All other joints failed in the HAZ. The YSs and UTSs of the joints decreased linearly with an enhancement of the TRS at a constant WS, while such strengths of the joints enhanced linearly with a rise in the WS at a constant TRS. The elongation values of FSW joints were smaller at a higher TRS or lower WS.

Investigating the single-sided butt FSW joints of 3 mm thick 3003-O non-heat-treatable Al alloy (Table 6), Aydin et al. [404] reported that the welding parameters strongly affected the fatigue behaviors of the 3003-O FS welds. The fatigue life of FS welds obtained under a WS of 40 mm/min at various rotating speeds was about 2–3 times longer than those of FS welds with the WSs of 80 mm/min and 112 mm/min at various TRSs at a fixed stress amplitude under the stress ratio $R = -1$. At a much lower WS and a higher TRS, the fatigue life of the joints increased due to the enhanced amount of heat supplied to the weld per unit length.

For the FSW joints of 4 mm thick plates made of 2024 alloy (Table 6) without post-processing heat treatment, Weglowski et al. [405] reported that the weldability of Al alloys used for the FSW process was good and provided superior quality of welded joints for a wide range of welding parameters. The kind of tool had no effect on joint properties using the same welding parameters.

Nejad et al. [406] studied the structure and mechanical properties of FSW joints of plates made of 2024-T4 alloy (Table 6) with cylindrical outer and concave end surface shoulder and varied depth. The joints were obtained for two different tool designs, a threaded one and an unfeathered one. Obtaining a defect-free weld structure with both probe tools needed well different rotation and traverse speeds. A TRS of 500 rpm, a WS of 55 mm/min, and a plunge depth of 2.7 mm for the threaded tool, and a TRS of 1300 rpm, a WS of 115 mm/min, and a plunge depth of 2.9 mm for the unthreaded tool allowed for obtaining the finest grain in the stir zone; the best visual quality and smoothness; and the highest TS, elongation, and microhardness.

Studying the FSW joints of 6 mm thick plates made of the 2024-T351 alloy (Table 6), Milčić et al. [407] obtained the compounds without errors and with an acceptable flat surface under a constant TRS of 750 rpm, and the WS ranged from 73 to 150 mm/min. The relationship between the TRS and WS directly affected the fracture toughness and energy necessary for the initiation and propagation of the crack in the joint. The weld joint obtained under 750/116 rpm/(mm/min) exhibited better properties and microstructure compared to the joints obtained using (TRS = 750 rpm)/(WS = 73 mm/min) and (TRS = 750 rpm)/(WS = 150 mm/min), respectively. A WE of 97% was achieved under a TRS of 750 rpm and a WS of 116 mm/min.

For the FSW joints of 8 mm thick plates made of 2014-T6 alloy (Table 6), Lin et al. [408] reported that the weld TS was affected by welding parameters. The maximum UTS of 360 MPa equal to 78% was found at a TRS of 400 rpm and WS of 100 mm/min.

Investigating the FSW joints of components made of the 2014-T6 alloy (Table 6), Ugender et al. [409] reported that defect-free welds were obtained at a TRS of 900 rpm and a WS of 40 mm/min, using a taper cylindrical tool pin profile.

For the FSW joints of components made of the 2017-T351 alloy (Table 6), Liu et al. [57] found that the tensile properties and fracture locations of the joints strongly depended on the welding process parameters. Under the optimum revolutionary pitch of 0.07 mm/rev corresponding to a TRS of 1500 rpm and a WS of 100 mm/min, the maximum ultimate strength of the joints corresponded to 82% of that of the BM.

Investigating the FSW joints of components made of 1050-H24 alloy (Table 6), Liu et al. [277] reported that a softened region located at the weld and HAZs appeared in the joints. The degree of softening and tensile properties of the joints strongly depended on the WS and TRS. The optimum FSW parameters were affected by both the tensile properties and the welding parameters. They were obtained for a WS of 200 mm/min and a TRS of 1000 rpm.

The FSW joints of cast AlSi9Mg/2017A alloys (Table 6), studied by Mroczka [352], were obtained under a TRS of 560 rpm and a WS of 1120 mm/min. The FSW joints of 2017A alloy (Table 6), studied by Mroczka et al. [353], were obtained under a TRS of 355 rpm and a WS of 280 mm/min. Studying the FSW joints of sheets made of 2017A alloy, Mroczka et al. [410] found that with a higher TRS (900 rpm compared to 355 rpm), the properties of the joint worsened. Cracks along grain boundaries and the separation of grains in the welds occurred at higher TRSs. This was because the grain boundaries within the NZ lost cohesion during the welding process at a high rate.

Takhakh and Abdullah [411] compared the fatigue properties of the welded joints of plates made of 3003-H14 alloy (Table 6) obtained by FSW (at TRS of 1500 rpm and WS of 80 mm/min) and TIG welding. They found that the fatigue properties of FSW joints were slightly worse than those of the BM and better than those of TIG welding.

For the FSW joints of components made of 3003 alloys (Table 6), Chekalil et al. [412] reported that the joint mechanical properties were affected in the order of the TRS, the WS, and the tool tilt angle. The best mechanical properties of a welded joint were obtained under a TRS of 1423.9 rpm, a WS of 400 mm/min, and a tool tilt angle of 1.28°.

Investigating the butt FSW joints of plates made of 3003-H24 alloys (Table 6), Kasman and Ozan [413] reported that, at a WS of 50 mm/min, tunnel-type defects with enormous size appeared in the joints welded with a TRS of 500 and 1000 rpm. The tunnel-type

defects also occurred under a WS of 80 mm/min and TRS of 500 and 800 rpm. However, cavity-type defects occurred at both WSs. All welded joints fractured between the BM and the HAZ, except for the joints welded under a WS of 50 mm/min and a TRS of 500 and 1000 rpm. The highest UTS among all the welded joints, equal to 128 MPa, was obtained under a WS of 50 mm/min and TRS of 800 rpm. The welded joints were fractured in a ductile manner except for the joint produced under a WS of 50 mm/min and a TRS of 500 rpm.

Studying the butt FSW joints of 6013 Al plates (Table 6), obtained via a pin offset technique, Kasman and Ozan [355] found that the highest TS of 206 MPa was obtained under a 1.5 mm pin offset toward the AS and at a TRS of 500 rpm, leading to the WE of 74%.

Kasman and Yenier [365] reported that a defect-free joint was obtained under a TRS of 1000 rpm and a WS of 80 mm/min and using a 22 mm tool shoulder diameter (Table 6). The UTS decreased with an enhancement of a WS or a TRS. The WE for the 5754 alloy decreased with an enhancement in the WS; however, it could exceed 100% for some weld cases. As for the 7075 alloy, the efficiency varied in the range of 23.3%–41.9%.

Xu [414] studied the FSW joints of 5 mm thick plates made of 3003-H17 alloys (Table 6) under the WSs of 1500 and 3000 mm/min and a constant TRS. They found that the joint UTS decreased with an increase in the WS from 1500 mm/min to 3000 mm/min at a TRS of 2000 rpm and a shoulder plunge depth of 0.2 mm. The WE reached 87% at the WS of 1500 mm/min.

Studying the FSW joints made of 3003 alloys (Table 6), Goyal et al. [415] reported that the best UTS was obtained for the process parameters including a WS of 74.64 mm/min, a TRS of 971.77 rpm, and a tool tilt angle of 1.52° .

Janeczek et al. [416] studied the effect of tool shape and welding parameters on the quality of FSW joints of components made of the 3004 alloy (AlMn1Mg1) (Table 6). Various butt joints were made with a cylindrical and tapered threaded tool with a TRS of 475 rpm. The other joints were obtained with a TRS of 475 rpm and a WS of 300 mm/min with the use of a cylindrical threaded pin. Most of the specimens were properly joined for a TRS of 475 rpm. In the joints obtained under a WS of 300 mm/min, the material was not stirred properly. The best joint quality was achieved for a TRS of 475 rpm and various WS values between 150 and 475 mm/min. The WE widely varied in the range of 61.9%–87.6%; however, individual cases of below 27% were also observed.

Studying the butt FSW joints of components made of dissimilar 7020-T651/5083-H111 alloys (Table 6), Torzewski et al. [17] found that the FSW samples obtained under a TRS of 800 rpm and WS of 200 mm/min exhibited the best strength properties, including a UTS of 303 MPa, a YS of 157 MPa, and elongation of 11.6%. All the joints obtained at a WS of 100 mm/min exhibited a WE of 95%.

Choi et al. [417] studied the spot FSW joints of sheets made of the 5454 alloy (Table 6) with different thicknesses of 1.4 and 1.0 mm obtained under a TRS ranging from 500 to 2500 rpm and a plunging depth of 1.8 mm with a constant tool plunge speed of 100 mm/min. The rotating tool was maintained at the plunge depth during the dwell time ranging from 0 to 7 s. The pull-out speed of the rotating tool was 100 mm/min. The enhancement of TRS changed the macrostructure of the friction-stir-spot-welded zone, especially the geometry of the welding interface.

Studying the FSW joints of components made of the 1100 alloy (Table 6), Selvarajan and Balasubramanian [418] reported that a maximum TS of 105 MPa, a hardness value of 67 HV, and a minimum corrosion rate of 0.69×10^{-4} in the stir zone region were obtained under the optimized parameters comprising a TRS of 893 rpm, a WS 100 mm/min, an AF of 6.5 kN, a shoulder diameter of 14.8 mm, a pin diameter of 4.9 mm, and a tool material hardness of 45.4 HRC.

Dong et al. [419] studied the microstructure and mechanical properties of the welded joints of components made of dissimilar 7003-T4/6060-T4 alloys (Table 6), obtained by underwater friction stir welding (UFSW). They reported that sound and defect-free joints were obtained in the UFSW process; however, tunnel defects appeared with a high WS of

240 mm/min. With the enhancement of the WS, more η and η' phases remained because of the lower heat input.

Sheikhi and dos Santos [420] studied the effect of welding parameters and welding tools on the weld quality and mechanical properties of FSW joints of tailor-welded blanks (TWBs) made of 6181-T4 alloy in a 1 to 2 mm thickness combination of the as-produced product (Table 6). Changing the WS highly affected the measured temperature and the heat input.

Zhou et al. [421] studied the FSW joints of 6061-T6 alloy sheets obtained under a TRS of 11,000 rpm and a WS varying from 200 mm/min to 500 mm/min. Sound joints were obtained under a travel speed of 300 mm/min. Due to the stirring effect of a high TRS, the proportion of low-angle boundaries in all zones was less than that of the traditional FSW, while the average grain size was like traditional FSW. The WE reached up to 87.2%. For the lap FSW process, when the TRS was high, and the WS was low, the NZ occurred with an onion ring shape, and when the rotation speed was low, and the WS was high, void-type defects appeared on the AS or the center of the nugget [357].

The proper FSW joints of 6 mm thick dissimilar 6351/and 5083-H111 alloys (Table 6), studied by Palanivel et al. [422], were obtained under a TRS of 950 rpm, a WS of 1.05 mm/s, and an AF of 10 kN.

The FSW joints of 6061-T6 alloys (Table 6), studied by Juarez et al. [358], were obtained at a TRS of 1000 rpm, a WS of 90 mm/min, a penetration speed of 9 mm/min, and a holding time of 10 s. The last parameters allowed for a reduction in welding defects.

Godhani et al. [359] obtained the FSW joints of dissimilar 6061/7075 alloys (Table 6) under a WS of 31.5 mm/s, a TRS of 765 rpm, and a forward tool tilt angle of 2°.

Various FSW process parameters for different FSW joints between Al alloys were presented by Patel et al. [254].

Studying the FSW of 5 mm thick plates made of 5086-O/and 6061-T6 alloys, Aval et al. [423] reported that an increase in TRS and a decrease in WS provided weaker welds and coarser grain size in the NZ.

For the butt FSW plates of 2219-T62 alloy, Xu et al. [424] found that, with the enhanced TRS, the longitudinal residual stress decreased on the top surface but increased on the bottom surface.

Studying the FSW joints of components made of 2014 alloy (Table 6), Sinhmar and Dwivedi [425] reported that after welding was carried out at a TRS of 931 rpm and WS of 41 mm/min, the mechanical performance of the 2014 alloy decreased. Simultaneously, the corrosion resistance of the weld joint was higher than that of the BM.

For the FSW joints of 5 mm thick plates made of 7075AA7075-T651 and 2024AA2024-T351 similar and dissimilar alloys, Zhang et al. [361] found that enhancing the TRS caused a widened TMAZ on the AS and the RS. The mixing degree in the joints is remarkably affected by the TRS. A low TRS limited material mixing, while a typical onion ring of mixing pattern appeared at a high TRS. Compared to the BMs, significant grain refinement (average grain size: 1.7 μm) occurred at a TRS of 600 rpm. The enhanced TRS caused grain coarsening. The NZ of all the joints was dominated by a simple shear texture and varied with the TRS.

Sivachidambaram et al. [397] studied the butt FSW joint of 6mm thick components made of dissimilar 5383/7075 alloys using a tool with a shoulder diameter of 24 mm, a square pin with diameter of 8 mm, and a length of 5.7 mm under a TRS in the range of 700–900 rpm, a WS in the range of 40–80 mm/min, a tilt angle of 0°, and an AF of 10 kN. They found that varying the WS affected the YS, and a lower WS caused the maximum YS. A TRS of 700 rpm and WS of 40 mm/min provided a remarkably high TS and hardness.

Studying the FSW joints of 2198 to 7075 Al alloys in a single-lap configuration obtained at various TRS values (i.e., 1200, 1500, and 1800 rpm) at two WSs (i.e., 60 and 120 mm/min), with the revolutionary pitch ranging from 10 to 30 rot/mm and using an H13 steel tool with concave shoulder and tapered left-hand threaded pin, Astarita et al. [426] reported that internal and surface defects (mainly grooves and tunnels) occurred for all the welds

produced with a WS of 120 mm/min and TRS of 1800 rpm, but the processing window leading to sound joints was clearly defined. Defects such as grooves and tunnels hardly occurred with a WS of 60 mm/min, TRSs of 1200 and 1500 rpm, and the revolutionary pitch ranging from 20 to 25 rot/mm.

The trend of force loading in the welding tool varied during the plunging, dwelling, and travel phases, exhibiting several peaks. Forces increased with a decrease in the heat input, i.e., they increased with an increase in the WS and a decrease in the TRS. The recorded values of the F_z force were always higher than the ones recorded for the F_x one.

Single-lap shear tests highlighted that the presence and size of the hook, rather than internal defects, mainly affected the failure load. Such a fact confirmed that the hook had a detrimental effect on the strength of the joints, providing a preferential path for crack propagation. Additionally, lap shear strength showed a non-monotonic peak, initially increasing and then decreasing with the TRS. The WS had less effect.

For the lap FSW joint of dissimilar 2198–6082 Al alloys, Tucci et al. [427] reported that the TRS and WS together affected the joint quality. The increase in the WS caused inferior weld joint quality due to insufficient material mixing and the appearance of hooks and other defects. Additionally, the increased TRS generated heat and enhanced temperature, inducing material softening and less resistance during the FSW process. The F_z force resisting the plunging and F_x reacting to the tool advancement governed the thermal and microstructural evolution of the involved Al alloy sheets. The peaks of resistance and the steady-state values in the force were strongly affected by TRS and WS combinations. Enhancing the TRS reduced both the plunging and dwelling stage force peak values. An enhanced WS caused a decrease in the failure load required during the lap shear test. The highest value of failure load was obtained in the case of (TRS = 1500 rpm)/(WS = 60 mm/min).

Table 6. FSW process parameters for FSW joints of various Al alloys.

Refs	Alloy Combinations	Thick	TRS	WS	Plunge Depth	Tool Tilt Angle	AF
		[mm]	[rpm]	[mm/min]	[mm]	[°]	[kN]
[308]	2024-T351/5083-H112	6.35	600	150			
[308]	7075-T651/2024-T351	6.35	600	150			
[310]	7075-T651/2024-T351	6	900	150			
[61]	7075-T6/2024-T3 Lap joint: 7075-upper; 2024-lower	3	600	30, 60, 90, 120	0.2	2.5	
[311]	7075-T651/5083-H111	6	280; 355; 450; 560	140			26.4
[312]	2024-T4/7075-T6	4	1140	32			
[313]	6351-T6/5083-H111	6	800; 1000; 1200	45; 60; 75			
[46,311,363]	2017A-T451/7075-T651	6	355	112		1.5	32.8
[383]	5083-O/6063-T6	6	900	60			
[315]	5052andAlMg ₂ Si	8	1000	80		2.5	
[316]	2024-T351/6061-T6	6	800	31.5		2	
[317]	6061-T6/6351-T6	6.35	600; 900; 1200	30; 60; 90			
[318,362]	6082-T6/7075-T6	10	950; 1000	80; 100		2	
[319]	6061-T651/5A06-H112	5	600; 900; 1200	100; 150	4.7	2	
[320]	6101-T6/6351-T6	12	900; 1100; 1300	16			
[321]	2024-T3/6063-T6	8	900; 1120; 1400	125; 160; 200		2.5	

Table 6. Cont.

Refs	Alloy Combinations	Thick	TRS	WS	Plunge Depth	Tool Tilt Angle	AF
		[mm]	[rpm]	[mm/min]	[mm]	[°]	[kN]
[322]	2219-T87/2195-T8	7.2	400; 600; 800	120; 180; 240; 300			
[323]	2017A-T451/cast AlSi9Mg	6	355	112			
[324]	5083-H12/6061-T6	1.5	700; 1800; 2500	25; 30; 212.5; 400			
[325]	6061-T6/7075-T6	5	1000; 1375; 1750; 2125; 2500	50; 125; 200; 275; 350	0.2	3	
[326]	5083-H111/6082-T6	5	400; 500; 630; 800	40; 50; 63; 80		2	
[144]	5083-H111/6351-T6	6	800–1200	45–85		1	15
[327]	5052/6061	1, 1.5	1500	63, 98			
[328]	2024-T6/ 7075-T6	5	1200	12			8
[296,329]	Al-Mg-Si/Al-Zn-Mg	15	800	180	0.2	2.5	
[330]	2024-T3/6061-T6	4.8	500; 650; 840	45; 65		2	
[331]	UFG 1050/6061-T6	2	800	400; 600; 800; 1000		3	8
[327]	2024-T6/ 6061-T6	4	1000	500		2.5	
[333,334]	6061-T6/7050-T7451	5	270; 340; 310	114			
[47]	6111-T4/5023-T4 Lap joint	1	1500 1000	100 700			
[335]	5086-O/6061-T6	6	1100	22		1	12
[336]	2050-T4/6061-T651	20	150; 300	101; 203; 406			
[337]	5083-O/6082-T6	NR (~7)	400	400			
[338]	A319/ A413 cast	10	630; 800; 1000	20; 40; 63	1	3	
[339]	7075-O/6061-O 7075-T6/6061-T6	3.17	1000 1500	150 400			
[295]	6061-T6/7075-T6	4.6	700–1450	100			
[340]	2024-T3/7075-T6 Lap joint	5	1500	50; 150; 225; 300	0.2	2.5	
[341]	5083-O/6061-T6	6	600; 750; 900	20; 40			
[342]	6351-T6/5083-H111	6	950	36, 63, 90			
[344]	2014-T6/6061-T6	4.7	500; 1500	90			
[343]	6351-T6/5083-H111	6	600–1300	36–90			9.8; 12.25; 14.7; 17.18; 19.6
[346]	A356/6061-T6	3	1000	70–240		3	
[385]	2198-T351/7075-T6 Lap joint	3 & 1.9	830	40		2	
[348]	2219-T87/5083-H321	6	400–800	15–60			
[349]	6061 cast/6061 rolled	6	800; 1000; 1200; 1400	50			8
[350]	6351-T6/5083-H111	6	600; 950; 1300	60		0	8
[127]	5052-H34/5023-T4	~1.5	1500	100–700		3	

Table 6. Cont.

Refs	Alloy Combinations	Thick	TRS	WS	Plunge Depth	Tool Tilt Angle	AF
		[mm]	[rpm]	[mm/min]	[mm]	[°]	[kN]
[347]	A356/6061-T6	3	1000; 1400	80; 240			
[304]	5052-H34/5023-T4	1.5 & 1.6	1000; 1500	100; 200; 300; 400		3	
[351]	7050-T7451/2024-T351	25.4	NA	50.8			
[398]	5182-O/5754-O 5182-O/6022-T4 5754-O/6022-T4	~2	500; 1000; 1500	130; 240; 400			
[399]	6061-T6/2024-T3	12.7	151–914	57–330			
[300]	2024-T351/6056-T4	4	500–1200	150–400			
[301]	cast A 356/wrought 6061	4	1600	78–267		3	
[354]	7003-T4/7046-T4	3	2000	400	0.3	2.5	
[367]	2219-T6/5083-H116	5	400; 800; 1200; 1600; 2000	30; 210; 390; 570; 750			
[401]	6063/5083	6	600; 800; 1000	40			4
[402]	2618-T87/5086-H321	6	450; 600; 750; 850	15; 35; 50; 65			
[428]	2014-T6	3	1070; 1520; 2140	40; 80; 112		2.5	
[403]	3003-H12	3	1070; 1520; 2140	40; 80; 112; 160; 224			
[404]	3003-O	3	1070; 1520; 2140	40; 80; 112			
[405]	2024-T4	4	350	210			
[406]	2024-T4	3	300–1300	40–145	2.7; 2.9	6	
[407]	2024-T351	6	750	73; 116; 150			
[408]	2014-T6	8	300–800	50–300			
[425]	2014	NA	931	41			
[409]	2014-T6	5	900	40		2.5	5
[57]	2017-T351	5	1500	25–600		3	
[277]	1050-H24	5	600–2000	100–800		3	
[352]	2017A-T451 /AlSi9Mg	6	560	1120		1.5	
[353]	2017A	6	355; 900	280		1.5	
[411]	3003-H14	3	1500	80			
[412]	3003	2	1000; 1500; 2000	200; 300; 400			
[412]	3003-H24	3	500; 800; 1000	50; 80			
[355]	6013-T6	5	500; 630; 800	50			
[365]	5754-H111/7075-T651	5	1000; 1250	80; 100; 125			
[414]	3003-H17	5	2000	1500; 3000	0.2		
[415]	3003	5	663; 800; 1000; 1200; 1336	20; 40; 70; 100; 120		0.65; 1; 1.5; 2; 2.35	
[416]	3004	5	95–600	115–925			
[17]	5083-H111/7020-T651	5	400; 800; 1200	100; 200; 300			
[417]	5454-O	1, 1.4	500–2500	100			
[418]	AA1100	5	562,700, 800, 900, 1037	40.54; 75; 100; 125; 159.5			3.62; 5; 6, 7; 8.38

Table 6. Cont.

Refs	Alloy Combinations	Thick	TRS	WS	Plunge Depth	Tool Tilt Angle	AF
		[mm]	[rpm]	[mm/min]	[mm]	[°]	[kN]
[419]	7003-T4/6060-T4	4.5	1000	40; 120; 240			
[357]	6111-T4/5023-T4	1	1000; 1250; 1500	100; 300; 500; 700			
[420]	6181-T4	1, 2	1300; 1600; 2000	800; 1000; 1125; 1500		1.5; 3	4.5; 5.5
[421]	6061-T6	1	11,000	200–500	0.05		
[358]	6061-T6	9.5	1000	90			
[359]	6061-T6/7075-T6	6	765	31.5		2	
[422]	6351/5083-H111	6	950	1.05			10

The influence of the TRS on mechanical properties and thus on the WE is not clear because it is strongly affected by other parameters, e.g., the WS, the AF, and the type of materials joined. The TRS and the WS often highly interact with each other under an inverse correlation. A higher TRS and a lower WS facilitate intensive mixing between alloys. An increase in the TRS (from 1000 to 1200 rpm) and a decrease in the WS (from 120 to 90 mm/min) both increase heat generation, provide higher peak temperatures, and reduce the maximum tensile residual stress. This agrees with the findings of Di Bella et al. [257]. The optimization of weld quality is very often achieved by considering the effect of both the TRS and the WS.

Table 7 summarizes the effect of the TRS on FSW joint properties (some of the data were published earlier in an excellent review by Di Bella et al. [257]).

Table 7. Effect of the TRS on the FSW joint properties.

Ref.	Alloys Position AS/RS/NA	Pin Profile	Tilt Angle [°]	TRS [rpm]	WS [mm/min]	AF [kN]	Main Results
[393]	(NA) 1100/(NA) 5052	NA	NA	1750; 2230; 3500	22	NA	A TRS of 3500 rpm provided a smooth surface and stable welding.
[391]	(AS) 2014/(RS) 7075	Straight cylinder Tapered Threaded	0; 1; 2	1000; 1200; 1400	30; 45; 60	3; 6; 9	The TRS and the AF strongly affected the joint TS and microhardness. The best set for TS comprised TRS of 1000 rpm, WS of 45 mm/min, AF of 6 kN, and tilt angle of 2°. The best set for hardness comprised the TRS of 1000 rpm, the WS of 60 mm/min, the AF of 6 kN, and the tilt angle of 2°. Such optimal parameters were accompanied by using a threaded tool pin profile.

Table 7. Cont.

Ref.	Alloys Position AS/RS/NA	Pin Profile	Tilt Angle [°]	TRS [rpm]	WS [mm/min]	AF [kN]	Main Results
[396]	(AS/RS)2195-T8/(RS/AS)2219-T8	Threaded cylindrical	NA	800; 1200	200; 400; 800	NA	Sound joints appeared under all the process conditions.
[367]	(RS)2219/(AS)5083	Frustum threaded	NA	400; 800; 1200; 1600; 2000;	30; 210; 390; 570; 750	NA	Higher TRSs and lower WSs favored radical mixing between alloys.
[387]	(NA)2024/(NA)6061	NA	1.5	900; 1120; 1400	40	5	The presence of a well-defined grain boundary region discerned the recrystallized area (SZ zone) from the distorted regions inside the TMAZ.
[392]	(AS)2519/(RS)5182	Cylindrical	NA	TRS = 500/WS = 380; TRS = 1000/WS = 760		NA	For both sets, defect-free joints were obtained. The set of TRS of 500 rpm and WS of 380 mm/min ratio induced a slightly higher joint UTS.
[395]	(NA)5052-H32/(NA)6061-T6	Cylindrical Conical Square	NA	900; 1100; 1400	40; 50; 60	NA	The optimal parameters comprised a square pin profile, a TRS of 1400 rpm, and a WS of 40 mm/min.
[379]	(AS)5083/(RS)6060	Hexagonal	2	800; 1000; 1200	100	NA	An enhanced TRS increased hardness inside NZ due to both the higher heat input and a more intensive recrystallization process.
[394]	(AS)5083/(RS)6061	Cylindrical threaded	2	1100; 1300; 1500;	30; 45; 60;	-	The enhanced TRS caused poor wear performance, whereas a higher WS provided better wear performance.
[380]	(RS)5083-H12/(AS)6061-T6	Diameter: 2, 3, 4 mm	NA	700; 1600; 2500	25; 212.5; 400	NA	An enhancement in TRS and WS caused increased input heat, inducing a higher joint TS.
[381]	(AS/RS)5083/(RS/AS)6082	NA	NA	280; 560; 840	100; 200; 300	NA	Higher TRS allowed for higher heat generation inducing grain growth in both alloys and Mg ₂ Si precipitation.

Table 7. Cont.

Ref.	Alloys Position AS/RS/NA	Pin Profile	Tilt Angle [°]	TRS [rpm]	WS [mm/min]	AF [kN]	Main Results
[350]	(RS) 5083- H111/(AS) 6351-T6	Straight square Straight hexagon Straight octagon Tapered square Tapered octagon	0	600; 950; 1300	60	NA	TRSs and WSs influenced the joint strength due to varying material flow behavior, loss of cold work in the 5083 HAZ, dissolution and 6351 overaging of precipitates, and creation of macroscopic defects in the weld zone.
[386]	(NA) 5083-O/(NA) 7075-T651	Straight square	NA	800; 1000; 1100; 1200; 1400	40	NA	The defect-free joint appeared at the TRS of 1100 rpm. At lower TRSs, heat was insufficient. At higher TRSs, heat became excessive.
[388]	(AS) 6082-T6/(RS) 7075-T6	Triangular frustum	2	800; 1000; 1200; 1400;	90; 120; 150	NA	Enhancing TRSs from 1000 to 1200 rpm and lowering the WSs from 120 to 90 mm/min provided enhanced heat generation, higher peak temperatures, and reduced maximum tensile residual stress.
[320]	(AS) 6101-T6/(RS) 6351-T6	Taper cylindrical thread	2	900; 1100; 1300	16	NA	With an increase in TRS, the impact energy first increased and then decreased. For a low TRS, the heat was insufficient. For a high TRS, the heat was high, causing a grain refinement.
[384]	(AS) 6101-T6/(RS) 6351-T6	Cylindrical threaded	2	900; 1100; 1300; 1500	60	4; 5; 6; 8	At lower TRSs, the TS strongly weakened mainly due to the inadequate tool stirring action. At the TRS of 1300 rpm, a sufficient heat input was generated, promoting higher joint quality. At a high TRS, the heat was excessive.

Table 7. Cont.

Ref.	Alloys Position AS/RS/NA	Pin Profile	Tilt Angle [°]	TRS [rpm]	WS [mm/min]	AF [kN]	Main Results
[361]	similar (AS/RS)7075-T651 and (AS/RS)2024-T351 and dissimilar (AS)7075-T651/(RS)2024-T351	Cylindrical tool with taper threaded pin	2.5	600; 950; 1300; 1650	100	NA	The higher TRSs widened TMAZ on the AS and the RS. Low TRS limited material mixing, while the onion ring mixing pattern appeared at the high TRS. The weld grain refinement greater than in BMS appeared at a TRS of 600 rpm. The higher TRS caused grain coarsening. The joint NZ dominated by a simple shear texture varied with the TRS. The increased TRS reduced the hardness in the NZ.
[311]	7075-T651/5083-H111	Triflute, tapered with a thread		280; 355, 450; 560	140	26.4	At higher TRSs and for the (AS) 5083/(RS) 7075 set, porosity, voids, or wormholes occurred in the stir zone. The highest TS defect-free joint was obtained for a TRS of 280 rpm. The higher TRS at a constant WS reduced the joint efficiency.
[313]	6351-T6/5083-H111	Cylindrical or conical with and without threads		800; 1000; 1200	45; 60; 75		The WE reached up to 78.7% at a WS of 60 mm/min and a TRS of 1000 rpm
[317]	6351-T6/6061-T6	Cylindrical		600; 900; 1200	30; 60; 90	6	The highest WE was obtained for TRS of 900 rpm, a WS of 60 mm/min, and an axial force of 6 kN
[319]	6061-T651/5A06-H112	Conical	2	600; 900; 1200	100; 150		For a higher TRS, more heat was generated, enlarging the size of HAZ, reducing the slant angle of HAZ, decreasing the fracture angle, and changing the dimples from inclined ones to normal ones.

Table 7. Cont.

Ref.	Alloys Position AS/RS/NA	Pin Profile	Tilt Angle [°]	TRS [rpm]	WS [mm/min]	AF [kN]	Main Results
[320]	6101- T6/6351-T6			900; 1100; 1300	16		With increasing the TRS the impact strength behaviour showed a high change in mechanical properties.
[321]	2024- T3/6063-T6			900; 1120; 1400	125; 160; 200	2.5	Microstructural and mechanical properties strongly depended on variations in welding parameters. At the lower TRS and the higher WS in all welding conditions, the Wohler curves showed maximum fatigue strength
[322]	2219- T87/2195-T8			400; 600; 800	120; 180; 240; 300		The WS only slightly affected the joint properties strongly depending on the TRS. The best joint properties occurred at TRS of 600 rpm and WSs of 180–240 mm/min for (RS) 2219-T8/ (AS) 2219-T87
[325]	6061/7075			1000; 1375; 1750; 2125; 2500	50; 125; 200; 275; 350	3	The max TS of 237.3 MPa and elongation of 41.2% occurred at a TRS of 1853 rpm and a WS of 50 mm/min. Thus, the WE reached up to 76.5%.
[326]	5083- H111/6082- T6	Triangular; pentagonal	2	400; 500; 630; 800	40; 50; 63; 80		NZ comprised onion rings. At a constant v ratio, the TRS affected the profile and structure of the NZ. At a lower TRS and WS lower UTS values occurred.

Table 7. Cont.

Ref.	Alloys Position AS/RS/NA	Pin Profile	Tilt Angle [°]	TRS [rpm]	WS [mm/min]	AF [kN]	Main Results
[414]	3003-H24	Pentagonal	2	500; 800; 1000	50; 80		Various tunnel-type defects appeared in joints welded for all TRSs and WSs. The cavity-type defects occurred at both 800/50 and 1000/80 ratios. All joints fractured between the BM and the HAZ, except for the joints welded at WS of 50 mm/min, and TRS of 500 and 1000 rpm. The highest UTS occurred at WS of 50 mm/min and TRS of 800 rpm. The joints fractured ductility except those obtained at WS of 50 mm/min and TRS of 500 rpm
[368]	5083- H116/7075- T6	Quadratic		500; 630; 800	30; 41.5; 50		An increase in a TRS from 500 to 800 rpm, at a selected WS initially decreased and then increased the joint UTS and efficiency. Increasing the WS increased the joint UTS. The max joint UTS appeared at the TRS of 500 rpm and the WS of 50 mm/min
[417]	5454			from 500 to 2500			Joints were obtained plunging to the depth of 1.8 mm under a constant tool plunge speed of 100 mm/min and TRS at the plunge depth during the dwell time ranging from 0 to 7 s. The pull-out speed of the rotating tool was 100 mm/min. The increase in TRS changed the macrostructure of the friction-stir-spot-welded zone, especially the geometry of the welding interface.

Table 7. Cont.

Ref.	Alloys Position AS/RS/NA	Pin Profile	Tilt Angle [°]	TRS [rpm]	WS [mm/min]	AF [kN]	Main Results
[358]	6061-T6			1000	90		The use of penetration speed of 9 mm/min, and holding time of 10 s allowed lowering the joint defects.
[423]	5086-O/ 6061-T6						An increase in TRS and a decrease in WS provided weaker welds and coarser grain size in the NZ
[424]	butt 2219-T62						The enhanced TRS decreased the longitudinal residual stress on the top surface but increased it on the bottom surface.
[361]	7075-T651 and 2024-T351 similar and dissimilar						Increasing the TRS caused a widened TMAZ on the AS and the RS. Low TRS limited material mixing, while the onion ring of the mixing pattern appeared at the high TRS. The grain refinement was much higher than in BMs appeared at the TRS of 600 rpm. The higher TRS caused grain coarsening. The simple shear texture dominated in all joint NZs varied with the TRS.
[397]	5383/7075	Squared pin with a diameter of 8 mm and length of 5.7 mm	0	700–900	40–80	10 k	The varying WS affected the YS and the lower WS caused maximum YS. The TRS of 700 rpm and the WS of 40 mm/min provided a remarkably high TS and hardness
[426]	lap 2198/7075	Tapered left-hand threaded		1800	120		Grooves and tunnels occurred for all joints produced with the WS of 120 mm/min and for the TRS of 1800 rpm, but a processing window leading to sound joints was determined

The welding speed

The WS in the FSW process is lower than in fusion welding processes such as arc welding or laser welding [257].

According to Di Bella et al. [257], typical WSs in FSW can range from a few centimeters per minute (cm/min) to several tens of centimeters per minute depending on the specific application. However, FSW using lower WSs is focused on the control of the process parameters, providing proper heat generation, mixing, and consolidation of the material compared to FWS performed solely on high WSs. The selection of the optimal WS is a balance between process efficiency and joint quality. A slower WS ensures better heat input control and material mixing, and improved joint integrity; however, it can cause defects such as tunneling. A higher WS improves productivity but should be carefully adjusted to maintain the required joint efficiency.

Studying FSW joints between 5083-H111/6351-T6 alloys obtained at three WSs (i.e., 36, 63, and 90 mm/min) and a TRS of 950 rpm and using high-carbon, high-chromium steel tool comprising a shoulder of 18 mm in diameter and a pin of 6 mm in diameter and 5.7 mm in length, with a straight square profile, Palanivel et al. [342] reported that at higher WSs, the exposure time in the weld area shortened, causing inadequate heat and insufficient material plastic flow. This resulted in voids occurring in the joints. Additionally, the reduced plasticity and material diffusion rates weakened the interface. The higher WSs decreased the heat input, intensifying the joint cooling down [346] and preventing the formation of a well-mixed flow region.

For the FSW joints of components made of dissimilar A356/6061 alloys (Table 4), Ghosh et al. [346] found that with a higher WS, matrix grain size became finer, without the incessant limitation of Si-rich particles' size being affected by interaction time between the tool and the substrate. The maximum WE of 116% with respect to that of the 6061 alloy occurred at the intermediate WS, providing a fine matrix grain size and a small size of Si-rich particles.

The WS governs the exposure time of frictional heat per unit weld length, thus influencing the grain growth and precipitates inside welded components. Using an optimal exposure time and the appropriate translation of stirred material provides effective material consolidation and a refining grain structure. The joint subjected to such conditions at a WS of 63 mm/min showed the highest resistance. Using a combination of the specific WS and a corresponding exposure time facilitated desired consolidation and grain refinement, highly increasing the overall strength and joint quality. The factors determining the joint TS are strongly affected by the occurrence of macroscopic defects in the weld zone, the degree of plastic flow, and the amount of mixing of both alloys [257].

WSs are usually chosen in combination with TRSs to provide a defect-free joint with enough metallurgical bond and mechanical properties [257].

Studying the FSW joints between (AS) 5083-H321/(RS) 6061-T6 alloys, obtained at a TRS of 1120 rpm, various WSs (i.e., 40, 63, 80, and 100 mm/min), and a tilt angle of 2.5, and using an H13 steel tool comprising a shoulder diameter of 18 mm, a pin of 6 mm in diameter and 4.7 mm in length, with a cylindrical taper threaded profile, Devaiah et al. [429] reported that the optimal joint was obtained at a TRS of 1120 rpm and a WS of 80 mm/min, providing adequate heat generation and proper material mixing in the weld zone. The latter showed the formation of finer grains due to dynamic recrystallization, which refined the grain structure inside the weld zone. Both tensile and impact specimens exhibited a ductile fibrous fracture, which was evident at the weld zones, thus confirming good joint ductility and toughness characteristics. The WS significantly affected the formation of the plastic flow region during FSW, determining the extent and quality of material mixing. At the lowest or highest WSs, the joints comprised no or a poorly formed mixed flow region.

For the FSW joint between (AS) 6061-T6/(RS) 5083-H111 alloys obtained at various TRSs (i.e., 2000, 2400, and 2800 rpm), WSs (i.e., 1200, 1500, and 1800 mm/min), and plunge depths (i.e., 0.20, 0.25, and 0.30 mm), with a tilt angle of 2.5, and using a welding tool comprising a shoulder of 14.0 mm in diameter and three involute grooves on, a pin of

3 mm in the bottom diameter and 2.65 mm in length, with a right-hand threaded surface, Jia et al. [430] reported that the joint YS first increased and then decreased with an increase in the WS. A higher WS reduced the amount of frictional heat generated and impeded achieving enough material flow and mixing. The simultaneous action of the TRS and WS generated frictional heat, softening the material, as well as facilitating plasticized material flow and mixing. However, the excessive WS provided insufficient time for the heat to build up, causing inadequate material softening. Insufficient frictional heat leads to challenges in achieving proper material flow and mixing. The softened material cannot flow and mix effectively, thus weakening the joint quality. Inadequate mixing induces defects, including incomplete bonding, lack of homogeneity, or improper joint consolidation of the weld. The WS strongly affects the material mixing of Al alloys, which is better at lower WSs.

Studying the FSW joint between 7050-T7651/2014A-T6 alloys obtained at a TRS of 1000 rpm, various WSs (i.e., 25, 45, 65, and 85 mm/min), and a tilt angle of 2, and using an H13 tool steel tool with cylindrical tapered pin, Anandan et al. [431] found better mechanical and metallurgical properties of the joints obtained at a WS of 65 mm/min compared to those for the other WSs due to proper material mixing and finer grains within the joint. At low WSs, the formation of keyholes and high concavity occurred, while at high WSs, the SZ decreased by about 37%. The formation of keyholes and concavity was caused by enhanced heat generation during the FSW process. Conversely, less heat generation decreased the size of the SZ.

Dimov et al. [432] studied the mechanical behavior of the FSW joint between 6061-T651/7075-T651 alloys by controlling the pin length, rotational speed, advancing speed, and vertical force to reach 5.75 mm, 400 rpm, 120 mm/min, and 10 kN, respectively. The meso-scale strain distribution was affected by the local alloy composition. Additionally, to a lesser extent, the occurrence of intermetallic Mg-Si- and Fe-rich particles also influenced strain localization within each individual alloy.

Investigating the FSW joint between (AS) 2219-O/(RS) 7475-T761 obtained at two TRSs (i.e., 710 and 1120 rpm) and two WSs (i.e., 160 and 250 mm/min), with a tilt angle of 2.5, and using a high-carbon, high-chromium steel tool comprising a shoulder of 14 mm in diameter and a cylindrical threaded pin of 4 mm in diameter, Khan et al. [433] found that an enhanced strain rate caused a greater flow stress required for plastic deformation. The relationship between the strain rate and the WS was more pronounced compared to the TRS. A higher WS reduced the heat input per unit joint length and increased the strain rate. Both TRS and WS enhanced the flow stress. Additionally, increasing the WS significantly increased the net traverse force exerted on the tool.

For the FSW joint between (RS) 7075-T6/(AS) 5083-H111 alloys obtained at a TRS of 300 rpm, various WSs (i.e., 50, 100, 150, and 200 mm/min), and a tilt angle of 3, and using an H13 steel tool comprising a concave shoulder of 18 mm in diameter and a 4.8 mm long unthreaded taper cylindrical pin, Ahmed et al. [434] revealed that despite using the same parameters for the two alloys, the FSW process caused various levels of recrystallized fine grains. For the 7075 alloy, an average grain size of 6 μm in the NZ was obtained at a WS of 50 mm/min, which decreased to 2 μm by increasing the WS to 200 mm/min. For the 5083 alloy, an average grain size of 9 μm in the NZ was obtained at the WS of 50 mm/min, which decreased to 3 μm at 200 mm/min. Thus, the initial characteristics of the BMs strongly affected the final grain structure after FSW. The NZ exhibited a simple shear texture only slightly dependent on the WS variation.

Investigating the FSW joint between 2198-T8/2024-T3 alloys obtained at a TRS of 960 rpm, at various WSs (i.e., 36, 76, 102, 146, and 216 mm/min), and a tilt angle of 2, and using a tool comprising a concaved shoulder and tapered threaded pin, Alemdar et al. [435] reported that increasing the WS from 36 mm/min to 216 mm/min first increased the HAZ area and then reduced it due to various welding temperatures. The joints obtained at a WS of 76 mm/min showed excellent tensile characteristics.

According to Di Bella et al. [257], thicker sheets need lower WSs to provide sufficient heat transfer and material plasticization. The lower WS allows enough time for the heat

generated by the friction stir process to propagate via the sheets' thickness and achieve the needed joint quality. A lower WS also helps to maintain better control over the material flow and mixing during the FSW. However, too-low WSs may induce excessive heat input and potential defects. Therefore, the WS should be optimized based on the specific material, sheet thickness, and needed joint characteristics.

For the FSW joints of 3 mm thick components made of the 2014-T6 alloy (Table 6) obtained at three TRSs (i.e., 1070, 1520, and 2140 rpm), WSs (i.e., 40, 80, and 112 mm/min), and a tilt angle of 2.5°, and using (X38CrMoV5-3) hardened steel tools comprising a flat shoulder of 17 mm in diameter and two different pin shapes (i.e., a threaded cylindrical with a length 2.9 mm along with a left-hand screw of 0.8 mm pitch and a conical with a large diameter of 5 mm and small diameter of 4 mm), Aydin et al. [428] found that the hardness in the softened weld region decreased with a decrease in the WS. Independent of the TRSs, the best tensile and fatigue properties of the joints occurred under the WS of 80 mm/min. The WE varied in the range of 93%–97%.

Table 8 presents the effects of the WS on the FSW joint properties (some of the data were published earlier in the excellent review by Di Bella et al. [257]).

Table 8. Effect of the WS on the FSW joint properties.

Ref.	Sheet Material Position AS/RS/NA Sheet Position AS/RS	Pin Profile	Tilt Angle [°]	TRS [rpm]	WS [mm/min]	AF [kN]	Main Results
[431]	(NA) 2014A-T6/(NA) 7050-T7651	Cylindrical tapered	2	1000	25; 45; 65; 85	NA	The intermediate WS value of 65 mm/min induces better mechanical and metallurgical properties due to proper material mixing and finer grains. At low welding speeds, keyholes and high concavity occur, while at high welding speeds, the stir zone decreases.
[435]	(NA) 2024-T3/(NA) 2198-T8	Tapered threaded	2	960	36; 76; 102; 146; 216	NA	As the WS increases, the area of the HAZ initially increases, and then the joints formed at 76 mm/min exhibit excellent tensile characteristics.
[433]	(AS) 2219-O /(RS) 7475-T761	Threaded	2.5	710; 1120	160; 250	NA	A higher traverse speed leads to a reduction in heat input per unit weld length and an increase in strain rate.
[429]	(AS) 5083-H321/(RS) 6061-T6	Cylindrical taper threaded	2.5	1120	40; 63; 80; 100	NA	The 1120 rpm/80 mm/min combination induced adequate heat generation and proper mixing of the material in the weld zone. The weld zone exhibited the formation of finer grains.

Table 8. Cont.

Ref.	Sheet Material Position AS/RS/NA Sheet Position AS/RS	Pin Profile	Tilt Angle [°]	TRS [rpm]	WS [mm/min]	AF [kN]	Main Results
[430]	(RS) 5083-H111/(AS) 6061-T6	Right-hand threaded	2.5	2000; 2400; 2800;	1200; 1500; 1800;	NA	The YS first increased and then decreased with an increase in the WS. A higher WS reduced the amount of frictional heat generated and made it difficult to achieve sufficient material flow and mixing. A lower WS is more conducive to the mixing of dissimilar Al alloys.
[342]	(NA) 5083-H111/(NA) 6351-T6	Straight square	-	950	36; 63; 90	NA	Higher WSs induce short exposure time leading to inadequate heat and insufficient plastic flow and affecting the grain growth and precipitates within the welded material. Increasing it promotes favorable consolidation and grain refinement.
[434]	(AS) 5083-H111/(RS) 7075-T6	Unthreaded taper cylindrical	3	300	50; 100; 150; 200	NA	Despite using the same parameters for two alloys, the alloys display different responses in terms of the recrystallized fine grains after FSW. An increased WS induced significant grain refinement in the NZ.
[432]	(NA) 6061-T651/(NA) 7075-T651	NA	NA	to 400	to 120	to 10	The meso-scale strain distribution is primarily influenced by the local alloy composition. Additionally, at a smaller scale, the presence of intermetallic Mg-Si- and Fe-rich particles further contributes to strain localization within each individual alloy.

Table 8. Cont.

Ref.	Sheet Material Position AS/RS/NA Sheet Position AS/RS	Pin Profile	Tilt Angle [°]	TRS [rpm]	WS [mm/min]	AF [kN]	Main Results
[428]	2014-T6	Threaded cylindrical	2.5	1070; 1520; 2140	40; 80; 112		The hardness in the softened weld region decreased with a decrease in the WS. Independent of the TRSs, the best tensile and fatigue properties of the joints occurred under the WS of 80 mm/min. The WE varied in the range of 93%–97%
[301]	(AS/RS) cast A356/(RS/AS) wrought 6061	screw-like	3	1600	78–267		The area of the SZ slightly decreased with an increase in the WS due to the different cooling rates.

Figure 4 shows the optimum TRS/WS combinations for the dissimilar joints of Al alloys [257].

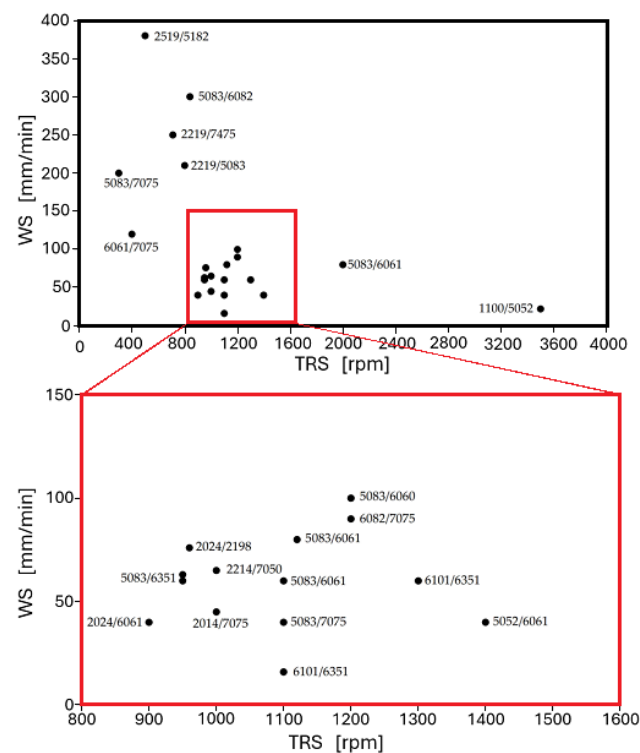


Figure 4. Optimal TRS/WS combinations for dissimilar joints of Al alloys [257].

The axial force

The axial force (AF) applied vertically onto the welded components via a rotating tool strongly affects FSW [317,343,436], providing a downward pressure that holds such components together and maintains contact between the tool and such components [437]. The FA magnitude varied depending on welded material type, thickness, and tool geometry. The FA affects the FSW through the following factors [257]:

- **Material Penetration:** ensuring the tool penetration into the required workpiece's depth facilitates proper material mixing and bonding between the adjacent surfaces.
- **Heat Generation:** the downward pressure increases the contact zone between the tool and the workpiece, thus generating frictional heat due to the relative motion between them, which softens the material, allowing deformation and the joining of the material.
- **Plastic Deformation:** the AF enables the deformation and stirring of the material, thus facilitating metallurgical bonding. Plastic deformation permits the material to flow around the tool and form a solid-state weld.
- **Quality of the Weld:** a properly applied AF provides sufficient contact between the tool and the workpiece, promoting enough heat transfer and material flow. Insufficient AF causes inadequate mixing, incomplete bonding, or defects in the weld, while excessive AF induces excessive material motion or even tool breakage.
- **Weld Strength and Integrity:** a properly applied AF ensures effective material consolidation, providing a sound weld joint with better mechanical properties.

Only optimized AF helps to achieve high-quality FSW joints.

The careful control of AF provides proper penetration, material flow, and bonding without compromising the tool integrity or inducing negative effects on the welded components. The optimal AF is affected by the material welded, its thickness, and the FSW process parameters.

The application of an unsuitable or improper FA causes various joint defects. For example, poor contact between the rotating tool and the welded components induces incomplete joint formation with poor material mixing or bonding. Such defect comprises visible gaps or voids along the weld line. An FA that is insufficient to induce enough plastic deformation and stirring prevents obtaining the desired material homogeneity and metallurgical bonding, resulting in poor mechanical properties and weakened weld strength. Under too-low FA, the rotating tool's penetration into the welded components can be inadequate, causing a tunnel defect, where the tool only partly engages with the material. Resulting joint voids or cavities are formed, thus compromising the joint integrity and mechanical properties. Excessive AF induces excessive material motion and flow around the rotating tool, causing a flash defect, with material pushed out of the joint line and forming an unwanted protrusion or flash on the joint surface. Flash defects weaken the joint and need additional post-weld machining or removal. Excessive AF subjects the rotating tool to high mechanical stresses, thus increasing the risk of tool breakage, disrupting the welding operation, and adding potential contaminants to the weld. Such risks can be reduced with the AF control within the recommended limits during the FSW. An inadequate AF often induces nonuniform deformation and inadequate thermal cycling during FSW, thus providing residual stresses and distortion in the joint and the surrounding material and affecting the structural integrity and dimensional accuracy of the welded component [438,439].

Evaluating the effect of axial force (5, 6, 7, and 8 kN) on the mechanical properties of the joint of 5086/6063 alloys obtained under a TRS of 2000 rpm and a WS of 60 mm/min, Ramamoorthi et al. [437] found that the FA directly affected the shoulder pressure, influencing the tool pin penetration depth into the process region and the resulting material flow. The mentioned tool shoulder pressure should also ensure sufficient and effective stirring of the material, leading to the refinement of Al alloy grains [440–442]. The AF also significantly limited the weld efficiency and joint strength, i.e., 5 kN and 6 kN axial forces led to inadequate mixing and inferior joint quality. Therefore, the joints obtained under an AF of 7 N exhibited the best performance.

As mentioned in [257], the AF applied to the FSW tool affects the contact pressure between the tool and the workpiece. Thicker sheets need higher AFs for providing good material contact and facilitating enough heat transfer. The enhanced AF facilitates overcoming the resistance to material deformation induced by the thickness of the sheets. It also helps to maintain a consistent material flow and proper mixing during FSW. However, excessive

AFs should be avoided, as they cause excessive material motion or tool wear. The AF needs optimization to achieve a balance between material deformation and FSW stability.

Table 9 presents the effects of the AF on the FSW joint properties. They are in line with some information given in [257].

Table 9. Effects of the AF on the FSW joint properties.

Ref.	Alloys Positions AS/RS	Pin Profile	Tilt Angle [°]	TRS [rpm]	WS [mm/min]	Axial Force (kN)	Main Result
[437]	(NA) 5086/(NA)6063			2000	60	5; 6; 7; 8	The AF affected the shoulder pressure, influencing the tool pin penetration depth into the process region and the resulting material flow. The 5 kN and 6 kN AF led to inadequate mixing and inferior joint quality. For the AF of 7 N, the joint exhibited the best performance.
[438]	(AS/RS) Squeeze Cast A413					2–7	The squeezing pressure of 140 MPa provided sound casting. The joint fabricated with an AF of 5 kN exhibited superior microstructural and mechanical properties.
[442]	(NA) 6351-T6/(NA) 5083-H111	Straight square (SS), tapered square (TS), straight hexagon (SH), straight octagon (SO) and tapered octagon (TO)		1200	75	10; 15; 20	The SS pin profile with AF of 15 kN produced better joint TS than other tool pin profiles and AFs.
[440]	(AS/RS) 6061-T6	Straight cylindrical, tapered cylindrical, threaded cylindrical, triangular, and square				6; 7; 8	The square tool pin profile produced mechanically sound and metallurgically defect-free welds compared to other tool pin profiles. AF 7 kN produced a defect-free FSP region, irrespective of tool pin profiles. With the square tool pin at AF of 7 kN joints had superior tensile properties due to a defect-free weld, smaller grains with uniformly distributed finer strengthening precipitates within, and higher hardness.

Table 9. Cont.

Ref.	Alloys Positions AS/RS	Pin Profile	Tilt Angle [°]	TRS [rpm]	WS [mm/min]	Axial Force (kN)	Main Result
[441]	(AS/RS) A319 (Al-Si-Cu)			800; 900; 1100; 1300	22; 40; 75; 100	2; 3; 4; 5	The joint fabricated at TRS of 900 rpm, WS of 75 mm/min, and AF of 3 kN showed a superior TS compared with other joints. The joint TS and microhardness for the optimum conditions were 166 MPa and 64.8 HV, respectively.

Interestingly, in the case of the TRS, the WS, and, less often, the AF, some authors only provided their values without investigating their effect on FSW joint properties, separately or in combination. Such values are probably based on recommendations from the literature for specific combinations of components made of Al alloys.

Tool Geometry

Tool Tilt Angle

The tilt angle affects the joint quality and mechanical properties [443,444].

The adjusting of the tilt angle during the FSW facilitates the control of the heat input and material flow. A larger tilt angle provides a higher heat input and material flow, inducing better material mixing and homogenization. This provides a more uniform grain structure, better joint mechanical properties, and enhanced joint strength. A larger tilt angle is beneficial for welding thicker materials or for achieving a needed weld shape. However, excessive defects such as tunneling and hooking occur, thus weakening the joint [64]. Additionally, a larger tilt angle increases the likelihood of thermal distortion and residual stresses in the joint. Contrarily, a smaller tilt angle provides less heat input and material flow, reducing the risk of defects and thermal distortion. However, a too-small tilt angle also induces defects such as hooking [257].

Di Bella et al. [445] studied the FSW joint between 6082/5083 alloys obtained under different TRS/WS ratios (i.e., 1000/100, 1300/75, and 1600/50) and using a taper threaded tool pin profile. They found that a small spindle inclination was sufficient to significantly improve the joint behavior by affecting the same effectiveness of the process.

Considering three values of the tool tilt angle (i.e., 2, 3, and 4°), Yuvaraj et al. [446] optimized it for the FSW joint between 7075-T651/6061 alloys utilizing a statistical technique. They reported that the tool tilt angle mainly affected the joint TS. For higher tool tilt angles, the gap expanded between the workpiece and the tool [447]. In particular, the square profile tool pin and a high tool tilt angle of 3 degrees improved the joint mechanical properties.

According to Di Bella et al. [257], various tool shoulder features machined onto the shoulder profile, including scrolls, ridges or knurling, grooves, and concentric circles, can enhance the amount of material deformation produced by the shoulder, inducing better-welded components' mixing and higher joint quality. Scrolls are the most commonly existing shoulder feature. The channels directly deform the material from the edge of the shoulder to the pin, thus preventing the necessity to tilt the tool [448]. Such tools are particularly preferred for curved joints [48,448].

For the tool tilt angle ranging from 1 to 3°, the material flow is more intensive, allowing for increasing the speed and preventing defects in the joint.

Tool Shoulder and Pin Geometry

The FSW tool is typically fabricated from tungsten carbide, tool steel, or ceramics. Its cylindrical shape comprises a shoulder of diameter D at one end and a pin of diameter d and length l at the other [449]. Using a shoulder with a D/d ratio exceeding the value of 1,

a downward force (AF) is applied to the welded components, and the material being stirred is contained during the welding process. The active tool pin possesses a specially shaped profile affected by the material being welded and the required process parameters. The pin profile comprises a threaded or fluted part that facilitates material mixing and stirring, as well as a smooth part providing a solid-state bond between the welded components. The main geometries of bottom pin surfaces were presented in [450]. Under a TRS typically ranging from 280 [311] to 2500 [324,325], the rotating tool traverses along the joint course at a controlled WS. The combination of TRS and WS allows for frictional heat generation, softening the material and inducing its plastic deformation. Then, the tool stirs the softened BMs together to form a solid-state joint with less filler material or fusion. The used tool geometry strongly affects the quality, strength, and efficiency of the FSW process [336]. In the butt FSW joints of 2050/6061 alloys, the pin with thread flats (Table 10) allowed for the production of high-quality welds in some cases. The D/d ratio influences joint mechanical strength and grain refinement [451]. Consequently, only an optimized tool geometry provides successful and cost-effective FSW [452]. The size of both the tool pin and shoulder controls the size of the SZ comprising the material plastically deformed and mixed. A greater tool pin diameter enhances the SZ, while a greater shoulder diameter widens the HAZ. The shape and structure of the tool pin and shoulder influence the direction and magnitude of material flow during the FSW process [453,454]. The joint strength depends on the tool geometry, particularly the pin one. The shape and size of the tool pin influence the level of plastic deformation and material during the FSW process, in turn impacting the joint strength and quality [455]. A threaded or fluted tool pin provides better material mixing, while a flat or smooth pin creates less material mixing [456]. The tool geometry influences the amount of frictional heat generated during the FSW process. A greater tool shoulder diameter provides more heat due to the enhanced contact area with the welded components [62,457]. The tool geometry also impacts its wear rate during the FSW process. With more complex geometry, tool wear occurs faster than in a tool with simpler geometry, thus increasing the cost of the FSW and reducing its efficiency [458].

Zhou et al. [421] reported that the geometry of the shoulder and the pin profile strongly affected heat generation and material flow during the welding process. They obtained various FSW joints of the 6061-T6 alloy (Table 10) using tools with three configurations of the pin, namely a quadrangular prism, a quadrangular frustum pyramid, and a frustum one. The use of the tool with a quadrangular frustum pyramid pin shape allowed for obtaining sound joints.

A high shoulder size governs heat input. Common shoulder profiles include flat, concave, and convex shapes. Pin features such as a spiral or groove improve frictional behavior and material flow in the joint. Threads guide material flow around the pin in a rotational and translational direction [310,311,335,425]. Polygonal pin profiles provide pulses in the flow during material stirring and mixing, causing the material to adhere to the pin [459–462]. This pulsating effect highly impedes the material flow in joints between dissimilar Al alloys. Thus, a cylindrical or conical pin profile with various features provides good material flow, which helps to obtain sound joints between dissimilar Al alloys.

Typical tool pin profiles are cylinder or straight cylinder, square, hexagonal, triangular, threaded cylinder, cylindrical cam, conical, taper, pentagonal, taper cylindrical tool, and taper square tools [452]. Commonly, tool shoulder profiles are flat, concave, and convex [463,464]. Special pin features like a spiral or groove ameliorate frictional behavior as well as material flow [73]. Material stirring and mixing are highly affected by the pin profile.

Investigating the influence of the tool pin profile on FSW joints between 6061-T6/5083-O alloys, Verma et al. [465] found that a tool comprising a straight cylindrical pin profile provided maximum joint strength and elongation for various combinations of FSW parameters. The joint obtained at a tool tilt angle of 1.11° , a TRS of 1568 rpm, and a WS of 39.53 mm/min reached the maximum UTS of 135.83 MPa and a tensile elongation of 4.35%.

Studying the effect of various tool shoulder profiles (partial impeller, full impeller, and flat groove) on the FSW joint between 5083/6351 alloys, Palanivel et al. [313] found that the full impeller profile was most effective in providing superior mechanical strength due to the generation of increased material flow.

Investigating the FSW joints between 7075/5083 alloys obtained at a WS of 40 mm/min and three TRSs (i.e., 600, 700, and 800 rpm) and using three different pin profiles (i.e., threaded straight cylindrical, tapered cylindrical, and threaded tapered cylindrical), Azmi et al. [466] found that the tool pin profile strongly affected the mechanical properties of the joint together with the varying TRSs. The highest joint TS and defect-free joints were produced at a TRS of 800 rpm and using the threaded tapered cylindrical pin tool.

Various FSW joints between dissimilar Al alloys are produced using cylindrical or conical tool pin profiles comprising threads or threads with flats, which significantly influences material stirring and mixing. A pin profile without threads provides less surface area for material interaction. However, pins with threaded and flat features enhance the contact area, and threads guide the material flow around the pin both rotationally and translationally [257].

Studying the effect of pin flute radius on the properties of FSW joints between 7075-T651/2024-T351 alloys (Table 10) obtained at a TRS of 900 rpm and a WS of 150 mm/min, and using five various pin tools with different flute radii (i.e., 0, 2, 3, 6, and ∞ mm), Hasan et al. [310] found that a pin tool with a flute of radius equal to that of the pin provided the strongest joint. The joint efficiency reached up to 94.3%.

Kalemba-Rec et al. [311] investigated the FSW joint between 7075-T651/5083-H111 alloys obtained using two various tools with similar dimensions and comprising a spiral shoulder but various pin shapes (i.e., triflute and tapered with a thread). A triflute pin provided the highest joint TS and WE at a TRS of 280 rpm for the configuration of (RS) 7075-T651/(AS) 5083-H111 alloys. Better material mixing was reached at higher TRS; however, under such conditions, the weld microstructure exhibited more defects such as porosity, voids, or wormholes.

Studying the FSW joints between (RS)5086-O/(AS) 6061-T6 alloys obtained at a TRS of 1100 rpm, a WS of 22 mm/min, an AF of 12 kN, and a tool tilt angle of 1° , and using high-speed steel tools comprising a shoulder of 18 mm in diameter and three pins of 5.7 mm in length with three different profiles (i.e., straight cylindrical, threaded cylindrical, and tapered cylindrical), Ilangovan et al. [335] found the following:

- The straight cylindrical profile was ineffective as it caused cross-sectional macro-level defects in the SZ;
- Threaded and tapered cylindrical profiles provided defect-free joints with similar tensile properties;
- The threaded cylindrical pin profile was the best as it allowed for the formation of finer and uniformly distributed precipitates, circular onion rings, and smaller grains. It provided a better material flow between both alloys and the generation of defect-free SZ. The studied configuration exhibited a higher hardness of 83 HV in the SZ, as well as a higher TS of 169 MPa in comparison to the other profiles. The increased hardness resulted from the formation of fine grains and intermetallics inside the SZ. The reduced size of weaker regions, such as the TMAZ and the HAZ, clearly improved the joint tensile properties. For the configuration of (AS) 5052-H32/(RS) 6061-T6 alloys, such a joint behavior varied.

Investigating the FSW joint between 5052-H32/6061-T6 alloys obtained at a WS of 60 mm/min and a TRS of 900 rpm and using M2 HSS tools comprising a shoulder of 18 mm in diameter and two pins of 4.7 mm in height with two various profiles (i.e., tapered cylinder and threaded cylindrical), Balamurugan et al. [467] found that such joints exhibited better TS, greater NZ, and smoother surface finish. However, the tapered pin profile provided such a fine-grain microstructure that the resulting connection was strong.

FSW is accompanied by high temperatures resulting from the frictional heat generated by the rotating tool, inducing deformations and strains in the material microstructure.

The translational motion of the rotating tool along the joint line forms a HAZ on either weld side. Inside such a zone, the Al alloy is subjected to a range of temperatures, from below its recrystallization temperature to a much elevated one. The tool reaching the alloy region induces grain deformation and alignment toward the tool rotation. During Al alloy cooling, grains start reverting to their original, strain-free state, inducing recrystallization and growth with the new relaxed, strain-free-oriented grains. The recrystallized grains reduce weld residual stresses, making a stronger and more ductile joint and providing a high-quality joint. By reducing residual stresses and ameliorating the joint ductility of the joint, recrystallization improves the mechanical properties of alloys and facilitates withstanding the applied stresses and strains [468,469].

The tool pin profile, including its shape, size, and geometry, influences the temperature distribution of the FSW joint, as well as its strain distribution and shear deformation, in turn affecting the recrystallization degree present. A higher FSW tool pin diameter and a more rounded profile provide more frictional heat and better material flow during the process, inducing a higher degree of recrystallization [335,467,470,471]. This is because the pin of a higher diameter generates more frictional heat, thus increasing the material temperature, while the more rounded pin profile ameliorates the material flow, increasing the number of grains deformed and realigned. Conversely, the use of a tool pin with a smaller diameter and a more angular profile reduces heat and material flow, thus decreasing the recrystallization degree. This is because a pin with a smaller diameter generates less frictional heat, thus reducing the material temperature, while the more angular profile weakens material flow, decreasing the number of grains deformed and realigned [335,467]. Additionally, the tool pin material also influences the recrystallization degree. Using a tool pin material with less thermal conductivity (W or Mo), more frictional heat is generated during FSW, increasing the recrystallization degree. Using a tool pin material with a higher thermal conductivity (Cu), heat dissipates more quickly, thus reducing the recrystallization degree. Consequently, this profile alone cannot affect the grain of the microstructure, leading to various behaviors, as observed in [335,467].

For FSW joints between dissimilar Al alloys, polygonal pin profiles induce a meaningful pulsating effect on material stirring and mixing, inducing adhesion between alloys, and the pin working surface intensifies the flow of plasticized alloy under the tool shoulder in the SZ [472]. Therefore, cylindrical or conical pins are more suitable for FSW [73].

Investigating the microstructural and mechanical features of the FSW joint between 2024-O/6061-T6 alloys obtained at various TRSs (i.e., 900, 1400, and 1800 rpm) and using various tool pin shapes, Tiwan et al. [473] found that the pin geometry influenced the size of the SZ. At a TRS of 1400, a tool comprising a cylindrical pin profile was more suitable as it facilitated the material flow upward of the lower sheet material around the pin without any retardation, contrary to the more complex stepped pin.

During welding dissimilar Al alloys using polygonal tool pin profiles, various defects including voids, tunnels, cracks, and fragmental defects occur [474].

Studying the effect of various pin profiles (i.e., square, pentagon, and hexagon) on the microstructure and TS of the FSW joint between 8011/6061-T6 alloys, Palani et al. [475] found that the hexagonal tool pin profile provided more effective joints obtained at a TRS of 1500 rpm, a WS of 40 mm/min, and a plunge depth of 2.5 mm.

Typical defects in FSW joints between dissimilar Al alloys are presented in [470].

Investigating the FSW joints between (AS) 6061-T6/(RS) 7075-T651 alloys obtained at four different TRSs (i.e., 660, 900, 1200, and 1700 rpm) and WSs (i.e., 36, 63, 98, and 132 mm/min) and using four different tool pin profiles (i.e., cylindrical, cylindrical tapered, cylindrical threaded with three flat faces, and truncated square pyramidal shaped profile, referred to as trapezoidal tapered), Raturi et al. [476] reported that at suitable intermediate TRS and WS values, the tool pin with cylindrical threaded profile and three flat faces and the cylindrical grooved one provided good tensile and flexural strength. The joint quality, TS, and flexural load of the welds are mainly affected by tool pin profiles and TRS. A too-high TRS induces a worse nugget shape and inadequate joining due to excessive

heat generation, significantly softening the joint material. Consequently, poor friction, slipping, insufficient material delivery, and low joint strength occur. Similarly, a high WS also reduces joint strength. The welded joints obtained with proper tool pin profiles and process parameters showed ductile failure, confirmed by the microvoids and dimples occurring in the well-bonded region. Contrarily, the welded joints obtained at very high TRS showed tearing, rupture, and brittle failure.

Raturi and Bhattacharya [477] studied the wear phenomenon of the same joints obtained at a TRS of 900 rpm and a WS of 98 mm/min and using a tool pin with a right-hand threaded profile and three intermittent flat faces.

Lower FSW joint mechanical performance was obtained using a complex tool pin profile (i.e., hexagonal) compared to the case using a simple pin profile (i.e., triangular), which resulted from the reduced traverse force and increased structural stiffness with the increase in the number of pin sides and the resulting weakened bending moment and shear force [478].

Studying the FSW joint between plates made of 7075-T651/6061 alloys obtained using simple HSS tools with three different pin profiles (i.e., square, cylindrical, and triangle), Yuvaraj et al. [446] found that the best joints were obtained using a square tool pin profile under a tool offset of 0.9 mm and a tool tilt angle of 2°. Such joints showed fine grains along the SZ, which resulted from adequate heat generation. Using the triangular pin, a granular grain structure was obtained due to additional heat generation and the resulting turbulent material flow of material.

Investigating the FSW joints between 6061/7075 alloys obtained with three tool pin profiles (i.e., straight cylinder, straight square, and tapered hexagon), Krishna et al. [479] found that at a TRS of 950 rpm and a WS of 60 mm/min with the (RS) 6061/(AS) 7075 alloys/configuration, the use of the straight cylinder tool pin profile allowed for obtaining higher joint mechanical properties owing to the tool pin geometry without sharp edges, also providing smooth and excellent joint. Other pin geometries comprising sharp edges cannot ensure efficient and smooth welding.

Investigating the FSW joint between 2024-T365/5083-H111 alloys obtained using three tools with various pin profiles (i.e., square, triangular, and stepped), El-Hafez and El-Megharbel [480] found that at a WS of 16 mm/min and a TRS of 900 rpm, the use of the square tool pin profile provided the best joint strength, which resulted from the pulsed action (four pulses per revolution), providing a good material flow and stirring, in agreement with [481,482].

Studying the FSW joint between 5083-H111/6061-T6 alloys obtained using three tools with various pin profiles (i.e., straight square, threaded cylinder, and tapered cylinder), Shine and Jayakumar [471] found that the use of the straight square tool pin profile provided higher hardness values in the NZ and higher joint TS compared to the other pin profiles.

Investigating the FSW joint between 2017-T6/6061-T6 alloys obtained at a TRS of 1600 rpm, a WS of 32 mm/min, and a tilt angle of 0°, and using tools with various pin profiles (i.e., straight hexagonal, straight pentagonal, straight cylindrical, straight square, and tapered square), Battina et al. [483] found that the straight square tool pin profile provided better metallurgical and mechanical properties. The properties were inferior to those of other pin profiles, but it was preferred due to providing defect-free joints.

Studying the FSW joint of 5083/7068 alloys obtained at four TRSs (i.e., 800, 1000, 1200, and 1400 rpm), four WSs (i.e., 30, 40, 50, and 60 mm/min), and four AFs (i.e., 3, 4, 5, and 6 kN), and using tools with three different tool pin profiles (i.e., straight cylindrical, taper cylindrical, and triangular), the authors of [484] found that the triangular tool provided the maximum TS and microhardness, which was obtained during studies with a TRS of 1200 rpm, a WS of 30 mm/min, and an AF of 3 kN.

Ge et al. [61] studied how EST affects the shear failure load of lap joints. A shear fracture occurred in lap joints obtained with a small pin (3 mm) at all WSs. A tensile fracture occurred in the lap joints obtained with a larger pin (4 mm or 5 mm).

Studying the FSW joints of components made of 7075-T651 and 5083-H111 alloys, Kalembe-Rec et al. [311] reported that using a triflute pin provided a greater TS and WE.

Palanivel et al. [313] studied the effect of shoulder profiles on the 5083–6351 combination properties (Table 10). They utilized three different shoulder features, namely the partial impeller, full impeller, and flat groove profiles. The full impeller shoulder tool provided the optimum mechanical strength due to the increased material flow in the joint. The pin profile strongly influences material stirring and mixing. Cylindrical or conical pin profiles without threads provide a smaller material surface. Such pin profiles with threaded and flat features enhance the contact area.

For studying the FSW sheets made of dissimilar 2017A-T451/7075-T651 alloys (Table 10), Hamilton et al. [363] obtained quality welds using a tool made of HS6-5-2 high-speed steel with a scrolled shoulder with a 24 mm diameter. The pin diameter tapered linearly from 6 mm at the shoulder to 4.5 mm at the tip with an overall height of 5.7 mm. The pin was also threaded.

Gupta et al. [383] conducted studies on the FSW joints of components made of dissimilar 5083-O/6063-T6 alloys (Table 10), focusing on the optimization of tool geometry, TRS, and WS. The multi-optimal set of weld properties comprising the TS, the average hardness at the NZ, and the average grain size at the NZ was obtained for a tool with an 18 mm shoulder diameter and 5 mm pin diameter.

The proper FSW joints of Al-Mg₂Si/Mg₂Si5052 alloys studied by Huang et al. [315] were obtained using an H13 steel-made pin tool comprising a concave shoulder 18 mm in diameter and a conical pin (the end and root diameter were 4 and 6 mm, respectively) with a pin length of 5.7 mm. The joints were obtained at a TRS of 1000 rpm, a WS of 80 mm/min, and a tool tilt angle of 2.5°. Thus, the effect of the TRS, WS, tilt angle, and tool geometry on the joint properties was studied neither solely nor in combination.

The correct FSW joints of dissimilar 2024/6061 alloys (Table 10), studied by Moradi et al. [316], were obtained using AISI H13 hot-work steel tool using a conical geometry with 18 mm shoulder diameter, a 4° conical cavity, and a square frustum probe measuring 3.5–7 mm in diameter and 5.9 mm in length. The effect of the tool geometry on the joint properties was not studied.

The proper FSW joints of dissimilar 6351-T6/6061-T6 alloys (Table 10), studied by Prasanth and Raj [317], were obtained using a cylindrical tool with a scroll with 0.75 mm taper at the tip of the pin and a 16 mm probe diameter, 14 mm shoulder diameter, 5 mm pin length, and of 4 mm pin diameter, made of molybdenum M42 with HRC 63. Thus, the effect of the tool geometry on the joint properties was not studied.

The correct FSW joints of dissimilar 6061-T651/5A06-H112 alloys (Table 10), studied by Peng et al. [319], were obtained using a tool with a cylindrical shoulder diameter of 16 mm and a conical pin with a diameter varying from 5 to 4.2 mm and a length of 4.6 mm. The effect of the tool geometry on the joint properties was not studied.

The proper FSW joints of dissimilar 2024-T3/6063-T6 alloys (Table 10), investigated by Sarsilmaz [321], were obtained using a D5 steel tool with a conical triangular pin profile quenched–tempered to 60 HRC. The effect of the tool geometry on the joint properties was not studied.

The sound FSW joints of dissimilar 2219-T87/2195-T8 alloys (Table 10), studied by No et al. [322], were obtained using a tool made of austenitized H13, with a spiral shape and a shoulder diameter of 16 mm. The effect of the tool geometry on the joint properties was not examined.

The proper FSW joints of dissimilar wrought 2017A/cast AlSi9Mg alloys (Table 10), studied by Kopyscianski et al. [323], were obtained using a modified Whorl-type tool made of HS6-5-2 high-speed steel with a 24 mm diameter and scrolled shoulder. The threaded pin diameter was tapered linearly from 6 mm at the shoulder to 4.5 mm at the tip with an overall height of 5.7 mm. The effect of the tool geometry on the joint properties was not studied.

The correct FSW joints of 5083-H12/6061-T6 alloys (Table 10), studied by Ghaffarpour et al. [324], were obtained using a tool with a shoulder diameter in the range of 10–14 mm and a pin diameter in the range of 2–4 mm.

The FSW joints studied by Bijanrostami et al. [325] were obtained using a tool made from heat-treated 2344 steel to obtain hardness by 52 HRC and comprised a shoulder with a diameter of 15 mm and a threaded conic pin with a conic angle of 5°, a length of 4.7 mm, and a diameter of 5 mm. The effect of the tool geometry on the joint properties was not studied.

Studying the FSW joints of dissimilar 6082-T6/5083-H111 alloys (Table 10), Kasman et al. [326] found that the pin shape significantly affected the tensile properties and microstructure of weld joints. The strengths of the weld joint obtained with the pentagonal-shaped pin were less than those with a triangular-shaped pin. The pin shape influenced each NZ profile containing onion rings.

Palanivel et al. [144] obtained proper FSW joints of 6 mm thick sheets made of dissimilar 5083-H111/6351-T6 alloys (Table 10) using a straight square tool pin with a shoulder diameter of 18 mm, a pin diameter of 6 mm, and a pin length of 5.6 mm. The effect of the tool geometry on the joint properties was not studied.

The proper FSW joints of 6 mm thick components made of dissimilar 6351/5083-H111 alloys (Table 10), studied by Palanivel et al. [422], were obtained using five tool pin profiles, namely straight cylinder, threaded cylinder, square, tapered square, and tapered octagon without draft. The ratio of shoulder diameter and pin diameter was 3. The tool material was HCHCr steel oil hardened to obtain a hardness of 60–62 HRC. The joint obtained using a tapered square pin profiled tool provided the least TS. Using tools with straight cylindrical, threaded cylindrical, tapered square, and tapered octagon pin profiles, the joint strength varied insignificantly. This resulted from the difference in dynamic orbit created by the eccentricity of the rotating tool during the FSW process.

Studying the FSW joints of components made of the dissimilar 2024-T6/7075-T6 alloys (Table 10), Saravanan et al. [328] found that the joint fabricated under a D/d ratio equal to 3 showed better mechanical properties in comparison to other joints.

Yan et al. [296,329] obtained proper the FSW joints of sheets made of dissimilar Al-Mg-Si/Al-Zn-Mg alloys (Table 10) using a tool with a shoulder diameter of 35 mm and a pin with diameters of the pin root and pin bottom equal to 20 and 12 mm, respectively, while the pin length was 14.5 mm.

The correct FSW joints of dissimilar 2024-T3/6061-T6 alloys (Table 10), studied by Zapata et al. [330], were obtained using a tool consisting of a 20 mm diameter concave shoulder with a 4 mm diameter tapered threaded pin.

The proper butt FSW joints of UFGed 1050/6061-T6 alloys (Table 10), studied by Sun et al. [331], were obtained using rotating tools made of tool steel, which contained a concave-shaped shoulder with a diameter of 12 mm and a threaded pin with a diameter of 4 mm and a length of 1.8 mm.

Sun et al. [485] studied the influence of various tool pin shapes, including conical thread, deep groove thread, and conical cam thread, on the plastic flow of 2024-T6/6061-T6 alloys (Table 10) during the FSW process. They found that the metal in the weld nugget zone (WNZ) came from the BM of the AS, and the thread was the driving force of the downward movement of the FSW plastic metal. The deep groove thread tool pin strongly drove the metal downward. The conical cam thread tool pin provided the strongest stirring of materials and the best metal fluidity. Welds were obtained using a tool with a shoulder with concentric circles and a diameter of 18 mm and a pin with a diameter varying from 7 to 5 mm and a length of 3.7 mm.

The proper FSW joints of dissimilar 6061/7050 high-strength Al alloys (Table 10), studied by Rodriguez et al. [333,334], were obtained using a tool consisting of a cylindrical threaded pin and a shoulder with diameters of 10 mm and 18 mm, respectively.

The sound lap FSW joints of plates made of dissimilar 6111-T4/5023-T4 alloys were studied by Yoon et al. [47], which were obtained using a tool with a shoulder diameter of

8 mm and a threaded pin with a diameter of 3 mm and a length of 1.45 mm. The effect of the tool geometry on the joint properties was not studied.

During studies on FSW components made of the heat-treatable 6061 and non-heat treatable 5086 alloys (Table 10), Ilagovan et al. [335] found that the use of a threaded tool pin profile provided a better flow of materials between the two alloys and the generation of defect-free stir zone. It also allowed for obtaining a higher hardness value of 83 HV in the stir zone and a higher TS of 169 MPa compared to the other two pin profiles.

During studies on the butt FSW joints of components made of dissimilar 2050/6061 alloys (Table 10), Reza-E-Rabby et al. [336] found that the joint quality, process parameters, and welding temperature depended on pin features. Pins with thread flats allowed for the production of quality welds in some cases.

The proper FSW joints of dissimilar 5083-O/6082-T6 alloys (Table 10) were studied by Donatus et al. [337], for which they used a tool with a diameter-to-length ratio of 1:0.8 with a 25 mm diameter scroll shoulder applicable at a tilt angle of 0°. The effect of the tool geometry on the joint properties was not studied.

The correct FSW joints of dissimilar cast Al-Si alloys A319/A413 (Table 10), studied by Karam et al. [338], were obtained using a tool with a shoulder diameter of 26 mm and a conical threaded pin with diameters varying from 10 to 6 mm and a length of 9 mm. The effect of the tool geometry on the joint properties was not examined.

The proper butt FSW joints of dissimilar 7075-O/6061-O and 7075-T6/6061-T6 alloys (Table 10), studied by Ipekoglu and Cam [339], were obtained using a tool with a concave shoulder diameter of 15 mm and an M4 threaded cylindrical pin with a diameter of 4 and a length of 3 mm. The effect of the tool geometry on the joint properties was not studied.

The correct FSW joints of dissimilar 6061-T6/7075-T6 alloys (Table 10), studied by Cole et al. [295], were obtained using a tool with a 4.4° concave shoulder with a diameter of 15 mm and a threaded, conical tapered pin with three flats with a diameter varying from 7.0 mm to 5.2 mm and a pin length of 4.7 mm. The effect of the tool geometry on the joint properties was not examined.

The proper lap FSW joints of dissimilar 2024-T3/7075-T6 alloys (Table 10), studied by Song et al. [340], were obtained using a tool with a 15 mm diameter concave shoulder and a 6 mm long threaded taper cylindrical pin with a top and bottom diameter of 4 mm and 6 mm, respectively. The effect of the tool geometry on the joint properties was not studied.

The sound butt FSW joints of dissimilar 2014-T6/6061-T6 alloys (Table 10), studied by Jonckheere et al. [344], were obtained using a tool with a 15 mm diameter scrolled shoulder and threaded pin with three flats with a diameter of 5 mm and length of 4.4 mm.

For welding, Palantivel et al. [343] utilized tools with a shoulder-to-workpiece interference surface with three concentric circular equally spaced slots of 2 mm in depth on all tools. The tools also had five pin configurations, namely straight square, tapered square, straight hexagon, straight octagon, and tapered octagon without draft. The most helpful was the straight square pin profiled tool.

The proper FSW joints of dissimilar A356/6061 alloys (Table 10), studied by Ghosh et al. [346], were obtained using a tool made of high-speed steel with a concave shoulder diameter of 15 mm and a cylindrical pin with a diameter of 5 mm and length of 2.6 mm. The effect of the tool geometry on the joint properties was not examined.

The correct FSW lap joints of 7075-T6/2198-T351 alloys (Table 10), studied by Velotti et al. [385], were obtained using a tool with a shoulder diameter of 15.5 mm and a conical pin with a maximum diameter of 4 mm and a length of 3.1 mm. The effect of the tool geometry on the joint properties was not studied.

Studying the FSW joints of plates made of dissimilar 2219-T87/5083-H321 alloys (Table 10), Koilray et al. [348] found the ratio between the tool shoulder diameter and the pin diameter affected joint soundness the most, while pin geometry also strongly influenced it. Welds were obtained using tools with a pin with a length of 5.7 mm and a diameter of

6 mm. The ratios between the tool shoulder diameter and the pin diameter were 1.5, 2, 2.5, and 3, increasing with the TRS and the WS.

The proper FSW joints of dissimilar cast and wrought 6061 alloys (Table 10), investigated by Dinaharan et al. [349], were obtained using a tool with a shoulder diameter of 19.2 mm and a hexagonal pin profile with a diameter of 6 mm and a length of 5.8 mm. The effect of the tool geometry on the joint properties was not studied.

Studying the FSW joints of components made of dissimilar 5083-H111/6351-T6 alloys (Table 10), Palanivel et al. [350] reported that the TRS and pin profile influenced the joint strength because of varying material flow, loss of cold work in the HAZ on the 5083 side, the dissolution and overaging of precipitates of the 6351 side, and the formation of macroscopic defects in the weld zone. Welds were obtained using a tool with a flat shoulder diameter of 18 mm, pins with a diameter of 6 mm and a length of 5.7 mm, and various profiles, including straight square, straight hexagon, straight octagon, tapered square, and tapered octagon. Square pins produced highly intense pulses, which lasted longer compared to hexagon and octagon pins, which caused severe and random layer-by-layer material movement.

The proper FSW joints of dissimilar 5052-H34/5023-T4 alloys, studied by Song et al. [125], were produced using a left-handed threaded tool with a shoulder diameter of 12 mm, and a pin with a diameter of 3.8 mm and a length of 1.45 mm. The effect of the tool geometry on the joint properties was not studied.

The correct FSW joints of dissimilar A356/6061 alloys (Table 10), studied by Ghosh et al. [347], were obtained using a tool with a concave shoulder diameter of ~15 mm and a cylindrical pin with a diameter of ~5 mm and a length of ~2.6 mm. The effect of the tool geometry on the joint properties was not examined.

The proper FSW joints of dissimilar 5052 and A5J32 alloys (Table 10), studied by Kim et al. [304], were produced using a tool with a shoulder diameter of 8 mm and a threaded cylindrical pin with a diameter of 3 mm and a length of 1.45 mm. The effect of the tool geometry on the joint properties was not studied.

The correct FSW butt joints of 7050-T7451/2024-T351 alloys, studied by Prime et al. [351], were obtained using a tool with a threaded pin. The effect of the tool geometry on the joint properties was not examined.

The sound FSW joints of dissimilar 5182-O, 5754-O, and 6022-T4 alloys (Table 10), studied by Miles et al. [398], were produced using a tool with a concave shoulder with a diameter of 10.2 mm and a cylindrical threaded pin with a diameter of 3.18 mm and a length of 1.95 mm. The effect of the tool geometry on the joint properties was not studied.

The proper butt FSW joints of 6061-Al used alone and with dissimilar 6061-T6/2024-T3 alloys (Table 10), studied by Ouyang and Kovacevic [399], were obtained using a tool with a threaded pin. The effect of the tool geometry on the joint properties was not examined.

The sound butt FSW joints of dissimilar 2024-T351/6056-T4 alloys (Table 10), investigated by Amancio-Filho et al. [300], were produced using a tool with a 5 mm diameter threaded cylindrical pin and a 15 mm concave shoulder. The effect of the tool geometry on the joint properties was not studied.

The correct FSW joints of cast A356/wrought 6061 alloys (Table 10), studied by Lee et al. [301], were obtained using a tool with a screw-like pin. The effect of the tool geometry on the joint properties was not studied.

The proper FSW joints of the 2017-T351 alloy, studied by Liu et al. [57], and the FSW joints of 1050-H24 alloy (Table 10), studied by Liu et al. [277], were produced using tools with a shoulder diameter of 15 mm and pins with a diameter of 5 mm and a length of 4.7 mm. The effect of the tool geometry on the joint properties was not examined.

The correct FSW joints of cast AlSi9Mg/2017A alloys (Table 10) studied by Mroczka [352] and the 2017A alloy studied by Mroczka et al. [353] were obtained using tools with a shoulder diameter of 22 mm, and cylindrical threaded pins with a diameter of 8 mm. The effect of the tool geometry on the joint properties was not studied.

The various FSW joints of a 6061-T6 alloy (Table 10), studied by Zhou et al. [421], were obtained using tools with three pin configurations, namely a quadrangular prism,

quadrangular frustum pyramid, and frustum one. When the shape of the pin was a quadrangular frustum pyramid, sound joints were obtained.

For the butt FSW joints of components made of 6063/5083 alloys (Table 10), Kumar and Kumar [401] reported that the joints of the higher TS, lower flexural strength, and lower impact strength with maximum hardness were fabricated using a tool with a cylindrical profile.

Sheikhi and dos Santos [420] studied the effect of welding parameters and welding tools on the weld quality and mechanical properties of FSW joints of tailor-welded blanks (TWBs) made of 6181-T4 alloy (Table 10) with a thickness combination of 1 to 2 mm. The peak temperature during welding slightly increased with an increase in the pin diameter. The effect of shoulder type on such peak temperature was negligible.

For the FSW joints of 2618-T87/5086-H321 alloys (Table 10), Sasikala et al. [402] reported that obtaining sound joints was affected by the ratio of tool contact area to pin diameter and to a lower extent by pin shape.

Investigating the FSW of 4 mm thick plates made of alloy 2024, Weglowski et al. [405] reported that the joints welded with different tools and under various conditions exhibited a characteristic shape of a nugget zone, heat-affected zone, and thermomechanically affected zone. The kind of tool had no effect on joint properties using the same welding parameters. The WE was 91.1% for the triflat tool with the flat bottom pin, while it was 95.7% for the triflute tool with the round bottom pin.

Nejad et al. [406] studied the structure and mechanical properties of FSW joints of plates made of 2024-T4 alloy (Table 10) with cylindrical outer and concave end surface shoulder and varied depth. Joints were obtained for two different tool designs, a threaded one and an unfeatured one. Obtaining a defect-free weld structure with both probe tools needed well different rotation and traverse speeds. Despite increasing the elongation and strength properties of joints obtained with the threaded tool, they exhibited elevated average hardness and less uniform properties over various welding zones in comparison to the joints prepared by the unfeatured tool.

Studying the FSW joints of components made of the 2014-T6 alloy (Table 10), Ugender et al. [409] reported that defect-free welds were obtained using a tapered cylindrical tool pin profile. The joints fabricated using a tapered cylindrical tool profile with a 3 mm radius of curvature exhibited better mechanical properties compared to the straight cylindrical tool profile. The WE was 69.5% for the taper cylindrical tool, while it was 63.4% for the straight cylindrical one.

Burek et al. [64] studied the tool wear effect on the quality of lap FSW joints of Al7075-T6 alloy sheets for two thicknesses (Table 10). They explained that due to the small diameter of the pin and the great forces occurring in the process, this element was most susceptible to tool wear. The welding process caused the tool to undergo friction wear, resulting in a lower tool dive depth in the jointed material. After creating 200m joints, the strength of the joints decreased, and the changes in the stirring conditions in the material became more intensive. The degradation of the tool led to a reduction in the characteristic sizes of the thermoplastic zone, which strongly affected the joint strength.

The FSW joints of 3003 alloy (Table 10), studied by Chekalil et al. [412], were obtained using a tool with a flat shoulder with a diameter of 19.5 mm and a conical pin with a diameter varying from 6.8 to 5 mm and a length of 1.7 mm. The effect of the tool geometry on the joint properties was not studied.

The FSW joints of 3003-H17 alloy (Table 10), studied by Xu [414], were obtained using a tool with a shoulder diameter of 16 mm, a conical threaded pin with a maximal diameter of 6 mm and a length of 4.7 mm, and a taper angle of 2.5°. Similar joints studied by Goyal et al. [415] were obtained using a tool with a concave shoulder with a diameter of 18 mm and a square pin with a diameter of 6 mm and a length of 4.75 mm. In both studies, the effect of the tool geometry on the joint properties was not examined.

Janeczek et al. [416] studied the effect of the shape of a tool and welding parameters on the quality of FSW joints of components made of 3004 alloys (Table 10). Various butt joints

were made with a self-developed tool with cylindrical threaded and tapered threaded pins. They found that the material outflow for the joints made with the cylindrical threaded pin was higher than that for the joints made with the tapered threaded pin. However, void-like defects appeared in the joints made with the tapered threaded tool. The use of the cylindrical tool provided higher mechanical properties, by about 37%, compared with those for the tapered threaded joint.

For the FSW joints of components made of the 1100 alloy (Table 10), Selvarajan and Balasubramanian [418] found that the optimized parameters of the welding process comprised a shoulder diameter of 14.8 mm, a pin diameter of 4.9 mm, and tool material hardness of 45.4 HRC.

The proper FSW joints of the 6061-T6 alloy (Table 10), studied by Juarez et al. [358], were obtained using a tool with a flat shoulder diameter of 25.4 mm, a composite pin with a hexagonal shank with a maximum diameter of 8 mm and a length of 9 mm, and a cylindrical collar with a diameter of 11 mm and a height of 3 mm made of H13 steel. The effect of the tool geometry on the joint properties was not studied.

Khan et al. [486] studied the influence of tool pin offset and tool plunge depth on the formation of defects such as tunnel (tunneling defect) and the kissing bond (KB) in 4.75 mm thick FSW plates made of AA5083-H116 and AA6063-T6 alloys. The joints were obtained using a tool made of tungsten carbide, with a tapered conical pin with a shoulder diameter of 20 mm, a pin length of 4.4 mm under a TRS of 450 rpm, a WS of 100 mm/min, a tilt angle of 2°, tool offset in range of 0.5–1.5 mm (from the AS to the RS), and a plunge depth of 0.3/0.4 mm. They found that the tunneling defects occurred at all offset (including zero offset) values in the stronger material (AS). The cross-section of the tunnel varied with the amount of offset. KBs appeared at the interface for all pin offset values except 0.5 mm in the softer material and high plunge depth, causing poor mechanical properties. Therefore, both the plunge depth and tool pin offset strongly affect the weld quality. The plunge depth provides heat generation and control over the forging action and welding thrust. Tool pin offset distributes the heat and mixes the joined alloys.

Table 10. Tools parameters used for the FSW process for joining various Al alloys.

Refs.	Alloy Combinations	Thick [mm]	Tool Profile		Shoulder Diameter [mm]	Pin Diameter/Length/Taper Angle [mm]/[mm]/[°]	Tool Material Hardness [HRC]
			Shoulder	Pin			
[310]	7075-T651/2024-T351	6	concave	conical threaded and with flute radius (0, 2, 3, 6, and ∞mm)	18	6/5.7	AISI H13
[61]	7075-T6/2024-T3 Lap joint: 7075-upper; 2024-lower	3	concentric-circles-flute	tapered	13.5	6/3,4,5/16.7	
[311]	7075-T651/5083-H111	6	spiral (convex scrolled)	triflute, tapered with a thread	24	10/5.8; 10 (6 on tip)/5.8	HS 6-5-2
[313]	6351-T6/5083-H111	6	partial impeller, full impeller, flat groove	cylindrical or conical with and without threads			
[46,314,363]	2017A-T451/7075-T651	6	scrolled	tapered threaded	24	6-4.5/5.7	HS 6-5-2

Table 10. Cont.

Refs.	Alloy Combinations	Thick [mm]	Tool Profile		Shoulder Diameter [mm]	Pin Diameter/Length/Taper Angle [mm]/[mm]/[°]	Tool Material Hardness [HRC]
			Shoulder	Pin			
[383]	5083-O/6063-T6	6			18	5	
[315]	5052/Al-Mg ₂ Si	8	concave	conical	18	6-4/5.7	H13 steel
[316]	2024-T351/6061-T6	6	conical with 4° cavity	square frustum	18	7-3.5/5.9	H13 steel
[317]	6061-T6/6351-T6	6.35	cylindrical scrolled	cylindrical	14	4/5	molybdenum M42/HRC 63
[319]	6061-T651/5A06-H112	5	cylindrical	conical	16	5-4.2/4.6	
[321]	2024-T3/6063-T6	8		conical triangular			D5 steel/60
[322]	2219-T87/2195-T8	7.2	spiral		16		H13 steel
[323]	2017A-T451/cast AlSi9Mg	6	scrolled	tapered threaded	24	6-4.5/5.7	HS 6-5-2
[324]	5083-H12/6061-T6	1.5			10-14	2-4	
[325]	6061-T6/7075-T6	5		conic threaded	15	5/4.7/5°	2344 steel/52
[326]	5083-H111/6082-T6	5		triangular, pentagonal	20	5-6	DIN EN 1.7131 steel
[144]	5083-H111/6351-T6	6		straight square	18	6/5.6	
[328]	2024-T6/7075-T6	5	flat	smooth cylindrical	15-16	3-8/4.7	high-carbon steel
[296,329]	Al-Mg-Si/Al-Zn-Mg	15			35	20-12/14.5	
[330]	2024-T3/6061-T6	4.8	concave	tapered threaded	20	4	
[331]	UFG 1050/6061-T6	2	concave	thread	12	4/1.8	steel
[485]	2024-T6/6061-T6	4	concentric circles	conical thread, deep groove thread, conical cam thread	18	7-5/3.7	
[333,334]	6061-T6/7050-T7451	5		cylindrical threaded	18	10	
[47]	6111-T4/5023-T4 Lap joint	1		threaded	8	3/1.45	
[335]	5086-O/6061-T6	6		straight cylindrical, threaded cylindrical, tapered cylindrical	18	6-5/5.7	steel HSS
[336]	2050-T4/6061-T651	20	single scroll	conical threaded	25.4	15.9/12.7/8°	steel H13
[337]	5083-O/6082-T6	NR(~7)	scroll	triflute	25	8/6.4	

Table 10. Cont.

Refs.	Alloy Combinations	Thick [mm]	Tool Profile		Shoulder Diameter [mm]	Pin Diameter/ Length/ Taper Angle [mm]/[mm]/ [°]	Tool Material Hardness [HRC]
			Shoulder	Pin			
[338]	A319/A413 cast	10		conical threaded	26	10–6/9	steel H13
[339]	7075-O/ 6061-O 7075-T6/ 6061-T6	3.17	concave	cylindrical threaded	15	4/3	steel H13/52
[295]	6061-T6/ 7075-T6	4.6	concave	conical threaded	15	7–5.2/4.7	steel H13
[340]	2024-T3/ 7075-T6 Lap joint	5	concave	cylindrical threaded	15	6–4/6	steel H13/52
[344]	2014-T6/ 6061-T6	4.7	scrolled	cylindrical threaded	15	5/4.4	
[343]	6351-T6/ 5083-H111	6	with concentric circular slots	straight square, tapered square, straight hexagon, straight octagon, tapered octagon without draft	18	6/5.6	high-carbon high-chromium steel
[300]	A356/6061-T6	3	concave	cylindrical	15	5/2.6	high-speed steel
[385]	2198-T351/7075-T6 Lap joint	3 and 1.9	flat	conical	15.5	max 4/3.1	
[348]	2219-T87/5083-H321	6		straight cylinder, tapered cylinder, cylindrical threaded tapered threaded	9, 12, 15, 18	6/5.7	steel H13/50–55 VHN
[349]	6061 cast/6061 rolled	6	with concentric circular slots	hexagonal	19.2	6/5.8	HCHCr steel/62
[350]	6351-T6/5083-H111	6	flat	straight square, straight hexagon, straight octagon, tapered square, tapered octagon	18	6/5.7	high-carbon high-chromium steel/63 HRC
[127]	5052-H34/ 5023-T4	~1.5		cylindrical threaded	12	3.8/1.45	
[347]	A356/6061-T6	3		cylindrical	15	5/2.6	HSS steel
[304]	5052-H34/ 5023-T4	1.5 & 1.6		cylindrical threaded	8	3/1.45	
[351]	7050-T7451/2024-T351	25.4		threaded			
[398]	5182-O/ 5754-O 5182-O/ 6022-T4 5754-O/ 6022-T4	~2	concave	cylindrical threaded	10.2	3.18/1.95	H13 steel

Table 10. Cont.

Refs.	Alloy Combinations	Thick [mm]	Tool Profile		Shoulder Diameter [mm]	Pin Diameter/ Length/ Taper Angle [mm]/[mm]/ [°]	Tool Material Hardness [HRC]
			Shoulder	Pin			
[399]	6061-T6/ 2024-T3	12.7		threaded			
[300]	2024-T351/6056-T4	4	concave	cylindrical threaded	15	5	
[301]	cast A356/ wrought 6061	4		screw-like			
[57]	2017-T351	5			15	6/4.7	
[277]	1050-H24	5			15	6/4.7	
[26]	2017A- T451/AlSi9Mg	6		cylindrical threaded	22	8	
[353]	2017A	6			25	8	
[421]	6061-T6	1	flat	quadrangular prism, quadrangular frustum pyramid, frustum	7	2–1.5/0.9	
[401]	6063/5083	6		straight cylindrical	20	5/5	steel HSS
[420]	6181-T4	1, 2	concave, scroll	cylindrical and threaded	13	5, 6.5, 7	
[402]	2618-T87/5086-H321	6		straight cylinder, tapered cylinder, cylindrical threaded tapered threaded	24, 30, 33, 36	12/5.7	steel H13
[405]	2024-T4	4		triflute with round bottom pin, triflat with round bottom pin, triflute with flat bottom pin, triflat with flat bottom pin			high-speed steel SW7M
[406]	2024-T4	3	cylindrical, concave	tapered unthreaded, tapered threaded	20	6/3	
[409]	2014-T6	5		straight cylindrical, tapered cylindrical	18	6/4.8	stainless steel
[487]	7075-T6	1, 0.8	concave	cylindrical threaded	10	4/1.2	Schilling 10S4ZGO/54–56
[412]	3003	2	flat	conical	19.5	6.8–5/1.7	X210Cr12 steel
[414]	3003-H17	5		conical threaded	16	6/4.7/2.5°	
[415]	3003	5	concave	square	18	6/4.75	steel H13/45
[416]	3004	5	flat	cylindrical threaded tapered threaded	21	10/4.5/10°	

Table 10. Cont.

Refs.	Alloy Combinations	Thick [mm]	Tool Profile		Shoulder Diameter [mm]	Pin Diameter/Length/Taper Angle [mm]/[mm]/[°]	Tool Material Hardness [HRC]
			Shoulder	Pin			
[418]	1100	5			7.86, 12, 15, 18, 22.13	2.6, 4, 5, 6, 7.37	high-carbon steel 33, 40, 45, 50, 56 HRC
[358]	6061-T6	9.5	flat	composite (hexagonal shank and a cylindrical collar)	25.4	11/9(3)	H13 steel
[359]	6061-T6/7075-T6	6	flat	cylindrical	21	6/6	

Table 11 presents the effect of tool geometry on the FSW joint properties (some information was published earlier in the excellent review by Di Bella et al. [257]).

Table 11. The effect of tool geometry on the FSW joint properties.

Ref.	Sheet Material Position [NA/AS/RS]	Pin Profile	Tilt Angle [°]	Rotational Speed [rpm]	Welding Speed [mm/min]	Axial Force [kN]	Main Results
[483]	(NA) 2017-T6/(NA) 6061-T6	Straight hexagonal Straight pentagonal Straight cylindrical Straight square Tapered square	0	1600	32	NA	Straight square tool pin profile produces better metallurgical and mechanical properties. The properties are inferior to those of other pin profiles, but it is preferred because the related joint is defect-free.
[480]	(NA) 2024-T365/(NA) 5083-H111	Square triangular stepped	-	900	16	-	Square pin produces a good metal flow and, consequently, a good stirring.
[473]	(NA) 2024-O/(NA) 6061-T6	Cylindrical stepped	NA	900; 1400; 1800	NA	NA	The cylindrical profile, at a TRS of 1400 rpm, promoted the material flow.
[310]	(NA) 2024-T351/(NA) 7075-T651	Flute radii: 0, 2, 3, 6, ∞ mm	NA	900	15	NA	A radius equal to that of the pin leads to the strongest joint.
[467]	(AS) 5052-H32/(RS) 6061-T6	Taper cylinder Threaded cylinder	NA	900	60	NA	The taper pin profile leads to a fine-grain microstructure.

Table 11. Cont.

Ref.	Sheet Material Position [NA/AS/RS]	Pin Profile	Tilt Angle [°]	Rotational Speed [rpm]	Welding Speed [mm/min]	Axial Force [kN]	Main Results
[471]	(NA) 5083-H111/(NA) 6061-T6	Straight square Threaded cylinder Tapered cylinder	NA	NA	NA	NA	A straight square profile shows better mechanical properties.
[465]	(NA) 5083-O/(NA) 6061-T6	Square cylinder Straight cylinder Tapered cylinder	1.11	1568	39.53	NA	Straight cylinder tool guarantees higher weld quality.
[313]	(NA) 5083/(NA) 6351	Partial impeller Full impeller flat groove	NA	NA	NA	NA	A full impeller generates enhanced material flow.
[484]	(NA) 5083/(NA) 7068	Straight cylindrical Taper cylindrical Triangular tool	NA	800; 1000; 1200; 1400	30; 40; 50; 60	3; 4; 5; 6	The triangular tool offers the maximum TS and microhardness of the investigation with the combination of the TRS of 1200 rpm, the WS of 30 mm/min, and the AF of 3 kN.
[311]	(RS) 5083-H111/(AS) 7075-T651	Triflute tapered with a thread	NA	140; 280; 355; 450; 560; 900	140	26.4	Triflute pin at the TRS of 280 rpm provided higher tensile properties and a defect-free joint with a wider stir zone.
[466]	(NA) 5083/(NA) 7075	Threaded straight cylindrical, Tapered cylindrical, Threaded tapered cylindrical	NA	600; 700; 800	40	NA	The highest TS and the defect-free joint were obtained by using the threaded tapered cylindrical pin tool at a TRS of 800 rpm.
[335]	(RS) 5086-O/(AS) 6061-T6	Straight cylindrical Threaded cylindrical Tapered cylindrical	1	1100	22	12	Threaded pin profile guarantees defect-free joints, finer and uniformly distributed precipitate formation, circular onion rings, and smaller grain.

Table 11. Cont.

Ref.	Sheet Material Position [NA/AS/RS]	Pin Profile	Tilt Angle [°]	Rotational Speed [rpm]	Welding Speed [mm/min]	Axial Force [kN]	Main Results
[476]	(AS) 6061-T6/(RS) 7075-T651	Cylindrical Cylindrical tapered Cylindrical threaded Trapezoidal tapered	NA	660; 900; 1200; 1700	36; 63; 98; 132	NA	Cylindrical threaded with three flat faces tool pin and cylindrical grooved tool pin—at intermediate tool rotation and feed rate—lead to good tensile and flexural strength.
[446]	(NA) 6061/(NA) 7075-T651 -	Square Cylindrical Triangle	2; 3; 4	NA	NA	NA	The square pin, with a 2° tilt angle, exhibits fine grains along the stir zone due to adequate heat generation. Triangular pin reveals granular grain structure.
[479]	(RS/AS) 6061/(AS/ RS) 7075	Straight cylinder Straight square Tapered hexagon	NA	950	60	NA	A straight cylinder provides smooth and perfect welding.
[326]	6082-T6/ 5083-H111						The pin shape highly affected the joint tensile properties and microstructure. The joint strengths obtained with the pentagonal-shaped pin were lower than those with triangular-shaped ones. The pin shape influenced each NZ profile containing onion rings.

Table 11. Cont.

Ref.	Sheet Material Position [NA/AS/RS]	Pin Profile	Tilt Angle [°]	Rotational Speed [rpm]	Welding Speed [mm/min]	Axial Force [kN]	Main Results
[355]	6351/5083-H111	Straight cylinder, threaded cylinder, square, tapered square, and tapered octagon without draft	NA	950	1.05	10	The D/d ratio was 3. The joint obtained using a tapered square tool pin provided the least TS. Using straight cylinder, threaded cylindrical, tapered square and tapered octagon tool pins such a strength varied insignificantly.
[328]	(AS) 2024-T6/(RS) 7075-T6	Smooth cylindrical		1200	12	8	The joint fabricated with a D/d ratio of 3 had better mechanical properties than the other joints.
[327]	2024-T6/6061-T6	Conical thread, deep groove thread, and conical cam thread	2.5	1000	500		The deep groove thread tool pin strongly drove the plastic metal downward. The conical cam thread tool pin provided the strongest stirring of materials and the best metal fluidity.

To summarize, it can be noticed that the pin length should be a little less than the plate thickness for the butt joint arrangement to prevent damage to the tool or the backing plate of the FSW machine used for the FSW process. Additionally, the tool pin profile and diameter, shoulder shape and diameter, the TRS, and the WS most significantly affect the FSW process, particularly in the case of dissimilar Al alloys. This agrees with observations from [364].

Similar to the findings of [257], for components made of Al alloys with thicknesses ranging from 3 to 8 mm, it was found that square pins provided intensive metal flow and, thus, good stirring compared to triangular or stepped ones. However, they are often affected by adhesion to the stirred material and can produce several defects. They cannot be used at higher TRSs, which promote the use of cylindrical or conical pins.

At intermediate TRSs and WSs, cylindrical threaded pins with three flat-face tool pins and cylindrical grooved tool pins are preferred due to providing good tensile and flexural strength. A tool shoulder with grooves or scrolls facilitates the material flow from the edge of the shoulder to the pin, thus limiting tool tilting, which prevents void or tunnel defects. However, there is a strong correlation between the TRS and WS and the tool tilt angle,

which should be optimized by also considering the thickness of Al alloy sheets and the tool material.

Microstructure Evolution

The typical microstructure of an FSW joint comprises three zones: the HAZ, TMAZ, and SZ [488]. The shapes of these zones are affected by the thermal and mechanical deformation induced by the tool during the welding process. The SZ exhibits fine-grain microstructures due to extensive grain refinement, while the TMAZ exhibits an elongated grain structure [489,490]. The welding parameters affect the microstructure evolution, due to the higher influence of the material movement or flow in joints between dissimilar Al alloys compared to joints between the same Al alloys. The appropriate selection of all process parameters leads to intensive material mixing on both the AS and the RS of the joint and thus a sound weld. Electron backscatter diffraction (EBSD)-based orientation maps for the 5083/2024 joint [491] revealed tilted and elongated grains in the TMAZ and refined grains in the SZ, which resulted from dynamic recrystallization. Grain boundary orientations also varied in all three zones. The SZ comprised a higher number of large ($>10^\circ$) angular grain boundaries, while more low-angular ($2\text{--}10^\circ$) grain boundaries were observed in the HAZ. The SZ also exhibited a more intense texture compared to other zones.

Studying the FSW joints of 7075-T651 and 2024-T351 alloys, Hasan et al. [310] found a difference in material flow and mixing related to the tool pin design. The grain size and shape of onion rings appearing in the nugget zone were affected by material placement and tool pin geometry. The mixing stir zone became more homogeneous when the flute radius reached that of the tool pin. Three different sublayers were observed in the weld nugget; two of them were close to each base welding material, and the other was a mix of both materials. The non-recrystallized heat-affected zone (HAZ) and thermomechanically affected zone (TMAZ) were similar in chemical composition to their corresponding BMs.

Ge et al. [61] reported that four typical zones, namely the BM, HAZ, TMAZ, and SZ, appeared in the lap weld's cross-section. The SZs presented a bowl-like shape due to the tool geometry effect and comprised nonuniform grain size along the joint thickness due to the differences in material flow and temperature during the welding process. Dynamic recrystallization also occurred, which was caused by the strong stirring of the tool and the elevated temperature effect. A material concentrated zone (MCZ) was also formed under the material plastic flow toward the tool zone during the welding process. Simultaneously, the lath-like microstructure of the BM transformed into fine equiaxed grains. The TMAZ comprised severely deformed and elongated grains, induced by the strong plastic deformation of SZ during FSW. The grains of 2024 alloys appeared in the upper sheet near the lap interface due to the laminar material flow. Also, microcracks occurred on the tip of the cold lap on the RS and gradually faded away in the SZ.

For the FSW joints of 7075-T651/5083-H111 alloys, Kalembe-Rec et al. [311] found that the weld centers comprised fine, equiaxed grains resulting from dynamic recrystallization. For a particular TRS, no differences in grain refinement were observed. The insufficient heat input had a negligible effect on grain size changes. However, the microstructure consisted of regions in the form of bands differing in grain size and chemical composition. The bands came from both base alloys: one formed by the 7075 alloy and the other by the 5083 alloy. The dominant region of the stir zone comprised elements from the alloy from the advancing side.

Studying post-weld heat-treated dissimilar FSW 7075 and 2024 joints, Safarballi et al. [312] reported that fracture existed at the interface between the TMAZ and the HAZ on the (RS) 7075 of the as-welded joint, while by applying post-weld heat treatment, fracture shifted toward the SZ of the welded joint. In post-weld heat-treated joints, the fracture surface was intergranular, while in the as-weld joint, the fracture surface was mostly transgranular. This was due to the dissolution and coarsening of precipitates within grains in post-weld heat-treated joints.

For the FSW sheets made of dissimilar 2017A-T451 and 7075-T651 alloys, Hamilton et al. [363] reported that due to the flow of surface material into the welded sheet thickness,

the weld nugget comprised alternating layers of 7075 and 2017A. Such layers exhibited distinctive precipitate distributions because of their unique temperature histories, which were affected by the material's initial position. Supersaturated surface material flew into the process zone and formed a core comprising GP zones reprecipitating upon cooling. The mid-plane and bottom-plane material flew toward the sheet surface and embraced the surface material core. Within this region, the weld temperatures exceeded the equilibrium θ phase in 2017A, reducing the hardness, and simultaneously dissolved the equilibrium η/T phase in the 7075, causing the reprecipitation of GP zones upon cooling and a hardness recovery.

During studies on the FSW joints of components made of dissimilar alloys 2017A-T451 and 7075-T651 Hamilton et al. [169] reported that the microstructures comprised many dislocations due to remnants from the extrusion process and post-solution treatment stretching. Due to the T6 temper, the 7075 base alloy contained a much higher number of second-phase particles than the 2017A alloy, which was in the T4 temper. The dislocation density and the average grain size in both base alloys extruded and stretched to the same degree under similar conditions. The microstructure of the weld nuggets was composed of interleaving bands of material from each alloy. The material from one side predominated on the other side of the nugget. On the RS of the nugget of the (AS) 2017A/(RS) 7075 weld, the number of second-phase particles in 7075 was much higher than that in 2017A, while the density of residual dislocations between the two alloys was comparable. In the TMAZ and HAZ, changes in the type and/or concentration of second-phase particles were observed, which were particularly distinct in the 2017A alloy placed on the advancing side during welding.

For the FSW joints of components made of Al-Mg₂Si and 5052 alloys, Huang et al. [315] identified three distinct zones in the FSW joint: the BM, the transitional zone, and the NZ. The primary Mg₂Si phases comprised coarse equiaxed crystals in the Al-Mg₂Si alloy in the BM. The NZ was a mixture rich in Al-Mg₂Si and 5052 alloys, forming a banded structure. In the NZ, equiaxed crystals transformed into polygonal particles with smaller sizes in the rich Al-Mg₂Si zone. Aside from the white Mg phase appearing in the rich 5052 zone near the interface, the 5052 alloy was unchanged.

Studying the FSW joints of components made of dissimilar 2024 and 6061 alloys, Moradi et al. [316] found grain refinement in the SZ via continuous and discontinuous recrystallization. The fraction of precipitates in the stirred zone of the retreating side exceeded that of the advancing side. The extent of continuous dynamic recrystallization in the TMAZ of the AS was less than that of the RS, and the recrystallized grains seldom occurred on the AS. The initial texture components became asymmetric after the FSW process. The overall texture intensity was weaker on the AS and stronger on the RS than in the starting materials. Discontinuous static recrystallization and/or meta-dynamic recrystallization occurred on the AS.

For the double-sided FSW joints of dissimilar 6082-T6/7075-T6 alloys, Azeez and Akinlabi [318] reported that the microstructure deviated from the conventional trend. The weld nugget exhibited no onion ring with a long flow arm. The wormhole defect occurred at the HAZ of the 6082-T6 alloy. The small abnormalities at the retreating side were caused by the preheating of the plates during the initial welding process.

Studying the single-sided FSW joints of components made of dissimilar 6082-T6 and 7075-T6 alloys, Azeez et al. [362] reported that the equiaxed grain structures resulted from the dynamic recrystallization mechanism at the NZ. Some microstructure imperfection occurred at the NZ when 6082 Al plates were clamped on the RS of the backing plate. However, deviation in the positioning of the Al plates prevented the fabrication of good bonding and quality welds despite the material flow and mixing occurrence.

For the FSW joints of dissimilar 6061-T651 and 5A06-H112 alloys, Peng et al. [319] noticed that the grain structure evolution in the stir zone was dominated by continuous dynamic recrystallization. The grain size in the HAZ and TMAZ was refined. Fractures in all tensile specimens were of a ductile nature due to the presence of dimples. The enhancement of heat input enlarged the size of the HAZ and reduced the slant angle of the

HAZ, leading to a decrease in the fracture angle and changing the dimples from inclined ones to normal ones. Shear stress formed shallow and inclined dimples, while equiaxed and normal dimples resulted from normal stress.

The FSW joints of dissimilar 2024-T3 and 6063-T6 alloys, studied by Sarsilmaz [321], comprised several weld zones, including the BM, the SZ, the TMAZ, and the HAZ formed in close relation to plastic flow and frictional heat generation during the welding process. Such joints were sound without any microcracks, microvoids, and unbounded regions in the welded interface. There were different morphologies of the microstructure at the interface zone of the joint. All welds exhibited the formation of the elliptical onion structure in the weld center. The SZ also included onion rings where the tool pin contacted the welded parts. Onion ring patterns exhibited lamellar-like structures of two stacked materials. Under a low WS and a high TRS, when higher frictional heat was generated, the generated weld nugget was wider than that under other parameters. The higher temperature and severe forging deformation resulted in grains smaller than those of the BM. The SZ had a fine equiaxed grain structure. Under a low TRS and WS, a clear vase-like boundary line appeared between the TMAZ and the SZ due to the high deformation and frictional heat between the weldment and the tool pin.

Studying the FSW joints of components made of 2219-T87 and 2195-T8 dissimilar alloys, No et al. [322] found that the microstructure of the weld joint underwent dynamic recrystallization due to high deformation and frictional heat. During studies on the FSW joints of components made of dissimilar Al alloys, namely wrought 2017A and cast AlSi9Mg, Kopyscianski [323] reported that the weld microstructure comprised alternating bands of the welded alloys. The AlSi9Mg alloy on the advancing side dominated the weld center. The grain size within the bands was close in both alloys. The nugget side comprised a high density of the bands of the 2017A alloy.

For the FSW joints of the 6061–7075 alloy, Bijanrostami et al. [325] found that under high heat input conditions, including high rotation and low WSs, large grains and smaller dislocation densities appeared in the SZ. Contrarily, under low heat input conditions, various defects developed.

Studying the effect of the TRS-to-WS ratio (v ratio) on the strength of the FSW joints of dissimilar 6082-T6 and 5083-H111 alloys, Kasman et al. [326] found that small cavities and tunnel-type defects occurred at the nugget zone, the profile of which contained various onion rings.

According to Palanivel et al. [422], FSW joints can comprise defects such as pinholes, tunnel defects, piping defects, kissing bonds, cracks, etc., which are caused by the improper flow of metal and insufficient consolidation of the metal in the weld zone.

For the FSW joints of components made of 5052- H32 to 6061-T6 blanks, Doley and Kore [327] observed dynamic recrystallization and finer grain size with uniform mixing at the center of SZ. Intermetallic compounds were also formed during FSW.

For the FSW joints of components made of the dissimilar 2024-T6 and 7075-T6 alloys, Saravanan et al. [328] found that the joint fabricated under a D/d ratio equal to 3 provided a fine recrystallized structure in the SZ, and the grain size was smaller than the BM grain size due to a smaller shoulder diameter.

Studying the FSW joints of sheets made of dissimilar Al-Mg-Si/Al-Zn-Mg alloys, Yan et al. [329] found that different joint cross-sections were obtained for different sheet configurations. Coarser β' phases occurred at the HAZ of the AlMgSi alloy side.

Yan et al. [329] reported that for Al-Zn-Mg AS joints, precipitated phases were the AlFeMnSi or AlMnCrSi phases, and the β' phase had sizes of about 0.5–0.8 μm . For Al-Mg-Si AS joints, similar precipitated phases occurred, with a smaller β' phase with sizes of about 0.3–0.5 μm . The quantity of the β' phase on the Al-Mg-Si AS joints was more than that on the Al-Zn-Mg AS joints. Second-phase particles at the joint fracture region were characterized by the submicron β' phase. For the Al-Zn-Mg AS joint, the β' phases were more dispersed, which was beneficial to the bridging effect.

The FSW joints of dissimilar 2024-T3 and 6061-T6 alloys, studied by Zapata et al. [330], exhibited various regions, including the TMAZ and HAZ, with similar shapes, locations, and sizes in all the samples. All sample cross-sections presented a ring flux pattern in the nugget region, indicating the vertical movement of the material.

Studying the butt FSW joints of 2 mm thick plates, including one rolled from ultrafine-grained UFGed 1050 Al alloy and the other made of the 6061-T6 alloy, Sun et al. [331] found that in the stir zone, the initial nanosized lamellar structure of the UFGed 1050 Al alloy plate took the form of an equiaxial grain one, with a larger average grain size caused by dynamic recrystallization and subsequent grain growth. Simultaneously, an equiaxial grain structure, with a significantly smaller grain size occurred in the 6061 alloy plates, together with the coarsening of the precipitates.

For the FSW joints of the 2024-T6 alloy, Sun et al. [485] found that the metal in the weld nugget zone (WNZ) came from the BM of the advancing side when the thread was the driving force of the downward movement of the FSW plastic metal. All joints formed a particularly good union, with an onion ring pattern appearing in the cross-section. The minimum grain size of the WNZ obtained with the conical cam thread stirring head was 7~12 μm . FSW usually allows for the elimination of porosity, small distortion, and so on [492,493].

During studies on the butt FSW joints of components made of dissimilar 6061 and 7050 alloys, Rodriguez et al. [334] found in the joint microstructure, there were distinct lamellar bands and various degrees of intermixing, which were affected by the TRS.

Studying the lap FSW joints of plates made of dissimilar 6111-T4 and 5023-T4 alloys, Yoon et al. [47] found that the threaded probe well correlated to the onion ring structure formed as soon as it touched the probe. The remnant of the original interface between the top and bottom plates after the welding process and asymmetrical flow around the rotating tool well correlated to the formation of void defects under low heat input conditions.

During studies on the FSW components of the heat-treatable 6061 and non-heat-treatable 5086 alloys, Ilagovan et al. [335] found that the use of threaded tool pin profiles provided better flow of materials between the two alloys and the generation of defect-free stir zone. Such a tool provided the formation of finer and uniformly distributed precipitates, circular onion rings, and smaller grains compared to the tapered pin profiled tool.

For the butt FSW joints of components made of dissimilar 2050 and 6061 alloys, Reza-E-Rabby et al. [336] found that the stir zone comprised bands of mixed and unmixed material, with the degree of material intermixing increasing with the increase in the TRS. Under monotonic tensile loading, welds failed via the heat-affected zone on the 6061 alloy side of the weld. For a low TRS, failure occurred in the stir zone due to poor material intermixing.

Studying the anodizing behavior of the FSW joints of dissimilar 5083-O and 6082-T6 alloys in 4M H_2SO_4 solution, Donatus et al. [337] found that the 5083-O rich zones were more oxidized during anodizing compared with the 6082-T6 rich zones. The nugget and the thermomechanically affected regions of the individual basic alloys exhibited a decrease in porous anodic oxide thicknesses. The sputtering deposition of pure Al on the weld, prior to anodizing, reduced the variations in the oxide thicknesses across the weld. Such a method prevented the boundary dissolution related to the activity of the Mg_2Si phase, which often occurs after anodizing dissimilar alloy welds.

Investigating the FSW joints of plates made of dissimilar cast Al-Si alloys A319 and A413, Karam et al. [338] found that the joints comprised Si particles and α -Al grains. At the center of the stirred zone, the Si particles could be more uniformly distributed than in the other zones.

For the butt FSW joints of dissimilar 7075-O/6061-O and 7075-T6/6061-T6 alloys, Ipekoglu and Cam [339] found that the as-welded 1500/400 O joint exhibited no welding defect except its root region, while some weld defects appeared in such a joint after post-weld heat treatment (PWHT). The joint areas of the dissimilar T6 joints obtained in both the as-welded and post-weld heat-treated conditions exhibited no weld defects. The dynamically recrystallized zones (DXZs) of all the as-welded joints both in the O and T6

temper conditions comprised a layered (banded) structure formed due to the mixing of two BMs, known as the intercalation of the BMs. The microstructure of the DXZs was dominated by the alloy located on the AS. The typical orientation of the grains in the TMAZ was strongly affected by the material flow resulting from the action of the stirring tool. PWHT only had a slight effect on the shape of the grains in the TMAZ. PWHT also caused the formation of abnormal grain growth AGG, both in the O and T6 joints. The AGG formation occurred all over the cross-section in the O joints, whereas in the shoulder regions, it occurred in the T6 joints.

Studying the lap FSW joints of dissimilar 2024-T3 and 7075-T6 alloys, Song et al. [340] found that the welded joints comprised four typical zones, namely the BM, the HAZ, the TMAZ, and the SZ. The grain structure in the HAZ of the upper 2024 sheet was like that of the BM. The TMAZ microstructure comprised severely deformed and elongated grains resulting from the drastic plastic deformation of the SZ during FSW. In the SZ, the microstructure included dynamically recrystallized fine equiaxed grains resulting from the drastic deformation induced by sufficient stirring during welding. Grains in the upper SZ were coarser than those in the bottom SZ because the former had more time to develop as a result of the higher temperature compared to those in the bottom SZ.

During studies on the FSW joints of components made of dissimilar 5083-H111 and 6351-T6 alloys, Palanivel et al. [342,350] reported that the weld zone comprised three types of microstructures, namely the unmixed region, mechanically mixed region, and mixed flow region.

Studying the FSW joints of components made of dissimilar A356 and 6061 alloys, Ghosh et al. [346] reported that the microstructure of WN had uniform dispersion of Si-rich particles and fine grain size in the 6061 alloy, and the second phase disappeared in the 6061 alloy.

For the FSW lap joints of 7075-T6 and 2198-T351, Velotti et al. [385] noticed that the hook defect comprising an S-shaped separation line between the two materials joined, which is typical for such joining technique in this specific configuration, is not fully avoidable, as the stirring action caused by the tool motion cannot completely mix the two materials initially stacked. Such a defect caused a preferential path for crack growth and propagation as well as localized corrosion, thus affecting the joint behavior. The kissing bonds resulted from inadequate material mixing and stirring that occurred in the core of the nugget zone and the radii between the skin and the stringer. Both alloys exhibited microstructures with round-shaped equiaxed grains. The average grain size for the 2198 alloy was about 30% of the one in the 7075 alloy.

Investigating the FSW joints of plates made of dissimilar Al–Cu alloy 2219-T87 and Al–Mg alloy, 5083-H321, Koilray et al. [348] found the material placed on the advancing side dominated the nugget region. The welds comprised the BM, the SZ or the NZ, the TMAZ, and the HAZ. The BM contained many undissolved second-phase intermetallic particles. The second-phase particles in alloy 2219 comprised Al_2Cu (θ) eutectic particles, while the 5083 alloy included iron/manganese aluminides. Compared to the 2219 alloy, 5083 comprised fewer and finer second-phase particles. The TMAZ on the advancing side exhibited highly deformed grains, with discernible SZ/TMAZ and TMAZ/HAZ boundaries. However, on the retreating side, these interfaces were diffused, especially the latter. In the HAZ, on either side of the weld nugget, the grain structure exhibited no noticeable changes compared to the respective BMs.

Studying the FSW dissimilar cast and wrought 6061 alloys, Dinaharan et al. [303] found that the microstructure of dissimilar joints comprised four zones: the BM, the HAZ, the TMAZ, and the WZ. The weld zone encompassed unmixed and mechanically mixed regions. The unmixed region consisted of microstructures of cast and wrought 6061 alloys. The mechanically mixed region occurred near the zigzag line containing the microstructure of both Al alloys. Some degree of penetration of one alloy into the other occurred. The plasticized dissimilar alloys were mechanically coupled in the mechanically mixed region.

After dynamic recrystallization that occurred during FSW, both materials exhibited finer grain structure than before FSW.

For the FSW joints of components made of dissimilar 5052-H34 and 5023-T4 alloys, Song et al. [125] noticed that in the same manner as constitutional liquation, at a high heating rate, the main liquation-inducing precipitates were not dissolved in the matrix and reacted with Al to form the partially melted zone (PMZ), after which liquation cracking occurred where strain was applied to the PMZ. The solid-solution-treated 5023 alloy comprised many precipitates in the matrix, including Mg_2Si , Al_6CuMg_4 , and $Al_6(CuFe)$. Al_6CuMg_4 formed a stable phase at room temperature and reacted with the Al matrix at around 470 °C. The main liquation-inducing precipitate was Al_6CuMg_4 , which formed the PMZ (constitutional liquation) at around 480 °C during the FSW process.

Studying the FSW joints of components made of dissimilar A356 and 6061 alloys, Ghosh et al. [347] reported that the structure of joints exhibited recovery–recrystallization in the stirring zone and breaking of a coarse eutectic network of Al–Si. The dispersion of fine Si-rich particles, the refinement of the 6061 alloy's grain size, low residual stress levels, and high defect density within the weld nugget facilitated an increase in bond strength. Reducing the tool's rotational and traversing speed increased the domination of such phenomena.

Studying the FSW joints of dissimilar 5052/A5J32 alloys, Kim et al. [304] reported that the weld nugget was formed according to the arrangement of the materials. The softened material moving from the AS toward the RS caused the formation of an empty region with the shape of the tool pin. The material on the RS filled most of the upper half of the empty region. When the A5J32 alloy was fixed on the RS, a high amount of the BM on the retreating side A5J32 was stirred toward the (AS) 5052 alloy, as the rigid material A5J32 was easily pushed out from the soft material, i.e., the 5052 alloy, and the two BMs were stirred in a zigzag shape. When the 5052 alloy was fixed on the RS, the flow of 5052 (retreating side) was limited by the more rigid material on the (AS) A5J32. The softened A5J32 accumulated unnaturally. Under conditions with a lower heat input, such as at a TRS of 1000 rpm and a WS of 400 mm/min, some welding defects occurred. Under opposite conditions, defect-free welds were obtained.

Studying the FSW butt joints of 7050-T7451/2024-T351 alloys, Prime et al. [351] noticed that the stirred zone, i.e., the weld nugget or dynamically recrystallized zone, comprised fine equiaxed grains. The nugget exhibited an onion ring structure. On both sides of the SZ, there were TMAZs comprising highly deformed grains from the stirring action. The TMAZ was more uniform on the advancing side and more diffuse on the retreating side. The heat-affected zones extended out of the TMAZs on both sides.

Miles et al. [398] reported the occurrence of failures in the HAZ of the 6022 alloy or in the NZ itself for the welded joints of components made of dissimilar 5182/6022 and 5754/6022 alloys. The 5182/5754 alloy pair was softening-free, as such alloys were in the annealed condition, while softening occurred in the 6022 side of 5182/6022 and 5754/6022 alloy pairs.

Ouyang and Kovacevic [399] studied the material flow and microstructural evolution in welded joints of components with one made of the 6061 alloy alone and the second using a combination of dissimilar 6061-T6 and 2024-T3 alloys both of 12.7 mm in thickness, obtained via FSW under different welding conditions. They found that plastic deformation, flow, and mechanical mixing of the material were characterized by asymmetry characteristics at both sides of the same and dissimilar welds. The microstructure in dissimilar 6061/2024 alloy welds highly differed from that in the case of the 6061 alloy used by itself. Vortex-like structures with concentric flow lines characteristic of welds using the 6061 alloy by itself, and alternative lamellae with various alloy constituents in the welds of 6061/2024 alloys resulted from stirring by the threaded tool, in situ extrusion, and traverse motion along the welding direction. The NZ of dissimilar 6061/2024 welds comprised a mechanically mixed region with dispersed particles of different alloy constituents, a stirring-induced plastic flow region with alternative vortex-like lamellae of the two Al

alloys, and an unmixed region with fine equiaxed grains of the 6061 alloy. Within these regions, the material withstood an extremely high degree of plastic deformation due to the occurrence of dynamic recovery or recrystallization of the microstructure. The degree of material mixing, the thickness of the deformed Al alloy lamellae, and material flow patterns were affected by the related positions in the NZ and the processing parameters.

Studying the butt FSW joints of dissimilar 2024-T351/6056-T4 alloys, Amancio-Filho et al. [300] reported that the welds comprised four different regions: the BM, the HAZ, the TMAZ, and the SZ. The BM of the 2024-T351 alloy microstructure exhibited elongated grains in the rolling direction. This BM contained copper-rich particles, which were in the second-phase θ -CuAl₂. The BM of 6056-T4 alloy also revealed a microstructure with grains oriented in the rolling direction. This BM comprised two kinds of particles: the ones rich in Mg and Si, identified as the intermetallic β -Mg₂Si, and the other rich in Mn and Fe. The stirred zone of the joint exhibited a lamellar material flow pattern due to material mechanical mixing. The SZ revealed a dynamically recrystallized microstructure with refined grains. The TMAZ of the 6056-T4 alloy possessed an annealed structure. Changes in grain orientation started in the transition between the TMAZ and the SZ. The grains were rotated by tool action, and after reaching approximately 90° tilting, some degree of recrystallization occurred, represented by a smaller grain size.

Lee et al. [301] found that the microstructures of the A356/6061 joint exhibited mixed structures of two materials. The SZ exhibited an onion ring pattern like a lamellar structure. The microstructure of the SZ comprised the material fixed at the RS.

Studying the FSW joints of components made of dissimilar 7003/7046 alloys, Yang et al. [354] observed an obvious “S”-shaped dividing line in the weld nugget area of the 7003/7046 dissimilar alloy FSW joint. Both sides of the S line comprised fine equiaxed grains, with a size of about 5 μ m; the grain size in the HAZ was higher than that in the NZ, and the structure in the HAZ comprised recrystallized grains and recovered grains. The coarsening of subgrains reduced the grain size of the HAZ on the 7003 side, and the grain size of the HAZ on the 7046 side was coarsened.

For the FSW joints of dissimilar 2219/5083 alloys, Mastenaiah et al. [367] found that the NZ revealed a mixing pattern highly affected by the tool offset, the TRS, and the WS. The intimate mixing of dissimilar alloys occurred at higher TRSs and lower WSs.

Studying the FSW joints of dissimilar 2618-T87/5086-H321 alloys, Sasikala et al. [402] reported that the nugget region was dominated by material on the forward-moving side. The weld contained four microstructural zones: the BM, the SZ, the TMAZ, and the HAZ. Both BMs contained particles of a second-phase intermetallic nature. Iron/manganese aluminides appeared in the 5086 alloy's second-phase particles, while eutectic Al₂Cu particles were in the 2618 alloy. Particles in the 5086 alloy's second phase were smaller and finer than those in the 2618 alloy. The grain structure of the weld nugget was like that in the HAZ. The SZ/TMAZ and TMAZ/HAZ boundaries were clearly distinguishable on the forward-moving side of the TMAZ. The dispersion of them was higher on the RS.

For the single-sided butt FSW joints of 3003-O alloys, Aydin et al. [404] reported that the welds comprised four zones: the BM, the HAZ, the TMAZ, and the SZ. The BM microstructure revealed elongated grains resulting from the rolling operation. The SZ revealed a fine-grained equiaxial dynamic recrystallized microstructure. The grain size in the SZ was smaller than that of the BM. An enhancement in rotation speed and a decrease in WS reduced the grain size in the SZ due to the higher heat input in the dynamically recrystallized microstructure. The TMAZ microstructure exhibited a highly deformed structure near the SZ zone due to less heat and deformation occurring in the TMAZ compared to those in the SZ. After the TMAZ, the HAZ was exposed only to a thermal cycle, but the plastic deformation therein was insufficient to modify the initial grain structure. The transition zones from the SZ to the TMAZ of the joints also occurred. On the AS, a distinct boundary between the SZ and the TMAZ was observed, while the boundary between the SZ and the TMAZ on the RS was unclear. The region with Al₂O₃

particles, stretching from the top to bottom across the whole section of all 3003-O weld zones at the RS, contained kissing bond defects.

Aydin et al. [428] found that the BM microstructure comprised elongated grains from the rolling process. In the weld center, the NZ occurred, which revealed dynamically recrystallized grains. On the AS, the microstructure varied rapidly due to the higher speed of plastic material than on the RS, and a distinct boundary between the NZ and the TMAZ was observed. On the RS, microstructures from the NZ to the TMAZ varied more smoothly. In the TMAZ, the grain structure was deformed, but no recrystallization occurred. The microstructure in the HAZ, affected by heat but not deformation, was like that of the BM; the grains were slightly overgrown due to exposure to welding heat.

Studying the FSW of 4 mm thick plates made of the 2024 alloy, Weglowski et al. [405] reported that the joints exhibited a characteristic shape of a nugget zone, heat-affected zone, and thermomechanically affected zone.

For the FSW joints of the 2024-T4 alloy, Nejad et al. [406] reported that the best weld features, including the finest grain in the stir zone, the best visual quality, and smoothness, were obtained with a rotation speed of 500 rpm, a traverse speed of 55 mm/min, a plunge depth of 2.7 mm, and using a threaded tool, as well as with a rotation speed of 1300 rpm, a traverse speed of 115 mm/min, a plunge depth of 2.9 mm and using an unthreaded tool. The unthreaded tool provided a more uniform structure in terms of smoothness. The WE widely varied in range, from 35.6% to 95.7%.

Investigating the FSW joints of 8 mm thick plates made of the 2014-T6 Al alloy, Lin et al. [408] found that the different regions of the joint exhibited different microstructures, affected by different thermomechanical actions therein.

Liu et al. [494] reported that defects, including voids, unbonded interface, and incomplete refilling, appeared when using the 7075 alloy as the upper sheet. No defects occurred when using the 6061 alloy as the upper sheet. With the enhancement of the sleeve plunge depth, better material mixing was observed between the upper and lower sheets.

Studying the FSW joints of components made of the 2017A alloy, Mroczka et al. [353] reported that the weld nugget exhibited an average grain size of 5 μm , moderate density of dislocations, and the presence of nanometric precipitates located mostly in grain interiors. The NZ presented a ductile fracture with brittle precipitates in the lower part.

Investigating the FSW joints of components made of cast AlSi9Mg and 2017A alloys, Mroczka [352] found that welds comprised defects, despite the greater plasticity of the material occurring due to the increase in temperature. The constituent stable phases within the cast alloy exhibited considerable fragmentation to various degrees. The material above the weld nugget was unmixed and comprised non-welding microdefects. A metastable state of the 2017A alloy occurred within the weld nugget zone due to the natural aging.

Studying butt FSW joints of 6013 Al plates obtained via the pin offset technique, Kasman and Ozan [355] found kissing bonds in welds, originating from the broken oxide layers and particularly forming in the stir zone. The microstructure of joints comprised phases belonging to Mg_2Si , $\text{Al}_4\text{Cu}_2\text{Mg}_8\text{Si}_7$, and $\text{Al}(\text{MnFe})\text{Si}$.

Kasman and Yenier [365] reported that the microstructure of the two BMs comprised elongated grains in the rolling direction. The nugget zone included the fine equiaxed grains formed by the occurrence of dynamic recrystallization. The structure of grains in the TMAZ was deformed, elongated, and oriented to the rotation of the pin. The size and orientation of grains of the TMAZ differed from that of the NZ. Compared to the TMAZ structure, that of HAZ comprised grains overgrown and was like that of the BM.

Investigating butt FSW joints of components made of dissimilar 7020-T651 and 5083-H111 alloys, Torzewski et al. [17] found various shapes of the stir zone and defects caused by excess and insufficient heat input.

Studying the spot FSW joints of sheets made of 5454 alloys, Choi et al. [417] found that the enhancement of tool rotation speed changed the macrostructure of the friction-stir-spot-welded zone, especially the geometry of the welding interface. However, the change

in the dwell time at the plunge depth of the tool only slightly affected the microstructure of the welds.

Dong et al. [419] reported that the SZ comprised fine and equiaxed grains due to dynamic recrystallization. With the enhanced cooling rate, the microstructure of the UFSW joint was finer than that of air-cooling FSW, and the area of the HAZ and TMAZ in the UFSW joint became smaller. The precipitation evolution was strongly affected by the processing parameters of UFSW. In the 1000–120 samples, fine precipitates existed in the HAZ, TMAZ, and SZ.

Zhou et al. [421] reported that the pattern of the weld cross-section was a “flat T” shape, and no obvious “S curve” occurred in the nugget zone (NZ). The HAZ and TMAZ were also narrow. The nugget zone (NZ) comprised finer grains than those in other zones. A clear band line appeared between the NZ and the TMAZ, located between the NZ and the HAZ. There was no clear dividing line between the HAZ and the BM. No obvious “S curve” appeared in any of the joints.

Tra et al. [495] reported that in the case of the FSW process, fatigue crack propagation (FCP) rates depended on the propagating location, the test temperature, and the PWHT conditions.

Studying the FSW joints of sheets made of the 6013-T6 alloy, Kafali and Ay [496] reported that the microstructure of the welding zone comprised four subzones: the BM, the HAZ, the TMAZ, and the NZ. The parent material and the weld region contained homogeneous distributions of the fine and coarse Mg_2Si particles. A dynamically recrystallized grain structure appearing in the weld nugget exhibited a smaller grain size compared to the BM. Such dynamically recrystallized grains were equiaxed contrary to the elongated grains in the rolled BM. Fine equiaxed grains in the FSW region occurred due to dynamic recrystallization as a result of plastic deformation during the welding process.

For the butt FSW joints of sheets made of dissimilar 2014-T3/5059-H11 Al alloys, Saleh [497] found a fine-grain structure in the nugget zone due to recrystallization.

Studying the FSW joints of components made of 2219-T87/2219-T62 alloys, Venkateswarlu et al. [498] found that the microstructure of the 2219-T62 welds exhibited coarse grains formation in the thermomechanically affected zone and the heat-affected zone.

For the FSW joints of the 2014-T651 alloy, Kollapuri [499] reported that the HAZ comprised a larger grain size than the NZ.

Studying the FSW joints of components made of the 3003 alloy with different initial microstructures, Tan et al. [500] reported that the size of recrystallized grains and the number of second-phase particles in the weld nugget zone (WZN) decreased with a decrease in welding ambient temperature. At the same welding condition, both the size of recrystallized grains and the volume fraction of $(Fe,Mn)Al_6$ particles in the hot bands were below those in the annealed hot bands.

Studying the FSW joints of plates made of 7204-T4 alloys, Deng et al. [501] reported that the average grain size (AGS) and recrystallization fraction of the nugget zone (NZ) reached $4.7\ \mu m$ and 81.9% in the as-welded AW treatment, $4.8\ \mu m$ and 82.4% under the post-weld artificial aging (AA) treatment, and $5.9\ \mu m$ and 86.5% with the heat treatment of solid solution followed by artificial aging SAA, respectively. The grain structure of the NZ was slightly influenced by the AA treatment, and the AGS and recrystallization fraction of the NZ increased by 25.5% and 5.6% under the SAA treatment.

Zhao et al. [356] studied the influence of exchanging the AS and the RS materials on the microstructure, mechanical properties, and electrochemical corrosion resistance of the FSW joints of components made of dissimilar 6013-T4 and 7003 alloys. The joint with the 6013-T4 placed at the AS was called the A6R7 joint. Accordingly, A7R6 referred to the joint with the 7003 alloy placed at the AS. The authors reported that there were various joint cross-sections when exchanging the AS and the RS materials. The material on the AS was more deformed during the welding process. When the 6013 alloy was positioned on the AS, the plastic flow of the weld was more sufficient.

Studying the FSW joints of components made of dissimilar 2024-T3 and 2198-T3 alloys, Texier et al. [332] found banded macrostructures with heterogeneous mechanical properties in the shoulder-affected region. They were accompanied by pronounced texture regions. The banded macrostructures appeared in the nugget region.

For the FSW joints of the 6061-T6 alloy, Juarez et al. [358] noticed four characteristic zones of friction welding: the SZ, the TMAZ, the HAZ, and the BM. The fracture surfaces of tension specimens revealed the presence of microvoids in the fracture zones for three cases: BMW, HTBW, and HTAW. The fracture surface of the BM presented microholes of 6–8 μm in diameter. For the case of BMW and HTBW, the diameter of microholes was greater than the BM at 8–10 and 10–12 μm , respectively. This was due to the reduction and separation of nucleation sites, allowing them to grow at a larger size. For the HTAW case, the microholes had small and shallow sizes, due to the occurrence of numerous nucleation sites causing the merge of microholes, limiting growth at a larger size. Solubilized and partial aging heat treatments of 6061-T6 alloy initiated the formation and distribution of the precipitates in the material. The predominant precipitates for the BMW and HTBW cases were Al-Mg and Al-Si, respectively, while for the HTAW case, it was Fe-Mg₂Si.

Unfried-Silgado et al. [502] studied the influence of the shoulder geometry of the tool (flat and featured by concentric circles and by spirals) on the microstructure and mechanical properties of FSW joints of the AA1100 alloy obtained using a milling machine revolutionary under a pitch value (R) constant of 0.1 mm/rev. They reported that the featured shoulder tools strongly affected the thermal cycles, generating a plasticized wide region and the largest grain size in the stir zone when compared with the flat shoulder tool. The featured shoulder tools induced thermal cycles in the regions out of the stir zone, which were less severe than in flat shoulders. The surface area of the tested tools was 27% and 11% smaller in flat shoulders and featured shoulders, respectively.

Studying the butt FSW joints of dissimilar 6061-T6/7075-T6 alloys, Godhani et al. [359] noticed that the size of the grains varies in the different joint zones, including the NZ, the TMAZ, the HAZ, and the BM. The size of the grain deciding the strength was affected by the amount of heat input, the mixing of the materials, and the rate of cooling. Due to the high grain density of the 7075 alloy, its strength was higher than that of the 6061 alloy. The grain density in the nugget zone was the highest, and hence the welded specimen had higher strength than the BMs. Failure could occur from the advancing side of the joint as the density of the grain was less than in other locations.

Aval et al. [423] studied the effect of the tool on the mechanical properties and microstructural behavior of FSW 5 mm thick plates made of 5086-O and 6061-T6 alloys. They found that the tool with a concave shoulder and a conical probe with three grooves provided higher heat input and temperatures promoting more homogeneous stir zones compared to tools with flat shoulders and threadless or threaded cylindrical probes. The grain sizes of the SZ on the 6061 side were finer than those on the 5086 side, and reducing the weld pitch, i.e., the ratio of WS/TRS, induced coarser grain structures in the SZ. The material in the NZ was a mixture of the two alloys, with closer to Mg content in the 6061 region.

Studying the FSW joints of components made of 5052 and 6061 alloys obtained with various pin-eccentric stir tools, Chen et al. [360] found that the welding heat input caused both the coarsening of strengthening precipitates and dynamic recrystallization and softening of the nugget zone (NZ). The use of pin eccentricity promoted material flow in the NZ and the higher area of the “onion ring”. The average grain size and fraction of recrystallized grain in the NZ decreased with an increase in the pin eccentricity.

Guo et al. [503] studied the FSW joints of components made of dissimilar 6061/7075 alloys. They found that the material mixing was much better for the 6061 alloy on the AS, and multiple vortexes centers formed vertically in the nugget center. The onion ring comprised three distinct sublayers: the 6061 alloy sublayer, the 7075 alloy sublayer, and the mixed sublayer of the two alloys. The thicknesses of these onion ring sublayers were in the range of 30–100 μm . Both AA6061 and AA7075 alloys were dynamically recrystallized. The grain size significantly decreased with an increase in WS. The grain size of the 7075 alloy sublayer was much lower

than that of the AA6061 sublayer in the same weld. The fractured surfaces of tensile tested specimens exhibited many equiaxed dimples of various sizes. Shallower dimples occurred in the fractured surface of the joints obtained under lower heat input. Second-phase particles comprising incoherent β -Mg₂Si and various Al-Fe-Si intermetallics effectively provided nucleation sites for microvoids during the fracture process.

Sato et al. [504] investigated the mechanical and microstructural behavior of FS welded joints of 2024/7075 alloys. They found that the amount of heat generation highly influenced the material movement around the pin. The high heat input caused onion ring patterns in the SZ, while a low heat input clearly divided the SZ into 2024 and 7075 regions.

Da Silva et al. [505] investigated the FSW joints between components made of dissimilar 2024/7075 alloys. The maximum WE was about 96% and the welded specimens were fractured in the HAZ of the RS.

Studying the FSW joints between (AS) 5083-H321/(RS) 6061-T6 alloys obtained at a TRS of 1120 rpm, various WSs (i.e., 40, 63, 80, and 100 mm/min), and a tilt angle of 2.5°, and using an H13 steel tool comprising a shoulder diameter of 18 mm, a pin of 6 mm in diameter and 4.7 mm in length, with a cylindrical taper threaded profile, Devaiah et al. [429] reported that the optimal joint was obtained with a combination of a TRS of 1120 rpm and a WS of 80 mm/min, which provided adequate heat generation and proper material mixing in the weld zone. The latter resulted in the formation of finer grains due to dynamic recrystallization refining the grain structure inside the weld zone. Both tensile and impact specimens exhibited a ductile fibrous fracture at the weld zones, confirming good joint ductility and toughness characteristics. The WS highly affected the formation of the plastic flow region during FSW, determining the extent and quality of material mixing. With the lowest or highest WSs, the joints comprised no or a poorly formed mixed flow region.

The 2.5 mm thick plates made of 2219/7475 alloys, studied by Khan et al. [506], were subjected to FSW using a tool made of high-carbon steel and possessing a cylindrical threaded pin, under a rotating speed of 900 rpm and WS of 100 mm/min, obtaining grain size below 6 μ m.

Abidi et al. [507] studied the T-FSW joint of 2 mm thick 7075/2024 alloys with the 7075 alloy placed as the stringer and the 2024 alloy used as the skin, which were obtained using a tool made of high-chromium high-carbon steel with shoulder diameter in the range of 12–16 mm, a tapered cylindrical pin with length of 1.9 mm, and a diameter of 1.8 mm on the insertion side and 5.6 mm on the shoulder side, under a TRS in the range of 560–900 rpm, a WS range of 40–63 mm/min, and a tilt angle of 2 degrees. They found that the TMAZ was subjected to induced plastic deformation caused by the lesser heat input. This led to partial recrystallization, thus forming coarse grains.

The types of defects formed during the FSW process of Al alloys depend on process parameters [508].

The formation of microcracks, fragmental defects, kissing bonds, voids, and tunnels is highly affected by the WS and softer alloy placement on the AS. The influence of the WS, the tilt angle, and the offset location toward soft material is much less. Insufficient heat and the formation of an intermetallic phase facilitate the formation of this type of defect [509,510]. An uneven alloy flow facilitates the creation of fragmental defects [511]. Insufficient alloy flow and the eventually formed oxide layer favor the generation of kissing bonds [512,513]. Improper alloy mixing and pressure in the contact zone between the tool and welded components favor the creation of voids and tunnels [511,512,514,515].

The generation of pores and surface defects strongly depends on the TRS and WS, as well as on softer alloy placement on the AS, while it depends to a much lower extent on the tilt angle and offset location toward the soft material. Insufficient heat generation facilitates the formation of such defects [511,516,517].

Surface defect formation is facilitated by low heat generation and improper pressure in the contact zone between the tool and welded components [518].

The lack of penetration strongly depends on the WS, the offset location toward the soft alloy, and the placement of the latter on the AS. Such defects are often obtained using tools with a short pin length [511,512].

The hooking defects' formation is highly affected by the TRS, while it is affected to a much lower extent by the WS, the tilt angle, the offset location toward the soft alloy, and its placement on the AS. Such defects occur due to an insufficient setup in the case of the lap FSW joint [512,519,520].

The formation of flash defects highly depends on the TRS, the tilt angle, and softer alloy placement on the AS, while it depends to a much lower extent on the WS and the offset location toward the soft alloy. Such defects are favored by excessive heat generation and improper pressure in the contact zone between the tool and welded components [516].

Mechanical Properties

Hardness

The hardness of the FSW joint was strongly associated with the joint strength and its deformation behavior. The hardness distributions exhibited high asymmetry along the cross-section of dissimilar material joints due to the various microstructural zones (SZs), TMAZs, and HAZs resulting from the thermomechanical history during welding. As the maximum temperature occurred at the SZ, precipitates or strengthening particles dissolved partially or completely, thus reducing the hardness in the SZ. The lowest hardness values appeared in the HAZ due to the coarsening of precipitates or overaging. Thus, failures occurred most in the HAZ. The hardness values in the SZ were higher than those in the BM (sometimes exhibiting low strength values) due to the combined influence of grain refinement and the effect of both the BMs in the SZ. However, various initial conditions of heat-treatable alloy combinations could make such hardness distribution completely different [254].

Studying the FSW joints of components made of 2024-T351/5083-H112 alloys in one sample and 7075-T651/2024-T351 alloys in a second sample, Niu et al. [308] characterized joint hardening by the ratio of HV_f/HV_w, where HV_f and HV_w are the microhardness of the fractured and as-welded joints, respectively. This ratio was higher than that in the SZ, TMAZ, and HAZ, which is related to the strain-hardening behavior of the joints. The hardness distribution in dissimilar material joints was strongly affected by strain hardening and the fracture origin.

For the FSW joints of 7075-T651/2024-T351 alloys, Hasan et al. [310] found that the distribution of weld hardness determines the TS of the welding joint. The welding hardness drops in the HAZ of the softer material. The maximum reduction in weld hardness in the heat-affected zone was achieved with a tool pin with a flute of radius equal to that of the pin.

Ge et al. [61] reported that the 7075 BM exhibited higher hardness than the 2024 BM. The SZ of the 7075 upper sheet possessed much higher microhardness than the HAZ or the TMAZ of the 2024 lower sheet.

Lee et al. [301] reported that for dissimilarly formed A356/6061, the joint hardness of the SZ was less than that of the 6061 alloy but higher than that of the A356 Al alloy. The hardness of the SZ was higher in the case in which the 6061 alloy was fixed at the RS due to the dominant microstructure of the SZ.

Kalemba-Rec et al. [311] reported that for the (AS) 7075/(RS) 5083 alloy set and the welds obtained using a triflute pin, the profiles for all TRSs were close; however, under a TRS of 560 rpm, an abrupt hardness drop in the SZ occurred due to the presence of voids in the weld area. For the (AS) 5083/(RS) 7075 alloys set, the hardness profiles were different. Under a TRS of 280 rpm, the hardness profile was like that for the (AS) 7075/(RS) 5083 configuration. For other speeds, the hardness in the stir zone decreased to 80 HV characteristic of the 5083 BM bands appearing in the SZ. For both configurations, the maximum hardness in the stir zone was 150 HV remaining constant from the weld center up to approaching the 7075 alloy. Regardless of the alloy configuration, on the 5083 alloy

side, the hardness was about 80 HV, and the weld remained in a constant transverse condition. On the 7075 alloy side, the hardness decreased from 150 HV to 120 HV and then increased to 160 HV (a half-characteristic of a W shape). Hardness profiles for the case of a threaded taper tool were like those for the triflute pin, but values of hardness were higher. The maximum hardness in the weld center reached a value of 180 HV for the (AS) 7075/(RS) 5083 joints, while for the (AS) 5083/(RS) 7075 alloy set, it was about 160 HV.

Investigating the FSW joints of components made of Al-Mg₂Si/5052 alloys, Huang et al. [315] reported that the hardness gradually enhanced from the BMZ of the 5052 to the welded joint to the Al-Mg₂Si BMZ.

For the FSW joints of components made of dissimilar 2024/6061 alloys, Moradi et al. [316] found that the microhardness profile on the AS was almost identical, while it comprised three distinguishable regions on the RS.

Investigating the double-sided FSW joints of components made of 6082-T6/7075-T6 alloys, Azeez and Akinlabi [318] reported irregular profiling in the Vickers hardness distribution, contrary to the conventional 'W'-shape trend, due to the difference in the chemical composition of the alloys and the rate of precipitation. The microhardness evolution deviated from the conventional trend.

For the FSW joints of dissimilar 6061-T651/5A06-H112 alloys, Peng et al. [319] reported that the nanohardness for each zone varied according to relation the BM > the NZ > the HAZ for the 6061 side, indicating that the mechanical properties of 6061 were weakened after FSW. On the 5A06 side, the change in mechanical properties for each zone was small after FSW. The nanohardness in the NZ and TMAZ was slightly higher than that in the BM. The mechanical properties of 6061 were more vulnerable to heat input than those of 5A06.

Investigating the FSW joints of components made of 2219-T87 and 2195-T8 alloys, No et al. [322] found that the microhardness in the upper part of the stirring part exhibited even distribution. In the middle and lower parts, hardness on the AS with the 2195 alloy was clearly higher than that on the RS of the joint. Hardness increased with an increase in the TRS and WS.

During studies on the effect of shoulder-diameter-to-pin-diameter ratio on the microstructure and mechanical properties of FSW joints of dissimilar 2024-T6 and 7075-T6 alloys, Saravanan et al. [328] placed the 2024-T6 alloy on the AS and 7075-T6 on the RS. They reported that the joints fabricated with ratios of 2 and 2.5 fractured in the heat-affected zone (HAZ) of the advancing side, and the joints fabricated with ratios of 3, 3.5, and 4 fractured in the stir zone (SZ). For all D/d ratios, the minimum hardness was seen in the HAZ on the advancing side and was maximum in the SZ and again decreased in the HAZ on the retreating side.

Studying the butt FSW joints of ultrafine-grained UFGed 1050/6061-T6 alloys, Sun et al. [331] reported that the BM of both the UFGed 1050 and 6061-T6 alloys exhibited the highest microhardness value. For both materials, from the BM to the HAZ, microhardness decreased gradually. For the 6061-T6 alloy, this decrease was due to the intensive solid solution of precipitates and the simultaneous occurrence of the coarsening of particles resulting from the weld's thermal cycles. The stir zone also comprised some regions with a high hardness value like that of the BM, due to the significantly refined grain size. For the UFG 1050 alloy, the hardness decreased due to grain growth and dislocation density.

For the FSW joints of dissimilar 2024-T3/2198-T3 alloys, Texier et al. [332] found significant differences between hardness and local tensile properties.

During studies on the butt FSW joints of components made of dissimilar 6061/7050 alloys, Rodriguez et al. [334] found that due to the distinct mechanical properties of the two alloys, there was a consistent asymmetric microhardness distribution profile across the weld nugget, independent of the TRS.

Ghosh et al. [346] found that the microhardness profile was related to the welded joint's microstructure. Low hardness was observed in the A356 alloy at the RS. Enhancement in hardness near the weld line occurred due to the composite microstructure affected by

both alloys. A Further increase was observed at the AS due to the higher strength of the 6061 alloy with respect to the A356 alloy.

Studying the FSW joints of plates made of dissimilar 2219-T87/5083-H321 alloys, Koilray et al. [348] found the lowest hardness in the weldment in the heat-affected zone on the 5083 alloy.

Kim et al. [304] reported that the 5052 and A5J32 BMs had hardness values of 72 HV and 78 HV, respectively. The hardness in the welded zone of A5052 was lower compared to that of the BM 5052 due to the dissolution of second-phase particles and annealing during the welding progress. When 5052 was fixed on the RS, the hardness in the vicinity of the shoulder exceeded that of the BM 5052. The flow of the softened 5052 alloy on the RS was restricted by the material on the advancing side A5J32, causing the concentration of work hardening. The hardness values in the welded zone of A5J52 exceeded that of the BM A5J52_78HV, due to the interaction of the recrystallized fine-grain microstructure and the agglomeration of the precipitates. When 5052 was fixed on the RS, excessive agglomeration occurred in a narrow region, due to the restricted flow, and higher hardness was observed compared with the other region. Therefore, the hardness of A5J32 in the welded zone significantly exceeded that of the A5J32 Al alloy fixed on the RS.

For the FSW joints of sheets made of 6013-T6 alloy, Kafali and Ay [496] reported that the average hardness of the BM reached 130 HV, while for the weld nugget, it was 100 HV. The average hardness in the TMAZ was lower than in the weld nugget.

During studies on the butt FSW joints of plates made of dissimilar 2014-T6/6061-T6 alloys, Jonkheere et al. [344] found that the welds' hardness profiles were affected by the proportion of each alloy included in the stirred zone, due to the difference between the softening temperatures of both alloys. The 6061 alloy's HAZ was the weak link in all dissimilar welds. Alloy placement and the tool lateral shift affect the weld hardness as they influence the precipitate radius and volume fraction.

Investigating the butt-fessed joints of sheets made of dissimilar 2014-T3/5059-H11 alloys, Saleh [497] found that the TMAZs and HAZs of the 2014 alloy possessed the lowest hardness values. The hardness decreased through the weld zone compared to both BMs.

Studying the FSW joints of components made of the 2014-T6 alloy, Aydin et al. [428] found that the hardness in the softened weld region decreased with a decrease in the WS.

For FSW of 4 mm thick plates made of the 2024 alloy, Weglowski et al. [405] reported that the hardness profile of welds had a characteristic run, typical for FSW joints.

Studying the FSW joints of 6 mm thick plates made of 2024-T351 alloys, Milčić et al. [407] reported that the distribution and allocation of microhardness were affected by the level of temperature and plastic deformation, which were highest under the tool shoulder and around the pin.

Investigating the FSW joints of plates made of the 2024-T4 alloy, Nejad et al. [406] reported that the joints obtained with the threaded tool exhibited elevated average hardness over various welding zones in comparison to the joints prepared by the unfeatured tool.

For the FSW joints of components made of 2219-T87/2219-T62 alloys, Venkateswarlu et al. [498] found that the hardness distribution in the stir zone differed significantly for the two different heat-treatment material conditions in 2219-T62 vs. 2219-T82.

Studying the stress corrosion cracking (SCC) of FSW joints of the 2014-T651 alloy, Kollapuri [499] reported that, at 70% yield, the induced stress was lower, so the material failure was determined by its hardness.

For the FSW joints of 8 mm thick plates made of the 2014-T6 alloy, Lin et al. [408] found that the different regions of the joint exhibited different microhardness distributions, which were affected by different thermomechanical actions therein.

During studies on the FSW joints of components made of dissimilar 2017A-T451 and 7075-T651 alloys, Hamilton et al. [314] found that the positron lifetime profiles across the weld comprised many local maxima and minima on the advancing and retreating sides, corresponding to the hardness behavior. Such variations in positron lifetime and hardness away from the weld center were due to the temperature distribution in these areas

relative to the critical temperatures for secondary phase nucleation and/or dissolution in the two alloys.

Studying FSW sheets made of dissimilar alloys 2017A-T451 and 7075-T651 Hamilton et al. [363] reported that during the flow of surface material into the welded sheet thickness, mid-plane and bottom-plane material flew toward the sheet surface and embraced the surface material core. Within such region, the weld temperatures exceeded the equilibrium θ phase in 2017A, lowering the hardness, and simultaneously dissolved the equilibrium η /T phase in the 7075, causing the reprecipitation of GP zones upon cooling and a hardness recovery.

For the FSW sheets of dissimilar 2017A-T451/7075-T651 alloys, Hamilton et al. [46] found that near the weld center, process temperatures allowed the fully dissolving of the equilibrium η phase in 7075 and the partially dissolving of the equilibrium S phase in 2017A. Upon cooling hardness recovered for both alloys. Due to the more complete dissolution of the equilibrium phase in 7075, the hardness recovery skewed toward the AS or the RS of the weld of the 7075 workpiece.

During studies on FSW joints of components made of dissimilar wrought 2017A and cast AlSi9Mg alloys Kopyscianski [323] reported that the hardness of the BMs was 80 HV1 and 136HV1 for the AlSi9Mg and 2017A alloys, respectively. The local maximum on the AS was on the nugget side with a high density of the bands of the 2017A alloy.

Studying the FSW joints of components made of 2017A alloy, Mroczka et al. [353] reported that microhardness in the cross-section of the joints only slightly varied; however, after the artificial aging process hardness enhanced. The variation in hardness of the joint after the aging process pointed out post-process partial supersaturation in the material and higher precipitation hardening of the joint. For the FSW joints of components made of cast AlSi9Mg and 2017A alloys, Mroczka [352] reported that the hardness distribution within the weld nugget zone revealed a low strengthening of both cast and wrought alloys. A metastable state of the 2017A alloy occurred, although, the alloy hardness enhanced within the weld nugget zone due to the natural aging. The hardness of the heat-affected zone in such an alloy slightly changed also due to the natural aging.

For the stud joints of 2017 alloy obtained by the friction welding process, Morikawa et al. [521] reported that at the weld interface, an SZ was formed with a hardness close to that of the BMs, while the HAZ of the bar and the plate was softened.

Studying the FSW joints of 2024-T6 alloy, Sun et al. [485] reported that with the conical cam thread stirring head, the obtained hardness was lowest at the junction of the HAZ and the TMAZ. The hardness obtained with the conical cam thread at that point exceeded that of other stirring heads.

For the FSW joints of components made of 7003–7046 dissimilar alloys, Yang et al. [354] found that the hardness was much higher on the retreating side of the 7046 alloy than that on the advancing side of the 7003 Al-alloy, and the average hardness difference between the two sides was about 30HV. After artificial aging, the hardness enhanced significantly, while the hardness difference increased to about 50HV for the two sides.

During studies on the butt FSW joints of components made of dissimilar 7075-O/6061-O and 7075-T6/6061-T6 alloys, Ipekoglu and Cam [339] found that hardness enhanced in the joint area for the joints produced under the O-temper condition, whereas hardness loss occurred in the joint area of the joints formed under the T6-temper condition.

Studying the FSW joints of components made of dissimilar cast Al–Si alloys A319 and A413, Karam et al. [338] reported that the average hardness of the welded regions enhanced with an increase in the WS and/or a reduction in the TRS.

For the FSW joints of components made of dissimilar 6013-T4 and 7003 alloys, Zhao et al. [356] found that irrespective of the AS or the RS, the 6013-T4 side was the weak region in terms of hardness. The fracture position coincided with the minimum hardness position.

During studies on the FSW components of the heat-treatable 6061 and non-heat-treatable 5086 alloys, Ilagovan et al. [335] found that the use of a threaded tool pin profile allowed for obtaining higher hardness values of 83 HV in the stir zone compared to those

of the other two pin profiles. The enhanced hardness resulted from the formation of fine grains and intermetallics in the stir zone.

Yoon et al. [357] found that when the soft material was on the top, the softening material and the deformed surface height resulted from friction heat generation by the rotating shoulder. The more influencing deformed surface height was reduced with the enhancement of the revolutionary pitch. When the soft material was at the bottom, the movement of the unbonded line and hooking occurred, which resulted from the vertical flow of the rotating tool pin. The more influencing unbonded line appeared along the interface between two materials deformed toward the hard material.

Studying the spot FSW joints of sheets made of 5454 alloys, Choi et al. [417] reported that, in all cases, the average hardness in the friction-stir-spot-welded zone exceeded that of the BM.

Investigating the FSW joints of components made of 5052-H32 to 6061 T6 blanks, Doley and Kore [327] reported that microhardness values of the dissimilar welds were lower in the HAZs on both the sides of weld line, whereas the lowest one occurred in the HAZ of 5052.

Studying the FSW joints of components made of 1100 alloy, Selvarajan and Balasubramanian [418] reported a hardness value of 67 HV in the SZ of the FSW joints, which was obtained under the optimized welding parameters and a tool material hardness of 45.4 HRC.

For the butt FSW joints of components made of 6063/5083 alloys, Kumar and Kumar [401] reported that the joints with maximum hardness were fabricated at a TRS of 1000 rpm with a cylindrical profile. The hardness enhanced with a rise in the TRS.

Studying the FSW joints of 6061-T6 alloy, Juarez et al. [358] reported that the microhardness at the SZ was 85 HV for the BM welded without heat treatment (BMW), 109 HV for the material with heat treatment before welding (HTBW), and 134 HV for the material with heat treatment after welding (HTAW). For the case of HTAW, the microhardness exhibited the lowest dispersion of values between 124 HV and 148 HV along the four characteristic zones. The hardness of the BMW case was much lower than the BM due to the aging of the material and the thickening of the precipitates resulting from mechanical work and heat generation during welding. The hardness for the HTAW case exceeded that of the BM due to a uniform distribution of precipitates in the zone of agitation inside the welded zone, combined with a smaller size of precipitates.

Dixit [522] studied the effect of different pin profiles, including straight cylindrical, triangular, and square, on the microhardness of butt FSW joints of 4 mm thick strips made of AA1200 alloy. The joints were obtained with the help of a high-carbon high-chromium alloy tool with various pin profiles under two different TRSs. The hardness of the stir zone varied with position and ranged from 30 HV to 40 HV and was higher than that of the parent metal, which was equal to 32 HV. This was due to grain refinement affecting material strengthening and since the grain size in the friction stir zone was much finer than that of the parent metal, thus enhancing the hardness of FSZ. In addition, the small particles of intermetallic compounds also increased the hardness.

Attah et al. [523] studied the influence of an AISI H13 steel-tapered tool on the FSW joints of components made of dissimilar 7075-T651 and 1200-H19 alloys. They found that the hardness values were 50 and 175 HV for 1200-H19 and 7075-T651, respectively, under three WSs (i.e., 30, 60, and 90 mm/min) at a constant TRS of 1500 rpm and a tool tilt angle of 2°. The hardness enhanced with the WS, increasing from 81.99 to 98.5 HV as the WS increased from 30 to 60 mm/min, and it decreased to 77 HV at 90 mm/min. The hardness at a TRS of 1500 rpm and WS of 60 mm/min increased from 70.22 to 98.58 HV with an increase in the tilt angle from 1 to 2°, and a further increase from 2 to 3° reduced the hardness to 66 HV.

Studying the FSW of 5 mm thick plates made of dissimilar 5086-O/6061-T6 alloys, Aval et al. [423] found that the hardness profile on the 6061 side quickly decreased. Such

hardness variation was smoother for samples subjected to FSW using a tool with a concave shoulder and a conical probe.

For the FSW joints of components made of dissimilar 6061/7075 alloys, Guo et al. [503] found that all joints failed in the HAZ on the 6061 side, where minimum hardness was observed regardless of the relative materials' position or the welding process parameters.

Studying the FSW joints of 5 mm thick similar and dissimilar 7075-T651/2024-T351 alloys, Zhang et al. [361] found that the hardness increased and then decreased from the top to the bottom along the welding center thickness direction. The tensile fracture locations coincided with that of minimum hardness values at various TRSs.

Tensile strength and residual stresses

The joint strength increased with the rotation speed due to the increased material mixing effect [313,341,343,350]. The tool rotation speed increased plastic deformation, and the WS governed the thermal cycle, residual stresses, and the rate of production. The selection of an appropriate combination of such speeds strongly affects weld quality and joint strength.

Studying the butt FSW plates of 2219-T62 alloy, Xu et al. [424] found that the residual stress on the top surface reached about 171 MPa, while it was only 243 MPa in the weld with tunnel defects and a conventional "M" profile with tensile stress peaks in the HAZ zone. Those on the bottom surface exhibited an inverted "V" profile with tensile stress peaks of 99.4 MPa in the weld center.

Bijanrostami et al. [325] studied the 6061/7075 joint and found that the maximum joint strength was reached under a combination of a moderate TRS and a low WS. However, the maximum joint strength of an A356-6061 joint was reached under a low TRS and WS, as indicated by Ghosh et al. [346,347]. The fine grain size and distribution of Si particles and lower residual stresses in the SZ occurred under low rotation and WSs. Together with rotation and WSs, the effect of tool geometry like the pin profile or features [310,313,335,336,350], pin shapes [326,343], and shoulder-diameter-to-pin-diameter ratio [328,348] influenced joint strength. The pin profile or feature governed the material flow and mixing at the joint interface, whereas the pin shape influenced the SZ size and material movement, and the shoulder-to-pin diameter ratio affected frictional heat generation between the tool and the BM. The conical threaded pin was the best configuration for the 6061/5086 joint, as it provided uniformly distributed precipitates and facilitated the generation of onion rings resulting from appropriate material mixing in the SZ, as reported by Ilangoan et al. [335]. The TS of dissimilar FSW Al joints depended on the microstructure evolution during FSW, which in turn was influenced by the heat input controlled by the welding parameters.

Studying the FSW joints of components made of 2024-T351/5083-H112 alloys in one sample and 7075-T651/2024-T351 alloys in the second sample, Niu et al. [308] reported that the TS and elongation of FSW joints were much deteriorated in comparison to the weaker BM, especially for 2024-T351/5083-H112 joint.

For the FSW joints of 7075-T651 and 2024-T351 alloys, Hasan et al. [310] found that placing the softer 2024 alloy on the AS slightly enhanced the tensile properties of welding joints. The introduction of pin tool flute/flat improved the UTS and elongation of welds regardless of the fixed location of the BMs. When using a truncated threaded pin tool with a flute of radius equal to that of the pin, the TS of the weld reached the maximum value of 424 MPa, which represents an efficiency of about 94.3% with respect to the softer material.

Ge et al. [61] studied how EST affects the shear failure load of lap joints. Shear and tensile fracture modes can occur. Mode I was the shear fracture mode, in which failure occurred along the original lap interface of the two sheets. This mode occurred in lap joints when the mixing of materials between the upper and lower sheets hardly occurred, and the nature of the joining mechanism at the interface was close to diffusion bonding. It was combined with the alclad layer, thus having low strength.

The tensile fracture mode exhibited two different fracture paths [54] as follows:

- Mode II—wherein the crack initiated from the tip of the cold lap defect (CLD), propagated upward along the SZ/TMAZ interface, and finally fractured at the top surface of the upper sheet;
- Mode III—wherein the crack initiated from the tip of the hook defect (HD), propagated downward along the HAZ/TMAZ interface, and fractured at the bottom surface of the lower sheet. These two different fracture modes are strongly affected by the size and orientation of the HD or CLD. The cracks occurring in the HD and the CLD of the lap joint continued their propagation upwards or downwards when the lap joint underwent tensile stress during the tensile test.

Lee et al. [301] reported that for dissimilar A356/6061 joints, the strengths of the SZ of similar A356 FSW joints had a UTS of 185 MPa and a YS of 87 MPa, which exceeded those of A356 BM. A UTS of 192 MPa and YS of 105 MPa were found in the WZ for the A356 alloy fixed at the RS. The higher strength of the WZ was obtained when the 6061 alloy was fixed at the RS.

Studying the FSW joints of components made of 7075-T651/5083-H111 alloys, Kalemba-Rec et al. [311] reported that a defect-free joint with the highest TS of 371 MPa was obtained with the 5083 alloy on the AS, the 7075 alloy on the RS, at a TRS of 280 rpm, and using the triflute tool pin.

Investigating the FSW joints of components made of Al-Mg₂Si and 5052 alloys, Huang et al. [315] reported that the UTS and elongation of the welded joint were greater than those of the BM of Al-Mg₂Si, whereas they were lower than those of the 5052 base alloy. The WE exceeded 100% relative to the softer material and reached 61% relative to the 5052 alloy. The particle–matrix interfacial debonding fracture mechanism was observed.

Studying the FSW joints of dissimilar 6061-T651/5A06-H112 alloys, Peng et al. [319] noticed that, after welding, the YS of 6061 decreased by 50%, to about 115 MPa, and the UTS decreased from 277 MPa to about 190 MPa, mainly because the unstable work-hardened state of rolled 6061 was destroyed by elevated temperature generated in FSW. The WE reached 68.5% relative to the 6061 alloy and decreased from 70% to 68% with an increase in the ratio of rotation speed to the WS from 4 to 12 r/mm.

For the FSW joints of dissimilar 2024-T3/6063-T6 alloys, Sarsilmaz [321] found that under a TRS of 900 rpm and a WS of 200 mm/min with the highest TS of 348 MPa was obtained, which was 74% of the TS of the 2024 BM. The increase in the TS was 45% higher than that in the TS of the 6063 BM. All tensile failures occurred at the HAZ location, always on the 6063 side.

Investigating the FSW joints of components made of 2219-T87/2195-T8 dissimilar alloys, No et al. [322] found a lack of correlation between the TS and WS; however, the TS increased with an increase in the TRS up to 800 rpm.

During studies on the FSW joints of components made of dissimilar wrought 2017A/cast AlSi9Mg alloys, Kopyscianski et al. [323] reported that the TS was 132 MPa, while elongation was below 1%.

Studying the FSW joints of dissimilar 6082-T6/5083-H111 alloys, Kasman et al. [326] obtained the highest TS for the weld joint obtained using a triangular-shaped pin, and the UTS was 198.48 MPa. At a lower TRS and WS, for each tool pin shape, lower UTS values were recorded. The UTS increased with an increase in the TRS and WS while keeping their v ratio constant for the triangular-shaped pin. The WE varied from 55% to 68% depending on both the presence of defects in the weld joint and the strength of the BM.

Saravanan et al. [328] reported that the TS increased with an increase in the shoulder-diameter-to-pin-diameter ratio up to 3 and then decreased by a further increase in the ratio. The maximum TS was 356 MPa at a ratio of 3, while the lowest one of 316 MPa was recorded at a ratio of 4. The WE varied from 76% to 86%, depending on the mentioned ratio.

Studying the FSW joints of sheets made of dissimilar Al-Mg-Si/Al-Zn-Mg alloys, Yan et al. [296] found that the TSs of dissimilar Al-Mg-Si/Al-Zn-Mg joints using both configurations exceeded that of the Al-Mg-Si FSW joint.

According to Sun et al. [331], FSW joints produced at the revolutionary pitches of 1.25 and 1 mm/rev exhibited a lower TS and elongation than those obtained at smaller revolutionary pitches. Due to the insufficient mixing of the two materials in the stir zone and several microdefects at the 6061-T6 alloy zone, the strength of the joints was reduced. Decreasing the revolutionary pitch to 0.75 or 0.5 mm/rev enhanced the heat input, intensifying the plastic deformation and the mixing of the two materials in the SZ. This resulted in a more homogenous microstructure of the stir zone, thus increasing the TS; elongation increased to about 110 MPa and 13% for the case of 0.75 mm/rev and 110 MPa and 22.5% for the case of 0.5 mm/rev. The largest joint efficiency was 55% with respect to the UFG 1050 BM. Remarkably, high heat input in the joints produced at 0.5 mm/rev caused grain growth in both materials, again causing a small decrease in the TS compensated for by a much enhanced elongation.

For the butt FSW joints of components made of dissimilar 6061/7050 alloys, Rodriguez et al. [334] found that under monotonic tensile loading, joint strength enhanced with the rise in the TRS. The WE reached up to 62%.

During studies on the FSW components of the heat-treatable 6061 and non-heat-treatable 5086 alloys, Ilagovan et al. [335] found that the use of threaded tool pin profiles allowed for obtaining a higher TS of 169 MPa compared to those of the other two pin profiles. The reduced size of weaker regions, such as the TMAZ and HAZ, caused higher tensile properties. The WE varied from 50.4% to 67.6%.

Studying the FSW joints of components made of dissimilar cast Al–Si alloys A319 and A413, Karam et al. [338] found that the welded joints exhibited better tensile properties than the base alloys. The A413 base alloy exhibited a lower UTS and YS when compared with the A319 base alloy; thus, under a tensile load, the welded specimens fractured in the A413 alloy.

During studies on the butt FSW joints of components made of dissimilar 7075-O/6061-O and 7075-T6/6061-T6 alloys, Ipekoglu and Cam [339] found that the strength values of all the O-joint specimens were close to those of the 6061-O BM, and all the specimens failed in the 6061 BM away from the joint area. This was due to the shielding effect provided by the strength overmatching, which resulted from the grain refinement or the precipitation of strengthening particles in this zone during the FSW process of Al alloys in the O-temper condition, i.e., the softened state. The WE in the case of the initial O state was about 100%. After PWHT (T6 treatment), the highest WE of about 93% was observed for the 1000/150-PWHT specimens, and this was 87.5% in the case of 1500/400-PWHT specimens. In cases with the initial T6 state, the highest WE was about 80% for the 1000/150 specimens, and 67.8% for the 1500/400 ones. After PWHT, the WE was 89.1% for 1000/150-PWHT specimens and 90.8% for the 1500/400-PWHT ones.

During studies on the butt FSW joints of 4.76 mm thick sheets made of dissimilar 6061-T6 and 7075-T6 alloys, Cole et al. [295] found that weld tool offsets into the (RS) 7075 enhanced the TS of the dissimilar joint. Such an enhancement was facilitated by lower average weld temperatures with the increased amount of 7075 stirred into the nugget. The WE increased with a lower amount of power input to the weld, whereas the subsequent WE was highly affected by the alloy most sensitive to heat input and weld temperature.

Ghosh et al. [346] found that the tensile properties of welding nuggets (WNs) were highly dependent on their microstructure.

Kim et al. [304] reported that the TS had similar values, regardless of the arrangement of the materials. The welding defects occurring under welding conditions with a lower heat input did not affect the tensile properties. When A5J32 was fixed on the retreating side, the highest strength of the welded joints, equal to 224.1 MPa, was recorded under the conditions of a TRS of 1000 rpm and a WS of 300 mm/min.

Prime et al. [351] studied the FSW butt joints of components made of 7050-T7451/2024-T351 alloys. They found that the stresses in the test specimen removed from the parent welded plate reached values up to 32 MPa and had the “M” profile with tensile stress peaks in the heat-affected zone outside the weld. The peak residual stress values were below 20%

of the material YS. Such low stresses were achievable only by solid-state welding with less distortion, while for fusion welding, such a low value was hardly possible. The fatigue behavior is strongly affected by these low values of residual stresses. The peak tensile residual stresses occurred in the HAZ on both sides due to local frictional heating at the tool material interface. The tensile residual stress resulting from the hotter material was forced by the other material during welding.

Studying the butt FSW joints of dissimilar 2024-T351/6056-T4 alloys, Amancio-Filho [300] reported that the TS of the weld joint was up to 90% of the 6056-T4 alloy. Fractures occurred in the thermomechanically heat-affected zone of the alloy 6056-T4, where an annealed structure led to reduced microhardness. The drop in the TS and the associated increase in strain were observed in the regions where microhardness decreased. The obtained joint efficiency in terms of the UTS was 55.8% for the 2024-T351 alloy and 71.4% for the 6056-T4 alloy. However, the joint efficiency in terms of elongation at the rupture was poor (9%–14%).

Ivanov et al. [400] studied the FSW joints of rolled sheets made of 2024/5056 alloys, obtained for various thicknesses. For weld joints with a TS not less than 0.9, the welding process parameters were complexly affected by the TS of the BM.

Investigating the butt FSW joints of components made of 6063/5083 alloys, Kumar and Kumar [401] reported that the joints with a higher TS were fabricated at a TRS of 1000 rpm with a cylindrical profile. The TS enhanced with a rise in the TRS. The WE varied from 32.3% to 43% when TRS increased from 600 to 1000 rpm.

Studying the FSW joints of components made of dissimilar 5083-H111/6351-T6 alloys, Palanivel et al. [350] reported that the TRS and pin profile influenced the joint TS because of varying material flow, the loss of cold work in the HAZ of 5083, the dissolution and overaging of precipitates of 6351 and the formation of macroscopic defects in the weld zone.

Investigating the FSW dissimilar cast and wrought 6061 alloys, Dinaharan et al. [349] found that the joint exhibited the maximum TS when the cast Al alloy was positioned on the advancing side at all TRSs.

Studying the FSW joints of components made of Al-Mg₂Si and 5052 alloys, Huang et al. [315] found that the UTS and elongation of the welded joint were greater than those of the BM of the Al-Mg₂Si, whereas they were lower than those of the 5052 base alloy.

Saleh [497] studied the microstructure and mechanical properties of the butt FSW joints of sheets made of dissimilar 2014-T3/5059-H11 alloys obtained by bonding the two materials perpendicular to their rolling directions. They found that the UTS values of the dissimilar joint varied in range, from 54% to 66%, compared to those of the BM.

Sasikala et al. [402] examined the effect of the TRS and WS, pin geometry, and the D/d on the TS of the FSW joints of plates made of dissimilar 2618-T87/5086-H321 alloys. The HAZs with tensile failures appeared on the 5086 alloy side of the weldment.

Lin et al. [408] studied the FSW joints of 8 mm thick plates made of the 2014-T6 alloy. They found that the weld TS was affected by welding parameters. The maximum UTS of 360 MPa, equal to 78% of that of the BM, was recorded at a TRS of 400 rpm and a WS of 100 mm/min. The different regions of the joint exhibited different TSs depending on microstructure variation and microhardness distribution, which were affected by different thermomechanical actions therein.

Morikawa et al. [521] examined the strength of the stud joints of the 2017 alloy obtained by friction welding. They reported that the TS of joints enhanced with pressure and friction time, and the highest TS reached 275 MPa (63.1% joint efficiency for the bar BM). The fatigue strength of joints increased under a high TS.

Studying the FSW joints of 2024-T6 alloy, Sun et al. [485] found that the TS for all joints was more than 80% of the BM, and the maximum TS of the joint welded with the conical cam thread tool pin reached 364.27 MPa, which was 86.73% of the BM. The elongation after breakage reached 14.95%. All joints were tensile-fractured due to plastic fracture.

For the FSW joints of the 3003 alloy, Chekalil et al. [412] found that the tensile properties of joints remained good. The TS of the weld joint was up to 75% of that of the BM.

Kasman and Ozan [413] studied the influence of the welding process on the structural properties of the butt FSW joints of plates made of 3003-H24 alloy. They found that the highest UTS among all the welded joints, equal to 128 MPa, was obtained under 50 mm/min WS and 800 rpm TRS. The WE was remarkably close to 100%. The size of the defects was affected by the tensile properties of the welded joints.

Aydin et al. [403] studied the effect of welding parameters (rotation speed and WS) on the mechanical properties of the FSW joints of components made of 3003-H12 alloys. The tensile weld strength increased with an increase in the WS or a decrease in the rotation speed. The tensile fractures of the joints were in the BM under welding parameter combinations of 1070 rpm and 40 mm/min or 2140 rpm and 224 mm/min. The UTSs of the joints decreased linearly with an increase in the rotation speed at a constant WS, while such strength of the joints increased linearly with a rise in the WS at a constant rotation speed.

Goyal et al. [415] studied the effect of welding parameters on the UTS of FSW joints made of the 3003 alloy. The best UTS equal to 127.2 MPa was obtained for process parameters including a WS of 74.64 mm/min, a TRS of 971.77 rpm, and a tool tilt angle of 1.52. The WE reached up to 89.4%.

Deng et al. [501] studied the effect of post-weld heat treatment on the microstructure and mechanical properties of the FSW joints of plates made of 7204-T4 alloys. They reported that the UTS of the FSW joints were 296.6, 318.2, and 357.4 MPa under the heat treatments of AW, AA, and SAA, respectively.

Yang et al. [354] studied the influence of post-weld artificial aging on the microstructure and mechanical properties of FSW joints of components made of 7003–7046 dissimilar alloys. They found that after artificial aging, the TS slightly increased, and elongation slightly changed for the joint. The WE slightly exceeded 100% in both cases of natural and artificial aging.

Kasman and Ozan [355] studied the butt FSW joints of 6013 Al plates obtained via the pin offset technique. They found that the highest TS equal to 206 MPa was obtained under a 1.5 mm pin offset toward the advancing side and 500 min⁻¹ TRS, leading to a ratio of the TS of the joint to the UTS of the BM (joint efficiency) equal to 74%.

Zhao et al. [356] studied the FSW joints of components made of dissimilar 6013-T4/7003 alloys. The joint with the 6013-T4 alloy placed at the advancing side (AS) was called the A6R7 joint. Accordingly, A7R6 referred to the joint with 7003 placed at the AS. The authors reported that irrespective of the AS or the RS, the 6013-T4 side was the weak region in terms of the TS. The WE for A6R7 was about 93%, while that for A7R6 was 87%.

Studying the FSW joints of sheets made of dissimilar Al-Mg-Si/Al-Zn-Mg alloys, Yan et al. [296] found that the TSs of dissimilar Al-Mg-Si/Al-Zn-Mg joints using both configurations exceeded that of the Al-Mg-Si FSW joint.

Liu et al. [277] studied the mechanical properties of the FSW joints of components made of 1050-H24 alloy. They reported that the maximum TS of the joints was equivalent to 80% of that of the BM. Under the deviation of the welding parameters from the optimum values, the tensile properties of the joints deteriorated, and the fracture locations of the joints varied.

For the butt FSW joints of ultrafine-grained (UFGed) 1050 alloy plates with a thickness of 2 mm with the 2 mm thick 6061-T6 alloy plates, Sun et al. [331] found that the maximum TS reached about 110 MPa. The WE reached up to about 55%.

Investigating the FSW joints of 1100 alloy, Selvarajan and Balasubramanian [418] reported that a maximum TS of 105 MPa was shown by the FSW joints obtained under the optimized welding parameters. The WE reached up to 95.4%.

For the underwater FSW joints of dissimilar 6061/7075 alloys, Bijanrostami et al. [325] found that the maximum TS of 237.3 MPa and elongation of 41.2% were reached under a TRS of 1853 rpm and WS of 50 mm/min. In comparison with the optimum condition, greater heat inputs induced a reduction in joint strength and higher elongation in the joints.

Investigating the welded joints of components made of dissimilar 7003-T4/6060-T4 alloys obtained by underwater friction stir welding (UFSW), Dong et al. [419] reported

that the UTS of the joints reached up to 185 MPa. The strength increased due to the microstructure modification caused by water cooling. The WE was 90.4% and higher compared to the classic FSW process.

Jassim and Al-Subar [524] studied the FSSWed joints of 3mm thick sheets made of 1100 alloy by overlapping the edges of the sheet as the lap joint. The joint TS increased with an increase in the TRS and the maximum TS of 233 MPa, twice higher than that of the BM, was obtained at a TRS of 2000 rpm. The WE varied in the range of 74.5%–141%.

For the FSW joints of components made of the 1100 alloy, Senapati and Bhoi [525] reported that the UTS of the welded specimen increased by 20%, compared to that of the parent material, due to the uniform dispersion of silicon particles present in the BM.

Joseph et al. [526] studied the effect of the spindle speed and the feed rate on the microhardness, YS, and UTS of the butt FSW joints of 3 mm thick strips made of 1200 alloys (Table 6), obtained using an H13 tool steel with 56 HRC and two different pin profiles (i.e., cylindrical with groove and tapered), which were used to fabricate the joints under three TRSs and three WSs. The two different sets of tools provided satisfactory joints. The author found that the UTS of the welded region decreased due to insufficient mixing of the material or due to the heat evolved during friction stir welding. The lower feed rate provided a joint with a higher TS due to better mixing of the material.

Investigating the FSW joints of components made of dissimilar 7075-T651 and 1200-H19 alloys, Attah et al. [523] found that the UTS increased from 126.04 to 151.54 MPa with an increase in the WS from 30 to 60 mm/min and decreased to 128.37 MPa at 90 mm/min. The UTS increased from 123.32 to 151.54 MPa as the tilt angle increased from 1 to 2° and decreased to 122.2 MPa as the tilt angle increased to 3°.

For the FSW joints of 6061-T6 alloy, Juarez et al. [358] reported that the TS for the BMW case was close to that in the joints obtained by fusion welding. For the HTBW case, the TS was enhanced by 10% compared to that obtained in BMW. For the HTAW case, an efficiency of 96% of the TS compared to that of the BM was observed.

Studying the FSW joints of dissimilar 7075-T651 and 1200-H19 alloys, Attah et al. [523] found the impact energy enhanced from 12.9 to 21.4 J with an increase in the WS from 30 to 60 mm/min, and it decreased to 5.4 J at 90 mm/min. The UTS increased from 126.04 to 151.54 MPa with an increase in the WS from 30 to 60 mm/min and then decreased to 128.37 MPa. The UTS increased from 123.32 to 151.54 MPa as the tilt angle increased from 1 to 2° and decreased to 122.2 MPa as the tilt angle increased to 3°. Under a tilt angle of 2°, as well as rotational and traverse speeds of 1500 rpm and 60 mm/min, respectively, the highest impact energy of 21.4 J was obtained.

Investigating the butt FSW joint of dissimilar 6061-T6/7075-T6 alloys, Godhani et al. [359] found that during the tensile tests of the specimens, fracture occurred in the HAZ of the 6061 side under all the investigated welding conditions. The breakage in the cup-and-cone form pointed to the ductile nature of the failure. The WE reached up to 61.4%.

Sato et al. [527] applied FSW to 1.5 mm thick pieces made of accumulative roll-bonded (ARBed) 1100 alloy with ultrafine-grained microstructure and high hardness. Transversely to the rolling direction, an elongated ultrafine-grained microstructure was observed. These pancake-shaped ultrafine grains with some dislocations and sub-boundaries therein, typically resulting from the ARB process, were surrounded by high-angle boundaries with misorientations above 15°. The mean thickness and length of the pancake-shaped grains were 260 and 450 nm, respectively. The initial material hardness was 30 HV, while after ARB, it increased to about 85 HV, due to grain refinement. The FSW joints were obtained under a rotation speed of 500 rpm and a WS of 12 mm/s using a tool with a shoulder diameter of 9 mm, a pin diameter of 3 mm, a pin length of 1 mm, and a threaded profile. The welding direction was identical to the rolling direction (RD) of the ARB process. The tool-to-workpiece angle was 3° from the vertical axis in the weld. The authors found that FSW suppressed the significant reduction in hardness in the ARBed material; however, the SZ and the TMAZ exhibited a small reduction in hardness due to dynamic recrystallization

and recovery. The FSW prevented softening in the ARBed Al alloy 1100 with an equivalent strain of 4.8 in the as-ARBed condition.

Studying the FSW of 5 mm thick plates made of 5086-O and 6061-T6 alloys, Aval et al. [423], in the 5086/6061 joint, obtained a weld UTS varying in the range of 219–240 MPa and weld elongation of 17%/23%, while the WE varied in the range of 87%–95%. In the 6061/5086 joint, the weld UTS varied in the range of 228–248 MPa, while the WE varied in the range of 90%–98%.

For the FSW joints of components made of dissimilar 5052/6061 alloys, obtained with various pin-eccentric stir tools, Chen et al. [360] found that all tensioned joints failed in the NZ, and the joint obtained with the 0.8 mm pin-eccentric stir tool exhibited the highest TS of 196 MPa due to the increased grain boundary and dislocation strengthening. The WE reached up to 86%.

Studying the FSW joints of sheets made of 2219 and 7475 alloys, Khan et al. [506] reported that the UTS of the weld region reached a value of 267.2 MPa, elongation was 5%, and the WE was 57%–92%.

For the FSW joints of components made of dissimilar 6061/7075 alloys, Guo et al. [503] found that the UTS of joints increased with the decrease in heat input. The highest UTS was 245 MPa. To summarize, it can be noticed that most studies conducted on FSW were focused on the BM in the as-rolled condition for 2xxx-5xxx, 2xxx-6xxx, 2xxx-7xxx, 5xxx-6xxx, and 5xxx-7xxx Al series. Some studies considered the effect of the BM placement of welded joint features, and the results remain inconclusive. BM placement is an issue for the cases of high differences in the mechanical properties of the BMs as in the 6xxx-7xxx and the 5xxx-7xxx combinations. Some studies concerned welding parameter optimization, particularly the effect of tool offset on weld quality. Further studies are necessary, including investigations using microstructure characterization to better understand material flow in the SZ.

During the FSW process, residual stresses are extremely low, much lower than those of the fusion processes.

The higher mechanical properties resulted from the fine grains in the stir zone of FSW joints.

The FSW weld (joint) efficiency can widely vary, in the range of 57%–98%, and even exceed 100% relative to the softer material.

Table 12 presents the resulting findings related to the hardness, TS, YS, residual stress, and elongation of various dissimilar and similar FSW joints of various Al alloys.

Table 12. The findings related to the hardness, TS, YS, residual stress, and elongation of various dissimilar and similar FSW joints between various Al alloys.

Refs	Alloys Placement Configuration	Hardness	TS	Residual Stress	Elongation
[308]	2024-T351/5083-H112 and 7075-T651/2024-T351	The joint HVf/HVw ratio exceeded the ones in the SZ, TMAZ, and HAZ due to the strain-hardening behavior. The hardness distribution depended on strain hardening and the fracture origin.	The joint TS much deteriorated compared to the weaker BM, especially for 2024-T351/5083-H112.		The joint elongation deteriorated compared to the weaker BM, especially for 2024-T351/5083-H112.

Table 12. Cont.

Refs	Alloys Placement Configuration	Hardness	TS	Residual Stress	Elongation
[310]	7075-T651/2024-T351	The joint hardness distribution determined the joint TS. The weld hardness dropped at the HAZ of softer material. Maximum reduction in joint hardness at the HAZ achieved with the pin tool with a flute of radius equal to that of the pin.	Placing the softer 2024 on the AS slightly increased the joint UTS. Using a flute/flat pin tool improved the joint UTS regardless of the fixed location of BMs. Using a truncated threaded pin tool with a flute of radius equal to that of the pin the joint TS reached the max value of 424 MPa (WE of 94.3% relative to softer BM).		Placing the softer 2024 on the AS slightly increased the joint elongation. Using a flute/flat pin tool improved the joint elongation regardless of the location of BMs.
[61]	Lap 7075/2024	7075 BM had higher hardness than 2024 BM. The 7075 SZ of the upper sheet had much higher microhardness than the 2024 HAZ or the TMAZ of the 2024 lower sheet.	Compared to a 4 mm pin or 5 mm pin, a 3 mm one easily reached higher EST and ELW. Under 4 mm pin and 5 mm pin, the EST gradually increased with the enhanced WS affecting the ELW in a complex manner due to the different formation mechanisms between EST and ELW. At a relatively high WS of 30 or 60 mm/min, the lap shear failure load decreased with the increased pin length. At WS of 90 and 120 mm/min, the lap shear failure load first reached the peak and then decreased with the increase in the pin length. The optimum pin length and WS combination effectively improved the joint TSs. Mode III can be attained under the combined function of HD with a small size, CLD with a small size, a small reduction in joint thickness, and high microhardness in the upper sheet. Compared to 2024/7075 lap joint, the 7075/2024 lap joint by 4 mm pin had higher strength when the alloy with high microhardness was placed as the upper sheet. All the fracture joints exhibited a ductile fracture mode.		

Table 12. Cont.

Refs	Alloys Placement Configuration	Hardness	TS	Residual Stress	Elongation
[311]	7075/5083	<p>For a triflute pin, the hardness profiles for all TRSs were close, for TRS of 560 rpm hardness dropped in the SZ due to voids in the weld area. For (AS) 5083/(RS) 7075, the hardness profiles differed. Under TRS of 280 rpm, the hardness profile was close to that for (AS) 7075/(RS) 5083. For other TRSs, the hardness in SZ decreased to 80 HV characteristic of the base 5083 alloy bands appearing in SZ. For both configurations, the max hardness in the SZ was 150 HV remaining constant from the weld center up to approaching the 7075. Regardless of the alloy configuration, on the 5083 side, the hardness was 80 HV remaining constant transverse the weld. On the 7075 side, the hardness decreased from 150 HV to 120 HV and then increased to 160 HV (characteristic half of a W-shape). Hardness profiles for the threaded taper tool were like those for the triflute pin, but with higher values. The max hardness in the weld center reached 180 HV for the (AS) 7075/(RS) 5083, while about 160 HV for the (AS) 5083/(RS) 7075.</p>	<p>Defect-free joints with the highest TS of 371 MPa were obtained for (AS) 5083/(RS) 7075, at the TRS of 280 rpm, and with a triflute pin tool.</p>		
[315]	Al-Mg ₂ Si/5052	<p>The hardness gradually increased from the BMZ of the 5052 through the welded joint to the Al-Mg₂Si BMZ</p>	<p>The joint UTS exceeded that of Al-Mg₂Si BM, whereas failed that of the 5052 BM. The WE exceeded 100% relative to Al-Mg₂SiBM and reached 61% relative to 5052 BM. The particle-matrix interfacial debonding fracture mechanism occurred.</p>		<p>The joint elongation exceeded that of Al-Mg₂Si BM, whereas failed that of 5052 BM.</p>

Table 12. Cont.

Refs	Alloys Placement Configuration	Hardness	TS	Residual Stress	Elongation
[316]	2024/6061	The microhardness profile on the AS was almost uniform, while it comprised three distinguishable regions on the RS.			
[318]	6082-T6/7075-T6	Irregular profiling in hardness distribution occurred, contrary to the conventional 'W'-shape trend, due to the difference in the chemical composition of alloys and the rate of precipitation. The NZ exhibited no onion ring with a long flow arm. The worm-hole defect occurred at the HAZ of the 6082-T6 alloy. An excellent bonding occurred despite the abnormal microhardness profile and microstructure evolution. Small flashes at the RS resulted from the preheating of the plates during the initial welding process.			
[319]	6061-T651/5A06-H112	The nano-hardness for each zone varied according to the relation BM > NZ > HAZ for the 6061 side, indicating that the mechanical properties of 6061 were weakened after FSW. On the 5A06 side, mechanical properties for each zone slightly changed after FSW. The nano-hardness in NZ and TMAZ was slightly higher than that in BM. The mechanical properties of 6061 were more vulnerable to heat input than those of 5A06.	After welding, the joint YS of 6061 decreased by 50% to 115 MPa and the joint UTS decreased from 277 MPa to 190 MPa mainly due to the unstable work-hardened state of rolled 6061 was destroyed by elevated temperature generated in FSW. The WE reached 68.5% against 6061 BM and decreased from 70% to 68% with the TRS/WS ratio increased from 4 to 12 r/mm.		

Table 12. Cont.

Refs	Alloys Placement Configuration	Hardness	TS	Residual Stress	Elongation
[322]	2219-T87/2195-T8	The microhardness in the upper part of the stirring part had an even distribution. In the middle- and lower-part hardness with 2195 on the AS was higher than that on the RS of the joint. Hardness increased with increasing the TRS and the WS.	Lack of correlation between the joint TS and the WS, the TS increased with increasing TRS, up to 800 rpm.		
[328]	(AS) 2024-T6/(RS) 7075-T6	For D/d of 2 and 2.5 joints fractured in the HAZ on the AS, and for D/d of 3, 3.5, and 4 fractured at the SZ. For all D/d, minimum hardness was in the HAZ on the AS, max hardness at SZ, and again decreased at HAZ in RS.	The joint TS increased with increasing D/d up to 3 and then decreased by further increasing D/d. The max TS was 356 MPa at D/d of 3, while the lowest one of 316 MPa at D/d of 4. The WE varied from 76% to 86%, depending on the D/d. The D/d ratio affects joint strength as it influences frictional heat generation between the tool and the BM.		Joints produced at the pitches of 1.25 and 1 mm/rev, exhibited less elongation than that obtained at smaller pitches. Lowering the pitch to 0.75 or 0.5 mm/rev increased the joint elongation to 13% for 0.75 mm/rev and to 22.5% for 0.5 mm/rev. The high heat input in the joints obtained at 0.5 mm/rev again caused a much increased elongation.
[331]	butt UFGed 1050/6061-T6	BMs exhibited the highest microhardness value. For both alloys from BM to HAZ microhardness decreased gradually. For 6061-T6, such a decrease was due to the intensive solid solution of precipitates and the simultaneous coarsening of particles resulting from the weld thermal cycles. The SZ also comprised some regions with a high hardness value close to that of BM, due to the refined grain size.	Joints produced at the pitches of 1.25 and 1 mm/rev, had TS lower than that obtained at the smaller pitches. Due to the insufficient mixing of the two materials in the SZ and a couple of microdefects in the 6061-T6 zone, the joint strength decreased. Decreasing the pitch to 0.75 or 0.5 mm/rev increased the heat input, intensifying the plastic deformation and the mixing of the two materials in the SZ. This resulted in a more homogenous SZ microstructure, increasing the TS to about 110 MPa		

Table 12. Cont.

Refs	Alloys Placement Configuration	Hardness	TS	Residual Stress	Elongation
		For UFG 1050, the hardness decreased due to grain growth and dislocation density.	for 0.75 mm/rev and 110 MPa for 0.5 mm/rev. The largest WE was 55% against UFG 1050 BM. Remarkably, high heat input in the joints produced at 0.5 mm/rev caused grain growth in both alloys, again slightly reducing the TS.		
[332]	2024-T3/2198-T3	Small correlation between hardness and local tensile properties.	In the top, shoulder-affected region, banded macrostructures with heterogeneous mechanical features appeared due to strain-rate gradient during one tool rotation. The banded macrostructures in the NZ induced early plasticity in the joint and are the fracture locations of the weld.		
[334]	butt 6061/7050	Distinct mechanical properties of two materials caused a consistent asymmetric microhardness distribution across the weld nugget, independent of TRS.	Under monotonic tensile loading, the joint TS increased with the rise in the TRS. The WE reached up to 62% relative to BMs.		
[346]	6061/A356	The Microhardness profile was related to joint microstructure. A low hardness of A356 was present at the RS. Hardness increased near the weld line due to the composite microstructure affected by both alloys. A further increase was observed in the AS due to the higher strength of 6061 compared to A356.	The max joint strength was reached at a low TRS and WS. This was accompanied by a fine grain size and distribution of Si particles. Tensile properties in the NZ were highly dependent on its microstructure.	Lower residual stresses in the SZ appeared under the low TRS and WS.	
[348]	2219-T87/5083-H321	The lowest hardness at HAZ was on the 5083 side.	The D/d ratio affected joint strength as it influenced frictional heat generation between the tool and the BM.		

Table 12. Cont.

Refs	Alloys Placement Configuration	Hardness	TS	Residual Stress	Elongation
[304]	5052/A5J32	<p>The 5052 BM hardness was 72 HV, and the A5J32 BM hardness was 78 HV. The 5052 hardness in the welded zone was lower than the 5052 BM one due to the dissolution of the second-phase particles and annealing during the welding progress. For RS 5052 the hardness near shoulder exceeded the 5052 BM one. The flow of the softened RS 5052 was restricted by the AS A5J32, causing the concentration of work hardening. The hardness values in the welded zone of A5J32 exceeded the BM A5J3 one, due to the interaction of the recrystallized fine-grain microstructure and agglomeration of the precipitates. For RS 5052 excessive agglomeration was in a narrow region, due to the restricted flow, and higher hardness than in another region. The A5J32 hardness in the welded zone exceeded that of RS A5J32.</p>	<p>The TS had similar values, regardless of the arrangement of the materials. The welding defects occurring under welding conditions with a lower heat input did not affect the tensile properties. For RS A5J32, the highest joint strength of 224.1 MPa appeared at TRS of 1000 rpm, and WS of 300 mm/min.</p>		
[344]	2014-T6/6061-T6	<p>The weld hardness profile is affected by the alloys' proportion in SZ, due to differences between the softening temperatures of both alloys. The 6061 HAZ was the weak link in all joints. The alloy placement or tool lateral shift affected the weld's hardness due to their effect on the precipitate radius and volume fraction. Obtained at TRS of 500 rpm joints with more 2014 alloy in the SZ (i.e., shifted joints) or in contact with the tool shoulder (i.e., 2014 AS)</p>	<p>The elevated temperature enhanced the precipitates' radius and reduced the precipitates' volume fraction weakening YS. However, the final YS was also affected by the remaining solid solution causing natural aging hardening, compensating for the less strengthening effect of larger precipitates in a lower volume fraction, as appeared in joints obtained at TRS of 1500 rpm.</p>		

Table 12. Cont.

Refs	Alloys Placement Configuration	Hardness	TS	Residual Stress	Elongation
		had a narrower softened zone. At TRS of 1500 rpm joint hardness profile was independent of the tool shift or the alloy placement.			
[497]	butt 2014-T3/5059-H11	The TMAZs and HAZs of 2014-T3 had the lowest hardness. Hardness decreased in the weld zone compared to both BMs.	The UTS reached 54% and 66% of those of the BMs		
[498]	Butt similar 2219-T87 and 2219-T62	The SZ hardness distribution differed significantly for 2219-T62 against 2219-T82	The joint TS and UTS of the 2219-T87 welds were higher than the 2219-T62 welds. The joint efficiency for the 2219-T82 alloy was 59.87%, while that for the 2219-T62 alloy was 39.10%. The joints' failure location characteristics were different for two different types of joint heat treatment.		The joint elongation was different for two different types of joint heat treatment.
[314]	2017A-T451/7075-T651	The positron lifetime profiles across the weld, corresponding to the hardness behavior, comprised many local maxima and minima on the AS and the RS. It was due to the temperature distribution in such areas relative to the critical temperatures for secondary phase nucleation and/or dissolution in both alloys.			
[363]	2017A-T451/7075-T651	During circular mixing of the material throughout the cross-section of the welded sheet, within such a region, the weld temperatures exceeded the equilibrium θ phase in 2017A, reducing the hardness, and simultaneously dissolved the equilibrium η/T phase in the 7075, causing reprecipitation of GP zones upon cooling and a hardness recovery.			

Table 12. Cont.

Refs	Alloys Placement Configuration	Hardness	TS	Residual Stress	Elongation
[46]	2017A-T451/ 7075-T651	Near the weld center, the full dissolving of the equilibrium η phase in 7075 and the partial dissolving of the equilibrium S phase in 2017A. Upon cooling, hardness recovered for both alloys. Due to the more complete dissolution of the equilibrium phase in 7075, the hardness recovery skewed toward the AS or the RS of the weld of the 7075 workpiece.			
[323]	wrought 2017A/ cast AlSi9Mg	The AlSi9Mg BM hardness was 80 HV1 and the 2017A BM hardness was 136HV1. The local max hardness on the AS was on the NZ with a high density of the bands of the 2017A.	The joint TS was 132 MPa		The joint elongation was below 1%.
[352]	cast AlSi9Mg/2017A	The hardness distribution within NZ revealed a low strengthening of both alloys. A metastable state of the 2017A occurred. Due to natural aging, the alloy hardness enhanced within NZ and slightly changed within HAZ.			
[354]	7003/7046	The hardness on RS 7046 was much higher than that on AS 7003, and the average hardness difference between both sides was about 30HV. After artificial aging, the hardness increased significantly, while the hardness difference between both sides rose to about 50 HV.	After artificial aging, the joint TS slightly increased. The WE slightly exceeded 100% for both natural and artificial aging.		After artificial aging, elongation slightly changed.

Table 12. Cont.

Refs	Alloys Placement Configuration	Hardness	TS	Residual Stress	Elongation
[339]	butt 7075-O/6061-O and butt 7075-T6/6061-T6.	The hardness increased in the joint area for the O-temper condition, whereas hardness loss occurred in the joint area under the T6-temper condition.	The strength values of all the O-joint specimens were close to those of the 6061-O BM, and all the specimens failed within the 6061 BM side away from the joint area. This was due to the shielding effect provided by the strength overmatching resulting from the grain refinement or precipitation of strengthening particles in this zone during the FSW process of Al alloys under the O-temper condition, i.e., softened state. The WE for the initial O state was about 100%. After PWHT (T6), the highest WE of about 93% for 1000/150-PWHT specimens and 87.5% for 1500/400-PWHT specimens was observed. For the initial T6 state, the highest WE was about 80% for the 1000/150 specimens, and 67.8% for the 1500/400 ones. After PWHT, the WE was 89.1% for 1000/150-PWHT specimens and 90.8% for the 1500/400-PWHT ones.		
[338]	cast A319/cast A413	The hardness of the welded regions increased with a rise in the WS and/or a decrease in the TRS.	The joint tensile properties exceeded those of BMs. The A413 BM had lower UTS and YSs than those of the A319 BM; thus, under tensile conditions, the welded specimens fractured at the A413 side.		
[356]	6013-T4/7003	Regardless of the AS or the RS, the 6013-T4 side was the weak region for the hardness. The fracture position coincided with the minimum hardness position.	Regardless of the AS or the RS, the 6013-T4 side was the weak region for TS. The WE for the AS 6013-T4 was about 93%, while that for the AS 7003 was 87%.		

Table 12. Cont.

Refs	Alloys Placement Configuration	Hardness	TS	Residual Stress	Elongation
[335]	6061/5086	For the threaded pin tool, the SZ hardness reached 83 HV, higher than those for the other two pin profiles. The increased hardness was due to the formation of fine grains and intermetallics in SZ.	<p>The conical threaded pin was the best, as it provided uniformly distributed precipitates and the generation of the onion rings resulted from the good material mixing in the SZ. The joint TS depended on the microstructure evolution during FSW, which in turn depended on the heat input controlled by the welding parameters. For threaded tool pin profiles, the joint TS of 169 MPa was higher than those of the other two pin profiles.</p> <p>The reduced size of weaker regions, such as the TMAZ and HAZ ones, caused higher tensile properties. The WE reached 50.4% and 67.6% relative to BMs.</p>		
[357]	lap 6111/5023		<p>The tensile shear load and fracture were mainly affected by the location of the soft material. For the soft material placed on top, the softening material and the deformed surface height occurred by friction heat generated by the rotating shoulder. The effect of the deformed surface height exceeded that of the softening material, and the deformed surface height decreased with the increase in revolutionary pitch. For the soft material placed at the bottom, the motion of the unbonded line and hooking appeared due to the vertical flow of the rotating probe. The effect of the position of the unbonded line exceeded that of the height of the hook. The unbonded line occurred along the interface between two alloys, affected by</p>		

Table 12. Cont.

Refs	Alloys Placement Configuration	Hardness	TS	Residual Stress	Elongation
			the lowest strength, which were deformed toward the hard material affected by a higher joint strength.		
[327]	5052-H32/6061 T6	The joint microhardness values were lower at HAZ on both sides of the weld line, whereas the lowest one was at 5055 HAZ.	Regardless of the sheet thickness and at TRS of 1500 rpm, the joints obtained at WS of 63 mm/min had higher ductility than those obtained at WS of 98 mm/min.		Joint elongation prior to failure of a 1.5 mm thick tailor-welded blank (TWB) was 47% more than that of a 1 mm thick weld.
[401]	butt 6063/5083	The max joint hardness values were obtained at TRS of 1000 rpm with a cylindrical profile. The hardness enhanced with the rise in the TRS.	Joints with higher TS were fabricated at TRS of 1000 rpm with a cylindrical profile. The TS increased with increased TRS. The WE increased from 32.3% to 43% when the TRS increased from 600 to 1000 rpm.		
[523]	7075-T651/1200-H19	For 1200-H19, hardness was 50 HV, and for 7075-T651, hardness was 175 HV, under three WSs, namely 30, 60, and 90 mm/min, at TRS of 1500 rpm and a tilt angle of 2°. The hardness increased from 81.99 to 98.5 HV with the WS increased from 30 to 60 mm/min, and decreased to 77 HV at 90 mm/min. At TRS of 1500 rpm and WS of 60 mm/min, the hardness increased from 70.22 to 98.58 HV with an increase in the tilt angle from 1 to 2°; a further increase from 2 to 3° reduced the hardness to 66 HV.	The UTS increased from 126.04 to 151.54 MPa with increasing the WS from 30 to 60 mm/min and decreased to 128.37 MPa at 90 mm/min. The UTS increased from 123.32 to 151.54 MPa as the tilt angle increased from 1–2° and decreased to 122.2 MPa as the tilt angle enhanced to 3°. The impact energy increased from 12.9 to 21.4 J with increasing the WS from 30 to 60 mm/min and decreased to 5.4 J at 90 mm/min. Under the tilt angle of 2°, TRS of 1500 rpm, and WS of 60 mm/m the highest impact energy of 21.4 J appeared.		
[423]	5086-O/6061-T6	The hardness profile on the 6061 side quickly decreased. Such hardness variation was smoother for joints obtained with a tool concave shoulder and a conical probe.	For (AS) 5086/(RS) 6061, the joint UTS varied in the range of 219–240 MPa, while WE varied in the range of 87%–95%. For (AS) 6061/(RS) 5086, the joint UTS varied in the range of 228–248 MPa, while WE varied in the range of 90%–98%.		For (AS) 5086/(RS) 6061, the elongation varied in the range of 17%–23%.

Table 12. Cont.

Refs	Alloys Placement Configuration	Hardness	TS	Residual Stress	Elongation
[503]	6061/7075	All joints failed in HAZ on the 6061 side with minimal hardness regardless of the relative material position or the welding process parameters.	The joint UTS increased with the decrease in heat input. The highest UTS was 245 MPa.		
[361]	7075-T651/ 2024-T351	The hardness increased and then decreased from the top to the bottom along the welding center thickness direction. The tensile fracture locations coincide with that of minimum hardness values at various TRSs. A softening behavior in the TMAZ and HAZ appeared in the as-welded joint due to the coarsening of strengthening precipitates due to the heat thermal cycle during FSW. After PWHT, the softening behavior in the TMAZ and HAZ disappeared, and the corresponding microhardness value was close to those of the adjacent BMs, due to fine and uniformly distributed precipitates.	The YS, UTS, and TE of the as-welded joint were about 304.6 MPa, 385.4 MPa, and 2.95%, respectively. However, the YS, UTS, and TE of the joints subjected to PWHT were in a range of 165.1–281.9 MPa, 173.2–292.6 MPa, and 0.9%–2.2%, failing those of the as-welded joint. The joint performances subjected to solution and subsequent aging treatment highly deteriorated.		
[426]	Lap 2198/7075	The microhardness map reflected the various metallurgical zones, whereas higher microhardness values accompanied the highly deformed and recrystallized grains of the hooks. The microhardness values in NZ were slightly higher than the ones of the BM, whereas lower values occurred in the HAZ. The hardness increased with the decrease in the heat input, typical for FSW.			

Table 12. Cont.

Refs	Alloys Placement Configuration	Hardness	TS	Residual Stress	Elongation
[427]	lap 2198/6082	The microhardness varied around the hook geometry. A gradual hardness rise from the BM to NZ appeared. A similar pattern of the gradual hardness increase, in the upward direction occurred for the boundary separating the TMAZ and hook region.			
[313, 341, 343, 350]			The joint strength increased with the TRS due to the increased material mixing effect, TRS increased plastic deformation, and WS governed the thermal cycle, residual stresses, and rate of production. The selection of the appropriate combination of TRS and WS strongly affected joint quality or joint strength. Together with TRS and WS, the pin shape affects joint strength, as it influences the SZ size and material movement.		
[325]	6061/7075		The max TS of 237.3 MPa was reached under TRS of 1853 rpm and WS of 50 mm/min. Compared to optimum conditions, greater heat inputs induced a reduction in joint strength.		The elongation of 41.2% occurred at TRS of 1853 rpm and WS of 50 mm/min. Compared to optimum conditions, greater heat inputs induced higher elongation.
[321]	2024-T3/6063-T6		At a TRS of 900 rpm and WS of 200 mm/min, the highest TS of 348 MPa was equal to 74% of that of the 2024 BM. An increase in TS was 45% higher than the TS of 6063 BM. All tensile failures occurred at the HAZ location always at the 6063 side. Under lower TRS and higher TS in all welding conditions, the joint Wöhler curves exhibited maximum fatigue strength.		

Table 12. Cont.

Refs	Alloys Placement Configuration	Hardness	TS	Residual Stress	Elongation
[326]	6082-T6/5083-H111		The highest joint TS was obtained with a triangular-shaped (T) tool pin and the UTS was 198.48 MPa. At a lower TRS and WS for each tool pin shape, UTS was lower. The UTS increased with an increase in TRS and WS, while the TRS/WS ratio was constant in all cases. The WE varied from 55% to 68% depending on both the presence of defects in the joint and the strength of BM. Together with TRS and WSs, pin shapes affect the joint strength, as they influence the SZ size and material movement.		For a T pin at TRS of 400 rpm elongation reached 0.49%. With an increase in TRS of up to 630 rpm elongation increased to 4.7% and decreased to 4.26% at TRS of 800. For pentagon-shaped (P) pin elongation varied in the range of 0.39%–4.31% with the TRS increasing from 400 to 800 rpm.
[350]	5083-H111/6351-T6		The TRS and pin profile affected the joint TS due to varying material flow, loss of cold work in the HAZ of the 5083 side, dissolution and overaging of precipitates of the 6351 side, and formation of macroscopic defects in the weld zone. The joint fabricated at TRS of 950 rpm and with a straight square pin profile had the highest strength of 273 MPa.		
[296]	Al-Mg-Si/Al-Zn-Mg	For both configurations, the hardness only slightly varied at the Al-Zn-Mg side. The average hardness at the Al-Zn-Mg side was about 100 HV on both joints. The hardness varied at the Al-Mg-Si side, decreasing in the TMAZ and HAZ and further increasing in the SZ. For (AS) Al-Zn-Mg joints, hardness at the joint top slightly exceeded that at the middle and bottom regions at the Al-Zn-Mg side. At the Al-Mg-Si side, the SZ top had the minimum values. A similar result occurred at	The joint TSs for both configurations exceeded that of the Al-Mg-Si FSW joint. The average TS of the Al-Mg-Si-AS joint is a little higher than that of the Al-Zn-Mg-AS joint. The maximum TS of 213.3 MPa for (AS) Al-Mg-Si joint reached 106.5% of the Al-Mg-Si joint and 61.4% of the Al-Zn-Mg- joint. For (AS) Al-Zn-Mg alloy, the joints had better fatigue properties due to the bridging effect of the large second-phase particles.		

Table 12. Cont.

Refs	Alloys Placement Configuration	Hardness	TS	Residual Stress	Elongation
		the (AS) Al-Mg-Si joint at the Al-Mg-Si side, while the SZ bottom region exhibited higher hardness at the Al-Zn-Mg side.			
[295]	6061-T6/7075-T6		The tool offsets into the 7075 RS increased the joint TS, which was facilitated by lower average weld temperatures with the increased amount of 7075 stirred into the NZ. The WE increased with a reduction in the amount of power input to the weld, whereas the subsequent WE was highly affected by the alloy most sensitive to heat input and weld temperature.		
[351]	7050-T7451/ 2024-T351		Tensile stresses in the BM test specimens reached up to 32 MPa and had the "M" profile with peaks in the HAZ outside the weld.	The low peak residual stress below 20% of BM YS was achievable only by solid-state welding with less distortion, while it was hardly possible for fusion welding. The fatigue behavior highly depended on such low residual stresses. The peak tensile residual stresses were in the HAZ on both sides due to local frictional heating at the tool material interface. Tensile residual stress resulting from the hotter material was forced by the other material during welding.	

Table 12. Cont.

Refs	Alloys Placement Configuration	Hardness	TS	Residual Stress	Elongation
[300]	2024-T351/6056-T4	Fracture occurred in the TMAZ of 6056-T4, where annealed structure led to reduced microhardness.	The joint TS was up to 90% of that for 6056-T4. The drop in TS and the associated increase in strain were observed in the regions where microhardness decreased. The UTS efficiency was 55.8% relative to 2024-T351 BM and 71.4% relative to 6056-T4 BM.		The elongation efficiency at the rupture was poor (9%–14%).
[400]	2024/5056		At lower WSs and high TRSs, the joint TS efficiency is above 90% of that of the BM TS. The welding process parameters complexly depended on the BM TS.		
[349]	Cast 6061/wrought 6061	The microhardness in some portions of the weld zone exceeded that of wrought alloy and in other portions exceeded that of cast alloy.	The joint reached max TS for cast alloy on the AS at all TRSs.		
[497]	2014-T3/5059-H11	The 2014 BM hardness was 128 HV, while that of 5059 BM was 158 HV. The hardness decreased in the weld region with TMAZ and HAZ, due to material softening, while recrystallization due to high plastic deformation increased the hardness in the NZ. The hardness varied in the NZ due to the varying concentration of alloying elements in this zone. In the NZ, hardness decreased on the 5059 side and increased on the 2014 side. Recrystallization of a very fine-grain structure caused hardness recovery in the NZ on the 2014 side. In the NZ on the 5059 side, as close to the 2014 side, hardness decreased, while toward the TMAZ side, it increased. The lowest hardness of about 87 HV was found in the TMAZ and HAZ on the AS 2014 side.	The joint UTS efficiency reached 54% and 66% relative to BMs.		

Table 12. Cont.

Refs	Alloys Placement Configuration	Hardness	TS	Residual Stress	Elongation
[402]	2618-T87/5086-H321		HAZs with tensile failures appeared on the 5086 side. The joint UTS was affected by the D/d ratio, TRS, and WS.		
[419]	7003-T4/6060-T4 UFSW	The microstructure of the NZ was much finer than that obtained with classical FSW. The evolution of the precipitants depended on the welding parameters. With the increased WS, more η and η' phases remained due to the lower heat input. Compared with normal FSW, The HAZ was narrower, and the joint soft region was near the weld center by the hardness distribution profiles. Compared with air-cooling FSW, the UFSW joint efficiency significantly increased.	The joint UTS reached up to 185 MPa at TRS of 1000 rpm, and WS of 120 mm/min. The joint strength increased due to the microstructure modification caused by water cooling. The WE of 90.4% exceeded that for the same alloy combination but under classic FSW.		The joint elongation of 13%, occurred at a TRS of 1000 rpm, and WS of 120 mm/min. The joint tensile failure occurred at the soft 6060 side, mainly comprising the HAZ and TMAZ with grains and precipitates finer than those of air-cooling FSW.
[359]	6061-T6/7075-T6		The tensed specimens fractured from the HAZ of the 6061 side for all conditions. The breakage in the cup-and-cone form pointed to the ductile nature of the failure. The WE reached up to 61.4%.		
[360]	5052/6061	The hardness distribution was asymmetric due to the different mechanical properties between both alloys. The hardness of all NZs decreased after FSW compared with BMs. FSW was accompanied by dynamic recrystallization eliminating the work hardening and the coarsening of precipitates causing overaging and inducing the softening of NZ. For (AS) 6061/(RS) 5052, the hardness of the NZ increased from 61 HV for joint P0 to 66 HV for joint P0.8 with the pin eccentricity increased from 0 to 0.8 mm.	All tensed joints failed in the NZ, and the joint obtained by the 0.8 mm pin-eccentric stir tool had the highest TS of 196 MPa due to the increased grain boundary and dislocation strengthening. The WE reached up to 86%.		The elongation was improved by utilizing the pin-eccentric stir tool

Table 12. Cont.

Refs	Alloys Placement Configuration	Hardness	TS	Residual Stress	Elongation
		The grains in the NZ became finer and the fraction of deformed/substructured grain increased with the increased pin eccentricity, which improved both the grain boundary and dislocation strengthening, increasing the hardness of the NZ.			
[506]	2219/7475	Minimum hardness was observed at TMAZ at RS for all joints due to the thermal softening.	The joint UTS was 267.2 MPa, and the WE was 57% and 92%, relative to BMs. Tensile specimen fractured from TMAZ and/or HAZ regions. Dissimilar joints exhibited lower strength compared to similar joints. The lowest strength for dissimilar joints was mainly due to the non-homogeneous motion of BMs caused by their different mechanical and physical properties.		The joint elongation was 5%.
[496]	6013-T6	The average BM hardness was 130 HV, while for the weld nugget, it was 100 HV. The average TMAZ hardness was lower than that in NZ.	Both the BM and the weld region comprised homogenous distributions of the fine and coarse Mg ₂ Si particles. Uniformly distributed, finer strengthening Mg ₂ Si precipitates, smaller grain size, the lack of a precipitate-free zone, and higher dislocation density allowed for the superior tensile properties of the FSW joints. WE was 64% and UTS(FSW)/UTS(BM) of 75%		
[428]	2014-T6	Hardness in the softened weld region decreased with decreasing WS. Hardness in the softened region slightly increased with increasing the TRS. Hardness in the softened weld regions decreased by 20% under the studied welding parameters.	The TS in the softened region slightly increased with increasing the TRS. The joint tensile and fatigue properties were strongly affected by WS. The joint ductility and strength were higher at the WS of 80 mm/min. The joints obtained at the WS of 80 mm/min and the TRS of 1520 rpm exhibited the best tensile and fatigue		

Table 12. Cont.

Refs	Alloys Placement Configuration	Hardness	TS	Residual Stress	Elongation
[405]	2024	The hardness profile of welds had a characteristic run, typical for FSWs.	<p>properties. The joint fatigue behavior was consistent with the tensile properties, especially elongations. The joint with a higher ductility was less sensitive to fatigue. Joints of high ductility welded at the WS of 80 mm/min tensely fractured near the HAZ and TMAZ on the AS, whereas the joints of low ductility welded at the WS of 112 mm/min failed near the NZ on the AS. The joints welded under high heat at the WS of 40 mm/min fractured in the interface between the NZ and TMAZ on the AS. High-stress fatigue fractures of joints welded at WS of 80 mm/min appeared near the NZ and TMAZ on the AS, whereas under low stresses and long times, they appeared in the HAZ, either on the AS or the RS. The fatigue fractures of the joints at the WS of 40 and 112 mm/min occurred near the NZ and TMAZ at all stress levels. The fracture locations were closer to the NZ at higher stress levels.</p>		
			<p>The best bend test results were achieved with the triflute flat bottom pin and the worst with the similar triflat one. The tensile test results were better for both triflute and triflat round bottom pins compared to the version with flat bottom pins. The fatigue properties of the FSW joint exceeded those of fusion welding, equal to 45 MPa.</p>		

Table 12. Cont.

Refs	Alloys Placement Configuration	Hardness	TS	Residual Stress	Elongation
[407]	2024-T351	The distribution and allocation of microhardness were affected by the level of temperature and plastic deformation being highest under the tool shoulder and around its pin.	Joint efficiency, reaching 97% that of BM and the highest ductility of 72%, was achieved at TRS of 750 rpm and WS of 116. The combination of TRS and WS directly affected the fracture toughness and energy needed for the initiation and propagation of the crack. The asymmetry of the welded joint and varying metallurgical transformations around the rotating tool pin and under the tool shoulder affected the impact strength in various joint zones.		
[406]	2024-T4	Joints obtained with the tapered threaded tool had elevated average hardness over various welding zones compared to the joints prepared with the unfeatured tool.	The joint strength properties were enhanced using tapered threaded tool pins compared to the joints prepared by unfeatured tools. The best achievable strength occurred at WS/TRS of 9.1 (55 mm/min/500 rpm). The highest strength for the unthreaded tool was obtained at WS/TRS of 11.3 (115 mm/min/1300 rpm).		Joint elongation increased using tapered threaded tool pins compared to the joints prepared by unfeatured tools. The best achievable elongation occurred at WS/TRS of 9.1 (55 mm/min/500 rpm). The highest elongation for unthreaded tools was obtained at WS/TRS of 11.3 (115 mm/min/1300 rpm).
[499]	2014-T651	At 70% yield, the induced stress was lower, so hardness determined the material failure. Since the HAZ had a large grain size compared to the NZ, the material failed therein.	The joint YS of the weld was 260.7 MPa. The WE was 61.81%. Joint fractured near the HAZ at 70% yield loading and near the NZ at 110% yield loading. In the case of 110% yield, the enhanced stress concentration appeared in the material and the presence of fine grains increased the number of grain boundaries in the NZ. The enhanced stress concentration and larger grain boundary corrosion attack promoted material failure near the NZ		The joint elongation was about 11%

Table 12. Cont.

Refs	Alloys Placement Configuration	Hardness	TS	Residual Stress	Elongation
[408]	2014-T6	Different joint regions of the joint had different microhardness distributions, which were affected by different thermomechanical actions therein.	The joint TS was affected by welding parameters. The max UTS of 360 MPa, equal to 78% of that of BM, appeared at a TRS of 400 rpm and WS of 100 mm/min. The joint's different regions had different TSs depending on microstructure variation and microhardness distribution, which were affected by different thermomechanical actions therein.		
[353]	2017A	Microhardness in the joint cross-section only slightly varied; however, after the artificial aging the hardness increased. The variation in the joint hardness after the aging pointed out post-process partial supersaturation in the material and higher precipitation hardening of the joint.			
[521]	2017	At the weld interface, the SZ was formed with a hardness close to that of BM, while the HAZs were softened.	The joint TS increased with pressure and friction time, and the highest joint TS reached 275 MPa (WE of 63.1%). The high joint fatigue strength was accompanied by its high TS.		
[485]	2024-T6	With the conical cam thread stirring head the obtained hardness was lowest at the junction of HAZ and TMAZ. The hardness obtained with the conical cam thread at that point exceeded that of other stirring heads.	The TS for all joints was more than 80% of the BM one, and the max TS of the joint welded with the conical cam thread tool pin reached 364.27 MPa, which was 86.73% of the BM. All joints were tensile-fractured due to plastic fracture		The elongation after break reached 14.95%.
[417]	5454	The hardness in the friction-stir-spot-welded zone exceeded that of BM.	The joint toughness increased with the enhanced TRS, although the maximum tensile shear load decreased.		
[418]	1100	The joint hardness reached 67 HV in the SZ under the optimized welding parameters and tool material hardness of 45.4 HRC.	The max joint TS of 105 MPa was obtained under the optimized welding parameters. The WE reached 95.4%.		

Table 12. Cont.

Refs	Alloys Placement Configuration	Hardness	TS	Residual Stress	Elongation
[358]	6061-T6	The SZ microhardness was 85 HV for BMW, 109 HV for HTBW, and 134 HV for HTAW. For HTAW, the microhardness had the lowest dispersion of values between 124 HV and 148 HV along the four characteristic zones. For BMW, hardness was much below that of BMW, due to the aging of the material and the thickening of the precipitates resulting from the mechanical work and heat generated during welding. For HTAW, the hardness exceeded that of the BMW due to a uniform distribution of precipitates in the zone of agitation inside the welded zone, combined with a smaller size of precipitates.	For BMW, the TS was close to that in fusion welded joints. For HTBW, the TS increased by 10% compared to that obtained in BMW. For HTAW, the joint TS reached 96% of that of BM.		
[522]	butt 1200	The FSZ hardness varied with position and ranged from 30 HV to 40 HV and exceeded the BM hardness of 32 HV. This was due to grain refinement affecting material strengthening and since the grain size in the FSZ was much finer than that of BM thus increasing the FSZ hardness. The small particles of intermetallic compounds also increased the hardness.			
[424]	2219-T62			The residual stresses on the top surface reached about 171 MPa, while only 243 MPa for the weld with tunnel defect and had the conventional "M" profile with tensile stress peaks in the HAZ	

Table 12. Cont.

Refs	Alloys Placement Configuration	Hardness	TS	Residual Stress	Elongation
				<p>zone. Those on the bottom surface had the inverted “V” profile with tensile stress peaks of 99.4 MPa in the weld center. Residual stress decreased on the top surface with the increased TRS. Residual stress increased on the bottom surface with increased TRS.</p>	
[412]	3003		<p>The joint TS was up to 75% of that of BM. The joint TS was affected by TRS, WS, and tool tilt angle. The best joint mechanical properties occurred at TRS of 1424 rpm, WS of 400 mm/min, and a tilt angle of 1.3°.</p>		
[413]	butt 3003-H24		<p>At a WS of 50 mm/min, and TRS of 500 and 1000 rpm joints showed tunnel-type defects with large size. The tunnel-type defects also occurred at WS of 80 mm/min and TRS of 500 and 800 rpm. The cavity-type defects appeared at both WSs. Despite defects, all welded joints fractured between the BM and the HAZ, except those obtained at WS of 50 mm/min and TRS of 500 and 1000 rpm. Joints fractured in a ductile manner except those obtained at WS of 50 mm/min and TRS of 500 rpm. The size of the defects well correlated with the joint tensile properties.</p>		<p>The joint elongations were highly improved with an increase in the TRS and the WS.</p>

Table 12. Cont.

Refs	Alloys Placement Configuration	Hardness	TS	Residual Stress	Elongation
			The highest joint UTS of 128 MPa occurred at TRS of 800 rpm and WS of 50 mm/min. The WE was close to 100%. The size of the defects depended on the joint tensile properties.		
[403]	3003-H12		The joint TS increased with increased WS or decreased TRS. The joint tensile fractures were in BM at TRS of 1070 rpm and WS of 40 mm/min or TRS of 2140 rpm and WS of 224 mm/min. The joint UTS decreased linearly with increased TRS at a constant WS, while UTS increased almost linearly with increased WS at a constant TRS.		The joint elongation was lower at higher TRS or lower WS.
[415]	3003		The best UTS of 127.2 MPa was for WS of 74.64 mm/min, a TRS of 971.77 rpm, and a tool tilt angle of 1.52°. The WE reached up to 89.4%.		
[501]	7204-T4		The joint UTS reached 296.6 MPa, 318.2 MPa, and 357.4 MPa under the heat treatments of AW, AA, and SAA, respectively.		
[355]	6013		The highest joint TS of 206 MPa occurred under a 1.5 mm pin offset toward the AS and the TRS of 500 rpm, leading to the joint efficiency of 74%.		
[277]	1050-H24	A minimum joint hardness zone was on the AS, facilitating fracture thereon. The minimum joint hardness value increased with the increase in revolutionary pitch.	The max joint TS reached 80% of that of BM. Deviation of the welding parameters such as revolutionary pitch from the optimum values made the joint tensile properties deteriorate, and the joint fracture locations varied.		The two-stage joint tensile fracture that occurred caused joint elongation at a significantly low level.
[524]	Lap 1100 FSSW	At the joint center zone, the hardness from 1.45 to 2.85 times exceeded that of the BM. At the optimum TRS of 1065 rpm, the hardness in the welding zone and TMAZ twice exceeded that of BM.	The joint TS increased with an increase in the TRS, the max joint TS of 233 MPa, twice higher than that of BM, occurred at a TRS of 2000 rpm. The WE reached 74.5% and 141% relative to BMs.		

Table 12. Cont.

Refs	Alloys Placement Configuration	Hardness	TS	Residual Stress	Elongation
[525]	1100		<p>The joint UTS increased by 20% compared to that of BM due to the uniform dispersion of Si particles within the BM. The grain size decreased with increasing TRS, whereas the joint TS increased with TRS increasing to 1400 rpm and then decreased at TRS of 1500 rpm. The grain size reduced with increasing WS while the TS increased. The grain size increased with increasing PD, whereas the TS decreased. For higher TRS and WS, and low PD the grain size decreased. Simultaneously, joint TS varied due to finer grains lowering possible pile-up at the grain boundaries increasing the amount of applied stress moving a dislocation, considering the needed stress increased with the higher TS. The joint obtained at TRS of 1500 rpm comprised finer grains that limited the slip lowering material ductility and providing brittle fracture.</p>	<p>The residual stress distribution was asymmetric with higher magnitudes in the AS. The residual stresses in joints obtained at high TRS and low WS were compressive in the nugget zone. In all cases, the tensile residual stress occurred in the crown region.</p>	
[527]	ARBed 1100	<p>The initial material hardness was 30 HV, while after ARB, it increased to about 85 HV, due to the grain refinement. The FSW suppressed the significant reduction in hardness in the ARBed material; however, the SZ and the TMAZ exhibited a small reduction in hardness due to dynamic recrystallization and recovery.</p>	<p>For a TRS of 500 rpm, WS of 12 mm/s, and a tilt angle of 3°, with tool shoulder D of 9 mm, threaded pin (d of 3 mm, l of 1 mm), the same welding direction as rolling one of the ARB process, the FSW prevented softening in an ARBed 1100 alloy with an equivalent strain of 4.8 in the as-ARBed condition.</p>		
[526]	1200		<p>The joint UTS decreased due to poor material mixing or heat evolved during FSW. The lower WS provided higher joint TS due to better material mixing.</p>		

Reinforcement of Weldment and Application of Coating

The mechanical properties and microstructure of the FSW joints can be enhanced by grain refinement via micro- and nanosized solid-particle reinforcement [528].

Various nanoparticles can be incorporated in the FSW of Al alloys [528–533].

Vimalraj et al. [63] stated that varying TRS, WS, number of passes, and the direction of the traveling tool affect joint fabrication. They found that the size, type, and quantity of reinforcing nanoparticles (SiC and TiC) beneficially influence the formation of microstructure and joint properties.

Moradi et al. [534] studied the effect of weld pass number on the microstructural, natural aging, and mechanical performance of SiC-incorporated FSW of Al alloys. They found a smaller size of grains at the nugget zone for two passes than that for a single pass due to a smaller initial grain size and more homogenized and finer distribution of SiC particles. However, the repeated thermal cycle and high hot deformation highly limited the precipitation hardening effect, thus significantly reducing hardness.

SiC particles with a size between 20 and 60 nm are most often used as reinforcing particles [364].

The properties of FSW joints and the extent of their service life can be improved by several effective methods [254], including heat treatment, cold spraying, laser cladding, microarc oxidation, and electrochemical deposition [535–539].

Friction stir welding (FSW) joints often need coatings with good adhesion and corrosion resistance to enhance durability. One of them is a traditional zincated Nisingle bondP coating. Chen et al. [540] developed duplex Nisingle bondP coating fabricated on the FSW joint of 6061-T6 Al alloy. An anodic Al oxide (AAO) layer formed on the joint substrate was the intermediate layer enhancing adhesion. On its top, a Nisingle bondP layer was electroplated to improve the corrosion and wear features. The duplex Nisingle bondP coating provided very high adhesion and significantly enhanced anti-corrosion properties compared to the traditional Nisingle bondP layer. The friction feature of the FSW joint with duplex Nisingle bondP coating was 88% greater than that of the original FSW joint and 75% greater than that of the FSW joint coated with zincated Nisingle bondP layer.

The other direction for improving the quality of FSW joints of Al alloys is to use coating on the welding tools. Such coatings should be good adherents and inert. Ehi-asarian et al. [541] used coated tools for the stationary shoulder friction stir welding (SS-FSW) of 6082-T6 alloy. They compared the performance of a nanoscale multilayer TiAlN/VN coating deposited by high-power impulse magnetron sputtering (HIPIMS) with amorphous diamond-like carbon (a-C:H) obtained by plasma-assisted chemical vapor deposition (PACVD), AlTiN deposited by arc evaporation, and TiBCN along with TiB₂ produced by chemical vapor deposition (CVD) methods. The TiAlN/VN coating had a low affinity to Al, and an acceptable coefficient of friction and provided excellent weld quality by inhibiting intermixing between the tool and welded component materials, causing a significant decrease in tool wear. DLC coatings could not match the harsh conditions experienced by probes; however, their low friction and medium temperature enabled them to produce an excellent weld surface finish when applied to SS-FSW shoulders. Of the two CVD coatings—TiBCN and TiB₂—TiBCN showed the highest friction of all coatings tested at both room temperature and 350 °C and the lowest value at 550 °C; both had similar wear performance. The AlTiN coating exhibited high performance (slightly better than TiAlN/VN) at the probe; however, it generated buildup on the shoulder. It displayed the most consistent friction coefficient over all tested temperatures, while its wear resistance exhibited a peak at 350 °C, which was seven times greater than that at room temperature and over four times greater than that at 550 °C.

4.8.2. Friction Stir Spot Welding

Friction stir spot welding (FSSW) is a kind of friction stir welding (FSW) process. It provides a spot, lap weld without the bulk melting of joined materials. The tensile shear strength of the FSSW-welded joints is affected by the pin height, tool rotation, and

welding time [542]. The FSSW process of Al alloys provides significant energy and cost savings compared to electric resistance spot welding [543]. The FSSW process for Al alloys (Table 13) is more beneficial than other welding processes such as RSW, MIG-Spot, and mechanical joining techniques [544]. FSSW is cheap due to improved energy efficiency and a virtual lack of a consumable; that is, FSSW requires no water, no compressed air, and no complex electrical transforming equipment [545].

Jassim and Al-Subar [524] studied FSSWed joints of 3mm thick sheets made of AA1100 alloy (Table 13) by overlapping the edges of the sheet as the lap joint. The process was carried out using a drilling machine instead of a milling machine under a TRS varying in the range of 760–2000 rpm with manual and automatic compression. Hardness enhanced at the center zone of the welded joint, which was 1.45–2.85-fold higher than the hardness of the BM. The optimum TRS was 1065 rpm. The joint TS enhanced with an increase in the TRS, and the maximum TS of 233 MPa, twice higher than that of the BM, occurred at a TRS of 2000 rpm. The depth of tool penetration was in the range of 3.25 to 6 mm depending on the load and heat.

Senapati and Bhoi [525] studied the FSW joints of components made of 1100 alloy (Table 13), obtained using a square pin tool. They reported that the temperature on the AS of the weld was about 20–25 °C higher than its RS. The UTS of the welded specimen enhanced by 20% compared to that of the parent material due to the uniform dispersion of silicon particles present within the BM. The finely arranged equiaxed grains appeared in the nugget region of the weld. The formation of alumina Al_2O_3 occurred in the weld nugget due to high heat generation and exposure to atmospheric oxygen during welding. Residual stress possessed an M-shaped distribution. The samples joined at the low WS and the high TRS exhibited compressive residual stress in the joint region. Contrarily, the residual stress of the material lying below the tool shoulder was tensile. The residual stress in the AS possessed a higher magnitude than the RS of the weld specimen.

According to Praveen and Yarlagadda [546], pulsed gas metal arc welding (GMAW-P) is one of the ways to weld joints of various Al alloys, as it achieves less heat input in the weld. The hardness increased in the welded area. The YS and UTS of the welded region decreased due to the insufficient mixing of the material or due to the heat evolved during friction stir welding. The 750 rpm spindle speed provided the best weld results. The lower feed rate provided a joint with a higher TS due to the better mixing of the material. The tapered tool provided a better weld than the cylindrical one.

Levise et al. [547] studied the effect of the process parameters on the mechanical properties of the FSSWed joints of components made of dissimilar 2024/7075 alloys (Table 13). They found that the tensile shear force increased to the maximum with changes in the TRS. The optimal tensile shear force and hardness equal to 4.18 kN and 134 HV, respectively, were obtained for a tool plunge depth of 3.3 mm, a TRS of 2000 rpm, and a tool dwell time of 40 s.

Kulekci et al. [542] studied the effect of the welding pin height, TRS, and WS on the tensile shear strength of FSSWed joints of components made of 5005 alloys (Table 13). They found that the pin height was the major factor affecting the tensile shear strength of FSSW joints, whereas the TRS and WS were the second-ranking factors. The enhancement of tool plunge depth increased the weld tensile shear strength of FSSW joints. The maximum tensile shear strength of 122.16 MPa was obtained for a pin height of 2.60 mm, a TRS of 1500 rpm, and a welding time of 10 s. However, the minimum tensile shear strength of 58.92 MPa was obtained for a pin height of 2.20 mm, a TRS of 1500 rpm, and a welding time of 10 s. The WE widely varied in the range of 54.5%–111%.

Borah et al. [548] studied the FSSWed joints made of 6063 series of 1 mm thickness (Table 13). A process combining double-spot friction stir welding (DSFSW) and double-spot zigzag friction stir welding (DSZFSW) to provide higher strength in the welded joints was considered. They compared various mechanical properties of the joints with single-spot friction stir welding, obtained using tools with three different probe shapes at three different spindle speeds. They found that at low WSs, the tensile–shear strength of the welding

specimen was higher. The DSFSW joints, welded with a triangular probe tool, exhibited a higher TS than that of a single-spot and DSZFSW joint. Under high spindle speed, the hardness value of the welding specimen decreased, while the grain size increased.

Suresh et al. [549] reported that in FSSW, a rotating hardly wearing tool is pressed with a high force against the upper surface of two overlapping sheets. The simultaneous effect of frictional heat and the applied pressure results in the metallurgical bonding of the components without melting. The tool is drawn out of the welded piece after a dwell time.

The welded joints of the 6061-T6 alloy (Table 13), studied by Suresh et al. [549], were obtained by swept friction stir spot welding. Al₂O₃ nanoparticles were added to a guide hole to improve the weld characteristics. The percentage of reinforcement varied by changing the guide hole diameter in the range of 1.5–3.0 mm. Using a non-dominated-sorting teaching–learning–based optimization algorithm, the optimum welding parameters were determined as a guide hole diameter of 2.8 mm, a TRS of 1387 rpm, and a WS of 17 mm/min.

Table 13. FSSW process parameters applied for joints of various Al alloys.

Refs.	Joint	Thickness [mm]	Rotational Speed [rpm]	Welding Speed [mm/min]	Welding Time [s]	Plunge Depth [mm]	Tool
[542]	EN AW 5005	1.5	1500/2000		5/10		Cylindrical shoulder diameter 10/shoulder length 50/cylindrical pin diameter 4 mm/pin height 2.2/2.6 mm/AISI 1050 steel 52 HRC
[544]	EN AW 5005	1.5	1500/2000		5/10		Cylindrical shoulder diameter 10/shoulder length 50/cylindrical pin diameter 4 mm/pin height 2.2/2.6 mm/AISI 1050 steel 52 HRC
[524]	1100	3	760/1065/ 1445/2000		40–64/28– 40/23– 57/32–40		Cylindrical shoulder diameter 10/shoulder length 55/tapered pin min diameter 3, pin length 2/5/tilt angle 10/HSS material
[525]	1100	5	1100–1500	20–60		0.1–0.5	Cylindrical shoulder diameter of 21 mm/square pin width 7 mm/pin length of 4.5 mm/tool steel
[547]	2024 up/7075 bottom	5	1500/2000/ 2500	20/40/60		3/3.3/3.6	Cylindrical shoulder diameter 16 mm/shoulder length 50 mm/cylindrical pin diameter 4 mm/pin length 2.5 mm
[548]	6063	1	1220/660/380				Cylindrical shoulder diameter 12 mm/pin length 1.7 mm/ Pin circular/square/triangular
[549]	6061-T6	2	1200/1400/ 1600/1800	10/15/20/25			Cylindrical shoulder Diameter 12/threaded pin diameter M5/pin Length 2.85/ H13 tool steel

To summarize, it can be noticed that FSSW can be applied for similar Al alloys with a thickness of up to 5 mm, although joining dissimilar 2024/7075 alloys is also possible. The FSSWed joint strength is highly affected by the pin height, TRS, WS, and welding time. The joint strength is higher than that of that of the parent material. Suresh et al. [549] reported that the FSSW process resulted in no contamination, blowholes, porosity, or cracks in the weld.

4.9. Gas Metal Arc Welding (GMAW)

Zhu et al. [550] studied welded butt joints of 5 mm thick plates made of 7003-T5 alloys, obtained by the gas metal arc welding (GMAW) method, focusing on the effect of stress concentration introduced by weld reinforcement on fatigue strength. They found that the fatigue strength of 7003-T5 alloy butt joints with weld reinforcement reached values of 50 MPa, which was 45% higher than that for joints without weld reinforcement. The fatigue source and propagation differed for the specimens with and without the welder due to the stress concentration at the weld root. The stress concentration with a factor of 1.7 strongly affected the fatigue strength but slightly influenced the TS.

Sangduang et al. [551] studied the welded joints of the 5154 alloy obtained by GMAW. They noted that weld porosity defects often occur in Al alloy welding, which affects mechanical properties. The best condition for the finest weld bead was at a current of 200 A with a travel speed of 75 cm/min.

Praveen and Yarlagadda [546] reported that fabricators of Al alloys utilize the pulse gas metal arc welding (GMAW-P) technology, facilitating a reduction in the heat input to the BM of the joined parts. It operates in one drop per pulse, providing a stable arc and producing lesser distortions and fumes. Such a technology operates with an electrode wire with a large diameter for a wider range of applications and limits wire-feeding problems in welding equipment and porosity incidence due to a lower surface area-to-volume ratio. GMAW-P provides improved deposition characteristics such as better wetting and is useful for overcoming viscosity at the joint in comparison to conventional GMAW. GMAW-P technology is well suited for joining extruded parts, as they are more tolerant to undergo fitting and can be welded with varying thickness sections.

Ramaswamy et al. [552] evaluated the tensile properties of single V butt joints of thin sheets made of the 6061-T6 alloy obtained by four variants of the GMAW process (constant current, pulsed current, cold metal transfer, and pulsed cold metal transfer) under optimized conditions. They found that the hardness in the weld metal, i.e., 79 HV, for the pulsed cold metal transfer (PCMT) joints was 14% higher than that of the continuous current GMAW joints. The PCMT-welded joint also exhibited the highest TS of 227 MPa, which was 16% higher than the continuous current GMAW joints. The fracture surface of the tensile specimens was highly dominated by dimples with tearing ridges due to high joint plastic deformation before failure, which was independent of the welding process. The PCMT joints exhibited superior tensile properties with controlled segregation of phases compared to other variants of the GMAW process due to the pulsing effect associated with the retraction of the wire.

Mercan et al. [553] studied dissimilar 5754 and 6013 alloys joined by the GMAW method under various welding parameters. While the welded samples were bent 180°, cracks and fractures occurred on the fusion line boundary due to unsuitable welding parameters. The highest toughness value was observed in the HAZ of the 5754 alloy. The toughness values in the HAZ of the 6013 alloy on the joints and weld metal were the same. The maximum hardness value was in the HAZ of the 6013 alloy, followed by that of the weld metal and that of the HAZ of the 5754 alloy. The structures of all weld metals were dendritic.

Kaushal and Sharma [554] studied the effect of GMAW parameters, including the welding current, voltage, and gas flow rate, on mechanical properties such as the TS, hardness, microstructure, and microhardness of 6mm thick alloy 6061 plates. As Al alloys exhibit large microstructural changes after welding, the welding current should be controlled as too-high values result in high heat input and the weakening of the weld profile.

Çevik [555] studied 3 mm thick 7075/T651 alloys that were joined using different welding currents via the GTAW method. They reported that the grain size of the weld center increased due to the heat input occurring with the enhancement of the welding current. Microcracks (hot cracking) appeared in the roots of welding seams. The enhancement in the welding current affected the hardness distribution of the weld zone. The impact strength

of the welded sample was negatively affected by the grain coarsening and microcracks in the welds.

Gierth et al. [189] studied the wire arc additive manufacturing of AlMg5Mn alloy by using the gas metal arc welding (GMAW) process. The temperature–time regimes affected the resulting microstructure, weld seam irregularities, and the mechanical properties of additively manufactured Al parts. Therefore, multilayer walls were built layer-wise using the cold metal transfer (CMT) process, including conventional CMT, advanced CMT, and pulse advanced arc CMT modes.

Jin et al. [556] compared the difference in pulse base currents (ΔI_b) and the difference in pulse peak currents (ΔI_p) for the welded joints of 6061-T6 alloys obtained using the double-pulse gas metal arc welding (DPGMAW). They found that changing ΔI_p caused welding defects or even welding failure. The welding stability after changing ΔI_b was much better than that after changing ΔI_p . The individual fish-scale width of the weld joint remained unchanged when ΔI_b was at various values. The average absorbed work, TS, YS, and elongation of the weld joints obtained by various $\Delta I_b/\Delta I_p$ values reached 31.1%, 60.2%, 52.9%, and 37.9% of the BM, respectively.

Gas metal arc welding (GMAW) needs trivial bevel preparation, increasing costs [557]. Kim et al. [558] studied multi-pass deposition with GMAW, noticing that it is time-consuming both with the single-wire and twin-wire methods. The use of high heat input leads to severe distortions, thus significantly limiting the productivity and weld quality obtained with this method. Gas metal arc welding (GMAW) is used for the same alloys with a thickness of up to 5 mm, although joining dissimilar 5754 and 6013 alloys is also possible. The developed type of GMAW, namely double-pulse gas metal arc welding (DPGMAW), was highlighted.

It is also worth noting the recent developments in GMAW process modeling. Rubino et al. [559] discussed a numerical sequential approach to predict the geometry of the weld line, filler deposition, heat transfer, the dimension of the HAZ, and stress–strain fields in automated GMAW. This method utilized field variables to describe phase transitions/additions and the multiphysics integration of different numerical models. The method was experimentally verified via a case study involving welding two blanks in AISI 441 steel, which is used in the automotive industry, and using AISI 307 as the filler material. The investigation focused on the base configuration of the joint and eight configurations replicating typical geometrical perturbations due to imprecise clamping or positioning of the plates.

Arghode et al. [560] elaborated on a three-dimensional transient model for heat transfer, fluid flow, and species distribution during the continuous gas metal arc welding (GMAW) of dissimilar Al alloys. The phase-change process during melting and solidification was modeled via a fixed-grid enthalpy–porosity technique, and Scheil’s model allowed for the determination of couplings among composition, temperature, and liquid fraction. The effect of adding a molten droplet to the weld pool was simulated via a “cavity” model, in which droplet heat and species addition to the molten pool were treated as volumetric heat and species sources, respectively, distributed in an imaginary cylindrical cavity within the molten pool. The developed model was applied to the case of equally thick butt-GMAW plates, one of wrought Al alloy (with about 0.5 wt.% Si) and the other of cast Al alloy (with about 10 wt.% Si), which allowed researchers to analyze the differential heating of the two alloys, asymmetric weld pool development, the mixing of the molten alloys, and the final composition after solidification.

Guo et al. [561] conducted numerical modeling and experiments on the formation of the crater in a GMAW study of Al alloy 6005-T4. The elaborated three-dimensional numerical model allowed for the calculations of a transient weld pool shape and the distributions of temperature and velocity. The final weld bead shape and dimensions were obtained therein.

To better adapt the DP-GMAW method to aluminum alloy arc additive manufacturing, Du et al. [562] optimized the single-pass deposition layer parameters (double-pulse amplitude, double-pulse frequency, and travel speed) of DP-GMAW using the response

surface method (RSM), which fitted the equation from the data of the experiment, with the width, height, and penetration of the deposition layer as response values.

Considering the occurrence of material anisotropy in modeling, the properties of aluminum alloys can be a difficult issue. Using the experimental data obtained from the GMAW process applied to 3003-H14 plates, Hernández et al. [563] developed thermomechanical simulation models for two restricted conditions, namely restricted and unrestricted thermal expansion. A double-ellipse heat distribution geometry was used to model the heat-moving source using the finite element method. Thermal rates and peak temperatures were approximated using the finite element model with a 2% difference, with respect to the experimental weld thermal cycles. The longitudinal and transverse normal residual stresses obtained agreed with experimental measurements. Larger residual stresses occurred in the transverse direction for both clamping conditions.

4.10. Magnetic Pulse Welding (MPW)

Magnetic pulse welding is more widely used to join Al alloys with steel [75,564–567], Ti alloys [568], or Mg alloys [569]. However, some applications for joining only Al alloys were also found.

According to Zhang et al. [570], magnetic pulse welding can be used for both linear welding and tubular welding of 6061-T6 components. Linear-seam MPW was performed under 4–8 kJ discharge energy with 210 kA peak current for 6061-T6 plates of 0.5 mm thickness. The standoff distance between the flyer plate and the stationary plate was 4.5 mm, and the overlap was 12.7 mm. The tubular MPW joint specimen was obtained by 45 kJ discharge energy, with 860 kA peak current. The outer and inner diameters for the 6061-T6 tube were 50.8 and 47.5 mm, respectively. The 6061-T6 rod had an outer diameter of 40.89 mm and an inner one of 25.4 mm. The standoff distance was 3.30 mm, and the overlap was set as 19.05 mm. The microstructure of MPWed joints of 6061-T6 exhibited almost one-order-of-magnitude grain refinement in the welded interface in comparison to the BMs. Large crystallographic misorientations between these grains were also observed. This resulted from local deformation caused by a high strain rate near the faying interfaces during high-velocity impact. The interface was formed by true solid-state bonding. Intensive spalling occurred away from the welded region after the tubular MPW process. In such a spalled region, the strain gradient and extensive plastic deformation occurred. The local deformation in the bulk matrix occurred away from the impacting surface due to the progression of alternating compression and tension deformation waves.

During studies on the welded joints of components made of dissimilar 4014 and 7075 alloys, using magnetic pulse welding (MPW), Pourabbas et al. [119] found that depending on collision angle and discharge energy, three different welding interfaces with wavy, molten wavy, and porous morphologies were developed. The hardness of the welding interface with the molten layer was much greater than that of the BMs because of the grain refinement phenomenon resulting from rapid melting and solidification during the MPW process. The formation of a porous welding interface resulted from gas entrapment and BM vaporization. The sample welded under a collision angle of 6° and discharge energy of 7.35 kJ showed the highest rupture force of about 13.8 kN among all samples because the wavy welding interface of this sample provided adequate bonding between the two metals. The lower rupture force of the samples welded with higher collision angles and/or discharge energy was due to the microcracks caused by huge plastic deformation.

Pereira et al. [571] reported that continuous joining along the complete perimeter of the 6083-T6 tube to the rod was provided under a combination of optimal welding parameters, including 2 kJ of discharge energy, 1 mm of standoff distance, and an impact angle above 15°, which corresponds to a six-turn coil positioned on the tube center. The obtained joint exhibited a mechanical resistance like the BM. No modifications of the grain size or precipitates were observed at the joint interface. It can be noticed that the MPW process can be applied for components made of both similar and dissimilar Al alloys and for both linear and tubular welds.

Okagawa and Aizawa [572] proposed a parallel MPW arrangement leading to seam welds between 1 mm thick Al sheets. They experimentally investigated the seam weld shearing strength affected by the kinetic energy of the sheets before the collision and magnetic pressure after the collision.

Raelison et al. [573] simulated the MPW process by assuming a linear flyer velocity distribution with a mean value of 600 m/s for Al workpieces. The simulation model allowed for the prediction of thermomechanical material flow in the form of particle jetting.

It seems that MPW can be potentially used for some pairs of both similar and dissimilar Al alloys.

4.11. Vaporizing Foil Actuator Welding (VFAW)

A vaporizing foil actuator (VFA) can be used for the impact welding of Al flyer sheets to high-strength steel and magnesium plates [574]. In VFAW, a sudden capacitor discharge produces an extremely high current via a thin conducting foil, vaporizing it instantaneously. This generates a very high-pressure plasma, accelerating the flyer plate toward the target plate [359]. Vivek et al. [575] elaborated on the so-called vaporizing foil actuator welding (VFAW) technique using the same dimensions as in magnetic pulse welding (MPW).

Hahn et al. [576] compared magnetic pulse welding and vaporizing foil actuator welding against each other using lap joints of 1 mm thick sheets made of the 5005A alloy under identical conditions in terms of charging energies of the pulse generator, specimen geometry, and initial distances between the flyer and target plate. The impact velocities obtained from rapidly vaporizing Al foils were up to three times greater than those of purely electromagnetically accelerated flyer plates. No magnetic pulse welds were achieved, while each vaporizing foil process provided a strong weld in that failure always occurred in the joining partners instead of in the weld seam during tensile tests.

Meng et al. [120] studied the microstructure of the welded joints of sheets made of 2024-T3 and 7075-T6 alloys, obtained by vaporizing foil actuator welding (VFAW). They stated that dynamic pre-forming solved the poor formability problem of the target material. However, with a standoff sheet inserted in the flyer and the target, the joints exhibited higher weld strength than that with the pre-formed flyer method. The microstructure of the circular weld area of the joint exhibited a wave interface with a thin melt layer formed at the center and edge parts. The crystal grains near the bonding interface were elongated and refined. Therefore, the weld joining was facilitated through plastic forming and melting.

Kapil [577,578] elaborated on a type of solid-state impact welding technique VFAW utilizing the high pressures from the rapid vaporization of a foil actuator to drive a flyer sheet at extremely high speeds, which causes a high-speed impact with a target sheet, leading to the formation of a solid-state joint. The process provides a joint devoid of any HAZ and thus facilitates the joining of various materials.

Kapil [577] studied the effect of natural aging and the application of heat treatments on material weldability, the mechanical properties of the joints, and the weld interface characteristics of spot welds of similar 6111-T4 alloys. Such alloys were naturally aged at room temperature for a period of 6 months and welded to themselves as-received (AR) and under a combination of different heat treatments using VFAW. It was found that aging and different heat treatment cycles had little to no effect on weldability, and all samples exhibited repeated button pullout (BP)-type failure. The joint failure was governed by the thinning and tearing of the region around the bond and affected by the mechanical properties of the BM. The strength of the welds was close to that of the parent metal. The PFHT cycle provided the highest strength values, while paint-baked samples had the highest energy absorption and ductility. The welded samples were significantly hardened compared to the BM due to severe plastic deformation upon the high-speed impact and cold working during pre-forming operations before welding. Microhardness had constant values through the weld region. Impact-induced strain hardening had the maximum effect in AR-AR samples and the least effect in PFHT-PFHT samples. The samples welded as-received and samples paint-baked after being welded as-received had similar widespread

resolidified molten zones along the wavy interface, while the PFHT-PFHT and PFHT-PFHT PB samples had very narrow and localized zones. Such resolidified molten zones were softened; however, they were observed in the weld interior and had less effect on joint performance. It can be noticed that the VFAW process can be applied for components made of both similar and dissimilar Al alloys.

Nassiri and Kinsey [579] simulated VFAW for a 2 mm thick flyer and 3 mm thick base Al plates using the arbitrary Lagrangian–Eulerian (ALE) and the smoothed particle hydrodynamics (SPH) methods. In both methods, they assumed an initial constant flyer velocity and impact angle. They found that the SPH method properly simulated material jetting but was less accurate than the ALE one.

Groche et al. [580] experimented with process window acquisition in HVIW. They used 2 mm thick Al workpieces and achieved total normal impact velocities of up to 262 m/s. When the collision point velocity exceeded the sound speed in Al, jetting did not occur, leading to the absence of bonding.

Hansen et al. [581] studied the VFAW joints of components of 0.96 mm thick 6061-T6 alloy and 0.76 mm thick 5052 alloy in lap and spot-like configurations at a variety of impact velocities. They found that welds failed in coach-peel joints outside the joint interface. The 5052 alloy hardened within 100 μm of the interface. The 6061-T6 alloy softened slightly within 50 μm of the interface.

Hansen et al. [582] reported that VFAs can be used to consistently launch AA2024 sheet metal flyers of about 0.5 mm thick to velocities between 300 and 1000 m/s within distances from 0.25 to 3 mm. The velocity can be controlled by jointly or separately varying the VFA thickness and the input energy. A faster current source provided higher pre-vaporization energy deposition (E_d), but the relationship between the ratio of E_d/E_{vap} and the vaporization pressure was linear regardless of foil thickness. Thicker foils needed more input energy to vaporize, better pressure confinement in the setup, and a higher acceleration distance. The temporal development of pressure from thinner foils was beneficial for the VFA welding setup with a shorter acceleration distance and the same workpiece velocity. The flyer sheet launch and flight were planar across the active area of the foil, with a $<0.5 \mu\text{s}$ delay in the center as compared to the edges. The delay was reduced with the increase in the E_d/E_{vap} ratio. The lag in the center can be compensated for by using a foil actuator with no end effect.

Meng et al. [583] found that VFAW was a feasible method for welding 2024/7075 alloys. The strengths of the welds made with standoff sheets were higher than those of the ones made with the pre-formed target sheet. Dynamic pre-forming is one solution for forming materials with poor formability.

VFAW is still under development; however, it can provide better results than MPW in the case of Al alloys.

The mechanical properties associated with FSW joints are better than those obtained with arc welding. Although the strength properties of welds obtained using FSW are comparable to or even lower than those obtained by laser welding or the MIG process, the fatigue performance of FSW joints is better than those produced by laser welding or the MIG process. Additionally, mismatch tolerance, low weld-to-weld variability, and exceedingly rare weld defects make the FSW process superior to competitive processes.

4.12. Aging, Gas Content, Hot Cracking, and Porosity of Al Alloys Affecting Their Welding Process

Age-hardening Al alloys commonly used in the automotive industry (for example, the 6xxx series) are usually in the T4 temper, thus exhibiting lower strengths. The strength of such alloys is enhanced by cold working and heat treatment cycles. Paint-baking (PB) cycle precipitation hardens the material to a T6 temper, and post-form heat treatment (PFHT) overages the material, sacrificing ductility for increased strength. The PB treatment of the parts painted and cured in an oven at temperatures of 180 °C allows for the development of simultaneous cure paints and strengthens the alloy [584].

The natural aging of the 6xxx series Al alloys changes their mechanical properties [585]. The prolonged natural aging of Al alloys in the T4 temper enhances the YS; however, it lowers formability and affects bending and hemming properties. Heat-treatable 6xxx series Al alloys are naturally aged by clustering and GP-zone formation, which worsens age hardenability during the PB cycle [586].

However, the precipitation strengthening effect strongly depends on the welding heat input. The improvement in the performance of joints welded by conventional fusion welding was investigated, and it was found that a large welding softening range and severe softening degree reduced the joint performance. To improve the latter, many effective methods, including low-heat-input welding methods, externally assisted cooling techniques, and post-weld treatment techniques, were adopted. However, the joint performance remains lower than that of the base metal but can be further improved. The PWHT for dissimilar age-hardening Al alloys is a challenge because various base metals need different optimal treatment processes. Therefore, it is necessary to conduct further studies in such areas [16].

Al castings from various processes possess different gas content, surface finish, and mechanical properties, causing variations in joinability by fusion welding and mechanical joining [587].

Various grades of Al castings exhibit different degrees of cracking susceptibility and joint porosity issues. Al-Si alloys are less sensitive to solidification cracking during welding, while Al-Cu, Al-Mg, Al-Mg-Si, and Al-Zn-Mg alloys are more sensitive to it. A higher solidification/freezing range leads to higher susceptibility to hot cracking, whereas a higher fraction of the eutectic phase in the microstructure and a eutectic phase with sufficient wettability result in lower susceptibility to hot cracking. The same grade of castings obtained from different casting processes can differ in their gas content and joinability. Castings made by high-quality high-pressure die casting (HPDC), squeeze casting, and semi-solid metal SSM casting possess a much lower gas content [587].

The important problem during the welding of components made of Al alloys is the gas content therein. Friction stir welding (FSW) is less sensitive than other welding techniques in terms of the gas content of cast Al components. However, FSW is only suitable for simple smooth welding lines, welded components should be clamped rigidly, and a backing plate is needed for poorly stiff components. The Al castings for fusion welding need to have low gas content like hydrogen. Air pockets and hydrogen content in cast Al components induce porosity in the weld bead. Due to the large weld pool and lower welding speed, arc welding processes are less sensitive to gas content, and therefore the parameters for degassing are very important. Electron-beam welding is the least sensitive fusion welding process to gas content due to the degassing effect of vacuum, although the size of the welded components is limited. Due to outgassing, high heating and cooling rates, and complex weld fluid flow, laser welding is the most sensitive to gas content, and for this reason, Al castings for laser welding need very low gas content to avoid high porosity in the welded joints. Hybrid welding, with a combination of laser beam welding and TIG or MIG welding, can be beneficial to the welding of Al castings [587].

Electron-beam welding, using a multiple-process technique, or hybrid laser welding can configure the molten baths to facilitate degassing and limit inhomogeneous porosity in the joint area. With such processes, joints with low porosity can be achieved [587].

Mechanical joining methods, such as SPR and clinching, are not as sensitive to gas content as fusion welding processes, but Al castings should be ductile enough to limit the generation of severe cracks during the joining process. Sometimes, the heat treatment of Al castings increases their ductility. Using process optimization can limit the number and severity of the cracks generated [587].

The FSW process is advised for heat-treatable Al alloys prone to hot cracking [512].

As to fusion welding and the FSW of Al castings, if the casting is suitable for heat treatment, then heat treatment after welding or a combination of pre- and post-welding heat treatments more efficiently improves joint mechanical properties than heat treatment before welding. The heat treatment used before the welding process has no effect on the

improvement in the mechanical properties of the joint. For mechanical joining processes such as SPR and clinching, because sufficient ductility in Al castings is required to avoid severe cracking, heat treatments to improve ductility will need to be conducted before the joining procedure [587].

A still unsolved problem is the hot cracking of welded components made of Al alloys, particularly casting ones. Hot cracking susceptibility is affected by alloying content, grain structures, solidification rate, constraints, etc. During fusion welding, hot cracking can be limited using proper filler wires, adding grain refining elements, reducing welding speed, using methods to limit residual stress or solidification rate, etc. To diminish the occurrence of such cracking, excess material restraint should be avoided. For crack-sensitive alloys, careful selection and control of process parameters, together with the use of an appropriate filler wire, provide high-quality welds. Welded Al alloys should have a weld metal composition away from the peak of the crack sensitivity curve. Dual-beam laser welding, electron-beam welding, and laser-arc hybrid welding are beneficial for reducing solidification cracks [587].

The other unsolved problem encountered during the welding of components made of Al alloys is porosity, which causes the loss of mechanical strength, creep, fatigue, and corrosion failures [585].

Porosity is formed during the fusion welding of Al castings due to the following factors:

- The absorption and subsequent entrapment of ambient gases during welding;
- The existing gas content in the base material;
- The entrapment of gas bubbles due to the imperfect collapse of the keyhole during keyhole welding [587].

Hydrogen is the main compound causing porosity and it exists in this process due to its significantly different solubility in liquid and solid Al. Cleaning the surface of parts before welding reduces the source of hydrogen and the resulting porosity. The optimized welding parameters limit the joint porosity of Al castings, but the most efficient way is to improve the casting process to reduce the gas content of cast parts. The following methods limit the welding porosity of Al casting: laser-arc hybrid welding, dual-beam laser welding, electron-beam welding, beam oscillation, electromagnetic field degassing, etc. Increasing the size of the weld pool and reducing the solidification rate gives more time for the gas bubbles to move out of the weld pool, which is beneficial for reducing weld porosity [587].

5. Summary

This review, apart from capturing the current state of the art, evaluated reaching the possible highest joint quality and the disadvantages of welding such as porosity, poor surface quality, a tendency toward hot cracking, and low ductility for Al alloys applied in the automotive industry.

The joining of various components made of various Al alloys, both casting and wrought, that are used in the automotive industry is a complex problem. The components used in electrical vehicles can be joined by conventional adhesive bonding, weld bonding and self-piercing riveting, friction stir spot welding, ultrasonic spot welding, laser braze welding, and cold metal transfer welding [588]. Despite the prevalence of advantages, the welding of Al alloys with MIG and TIG processes, commonly used in the automotive industry, can be accompanied by either poor functional properties of the joint or low relative efficiency [43,44].

The TIG and MIG techniques are suitable for the fusion welding of most of the wrought grades in the 1XXX, 3XXX, 5XXX, and 6XXX series; particularly, the 5XXX alloys exhibit excellent weldability. They are also well suited for medium-strength 7XXX series alloys. Fusion welding is recommended for high-strength alloys, such as 7010 and 7050, whereas the majority of the 2XXX alloys are not advised due to being prone to liquefaction and solidification.

The FSW process is well suited for producing sound welds in Al alloys and is a suggested method for heat-treatable alloys prone to hot cracking [512]. It is also well suited

for Al/steel combination [364]. Laser welding is applicable for Al/Al joints [29,206,207] and for dissimilar joints of some steel types (stainless steel, low-carbon steel, etc.), and Al alloys such as 1050, 5052, 5083, 6016, 6061, 6082, 6111, and 7075.

Resistance spot welding is also appropriate for both Al/Al joints [251] and Al/steel joints [239]. However, Al alloys are harder to join using resistance spot welding compared to steels due to their high conductivity and the oxide layer on the surface. Casting alloys are harder to join using this technique compared to wrought alloys as they have lower melting temperatures due to higher amounts of added elements, more porosities, and inconsistent thicknesses [589].

Joining Al castings is difficult due to their often-occurring porosity, poor surface quality, a tendency toward hot cracking, and low ductility [587].

Al castings can be joined via friction stir welding, CMT, laser welding, arc welding, electron-beam welding, laser-arc hybrid welding, self-piercing riveting, clinching, flow drill screw, etc. The abovementioned and other welding techniques are also used for joining both similar and dissimilar Al wrought alloys that are applied in the automotive industry; however, it can be noticed that the friction stir welding process is the most often used. Additionally, other forms of the FSW process are being developed, for example, FSSW.

CMT welding is an expected method for joining thin sheets and plates made of Al alloys [175,185]; however, its use is limited by spatter and the distortion of joints and requires limited cleanup. CMT requires less current for the same amount of material deposition in comparison with conventional pulsed MIG welding [175].

In particular, successful FSW joining of Al alloys was obtained between, inter alia, 6061/7050 [334], 6061/7075 [503], 6082/2024 [298], 2024/7075 [340,590], 5083/6351 [204], 2219/5083 [202], 6082/7075 [591], 6061/5086 [189], and 2219/7039 [592]. This welding technique seems to be quite universal, relative to the automotive industry, as it is also applicable to common joints between dissimilar Al alloy/steel [593] and dissimilar Al/Cu alloys [594].

The thermal, mechanical, and metallurgical aspects of the FSW process are very complex, and their possible interactions impede the determination of the effects of individual process parameters on joint strength, microhardness, or other mechanical properties.

The effect of Al alloys' position on the FSW joint properties is seldom studied, as some authors probably based their studies on recommendations from the literature for a given pair of Al alloys. Therefore, more such studies are needed for various Al alloys' placements.

Similarly, some authors, in the case of TRS, WS, and, less often, AF, only provide their values without examining their effect on the FSW joint properties, neither separately nor in combination. The mentioned values are probably based on recommendations from the literature for specific combinations of components made of Al alloys. Therefore, more studies are needed for the optimization of combinations comprising such FSW process parameters for various arrangements of Al alloys.

Tool geometry highly affects metal flow, heat generation, the stirring effect, and recrystallization; thus, the correlation between material flow and the resultant microstructure of the FSW joints is distinct in each tool.

Also, laser welding is a very often used technique for various Al alloys in the automotive industry; however, classical MIG and TIG methods are also often applied in practice. They can be linked, as in the case of laser-MIG hybrid welding or plasma-MIG welding, providing even better weld quality.

The use of laser welding and FSW for joining various Al alloys can help to obtain a WE close to or even exceeding 100%. The use of laser welding for Al alloys can be limited by the occurrence of porosity related to the hydrogen released from the solid phase during solidification, partial keyhole collapse, swirl flow in the welding bath, the selective evaporation of Mg and Zn reducing the degree of hardening and mechanical properties, hot cracks, and high reflection [595].

Underwater friction stir welding (UFSW) can provide a higher WE compared to the classic FSW process [419].

The mechanical properties and microstructure of FSW joints can be improved by grain refinement via reinforcement with micro- and nanosized solid particles, for example, SiC or TiC [528].

Commonly used fusion welding techniques like RSW leads to inhomogeneous material microstructure distribution and the presence of a HAZ, reducing the mechanical and fatigue properties of the produced joints, as described in [596].

Electron-beam welding is advantageous for joining Al alloys compared to other traditional fusion welding methods due to its high energy density, deep penetration, large depth-to-width ratio, and exceedingly small HAZ [239]. However, EBWed joints are sensitive to a proper combination of process parameters as their improper selection induces joint defects affecting the weld mechanical properties [597].

Solid-state welding techniques like FSW, impact welding, UW, etc., can replace conventional fusion welding techniques and mechanical fastening processes, as mentioned in [549]. Age-hardening Al alloys widely used in the automotive industry exhibited high specific strength, good formability, and corrosion resistance [16]. The aging of components after their welding using various welding processes can be a good practice in the case of some Al alloys, for example, 6061-T4 one, as it significantly improves weld strength; however, it depends on the joint type, joined materials, and filler metal [598].

Author Contributions: Conceptualization, A.R. and B.D.; Methodology, K.S.; Software, M.W.; Validation, A.O., B.D. and A.R.; Formal Analysis, M.W.; Investigation, A.R.; Resources, K.S.; Data Curation, A.R.; Writing—Original Draft Preparation, K.S.; Writing—Review and Editing, A.O.; Visualization, M.W.; Supervision, A.R.; Project Administration, B.D.; Funding Acquisition, B.D. All authors have read and agreed to the published version of the manuscript.

Funding: This research received no external funding.

Institutional Review Board Statement: Not applicable.

Informed Consent Statement: Not applicable.

Data Availability Statement: All data are presented in the paper.

Conflicts of Interest: Authors declare no conflicts of interest.

Abbreviations

AA	artificial aging
AGG	abnormal grain growth
AGS	average grain size
AR	as-received
ARBed	accumulative roll-bonded
AS	advancing side
BM	base metal
BMW	base material welded
BMZ	base material zone
BP	button pullout
CFRPs	carbon fiber reinforced plastics
CET	columnar to equiaxed transition
CLD	cold lap defect
CMT	cold metal transfer
DC	direct current
DPGMAW	double pulse gas metal arc welding
DXZs	dynamically recrystallized zones
DSAW	double-sided double-arc welding
DSFSW	double spot friction stir welding
DSZFSW	double spot zigzag friction stir welding
EB	electron beam
EBSD	electron backscatter diffraction
EBW	electron beam welding

EXW	explosive welding
FCG	fatigue crack growth
FCP	fatigue crack propagation
FSP	friction stir processing
FSLW	friction stir lap welding
FSW	friction stir welding
FSSWed	friction stir spot welded
FZs	fusion zones
FSWed	friction stir welded
GMA	gas metal arc
GP zones	Guinier-Preston zones
GMAW	gas metal arc welding
GTAW	gas-tungsten-arc welding
HAZ	heat affected zone
HD	hook defect
HSS	high-strength steel
HTAW	heat treatment after welding
HTBW	heat treatment before welding
JI	J integral
KI	stress intensity factor
LADSW	laser double sided welding
LB	laser beam
LBW	laser beam welded
LIW	laser impact welding
MCZ	material concentrated zone
MIG	metal inert gas
MMCs	metal matrix composites
MPW	magnetic pulse welding
MPWed	magnetic pulse welded
NA	natural ageing
NZ	nugget zone
NVEB	nonvacuum electron beam
PAW	plasma arc welding
PB	paint baking
PCMT	pulsed cold metal transfer
PFHT	post form heat treatment
PGMAW	pulse gas metal arc welding
PWHT	post weld heat treatment
PM	parent material
PMZ	partially melted zone
RFSP	reverse of rotation of stir processing
RP	revolutionary pitch
RS	retreating side
RSW	resistance spot welding
RWF	reciprocating wire feeding
SCR	silicon controlled rectifier
SCC	stress corrosion cracking
SWed	stir welded
SFSSW	swept friction stir spot welding
STC	straight cylindrical
SZ	stir zone
TAC	tapered cylindrical
THC	threaded cylindrical
TIG	tungsten inert gas
TMAZ	thermo mechanically affected zone
TRS	tool rotational speed
TS	tensile strength/stress
TWBs	tailor welded blanks

UFG	ultrafine grain
UFGed	ultrafine grained
UFM	unaffected material
UFSW	underwater friction stir weld
UFSWed	underwater friction stir welded
UTS	ultimate tensile strength
VFA	vaporizing foil actuator
VFAW	vaporizing foil actuator welding
WAAM	wire arc additive manufacturing
WN	weld nugget
WNZ	weld nugget zone
WS	welding speed
WZ	welded zone
YS	yield strength

References

- Dzikuc, M.; Adamczyk, J.; Piwowar, A. Problems associated with the emissions limitations from road transport in the Lubuskie Province (Poland). *Atmos. Environ.* **2017**, *160*, 1–8. [[CrossRef](#)]
- Lyu, P.; Wang, P.S.; Liu, Y.; Wang, Y. Review of the studies on emission evaluation approaches for operating vehicles. *J. Traffic Transp. Eng. (Engl. Ed.)* **2021**, *8*, 493–509. [[CrossRef](#)]
- Angnunavuri, P.N.; Kuranchie, F.A.; Attiogbe, F.; Nerquaye-Tetteh, E.N. The potential of integrating vehicular emissions policy into Ghana's transport policy for sustainable urban mobility. *SN Appl. Sci.* **2019**, *1*, 1201. [[CrossRef](#)]
- Correia, G.N.; Batista, T.P.; Marques, S.S.; Silva, C.M. How car material life-cycle emissions are considered in environmental rating methodologies? Suggestion of expedite models and discussion. *Renew. Sustain. Energy Rev.* **2014**, *38*, 20–35. [[CrossRef](#)]
- Serrenho, A.C.; Norman, J.B.; Allwood, J.M. The impact of reducing car weight on global emissions: The future fleet in Great Britain. *Philos. Trans. A Math. Phys. Eng. Sci.* **2017**, *375*, 20160364. [[CrossRef](#)] [[PubMed](#)]
- Neuer Audi Space Frame Mit Hohem Anteilen an Aluminium und CFK-Audi Technology Portal (audi-technology-portal.de). Available online: <https://www.audi-technology-portal.de/de/karosserie/aluminiumkarosserien/neuer-audi-space-frame-mit-hohen-anteilen-an-aluminium-und-cfk> (accessed on 15 April 2024).
- Anwar, M.; Cahyono, S.I.; Wijang, W.R.; Diharjo, K. Application of Carbon Fiber-Based Composite for Electric Vehicle. *Adv. Mater. Res.* **2014**, *896*, 574–577. [[CrossRef](#)]
- Ahmad, H.; Markina, A.A.; Porotnikov, M.V.; Ahmad, F. A review of carbon fiber materials in automotive industry. In *IOP Conference Series: Materials Science and Engineering*; IOP Publishing: Bristol, UK, 2020; Volume 971, p. 032011.
- Harrison, N.R.; Luckey, S.G. Hot Stamping of a B-Pillar Outer from High Strength Aluminum Sheet AA7075. *SAE Int. J. Mater. Manuf.* **2014**, *7*, 567–573. [[CrossRef](#)]
- Kutsuna, M.; Kitamura, S.; Shibata, K.; Sakamoto, H.; Tsushima, K. Improvement of the joint performance in laser welding of aluminium alloys. *Weld. World* **2006**, *50*, 22–27. [[CrossRef](#)]
- AlShaer, A.W.; Li, L.; Mistry, A. Effect of filler wire properties on porosity formation in laser welding of AC-170PX aluminium alloy for light-weight automotive component manufacture. *Proc. Inst. Mech. Eng. Part B J. Eng. Manuf.* **2015**, *231*, 1–13.
- Arun, N.; Cijo, M.; Joby, J. Influence of Gas Tungsten Arc welding parameters in Aluminium 5083 alloy. *Inter. J. Eng. Sci. Inno. Technol.* **2013**, *2*, 269–277.
- Kumar, A.; Sundarajan, S. Optimization of pulsed TIG welding process parameters on mechanical properties of AA 5456 Aluminum alloy weldments. *Mater. Des.* **2009**, *30*, 1288–1297. [[CrossRef](#)]
- Szczucka-Lasota, B.; Wegrzyn, T.; Jur, A. Aluminum alloy welding in automotive industry. *Transp. Probl.* **2020**, *15*, 67–78. [[CrossRef](#)]
- Red-Bag. Joint Quality Factor (Joint Efficiency Coefficient). PCC User Manual Version 4.4.x. Calculation. 10 January 2024. Available online: <https://redbag.com/pcc/doc/calculations/jointqualityfactor.html> (accessed on 15 April 2024).
- Cheng, J.; Song, G.; Zhang, X.; Liu, C.; Liu, L. Review of Techniques for Improvement of Softening Behavior of Age-Hardening Aluminum Alloy Welded Joints. *Materials* **2021**, *14*, 5804. [[CrossRef](#)] [[PubMed](#)]
- Torzewski, J.; Łazińska, M.; Grzelak, K.; Szachogłuchowicz, I.; Mierzyński, J. Microstructure and Mechanical Properties of Dissimilar Friction Stir Welded Joint AA7020/AA5083 with Different Joining Parameters. *Materials* **2022**, *15*, 1910. [[CrossRef](#)] [[PubMed](#)]
- von Strombeck, A.; dos Santos, J.F.; Torster, F.; Laureano, P.; Kogak, M.; Threadhill, P.L. (Eds.) Fracture Toughness Behaviour of FSW Joints on Aluminium Alloys. In Proceedings of the First International Symposium on Friction Stir Welding—Proceedings, Thousands Oaks, CA, USA, 14–16 June 1999; CD-ROM. The Welding Institute Ltd.: Cambridge, UK, 1999.
- Kim, S.S.; Kang, D.H.; Jeong, Y.J.; Park, J.M. Experimental Investigation on Tensile Test Properties of EB Welded Joints of Aluminum 6061-T6 Alloy for Plate-type Fuel Assembly Fabrication. In Proceedings of the Transactions of the Korean Nuclear Society Spring Meeting, Jeju, Republic of Korea, 23–24 May 2019.
- Lippold, J.C. *Welding Metallurgy and Weldability*; John Wiley & Sons, Inc.: Hoboken, NJ, USA, 2015.

21. Wojdat, T.; Kustróń, P.; Jaśkiewicz, K.; Pabian, J. Study of Corrosion, Structural, and Mechanical Properties of EN AW-6082 and EN AW-7075 Welded Joints. *Materials* **2021**, *14*, 4349. [CrossRef] [PubMed]
22. Lee, J.; Park, S.-Y.; Choi, B.-H. Evaluation of Fatigue Characteristics of Aluminum Alloys and Mechanical Components Using Extreme Value Statistics and C-Specimens. *Metals* **2021**, *11*, 1915. [CrossRef]
23. Li, H.; Gao, J.; Li, Q. Fatigue of Friction Stir Welded Aluminum Alloy Joints: A Review. *Appl. Sci.* **2018**, *8*, 2626. [CrossRef]
24. Bahaideen, F.B.; Saleem, A.M.; Hussain, K.; Ripin, Z.M.; Ahmad, Z.A.; Samad, Z.; Badarulzaman, N.A. Fatigue Behaviour of Aluminum Alloy at Elevated Temperature. *Mod. Appl. Sci.* **2009**, *3*, 52–61. [CrossRef]
25. Azadi, M.; Aroo, H. Creep properties and failure mechanisms of aluminum alloy and aluminum matrix silicon oxide nano-composite under working conditions in engine pistons. *Mater. Res. Express* **2019**, *6*, 115020. [CrossRef]
26. Chen Pfan, X.; Yang, Q.; Zhang, Z.; Jia, Z.; Liu, Q. Creep behavior and microstructural evolution of 8030 aluminum alloys compressed at intermediate temperature. *J. Mater. Res. Technol.* **2021**, *12*, 1755–1761. [CrossRef]
27. Li, Z.; Fu, X.-S.; Chang, Z.-L.; Zhou, W.L.; Chen, G.-Q. Creep behavior and forecast of welded joint for 2219T87 aluminum alloy at room temperature. *Zhongguo Youse Jinshu Xuebao/Chin. J. Nonferrous Met.* **2014**, *24*, 2235–2242.
28. Fourmeau, M.; Børvik, T.; Benallal, A.; Hopperstad, O.S. Anisotropic failure modes of high-strength aluminium alloy under various stress states. *Int. J. Plast.* **2013**, *48*, 34–53. [CrossRef]
29. Bunaziv, I.; Akselsen, O.M.; Ren, X.; Nyhus, B.; Eriksson, M. Laser Beam and Laser-Arc Hybrid Welding of Aluminium Alloys. *Metals* **2021**, *11*, 1150. [CrossRef]
30. Petrie, E.M. Adhesive Bonding of Aluminum Alloys. *Met. Finish.* **2007**, *105*, 49–56. [CrossRef]
31. Li, Y.D.; Zhao, P.Z.; Feng, Y.J.; Cao, H.L. Influence of anodic oxide film structure on adhesive bonding performance of 5754 aluminum alloy. *Trans. Nonferrous Met. Soc. China* **2019**, *29*, 1836–1841. [CrossRef]
32. Lathabai, S. 20—Joining of Aluminium and Its Alloys. In *Metals and Surface Engineering, Fundamentals of Aluminium Metallurgy*; Lumley, R., Ed.; Woodhead Publishing: Cambridge, UK, 2011; pp. 607–654.
33. He, X. A review of finite element analysis of adhesively bonded joints. *Int. J. Adhes. Adhes.* **2011**, *31*, 248–264. [CrossRef]
34. Barnes, T.A. Pashby IR 99 Joining techniques for aluminium spaceframes used in automobiles: Part II—Adhesive bonding mechanical fasteners. *J. Mater. Process. Technol.* **2000**, *99*, 72–79. [CrossRef]
35. Groche, P.; Wohletz, S.; Brenneis, M.; Pabst, C.; Resch, F. Joining by forming—A review on joint mechanisms, applications and future trends. *J. Mater. Process. Technol.* **2014**, *214*, 1972–1994. [CrossRef]
36. Kim, D.C.; Park, H.J.; Hwang, I.S.; Kang, M.J. Resistance spot welding of aluminum alloy sheet 5J32 using SCR type and inverter type power supplies. *Arch. Mater. Sci. Eng.* **2009**, *38*, 55–60.
37. Sun, Z.; Karppi, R. The application of electron beam welding for the joining of dissimilar metals: An overview. *J. Mater. Process. Technol.* **1996**, *59*, 257–267. [CrossRef]
38. Selvi, S.; Vishvakshnan, A.; Rajasekar, E. Cold metal transfer (CMT) technology—An overview. *Def. Technol.* **2018**, *14*, 28–44. [CrossRef]
39. Singh, L.; Singh, R.; Singh, N.K.; Singh, D.; Singh, P. An Evaluation of TIG Welding Parametric Influence on Tensile Strength of 5083 Aluminum Alloy. *Int. J. Mech. Ind. Sci. Eng.* **2013**, *7*, 795–798.
40. Liu, Y.; Wang, W.; Xie, J.; Sun, S.; Wang, L.; Qian, Y.; Meng, Y.; Wei, Y. Microstructure and mechanical properties of aluminum 5083 weldments by gas tungsten arc and gas metal arc welding. *Mater. Sci. Eng. A* **2012**, *549*, 7–13. [CrossRef]
41. Wadelton, F. Aluminum 7005-6061 Custom Frames. Bicycle Fabrication. Available online: www.frankthewelder.com (accessed on 15 April 2024).
42. How To Advice and Tips for Welders of All Experience Levels. 10 January 2024. Available online: <https://www.weldinghandbook.com/types-of-welding/> (accessed on 15 April 2024).
43. Haboudou, A.; Peyre, P.; Vannes, A.B.; Peix, G. Reduction of porosity content generated during Nd:YAG laser welding of A356 and AA5083 aluminium alloys. *Mater. Sci. Eng.* **2003**, *363*, 40–52. [CrossRef]
44. Peng, Z.; Yang, S.; Wang, Z.; Gao, Z. Fatigue Property and Small Crack Propagation Mechanism of MIG Welding Joint of 6005A-T6 Aluminum Alloy. *Materials* **2022**, *15*, 4698. [CrossRef] [PubMed]
45. Grujicic, M.; Arakere, G.; Pandurangan, B.; Hariharan, A.; Yen, C.-F.; Cheeseman, B.A. Development of a Robust and Cost-Effective Friction Stir Welding Process for Use in Advanced Military Vehicles. *J. Mater. Eng. Perform.* **2011**, *20*, 11–23. [CrossRef]
46. Hamilton, C.; Dymek, S.; Kopyściański, M.; Węglowska, A.; Pietras, A. Numerically Based Phase Transformation Maps for Dissimilar Aluminum Alloys Joined by Friction Stir-Welding. *Metals* **2018**, *8*, 324. [CrossRef]
47. Yoon, T.-J.; Yun, J.-G.; Kang, C.-Y. Formation mechanism of typical onion ring structures and void defects in friction stir lap welded dissimilar aluminum alloys. *Mater. Des.* **2016**, *90*, 568–578. [CrossRef]
48. Mishra, R.S.; Ma, Z.Y. Friction stir welding and processing. *Mater. Sci. Eng. R Rep.* **2005**, *50*, 1–78. [CrossRef]
49. Mishra, R.; Komarasamy, M. *Friction Stir Welding of High Strength 7XXX Aluminum Alloys. 1*; Butterworth-Heinemann: Waltham, MA, USA, 2016; ISBN 978-0-12-809465-5.
50. Mishra, R.; Sidhar, H. *Friction Stir Welding of 2XXX Aluminum Alloys including Al-Li Alloys. 1*; Butterworth-Heinemann: Waltham, MA, USA, 2016; ISBN 978-0-12-805368-3.
51. Uday, M.B.; Fauzi, M.N.A.; Zuhailawati, H.; Ismail, A.B. Advances in friction welding process: A review. *Sci. Technol. Weld. Join* **2010**, *15*, 534–558. [CrossRef]

52. Threadgill, P.L.; Leonard, A.J.; Shercliff, H.R.; Withers, P.J. Friction stir welding of aluminium alloys. *Int. Mater. Rev.* **2009**, *54*, 49–93. [[CrossRef](#)]
53. Kumar, N.; Mishra, R.; Yuan, W. *Friction Stir Welding of Dissimilar Alloys and Materials*. [ed.]; Butterworth-Heinemann: Waltham, MA, USA, 2015; ISBN 978-0-12-802418-8.
54. DebRoy, T.; Bhadeshia, H.K.D.H. Friction stir welding of dissimilar alloys: A perspective. *Sci. Technol. Weld. Join* **2010**, *15*, 266–270. [[CrossRef](#)]
55. Murr, L.E. A review of FSW research on dissimilar metal and alloy systems. *J. Mater. Eng. Perform.* **2010**, *19*, 1071–1089. [[CrossRef](#)]
56. Chen, Y.C.; Liu, H.J.; Feng, J.C. Friction stir welding characteristics of different heat-treated-state 2219 aluminum alloy plates. *Mater. Sci. Eng. A* **2006**, *420*, 21–25. [[CrossRef](#)]
57. Liu, H.J.; Fujii, H.; Maeda, M.; Nogi, K. Tensile properties and fracture locations of friction stir welded joints of 2017-T351 aluminum alloy. *J. Mater. Process. Technol.* **2003**, *142*, 692–696. [[CrossRef](#)]
58. Meng, X.C.; Xu, Z.; Huang, Y.; Xie, Y.; Wang, Y.; Wan, L.; Lv, Z.; Cao, J. Interface characteristic and tensile property of friction stir lap welding of dissimilar aircraft 2060-T8 and 2099-T83 Al-Li alloys. *Int. J. Adv. Manuf. Technol.* **2018**, *94*, 1253–1261. [[CrossRef](#)]
59. Costa, M.L.; Verdera, D.; Leitão, C.; Rodrigues, D.M. Dissimilar friction stir lap welding of AA 5754-H22/AA 6082-T6 aluminium alloys: Influence of material properties and tool geometry on weld strength. *Mater. Des.* **2015**, *87*, 721–731. [[CrossRef](#)]
60. Lohwasser, D.; Chen, Z. (Eds.) Industrial applications of friction stir welding. In *Welding and Other Joining Technologies, Friction Stir Welding*; Woodhead Publishing: Cambridge, UK, 2010; pp. 118–163.
61. Ge, Z.; Gao, S.; Ji, S.; Yan, D. Effect of pin length and welding speed on lap joint quality of friction stir welded dissimilar aluminum alloys. *Int. J. Adv. Manuf. Technol.* **2018**, *98*, 1461–1469. [[CrossRef](#)]
62. Khan, N.Z.; Khan, Z.A.; Siddiquee, A.N. Effect of Shoulder Diameter to Pin Diameter (D/d) Ratio on Tensile Strength of Friction Stir Welded 6063 Aluminium Alloy. *Mater. Today Proc.* **2015**, *2*, 1450–1457. [[CrossRef](#)]
63. Vimalraj, C.; Kah, P. Experimental Review on Friction Stir Welding of Aluminium Alloys with Nanoparticles. *Metals* **2011**, *11*, 390. [[CrossRef](#)]
64. Burek, R.; Wydrzyński, D.; Sęp, J.; Więckowski, W. The effect of tool wear on the quality of lap joints between 7075 T6 aluminum alloy sheet metal created with the FSW method. *Ekspluat. Niezawodn. Maint. Reliab.* **2018**, *20*, 100–106. [[CrossRef](#)]
65. Brown, B.M. A comparison of AC and DC resistance welding of automotive steels. *Weld. J.* **1987**, *66*, 18–23.
66. Guo, H.; Hu, J.; Tsai, H.L. Three-Dimensional Modeling of Gas Metal Arc Welding of Aluminum Alloys. *ASME J. Manuf. Sci. Eng.* **2010**, *132*, 021011. [[CrossRef](#)]
67. Furukawa, K. New CMT arc welding process—Welding of steel to aluminium dissimilar metals and welding of super-thin aluminium sheets. *Weld Int.* **2006**, *20*, 440–445. [[CrossRef](#)]
68. Chinnasamy, R.; Chelladurai, S.J.S.; Sonar, T. Investigation on Microstructure and Tensile Properties of High-Strength AA2014 Aluminium Alloy Welds Joined by Pulsed CMT Welding Process. In *Advances in Materials Science and Engineering (Hindawi)*; Adam House: London, UK, 2021; p. 8163164.
69. Pickin, C.G.; Young, K. Evaluation of cold metal transfer (CMT) for welding aluminium alloy. *Sci. Technol. Weld Join* **2006**, *11*, 583–585. [[CrossRef](#)]
70. Pickin, C.G.; Williams, S.W.; Lunt, M. Characterisation of the cold metal transfer (CMT) process and its application for low dilution cladding. *J. Mater. Process. Technol.* **2011**, *211*, 496–502. [[CrossRef](#)]
71. Kah, P.; Suoranta, R.; Martikainen, J. Advanced gas metal arc welding processes. *Int. J. Adv. Manuf. Technol.* **2013**, *67*, 655–674. [[CrossRef](#)]
72. Schierl, A. The CMT-process—A revolution in welding technology. *Weld World* **2005**, *49*, 38.
73. Gullino, A.; Matteis, P.; D’Aiuto, F. Review of Aluminum-To-Steel Welding Technologies for Car-Body Applications. *Metals* **2019**, *9*, 315. [[CrossRef](#)]
74. Dutra, J.C.; Goncalves e Silva, R.H.; Marques, C. Melting and welding power characteristics of MIG–CMT versus conventional MIG for aluminium 5183. *Weld Int.* **2015**, *29*, 181–186. [[CrossRef](#)]
75. Zhang, Y. Investigation of magnetic pulse welding on lap joint of similar and dissimilar materials. Ph.D. Thesis, The Ohio State University, Columbus, OH, USA, 2010.
76. Bellmann, J.; Lueg-Althoff, J.; Niessen, B.; Böhme, M.; Schumacher, E.; Beyer, E.; Leyens, C.; Tekkaya, A.; Groche, P.; Wagner, F.-X.; et al. Particle Ejection by Jetting and Related Effects in Impact Welding Processes. *Metals* **2020**, *10*, 1108. [[CrossRef](#)]
77. Niessen, B.; Schumacher, E.; Lueg-Althoff, J.; Bellmann, J.; Böhme, M.; Böhm, S.; Tekkaya, A.E.; Beyer, E.; Leyens, C.; Wagner, M.F.-X. Interface Formation during Collision Welding of Aluminum. *Metals* **2020**, *10*, 1202. [[CrossRef](#)]
78. Wang, H.; Wang, Y. High-Velocity Impact Welding Process: A Review. *Metals* **2019**, *9*, 144. [[CrossRef](#)]
79. Schumacher, E.; Rebensdorf, A.; Böhm, S. Influence of the jet velocity on the weld quality of magnetic pulse welded dissimilar sheet joints of aluminum and steel. *Materialwiss. Werkst.* **2019**, *50*, 965–973. [[CrossRef](#)]
80. Carpenter, S.H.; Wittman, R.H. Explosion Welding. *Ann. Rev. Mater. Sci.* **1975**, *5*, 177–199. [[CrossRef](#)]
81. Deribas, A.A.; Zakharenko, I.D. Surface effects with oblique collisions between metallic plates. *Combust. Explos. Shock Waves* **1974**, *10*, 358–367. [[CrossRef](#)]
82. Patra, S.; Arora, K.S.; Shome, M.; Bysakh, S. Interface characteristics and performance of magnetic pulse welded copper-Steel tubes. *J. Mater. Process. Technol.* **2017**, *245*, 278–286. [[CrossRef](#)]

83. Zhang, Y.; Babu, S.S.; Prothe, C.; Blakely, M.; Kwasegroch, J.; LaHa, M.; Daehn, G.S. Application of high velocity impact welding at varied different length scales. *J. Mater. Process. Technol.* **2011**, *211*, 944–952. [[CrossRef](#)]
84. Kapil, A.; Sharma, A. Magnetic pulse welding: An efficient and environmentally friendly multi-material joining technique. *J. Clean. Prod.* **2015**, *100*, 35–58. [[CrossRef](#)]
85. Jassim, A. Comparison of magnetic pulse welding with other welding methods. *J. Energy Power Eng.* **2011**, *5*, 1173–1178.
86. Aizawa, T.; Kashani, M.; Okagawa, K. Application of Magnetic Pulse Welding for Aluminum Alloys and SPCC Steel Sheet Joints. *Weld. J.* **2007**, *86*, 119–124.
87. Qi, N.; Wang, L.; Zhao, Y.; Tian, S.; Zhan, X. The tensile properties of 2219 aluminum alloy plate butt joint welded by novel laser mirror welding. *Opt. Laser Technol.* **2022**, *149*, 107796. [[CrossRef](#)]
88. Theron, M.; Burger, H.P.; Van Rooyen, C.; Ivanchev, L.H. Laser welding of A357 aluminium alloy. In *International Congress on Applications of Lasers & Electro-Optics*; Laser Institute of America: Orlando, FL, USA, 2008; Volume P112.
89. Peterson, W.; Pakalnins, E.; Carpenter, J.A. *Longlife Electrodes for Resistance Spot Welding of Aluminium Sheet Alloys and Coated High Strength Steel Sheet*; FY Progress Report; U.S. Department of Energy Hydrogen Program Contractor: Washington, DC, USA, 2004; pp. 237–244.
90. Boomer, D.R.; Hunter, J.A.; Castle, D.R. A new approach for robust high productivity resistance spot welding of aluminium. *SAE Trans.* **2003**, *112*, 280–292.
91. Spinella, D.J.; Brockenbrough, J.R.; Fridy, J.M. Trends in aluminium resistance spot welding for the auto industry. *Weld. J.* **2005**, *84*, 34–40.
92. Bamberg, P.; Seewald, R.; Schiebahn, A.; Reisgen, U.; Precoma, N.; Epperlein, M. Improvement of the resistance spot welding of Al-Mg-Si alloys by using cladding technology: An optical and mechanical characterization study. *J. Adv. Join. Process.* **2022**, *5*, 100090. [[CrossRef](#)]
93. Indira Rani, M.; Marpu, R.N. Effect of Pulsed Current TIG Welding Parameters on Mechanical Properties of J-Joint Strength of AA6351. *Int. J. Eng. Sci.* **2012**, *1*, 1–5.
94. Howard, R.D. Industrial Heating. Aluminum Heat Treatment Processes, Applications and Equipment. 1 February 2007. Available online: <https://www.industrialheating.com/articles/87310-aluminum-heat-treatment-processes-applications-and-equipment> (accessed on 15 April 2024).
95. Spira, N. Aluminum in Cars: Aluminum Alloys for Car Bodies. Kloeckner Metals. 7 July 2021. Available online: <https://www.kloecknermetals.com/blog/aluminum-in-cars> (accessed on 15 April 2024).
96. EngineersEdge. Aluminium plate, Aluminium Cast and Wrough Engineering Specifications. 15 March 2023. Available online: https://www.engineersedge.com/aluminum_plate.htm (accessed on 15 April 2024).
97. Davis, J.R. *Aluminum and Aluminum Alloys*; ASM International: Cleveland, OH, USA, 1993.
98. Bamberg, P.; Gintrowski, G.; Liang, Z.; Schiebahn, A.; Reisgen, U.; Precoma, N.; Geffers, C. Development of a new approach to resistance spot weld AW-7075 aluminum alloys for structural applications: An experimental study—Part 1. *J. Mater. Res. Technol.* **2021**, *15*, 5569–5581. [[CrossRef](#)]
99. Elrefaey, A. Effectiveness of cold metal transfer process for welding 7075 aluminium alloys. *Sci. Technol. Weld Join* **2015**, *20*, 280–285. [[CrossRef](#)]
100. Kumar, N.P.; Vendan, S.A.; Shanmugam, N.S. Investigations on the parametric effects of cold metal transfer process on the microstructural aspects in AA6061. *J. Alloys Compd.* **2016**, *658*, 255–264. [[CrossRef](#)]
101. Zhang, C.; Li, G.; Gao, M.; Yan, J.; Zeng, X.Y. Microstructure and process characterization of laser-cold metal transfer hybrid welding of AA6061 aluminum alloy. *Int. J. Adv. Manuf. Technol.* **2013**, *68*, 1253–1260. [[CrossRef](#)]
102. Ahmad, R.; Bakar, M.A. Effect of a post-weld heat treatment on the mechanical and microstructure properties of AA6061 joints welded by the gas metal arc welding cold metal transfer method. *Mater. Des.* **2011**, *32*, 5120–5126. [[CrossRef](#)]
103. Benoit, A.; Paillard, P.; Baudin, T.; Klosek, V.; Mottin, J.-B. Comparison of four arc welding processes used for aluminium alloy cladding. *Sci. Technol. Weld Join* **2015**, *20*, 75–81. [[CrossRef](#)]
104. Cong, B.; Ding, J.; Williams, S. Effect of arc mode in cold metal transfer process on porosity of additively manufactured Al-6.3%Cu alloy. *Int. J. Adv. Manuf. Technol.* **2015**, *76*, 1593–1606. [[CrossRef](#)]
105. Rajeev, G.P.; Kamaraj, M.; Bakshi, S.R. Al-Si-Mn alloy coating on aluminum substrate using cold metal transfer (CMT) welding technique. *JOM J. Miner. Met. Mater. Soc.* **2014**, *66*, 1061–1067. [[CrossRef](#)]
106. Luijendijk, T. Welding of dissimilar aluminium alloys. *J. Mater. Process. Technol.* **2000**, *103*, 29–35. [[CrossRef](#)]
107. Kaba, L.; Djeghlal, M.E.; Ouallam, S.; Kahla, S. Dissimilar welding of aluminum alloys 2024 T3 and 7075 T6 by TIG process with double tungsten electrodes. *Int. J. Adv. Manuf. Technol.* **2022**, *118*, 937–948. [[CrossRef](#)]
108. Jweeg, M.J.; Resan, K.K.; Abbod, E.A.; Al-Waily, M. Dissimilar Aluminium Alloys Welding by Friction Stir Processing and Reverse Rotation Friction Stir Processing. *IOP Conf. Ser. Mater. Sci. Eng.* **2018**, *454*, 012059. [[CrossRef](#)]
109. Friedman, P.A.; Kridli, G.T. Microstructural and mechanical investigation of aluminum tailor-welded blanks. *J. Mater. Eng. Perform.* **2000**, *9*, 541–551. [[CrossRef](#)]
110. Buste, A.; Lalbin, X.; Worswick, M.J.; Bouchard, M.; Faucher, A. (Eds.) *Prediction of Strain Distribution in Aluminium Tailor Welded Blanks for Different Welding Techniques*; Proc. Int. Symp. on Light Metals; Canadian Institute of Mining, Metallurgy, and Petroleum: Montreal, QC, Canada, 1999; pp. 485–500.

111. Davies, R.W.; Grant, G.J.; Khaleel, M.A.; Smith, M.T.; Oliver, H.E. Forming-limit diagrams of aluminum tailor-welded blank weld material. *Metall. Mater. Trans. A* **2001**, *32*, 275–283. [[CrossRef](#)]
112. Pickering, E.; Glagola, M.; Ramage, R.; Taylor, G. *Production and Performance of High Speed GTA Welded Aluminum Tailored Blanks*; SAE Technical Paper: Warrendale, PA, USA, 1995; p. 950722.
113. Gungor, B.; Kaluc, E.; Taban, E.; SIK ŞŞ, A. Mechanical and microstructural properties of robotic Cold Metal Transfer (CMT) welded 5083-H111 and 6082-T651 aluminum alloys. *Mater. Des.* **2014**, *54*, 207–211. [[CrossRef](#)]
114. Totten, G.E.; Mackenzie, S. Handbook of aluminum. In *Physical Metallurgy and Processes*; Marcel Dekker Inc.: New York, NY, USA, 2003; Volume 1, pp. 66–73.
115. Mathers, G. *The Welding of Aluminium and Its Alloys*; Woodhead Publishing Limited: Cambridge, UK, 2002.
116. Elrefaey, A.; Ross, N.G. Microstructure and mechanical properties of cold metal transfer welding similar and dissimilar aluminum alloys. *Acta Met. Sin. Engl. Lett.* **2015**, *28*, 715–724. [[CrossRef](#)]
117. Boşneag, A.; Constantin, M.A.; Nițu, E.; Iordache, M. Friction Stir Welding of three dissimilar aluminium alloy used in aeronautics industry. *IOP Conf. Ser. Mater. Sci. Eng.* **2017**, *252*, 012041. [[CrossRef](#)]
118. Sharma, S.; Upadhyay, V. Friction Stir Welding of Dissimilar Aluminum Alloys AA5086 and AA7039. *J. Phys. Conf. Ser.* **2019**, *1240*, 012160. [[CrossRef](#)]
119. Pourabbas, M.; Abdollah-zadeh, A.; Sarvari, M.; Pouranvari, M.; Miresmaeili, R. Investigation of structural and mechanical properties of magnetic pulse welded dissimilar aluminum alloys. *J. Manuf. Process.* **2019**, *37*, 292–304. [[CrossRef](#)]
120. Meng, Z.; Wang, X.; Guo, W.; Hu, Z.; Vivek, A.; Hua, L.; Daehn, G.S. Joining Performance and Microstructure of the 2024/7075 Aluminium Alloys Welded Joints by Vaporizing Foil Actuator Welding. *J. Wuhan Univ. Technol.-Mat. Sci. Edit.* **2019**, *34*, 368–372. [[CrossRef](#)]
121. Perović, M.; Balos, S.; Kozak, D.; Bajic, D.; Vuherer, T. Influence of kinematic factors of friction stir welding on the characteristics of welded joints of forged plates made of EN AW 7049 A aluminium alloy. *Teh. Gaz.* **2017**, *24*, 728–732.
122. Sánchez Amaya, J.M.; Amaya-Vázquez, M.R.; Botana, F.J. 8—Laser welding of light metal alloys: Aluminium and titanium alloys. In *Woodhead Publishing Series in Electronic and Optical Materials, Handbook of Laser Welding Technologies*; Katayama, S., Ed.; Woodhead Publishing: Cambridge, UK, 2013; pp. 215–254.
123. Kou, S. *The Partially Melted Zone. Welding Metallurgy*; A John Wiley & Sons, Inc.: Hoboken, NJ, USA, 2002; Volume 3, pp. 304–328.
124. Huang, C.; Kou, S. Liquation Mechanisms in Multi-Component Aluminum Alloys During Welding. *Weld. J.* **2002**, *81*, 211s–222s.
125. Huang, C.; Kou, S. Liquation cracking in partial-penetration aluminum welds: Effect of penetration oscillation and backfilling. *Weld. J.* **2003**, *82*, 184s–194s.
126. Huang, C.; Kou, S. Liquation Cracking in Full-Penetration Al-Mg-Si Welds. *Weld. J.* **2004**, *83*, 111s–122s.
127. Song, S.-W.; Lee, S.-H.; Kim, B.-C.; Yoon, T.-J.; Kim, N.-K.; Kim, I.-B.; Kang, C.-Y. Liquation Cracking of Dissimilar Aluminum Alloys during Friction Stir Welding. *Mater. Trans.* **2011**, *52*, 254–257. [[CrossRef](#)]
128. Cornacchia, G.; Cecchel, S. Study and Characterization of EN AW 6181/6082-T6 and EN AC 42100-T6 Aluminum Alloy Welding of Structural Applications: Metal Inert Gas (MIG), Cold Metal Transfer (CMT), and Fiber Laser-MIG Hybrid Comparison. *Metals* **2020**, *10*, 441. [[CrossRef](#)]
129. Dalle Donne, C.; Braun, R.; Staniek, G.; Jung, A.; Kaysser, W.A. Mikrostrukturelle, mechanische und korrosive Eigenschaften reibrührgeschweißter Stumpfnähte in Aluminiumlegierungen. *Mater. Werkstofftechnik./Mater. Sci. Eng. Technol.* **1998**, *29*, 609–617.
130. Hassan, K.A.A.; Prangnell, P.B.; Norman, A.F.; Price, D.A.; Williams, S.W. Effect of welding parameters on nugget zone microstructure and properties in high strength aluminium alloy friction stir welds. *Sci. Technol. Weld. Join.* **2003**, *8*, 257–268. [[CrossRef](#)]
131. Wang, P.; Chen, K.; Jiang, H.; Chen, S.; Hu, G. Microstructures and properties of TIG welded joint of 7003 aluminum alloy. *Mater. Sci. Eng. Powder Metall.* **2016**, *2016*, 832–839.
132. Alisibramulisi, A.; Myhr, O.; Lademo, O.-G.; Larsen, P. An Experimental Investigation of the Heat Affected Zone (HAZ) Properties of, A.A.6.0.6.0.; AA7046 Following Different Heat Treatment Schedules. In Proceedings of the 12th International Conference on Aluminium Alloys, Yokohama, Japan, 5–9 September 2010; The Japan Institute of Light Metals: Yokohama, Japan, 2010; pp. 994–999.
133. Haryadi, G.D.; Kim, S.J. Influences of post weld heat treatment on fatigue crack growth behavior of TIG welding of 6013 T4 aluminum alloy joint (Part 1. Fatigue crack growth across the weld metal). *J. Mech. Sci. Technol.* **2011**, *25*, 2161–2170. [[CrossRef](#)]
134. Hou, B.; Zhao, Y.; Zhou, C.; Xie, M.; Hu, Z. Research on Welding Properties of Al-Mg Alloy Welding Wire Containing In. *Mater. Sci.* **2019**, *9*, 189–195.
135. Shanavas, S.; Raja Dhas, J.E. Weldability of AA 5052 H32 aluminium alloy by TIG welding and FSW process—A comparative study. *IOP Conf. Ser. Mater. Sci. Eng.* **2017**, *247*, 012016.
136. Vijay Mohan Shetty, V.M.; Vattem, R.K.; Musku, S. Optimization and Evaluation of Ageing Parameters on Mechanical Properties of AA 6061AND AA 5154 Welded Joints using Taguchi Method. *Int. J. Eng. Sci. Res. Technol.* **2018**, *7*, 64–72.
137. Zhu, G.; Wang, S.; Zhang, M.; Yang, X.; Liu, W.; Wang, G. Application of laser cleaning in postwelding treatment of aluminum alloy. *Appl. Opt.* **2020**, *59*, 10967–10972. [[CrossRef](#)]
138. Mossman, M.M.; Lippold, J.C. Weldability Testing of Dissimilar Combinations of 5000- and 6000-Series Aluminum Alloys. *Weld. J.* **2002**, *81*, 188s–194s.

139. European Aluminium. Joining—Arc Welding, the Aluminium Automotive Manual. 2015. Available online: https://www.european-aluminium.eu/media/1518/3-arc-welding_2015_new.pdf (accessed on 18 February 2020).
140. Peter, I.; Rosso, M. Study of 7075 aluminium alloy joints. *Sci. Bull. Valahia Univ. Mater. Mech.* **2017**, *15*, 7–11. [[CrossRef](#)]
141. Kang, M.; Kim, C. A Review of Joining Processes for High Strength 7xxx Series Aluminum Alloys. *J. Weld. Join* **2017**, *35*, 79–88. [[CrossRef](#)]
142. Niu, L.-Q.; Li, X.-Y.; Zhang, L.; Liang, X.-B.; Li, M. Correlation Between Microstructure and Mechanical Properties of 2219-T8 Aluminum Alloy Joints by VPTIG Welding. *Acta Metall. Sin. (Engl. Lett.)* **2017**, *30*, 438–446. [[CrossRef](#)]
143. Kwon, Y.; Weckman, D.C. Analytical thermal model of conduction mode double sided arc welding. *Sci. Technol. Weld Joi.* **2008**, *13*, 539–549. [[CrossRef](#)]
144. Nyrkova, L.I.; Labur, T.M.; Shevtsov, E.I.; Nazarenko, O.P.; Dorofeev, A.V.; Osadchuk, S.; Yavorska, M.R.; Poklyatsky, A.G.; Fedorchuk, V. Complex of properties of 2219 alloy weld joint in T62 state under modeling operating conditions. *Space Sci. Technol.* **2022**, *28*, 14–29. [[CrossRef](#)]
145. Su, D.; Zhang, J.; Wang, B. The microstructure and weldability in welded joints for AA 5356 aluminum alloy after adding modified trace amounts of Sc and Zr. *J. Manuf. Process.* **2020**, *57*, 488–498. [[CrossRef](#)]
146. Palanivel, R.; Laubscher, R.F.; Dinaharan, I.; Murugan, N. Developing a Friction-StirWeldingWindow for Joining the Dissimilar Aluminum Alloys AA6351 and AA5083. *Mater. Technol.* **2017**, *51*, 5–9.
147. Singh, A.K.; Dey, V.; Rai, R.N. Techniques to improve weld penetration in TIG welding (A review). *Mater. Today Proc.* **2017**, *4*, 1252–1259. [[CrossRef](#)]
148. Chen, Q.; Lin, S.; Yang, C.; Fan, C.; Ge, H. Grain fragmentation in ultrasonic-assisted TIG weld of pure aluminum. *Ultrason. Sonochemistry* **2017**, *39*, 403–413. [[CrossRef](#)]
149. Gupta, Y.; Tanwar, A.; Gupta, R. Investigation of Microstructure and Mechanical Properties of TIG and MIG Welding Using Aluminium Alloy. *IOSR J. Mech. Civ. Eng.* **2016**, *13*, 121–126.
150. Zhang, Y.M.; Pan, C.; Male, A.T. Improved microstructure and properties of 6061 aluminum alloy weldments using a double-sided arc welding process. *Metall. Mater. Trans. A* **2000**, *31*, 2537–2543. [[CrossRef](#)]
151. Squillace, A.; Fenzo, A.D.; Giorleo, G.; Bellucci, F. A comparison between FSW and TIG welding techniques: Modifications of microstructure and pitting corrosion resistance in AA 2024-T3 butt joints. *J. Mater. Process. Technol.* **2004**, *152*, 97–105. [[CrossRef](#)]
152. Wang, X.; Wang, K.; Shen, Y.; Hu, K. Comparison of fatigue property between friction stir and TIG welds. *J. Univ. Sci. Technol. Beijing Miner. Metall. Mater.* **2008**, *15*, 280–284. [[CrossRef](#)]
153. Cabello, M.; Ruckert, G.; Huneau, S.B.; Marya, S. Comparison of TIG welded and friction stir welded Al–4.5Mg–0.26Sc alloy. *J. Mater. Process. Technol.* **2008**, *197*, 337–343.
154. Zhao, J.; Jiang, F.; Jian, H.; Wen, K.; Jiang, L.; Chen, X. Comparative investigation of tungsten inert gas and friction stir welding characteristics of Al–Mg–Sc alloy plates. *Mater. Des.* **2010**, *31*, 306–311. [[CrossRef](#)]
155. Malarvizhia, S.; Balasubramanian, V. Effects of welding processes and post-weld aging treatment on fatigue behavior of AA2219 aluminium alloy joints. *J. Mater. Eng. Perform.* **2011**, *20*, 359–367. [[CrossRef](#)]
156. Zhen, H.; Yong, P.; Zhi, Y.; Xue, L. Comparison of FSW and TIG welded joints in Al-Mg-Mn-Sc-Zr alloy plates. *Trans. Nonferrous Met. Soc. China* **2011**, *21*, 1685–1691.
157. Anjaneya Prasad, B.; Prasanna, P. Experimental Comparison of the MIG and Friction Stir Welding Processes for AA 6061(AlMgSiCu) Aluminium Alloy. *Int. J. Min. Metall. Mech. Eng.* **2013**, *1*, 137–140.
158. Jannet, S.; Mathews, P.K.; Raja, R. Comparative investigation of Friction stir welding & Fusion welding of 6061T-6 & 5083-0 Aluminium Alloys based on mechanical properties & microstructure. *J. Achiev. Mater. Manuf. Engg.* **2013**, *61*, 181–186.
159. Sasidharan, B.; Narayanan, K.P.; Prakash, R.S. Tensile & Microstructural characteristics of DCSP TIG welded & Friction stir welded AA2219 Aluminum Alloy. *Int. J. Des. Manuf. Technol.* **2014**, *5*, 121–129.
160. Kumar, A.; Gautam, S.S.; Kumar, A. Heat input & joint efficiency of three welding processes TIG, MIG & FSW using AA6061. *Int. J. Mech. Engg. Robot. Res.* **2014**, *1*, 89–94.
161. Navyashree, S.; Sivaramakrishna, V. Experimental Investigation of Friction Stir Welding and TIG Welding for Al-6082. *Int. J. Innov. Res. Sci. Engg. Technol.* **2015**, *4*, 5292–5298.
162. Vimalraj, C.; Kah, P.; Mvola, B.; Martikainen, J. Effect of nanomaterial addition using gmaw and gtaw processes. *Rev. Adv. Mater. Sci.* **2016**, *44*, 370–382.
163. Kumar, A.; Milton, M.S. A Comparison of Welding Techniques of Aluminium Alloys. A Literature Review. *Int. J. Sci. Res. Sci. Eng. Technol.* **2016**, *2*, 172–175.
164. Singh, S.; Kumar, V.; Kumar, S.; Kumar, A. Variant of MIG welding of similar and dissimilar metals: A review. *Mater. Today Proc.* **2022**, *56*, 3550–3555. [[CrossRef](#)]
165. Nie, F.; Dong, H.; Chen, S.; Li, P.; Wang, L.; Zhao, Z.; Li, X.; Zhang, H. Microstructure and Mechanical Properties of Pulse MIG Welded 6061/A356 Aluminum Alloy Dissimilar Butt Joints. *J. Mater. Sci. Technol.* **2018**, *34*, 551–560. [[CrossRef](#)]
166. Warinsiriruk, E.; Greebmalai, J.; Sangsuriyun, M. Effect of Double Pulse MIG Welding on Porosity Formation on Aluminium 5083 Fillet Joint. *MATEC Web Conf.* **2019**, *269*, 01002. [[CrossRef](#)]
167. Bai, Y.; Gao, H.M.; Qiu, L. Droplet transition for plasma-MIG welding on aluminium alloys. *Trans. Nonferrous Met. Soc. China* **2010**, *20*, 2234–2239. [[CrossRef](#)]

168. Liu, J.; Zhu, H.; Li, Z.; Cui, W.; Shi, Y. Effect of ultrasonic power on porosity, microstructure, mechanical properties of the aluminum alloy joint by ultrasonic assisted laser-MIG hybrid welding. *Opt. Laser Technol.* **2019**, *119*, 105619. [CrossRef]
169. Chen, C.; Fan, C.; Lin, S.; Cai, X.; Zhou, L.; Ye, S.; Yang, C. Effect of ultrasonic pattern on weld appearance and droplet transfer in ultrasonic assisted MIG welding process. *J. Manuf. Process.* **2018**, *35*, 368–372. [CrossRef]
170. Wojdat, T.; Kustron, P.; Jaskiewicz, K.; Zwierzchowski, M.; Margielewska, A. Numerical modelling of welding of car body sheets made of selected aluminum alloys. *Arch. Metall. Mater.* **2019**, *64*, 1403–1409. [CrossRef]
171. Pfeifer, T.; Rykała, J. Welding EN AW7075 Aluminium Alloy Sheets—Low-energy Versus Pulsed Current. *Inst. Weld. Bull. Gliw.* **2014**, *5*, 137–144.
172. Bruckner, J.; Wagner, J.; Arenholz, E. The CMT process a revolution in welding technology Bruckner. In Proceedings of the International Light Metals Technology Conference 2005, San Francisco, CA, USA, 11–13 July 2005; pp. 275–284.
173. Pfeifer, T.; Stano, S. Modern methods of weldbrazing in the aspect of quality and properties of joints. *Weld. Technol. Rev.* **2016**, *9*, 95–102.
174. Talalaev, R.; Veinthal, R.; Laansoo, A.; Sarkans, M. Cold metal transfer (CMT) welding of thin sheet metal products. *Est. J. Eng.* **2012**, *18*, 243–250. [CrossRef]
175. Feng, J.; Zhang, H.; He, P. The CMT short-circuiting metal transfer process and its use in thin aluminium sheets welding. *Mater. Des.* **2009**, *30*, 1850–1852. [CrossRef]
176. Dutra, J.C.; Gonçalves e Silva, R.H.; Martinello Savi, B.; Marques, C.; Alarcon, O.E. Metallurgical characterization of the 5083H116 aluminum alloy welded with the cold metal transfer process and two different wire-electrodes (5183 and 5087). *Weld World* **2015**, *59*, 797–807. [CrossRef]
177. Shu, F.Y.; Tian, Z.; Lu, Y.H.; He, W.X.; Lu, F.Y.; Lin, J.J.; Zhao, H.Y.; Xu, B.S. Prediction of vulnerable zones based on residual stress and microstructure in cmt welded aluminium alloy joint. *Trans. Nonferrous Met. Soc. China* **2015**, *25*, 2701–2707. [CrossRef]
178. Shu, F.Y.; Lu, Y.H.; Liu, Y.X.; Xu, F.J.; Sun, Z.; He, P.; Xu, B.S. FEM modeling of softened base metal in narrow-gap joint by CMT+Pmix welding procedure. *Trans. Nonferrous Met. Soc. China* **2014**, *24*, 1830–1835. [CrossRef]
179. Kotsikos, G.; Robinson, M.; Zangani, D.; Roberts, J. Investigation of the weld unzipping failure mode during collisions of welded aluminium rail vehicles. *Proc. Inst. Mech. Eng. Part F J. Rail Rapid Transit* **2008**, *222*, 59–68. [CrossRef]
180. Zangani, D.; Robinson, M.; Kotsikos, G. Improving the Crashworthiness of Aluminium Rail Vehicles. In *Engineering Against Fracture*; Springer: Dordrecht, The Netherlands, 2009.
181. Gay, R.; Robinson, M.; Zangani, D. Crashworthiness of Joints in Aluminium Rail Vehicles. 2022. Available online: https://trimis.ec.europa.eu/sites/default/files/project/documents/20091125_164508_79987_ALJOIN%20overview%20paper.pdf (accessed on 15 April 2024).
182. Zhao, Y.; Chen, F.; Cao, S.; Chen, C.; Xie, R. Effect of CMT Welding Heat Input on Microstructure and Properties of 2A14 Aluminum Alloy Joint. *Metals* **2022**, *12*, 2100. [CrossRef]
183. Shanker, H.; Wattal, R. Comparative study of microstructural and mechanical properties of robotic CMT and GMAW welded 7475-T7351 aluminium alloy joints. *Mater. Today Commun.* **2023**, *37*, 106994. [CrossRef]
184. Tian, Y.; Shen, J.; Hu, S.; Gou, J. Macrostructure, microstructure and wear performance of Al alloy cladding fabricated by CMT technique. *Eng. Res. Express* **2020**, *2*, 015026. [CrossRef]
185. Yang, G.; Guan, K.; Zou, L.; Sun, Y.; Yang, X. Weld Defect Detection of a CMT Arc-Welded Aluminum Alloy Sheet Based on Arc Sound Signal Processing. *Appl. Sci.* **2023**, *13*, 5152. [CrossRef]
186. Srinivasan, D.; Sevel, P.; Solomon, I.J.; Tanushkumar, P. A review on Cold Metal Transfer (CMT) technology of welding. *Mater. Today Proc.* **2022**, *64*, 108–115. [CrossRef]
187. Zhang, H.; Feng, J.; He, P.; Zhang, B.; Chen, J.; Wang, L. The arc characteristics and metal transfer behaviour of cold metal transfer and its use in joining aluminium to zinc-coated steel. *Mater. Sci. Eng. A* **2007**, *499*, 111–113. [CrossRef]
188. Shang, J.; Wang, K.; Zhou, Q.; Zhang, D.; Huang, J.; Li, G. Microstructure characteristics and mechanical properties of cold metal transfer welding Mg/Al dissimilar metals. *Mater. Des.* **2012**, *34*, 559–565. [CrossRef]
189. Cao, R.; Wen, B.; Chen, J.; Wang, P.-C. Cold Metal Transfer joining of magnesium AZ31B-to-aluminum A6061-T6. *Mater. Sci. Eng. A* **2013**, *560*, 256–266. [CrossRef]
190. Singh, I.J.; Murtaza, Q. A comprehensive review on effect of cold metal transfer welding parameters on dissimilar and similar metal welding. *J. Eng. Res.* **2023**. [CrossRef]
191. Gierth, M.; Henckell, P.; Ali, Y.; Scholl, J.; Bergmann, J. Wire Arc Additive Manufacturing (WAAM) of aluminum alloy AlMg5Mn with energy-reduced Gas Metal Arc Welding (GMAW). *Materials* **2020**, *13*, 2671. [CrossRef]
192. Bergmann, J.P.; Bielenin, M.; Feustel, T. Aluminum welding by combining a diode laser with a pulsed Nd:YAG laser. *Weld. World* **2015**, *59*, 307–315. [CrossRef]
193. Park, Y.W.; Rhee, S. Process modeling and parameter optimization using neural network and genetic algorithms for aluminum laser welding automation. *Int. J. Adv. Manuf. Technol.* **2008**, *37*, 1014–1021. [CrossRef]
194. Schempp, P.; Tang, Z.; Cross, C.; Pittner, A.; Seefeld, T.; Rethmeier, M. Influence of Alloy Solidification Parameters on Grain Refinement in Aluminum Weld Metal due to Inoculation. In *Proceedings of the ASM Proceedings of the 9th International Conference: Trends in Welding Research*; Chicago, IL, USA, 4–8 June 2012; pp. 98–107.
195. Zhao, H.; DebRoy, T. Macroporosity free aluminum alloy weldments through numerical simulation of keyhole mode laser welding. *J. Appl. Phys.* **2003**, *93*, 10089–10096. [CrossRef]

196. Pastor, M.; Zhao, H.; Martukanitz, R.P.; Debroy, T. Porosity, underfill and magnesium lose during continuous wave Nd: YAG laser welding of thin plates of aluminum alloys 5182 and 5754 78: 207-s. *Weld. J.* **1999**, *78*, 207s–216s.
197. Sheikhi, M.; Ghaini, F.M.; Assadi, H. Prediction of solidification cracking in pulsed laser welding of 2024 aluminum alloy. *Acta Mater.* **2015**, *82*, 491–502. [[CrossRef](#)]
198. Yi, H.; Jian, H.; Pulin, N. Microstructures and Textures of 6016 and 5182 Aluminum Laser Welded Joints. *Chin. J. Lasers* **2019**, *46*, 0402003.
199. Sánchez-Amaya, J.M.; Delgado, T.; González-Rovira, L.; Botana, F.J. Laser Welding of Aluminium Alloys 5083 and 6082 under Conduction Regime. *Appl. Surf. Sci.* **2009**, *255*, 9512–9521. [[CrossRef](#)]
200. Zhu, H.; Huang, L.; Li, J.; Li, X.; Ma, H.; Wang, C.; Ma, F. Strengthening mechanism in laser-welded 2219 aluminium alloy under the cooperative effects of aging treatment and pulsed electromagnetic loadings. *Mater. Sci. Eng. A* **2018**, *714*, 124–139. [[CrossRef](#)]
201. Wang, Z.; Oliveira, J.P.; Zeng, Z.; Bu, X.; Peng, B.; Shao, X. Laser beam oscillating welding of 5A06 aluminum alloys: Microstructure, porosity and mechanical properties. *Opt. Laser Technol.* **2019**, *111*, 58–65. [[CrossRef](#)]
202. Peng, G.; Li, L.; Wang, J.; Xia, H.; Meng, S.; Gong, J. Effect of subatmospheric pressures on weld formation and mechanical properties during disk laser welding of 5A06 aluminium alloy. *J. Mater. Process. Technol.* **2020**, *277*, 116457. [[CrossRef](#)]
203. Braun, R. Nd:YAG laser butt welding of AA6013 using silicon and magnesium containing filler powders. *Mater. Sci. Eng. A* **2006**, *426*, 250–262. [[CrossRef](#)]
204. Zhang, L.; Li, X.; Nie, Z.; Huang, H.; Sun, J. Microstructure and mechanical properties of a new Al–Zn–Mg–Cu alloy joints welded by laser beam. *Mater. Des.* **2015**, *83*, 451–458. [[CrossRef](#)]
205. Enz, J.; Khomenko, V.; Riekehr, S.; Ventzke, V.; Huber, N.; Kashaev, N. Single-sided laser beam welding of a dissimilar AA2024–AA7050 T-joint. *Mater. Des.* **2015**, *76*, 110–116. [[CrossRef](#)]
206. Viscusi, A.; Leitão, C.; Rodrigues, D.M.; Scherillo, F.; Squillace, A.; Carrino, L. Laser beam welded joints of dissimilar heat treatable aluminium alloys. *J. Mater. Process. Technol.* **2016**, *236*, 48–55. [[CrossRef](#)]
207. Enz, J.; Kumar, M.; Riekehr, S.; Ventzke, V.; Huber, N.; Kashaev, N. Mechanical properties of laser beam welded similar and dissimilar aluminum alloys. *J. Manuf. Process.* **2017**, *29*, 272–280. [[CrossRef](#)]
208. Bunaziv, I.; Akselsen, O.M.; Salminen, A.; Unt, A. Fiber laser-MIG hybrid welding of 5mm 5083 aluminum alloy. *J. Mater. Process. Technol.* **2016**, *233*, 107–114. [[CrossRef](#)]
209. Shibata, K.; Sakamoto, H.; Iwase, T. Laser-MIG Hybrid Welding of Aluminium Alloys. *Weld World* **2006**, *50*, 28–34. [[CrossRef](#)]
210. Han, X.; Yang, Z.; Ma, Y.; Shi, C.; Xin, Z. Porosity distribution and mechanical response of laser-MIG hybrid butt welded 6082-T6 aluminum alloy joint. *Opt. Laser Technol.* **2020**, *132*, 106511. [[CrossRef](#)]
211. Katayama, S.; Uchiumi, S.; Mizutani, M.; Wang, J.; Fujii, K. Penetration and porosity prevention mechanism in YAG laser-MIG hybrid welding. *Weld. Int.* **2007**, *21*, 25–31. [[CrossRef](#)]
212. Yan, J.; Zeng, X.; Gao, M.; Lai, J.; Lin, T. Effect of welding wires on microstructure and mechanical properties of 2A12 aluminum alloy in CO₂ laser-MIG hybrid welding. *Appl. Surf. Sci.* **2009**, *255*, 7307–7313. [[CrossRef](#)]
213. Ahn, J.; Chen, L.; He, E.; Davies, C.M.; Dear, J.P. Effect of filler metal feed rate and composition on microstructure and mechanical properties of fibre laser welded AA 2024-T3. *J. Manuf. Process.* **2017**, *25*, 26–36. [[CrossRef](#)]
214. Ahn, J.; He, E.; Chen, L.; Dear, J.; Davies, C. The effect of Ar and He shielding gas on fibre laser weld shape and microstructure in AA 2024-T3. *J. Manuf. Process.* **2017**, *29*, 62–73. [[CrossRef](#)]
215. Ahn, J.; Chen, L.; He, E.; Dear, J.P.; Davies, C.M. Optimisation of process parameters and weld shape of high power Yb-fibre laser welded 2024-T3 aluminium alloy. *J. Manuf. Process.* **2018**, *34*, 70–85. [[CrossRef](#)]
216. Yan, S.; Nie, Y.; Zhu, Z.; Chen, H.; Gou, G.; Yu, J.; Wang, G. Characteristics of microstructure and fatigue resistance of hybrid fiber laser-MIG welded Al–Mg alloy joints. *Appl. Surf. Sci.* **2014**, *298*, 12–18. [[CrossRef](#)]
217. Huang, L.; Wu, D.; Hua, X.; Liu, S.; Jiang, Z.; Li, F.; Wang, H.; Shi, S. Effect of the welding direction on the microstructural characterization in fiber laser-GMAW hybrid welding of 5083 aluminum alloy. *J. Manuf. Process.* **2018**, *31*, 514–522. [[CrossRef](#)]
218. Leo, P.; D’Ostuni, S.; Casalino, G. Hybrid welding of AA5754 annealed alloy: Role of post weld heat treatment on microstructure and mechanical properties. *Mater. Des.* **2016**, *90*, 777–786. [[CrossRef](#)]
219. Yan, S.H.; Chen, H.; Zhu, Z.T.; Gou, G.Q. Hybrid laser-Metal Inert Gas welding of Al–Mg–Si alloy joints: Microstructure and mechanical properties. *Mater. Design.* **2014**, *61*, 160–167. [[CrossRef](#)]
220. Zhang, C.; Gao, M.; Jiang, M.; Zeng, X. Effect of weld characteristic on mechanical strength of laser-arc hybrid-welded Al–Mg–Si–Mn aluminum alloy. *Metall. Mater. Trans. A* **2016**, *47*, 5438–5449. [[CrossRef](#)]
221. Yan, S.; Xing, B.; Zhou, H.; Xiao, Y.; Qin, Q.-H.; Chen, H. Effect of filling materials on the microstructure and properties of hybrid laser welded Al–Mg–Si alloys joints. *Mater. Charact.* **2018**, *144*, 205–218. [[CrossRef](#)]
222. Wang, H.; Liu, X.; Liu, L. Research on laser-TIG Hybrid welding of 6061-T6 aluminum alloys joint and post heat treatment. *Metals* **2020**, *10*, 130. [[CrossRef](#)]
223. Hu, B.; Richardson, I.M. Microstructure and mechanical properties of AA7075(T6) hybrid laser/GMA welds. *Mater. Sci. Eng. A* **2007**, *459*, 94–100. [[CrossRef](#)]
224. Ola, O.T.; Doern, F.E. Fusion weldability studies in aerospace AA7075-T651 using high-power continuous wave laser beam techniques. *Mater. Des.* **2015**, *77*, 50–58. [[CrossRef](#)]
225. Allen, C.M.; Verhaeghe, G.; Hilton, P.A.; Heason, C.P.; Prangnell, P.B. Laser and hybrid laser-MIG welding of 6.35 and 12.7 mm thick aluminium aerospace alloy. *Mater. Sci. Forum* **2006**, *519–521*, 1139–1144. [[CrossRef](#)]

226. Korzyhyk, V.; Khaskin, V.; Grinyuk, A.A.; Shcheretskiy, V.; Oleinychenko, T.; Babych, O. Hybrid Laser-MIG Welding of Aluminum Alloys Al-Mg-Mn, Al-Cu-Mg and Al-Mg-Li Systems. In Proceedings of the Environment Technology Resources Proceedings of III International Scientific and Practical Conference, Chicago, IL, USA, 1–3 September 2021; pp. 125–132.
227. Nathish, P.V.; Naveen Ram kumar, M.; Raghul Raaj, K.; Omprakasam, S. Hybrid Laser Beam Welding of Aluminium Alloys. *Int. Res. J. Eng. Technol.* **2017**, *4*, 520–524.
228. Daehn, G.S.; Lippold, J.C. Low-Temperature Spot Impact Welding Driven without Contact. U.S. Patent No. PCT/US09/36499, 27 December 2011.
229. Zhao, Y.B.; Lei, Z.L.; Chen, Y.B.; Tao, W. A comparative study of laser-arc double sided welding and double-sided arc welding of 6 mm 5A06 aluminium alloy. *Mater. Design.* **2011**, *32*, 2165–2171. [[CrossRef](#)]
230. Han, B.; Chen, Y.B.; Wang, T.; Lei, Z.L.; Li, H.; Guo, S.; Li, P. Nano-indentation investigation on the local softening of equiaxed zone in 2060–T8/2099–T83 aluminum-lithium alloys T-joints welded by double-sided laser beam welding. *J. Alloys Compd.* **2018**, *756*, 145–162. [[CrossRef](#)]
231. Chen, X.; Lei, Z.; Chen, Y.; Han, B.; Jiang, M.; Tian, Z.; Bi, J.; Lin, S. Nano-indentation and in-situ investigations of double-sided laser beam welded 2060–T8/2099–T83 Al-Li alloys T-joints. *Mat. Sci. Eng. A Struct.* **2019**, *756*, 291–301. [[CrossRef](#)]
232. Sadeh, S.; Gleason, G.H.; Hatamleh, M.I.; Sunny, S.F.; Yu, H.; Malik, A.S.; Qian, D. Simulation and Experimental Comparison of Laser Impact Welding with a Plasma Pressure Model. *Metals* **2019**, *9*, 1196. [[CrossRef](#)]
233. Wang, X.; Gu, C. Laser shock welding of aluminum/aluminum and aluminum/copper plates. *Mater. Des.* **2014**, *56*, 26–30. [[CrossRef](#)]
234. Peyre, P.; Berthe, L.; Fabbro, R. Laser shock processing of materials: Basics mechanisms and applications. In Proceedings of the 65th Laser Materials Processing Conference, Tokyo, Japan, 2–5 December 2005; pp. 95–109.
235. Wang, X.; Gu, Y. An experimental and numerical study of laser impact spot welding. *Mater. Des.* **2015**, *65*, 1143–1152. [[CrossRef](#)]
236. Çam, G.; Ventzke, V.; Dos Santos, J.F.; Koçak, M.; Jennequin, G.; Gonther-Maurin, P. Characterisation of electron beam welded aluminium alloys. *Sci. Technol. Weld. Join.* **1999**, *4*, 317–323. [[CrossRef](#)]
237. Fujii, H.; Umakoshi, H.; Aoki, Y.; Nogi, K. Bubble formation in aluminium alloy during electron beam welding. *J. Mater. Process. Technol.* **2004**, *155–156*, 1252–1255. [[CrossRef](#)]
238. Elseddig, Z.A.; Sobih, M.; Almazy, K.h.; Sallam, M. Experimental investigation of electron beam welding of AA1350 aluminum alloy. In Proceedings of the 14th International Conference on Applied Mechanics and Mechanical Engineering, Cairo, Egypt, 25–27 May 2010.
239. Sobih, M.; Elseddig, Z.; Almazy, K.; Youssef, A.; Sallam, M. Optimization of EBW parameters for 2219 Al-alloy using grey relation method. *Adv. Mater. Res.* **2012**, *591–593*, 507–514. [[CrossRef](#)]
240. Sobih, M.; Elseddig, Z.; Almazy, K.; Sallam, M. Experimental Evaluation and Characterization of Electron Beam Welding of 2219 AL-Alloy. *Indian J. Mater. Sci.* **2016**, *5*, 1–6. [[CrossRef](#)]
241. Saha, D.C.; Park, Y.D. A Review on Al-Al/Al-Steel Resistance Spot Welding Technologies for Light Weight Vehicles. *J. KWJS* **2011**, *29*, 397–402. [[CrossRef](#)]
242. Auhl, J.R.; Patrick, E.P. Auhl, J.R.; Patrick, E.P. A fresh look at resistance spot welding of aluminium automotive components. In *SAE Technical Paper*; SAE International: Warrendale, PA, USA, 1994; p. 940160.
243. Ronnhult, T.; Rilby, U.; Olefjord, I. The surface state and weldability of aluminium alloys. *Mater. Sci. Eng.* **1980**, *42*, 329–336. [[CrossRef](#)]
244. Li, Z.; Hao, C.; Zhang, J.; Zhang, H. Effects of Sheet Surface Conditions on Electrode Life in Resistance Welding Aluminum. *Weld. J.* **2007**, *86*, 81s–89s.
245. Newton, C.; Thornton, M.; Keay, B.; Sheasby, P.; Boomer, D. How to Weld Bond Aluminium with Structural Adhesives. In *SAE Technical Paper*; SAE International: Warrendale, PA, USA, 1997; p. 970018.
246. Miller, W.S.; Zhuang, L.; Bottema, J.; Wittebrood, A.J.; De Smet, P.; Haszler, A.; Vieregge, A. Recent development in aluminium alloys for the automotive industry. *Mater. Sci. Eng.* **2000**, *280*, 37–49. [[CrossRef](#)]
247. Shah, U.; Liu, X. Effect of ultrasonic energy on the spot weldability of aluminum alloy AA6061. *Mater. Des.* **2020**, *192*, 108690. [[CrossRef](#)]
248. Qi, L.; Zhang, Q.; Ma, Y.; Xu, Y.; Han, X.; Li, Y. A comparative study on mechanical performance of traditional and magnetically assisted resistance spot welds of A7N01 aluminum alloy. *J. Manuf. Process.* **2021**, *66*, 133–144. [[CrossRef](#)]
249. Metal Suppliers Online. Aluminum 7178 Aluminum—Material Property Data Sheet. Available online: <https://www.suppliersonline.com/propertypages/7178.asp> (accessed on 15 April 2024).
250. Davis, J.R. Aluminum and Aluminum Alloys—Chapter. In *Alloying: Understanding the Basics*; ASM International: Materials Park, OH, USA, 2001; pp. 351–416.
251. Fracchia, E.; Gobber, F.; Rosso, M. About weldability and welding of Al alloys: Case study and problem solving. *J. Achiev. Mater. Manuf. Eng.* **2017**, *2*, 67–74. [[CrossRef](#)]
252. Matokhnyuk, L.E.; Byalonovich, A.; Gopkalo, E.; Vorob'ev, E.; Karaush, D.; Malyshko, V. Fatigue Resistance of 2219 Aluminum Alloy and its Welded Joints. *Strength Mater.* **2019**, *51*, 860–867. [[CrossRef](#)]
253. Manladan, S.M.; Yusof, F.; Ramesh, S.; Fadzil, M.; Luo, Z.; Ao, S. A review on resistance spot welding of aluminum alloys. *Int. J. Adv. Manuf. Technol.* **2017**, *90*, 605–634. [[CrossRef](#)]

254. Ochi, H.; Sawai, T.; Yamamoto, Y.; Ogawa, K.; Suga, Y. Evaluation of Joint Performance of 5056 Aluminum Friction Welded Joints By Heat Input And Burn-Off Quantity. In *Paper presented at the Tenth International Offshore and Polar Engineering Conference*; ISOPE: Seattle, WA, USA, 2000.
255. Manjhi, S.K.; Das, A.; Prasad, S.B. Review on joining of aluminum alloy by solid-state welding technique. *Mater. Today Proc.* **2020**, *26*, 1255–1261. [[CrossRef](#)]
256. Patel, V.; Li, W.; Wang, G.; Wang, F.; Vairis, A.; Niu, P. Friction Stir Welding of Dissimilar Aluminum Alloy Combinations: State-of-the-Art. *Metals* **2019**, *9*, 270. [[CrossRef](#)]
257. Di Bella, G.; Favaloro, F.; Borsellino, C. Effect of Process Parameters on Friction Stir Welded Joints between Dissimilar Aluminum Alloys: A Review. *Metals* **2023**, *13*, 1176. [[CrossRef](#)]
258. Abnar, B.; Gashtiazar, S.; Javidani, M. Friction Stir Welding of Non-Heat Treatable Al Alloys: Challenges and Improvements Opportunities. *Crystals* **2023**, *13*, 576. [[CrossRef](#)]
259. de Viveiros, B.V.G.; da Silva, R.M.P.; Donatus, U.; Costa, I. Welding and Galvanic Coupling Effects on the Electrochemical Activity of Dissimilar AA2050 and AA7050 Aluminum Alloys Welded by Friction Stir Welding (FSW). *Electrochim. Acta* **2023**, *449*, 142196. [[CrossRef](#)]
260. Essa, A.; Ahmed, M.; Mohamed, A. Weld Pitch Effects on Friction Stir Welding of Aluminum Alloys. *J. Pet. Min. Eng.* **2021**, *23*, 102–106. [[CrossRef](#)]
261. Tiwari, S.; Shukla, D.K.; Chandra, R. Friction Stir Welding of Aluminum Alloys: A Review. *Int. J. Mech. Aerosp. Ind. Mechatron. Eng.* **2013**, *7*, 1315–1320.
262. Shyamlal, C.; Rajesh, S.; Suresh Kumar, S. A Comprehensive Review on the Effect of Precipitation on Mechanical Properties of Friction Stir Welded Aluminium Alloys. *Proc. Inst. Mech. Eng. C J. Mech. Eng. Sci.* **2021**, *235*, 6345–6356. [[CrossRef](#)]
263. Beygi, R.; Talkhabi, A.A.; Mehrizi, M.Z.; Marques, E.A.S.; Carbas, R.J.C.; da Silva, L.F.M. A Novel Lap-Butt Joint Design for FSW of Aluminum to Steel in Tee-Configuration: Joining Mechanism, Intermetallic Formation, and Fracture Behavior. *Metals* **2023**, *13*, 1027. [[CrossRef](#)]
264. Beygi, R.; Galvão, I.; Akhavan-Safar, A.; Pouraliakbar, H.; Fallah, V.; da Silva, L.F.M. Effect of Alloying Elements on Intermetallic Formation during Friction Stir Welding of Dissimilar Metals: A Critical Review on Aluminum/Steel. *Metals* **2023**, *13*, 768. [[CrossRef](#)]
265. Beygi, R.; Carbas, R.J.C.; Barbosa, A.Q.; Marques, E.A.S.; da Silva, L.F.M. Buttering for FSW: Enhancing the Fracture Toughness of Al-Fe Intermetallics through Nanocrystallinity and Suppressing Their Growth. *J. Manuf. Process.* **2023**, *90*, 233–241. [[CrossRef](#)]
266. Buffa, G.; Baffari, D.; Di Caro, A.; Fratini, L. Friction Stir Welding of Dissimilar Aluminium–Magnesium Joints: Sheet Mutual Position Effects. *Sci. Technol. Weld. Join* **2015**, *20*, 271–279. [[CrossRef](#)]
267. Ambrosio, D.; Wagner, V.; Dessein, G.; Paris, J.-Y.; Jlaiel, K.; Cahuc, O. Plastic Behavior-Dependent Weldability of Heat-Treatable Aluminum Alloys in Friction Stir Welding. *Int. J. Adv. Manuf. Technol.* **2021**, *117*, 635–652. [[CrossRef](#)]
268. Lu, H.; Xu, W.; Wang, H.; Wang, X.-Z. Microstructure Evolution and Its Effect on the Corrosion of Dissimilar Aluminum Alloys Friction Stir Welding Joint. *Corros. Sci.* **2023**, *220*, 111249. [[CrossRef](#)]
269. Meng, X.; Huang, Y.; Cao, J.; Shen, J.; dos Santos, J.F. Recent Progress on Control Strategies for Inherent Issues in Friction Stir Welding. *Prog. Mater. Sci.* **2021**, *115*, 100706. [[CrossRef](#)]
270. Leng, L.; Zhang, Z.J.; Duan, Q.Q.; Zhang, P.; Zhang, Z.F. Improving the Fatigue Strength of 7075 Alloy through Aging. *Mater. Sci. Eng. A* **2018**, *738*, 24–30. [[CrossRef](#)]
271. Liu, H.J.; Chen, Y.C.; Feng, J.C. Effect of heat treatment on tensile properties of friction stir welded joints of 2219-T6 aluminium alloy. *Mat. Sci. Technol.* **2006**, *22*, 237–241. [[CrossRef](#)]
272. Karlsen, M.; Frigaard, Ø.; Hjelen, J.; Grong, Ø.; Norum, H. SEM-EBSD Characterisation of the Deformation Microstructure in Friction Stir Welded 2024 T351 Aluminium Alloy. In *Materials Science Forum*; Trans Tech Publications: Bâch, Switzerland, 2003; pp. 2861–2866.
273. Linton, V.M.; Ripley, M.I. Influence of Time on Residual Stresses in Friction Stir Welds in Agehardenable 7xxx Aluminium Alloys. *Acta Mater.* **2008**, *56*, 4319–4327. [[CrossRef](#)]
274. Sato, Y.S.; Kokawa, H.; Enomoto, M.; Jogan, S.; Hashimoto, T. Precipitation Sequence in Friction Stir Weld of 6063 Aluminum during Aging. *Metall. Mater. Trans. A* **1999**, *30*, 3125–3130. [[CrossRef](#)]
275. Sato, Y.S.; Kokawa, H. Distribution of Tensile Property and Microstructure in Friction Stir Weld of 6063 Aluminum. *Metall. Mater. Trans. A* **2001**, *32*, 3023–3031. [[CrossRef](#)]
276. Kalemba, I.; Hamilton, C.; Dymek, S. Natural Aging in Friction Stir Welded 7136-T76 Aluminum Alloy. In *Friction Stir Welding and Processing VIII*; Springer International Publishing: Cham, Switzerland, 2015; pp. 107–114.
277. Liu, H.J.; Fujii, H.; Maeda, M.; Nogi, K. Mechanical properties of friction stir welded joints of 1050—H24 aluminium alloy. *Sci. Technol. Weld. Join.* **2003**, *8*, 450–454. [[CrossRef](#)]
278. Threadgill, P.L. Terminology in Friction Stir Welding. *Sci. Technol. Weld. Join.* **2007**, *12*, 357–360. [[CrossRef](#)]
279. Abnar, B.; Kazeminezhad, M.; Kokabi, A.H. Effects of Heat Input in Friction Stir Welding on Microstructure and Mechanical Properties of AA3003-H18 Plates. *Trans. Nonferrous Met. Soc. China* **2015**, *25*, 2147–2155. [[CrossRef](#)]
280. Beygi, R.; Zarezadeh Mehrizi, M.; Akhavan-Safar, A.; Mohammadi, S.; da Silva, L.F.M. A Parametric Study on the Effect of FSW Parameters and the Tool Geometry on the Tensile Strength of AA2024–AA7075 Joints: Microstructure and Fracture. *Lubricants* **2023**, *11*, 59. [[CrossRef](#)]

281. Bussu, G.; Irving, P. The Role of Residual Stress and Heat Affected Zone Properties on Fatigue Crack Propagation in Friction Stir Welded 2024-T351 Aluminium Joints. *Int. J. Fatigue* **2003**, *25*, 77–88. [[CrossRef](#)]
282. James, M.N.; Bradley, G.R.; Lombard, H.; Hattingh, D.G. The Relationship between Process Mechanisms and Crack Paths in Friction Stir Welded 5083-H321 and 5383-H321 Aluminium Alloys. *Fatigue Fract. Eng. Mater. Struct.* **2005**, *28*, 245–256. [[CrossRef](#)]
283. Frigaard, Ø.; Grong, Ø.; Midling, O.T. A Process Model for Friction Stir Welding of Age Hardening Aluminum Alloys. *Metall. Mater. Trans. A* **2001**, *32*, 1189–1200. [[CrossRef](#)]
284. Dimopoulos, A.; Vairis, A.; Vidakis, N.; Petousis, M. On the Friction Stir Welding of Al 7075 Thin Sheets. *Metals* **2020**, *11*, 57. [[CrossRef](#)]
285. Lertora, E.; Campanella, D.; Pizzorni, M.; Mandolino, C.; Buffa, G.; Fratini, L. Comparative Evaluation of the Effect of the Substrate Thickness and Inherent Process Defects on the Static and Fatigue Performance of FSW and Adhesive-Bonded Overlap-Joints in an AA6016 Alloy. *J. Manuf. Process.* **2021**, *64*, 785–792. [[CrossRef](#)]
286. Beygi, R.; Marques, E.; da Silva, L.F.M. *Computational Concepts in Simulation of Welding Processes*; Springer: Cham, Switzerland, 2022.
287. Imam, M.; Sun, Y.; Fujii, H.; Aoki, Y.; Ma, N.; Tsutsumi, S.; Murakawa, H. Friction Stir Welding of Thick Aluminium Welds—Challenges and Perspectives. In *Friction Stir Welding and Processing IX*; Springer: Cham, Switzerland, 2017; pp. 119–124.
288. Perrett, J.G.; Martin, J.; Threadgill, P.L.; Ahmed, M.M.Z. Recent Developments in Friction Stir Welding of Thick Section Aluminium Alloys. In Proceedings of the 6th World Congress, Aluminium Two Thousand, Florence, Italy, 13–17 March 2007.
289. Yuan, K.; Yu, H.; Xu, X.; Zheng, B. Semi-Analytical Model for Material Flow Behavior in Thick Plates via Friction Stir Welding. *Int. J. Adv. Manuf. Technol.* **2022**, *121*, 487–501. [[CrossRef](#)]
290. Mallieswaran, K.; Padmanabhan, R. Effect of Sheet Thickness on the FSW Parameters for Dissimilar Aluminium Grades Tailor Welded Blanks. *Adv. Mater. Process. Technol.* **2021**, *7*, 150–165. [[CrossRef](#)]
291. Mamgain, A.; Singh, V.; Pratap Singh, A. Influence of Welding Parameters on Mechanical Property during Friction Stir Welded Joint on Aluminium Alloys: A Review. *J. Kejuruter.* **2023**, *35*, 13–28. [[CrossRef](#)]
292. Thete, V.S.; Kadlag, V.L. Effect of Process Parameters of Friction Stir Welded Joint for Similar Aluminium Alloys H30. *Int. J. Eng. Res. Appl.* **2015**, *5*, 10–17.
293. Khalafe, W.H.; Sheng, E.L.; Bin Isa, M.R.; Omran, A.B.; Shamsudin, S.B. The Effect of Friction Stir Welding Parameters on the Weldability of Aluminum Alloys with Similar and Dissimilar Metals: Review. *Metals* **2022**, *12*, 2099. [[CrossRef](#)]
294. Niu, P.; Li, W.; Yang, C.; Chen, Y.; Chen, D. Low Cycle Fatigue Properties of Friction Stir Welded Dissimilar 2024-to-7075 Aluminum Alloy Joints. *Mater. Sci. Eng. A* **2022**, *832*, 142423. [[CrossRef](#)]
295. Cole, E.G.; Fehrenbacher, A.; Duffie, N.A.; Zinn, M.R.; Pfefferkorn, F.E.; Ferrier, N.J. Weld temperature effects during friction stir welding of dissimilar aluminum alloys 6061-t6 and 7075-t6. *Int. J. Adv. Manuf. Technol.* **2013**, *71*, 643–652. [[CrossRef](#)]
296. Yan, Z.; Liu, X.; Fang, H. Effect of Sheet Configuration on Microstructure and Mechanical Behaviors of Dissimilar Al–Mg–Si/Al–Zn–Mg Aluminum Alloys Friction Stir Welding Joints. *J. Mater. Sci. Technol.* **2016**, *32*, 1378–1385. [[CrossRef](#)]
297. Barbini, A.; Carstensen, J.; Dos Santos, J. Influence of Alloys Position, Rolling and Welding Directions on Properties of AA2024/AA7050 Dissimilar ButtWeld Obtained by Friction Stir Welding. *Metals* **2018**, *8*, 202. [[CrossRef](#)]
298. Cavaliere, P.; Santis, A.; Panella, F.; Squillace, A. Effect of welding parameters on mechanical and microstructural properties of dissimilar AA6082-AA2024 joints produced by friction stir welding. *Mater. Des.* **2009**, *30*, 609–616. [[CrossRef](#)]
299. Gérard, H.; Ehrström, J.C. Friction stir welding of dissimilar alloys for aircraft. In Proceedings of the 5th International Friction Stir Welding Symposium, Metz, France, 14–16 September 2004.
300. Amancio-Filho, S.T.; Sheikhi, S.; dos Santos, J.F.; Bolfarini, C. Preliminary study on the microstructure and mechanical properties of dissimilar friction stir welds in aircraft aluminium alloys 2024-T351 and 6056-T4. *J. Mater. Process. Technol.* **2008**, *206*, 132–142. [[CrossRef](#)]
301. Lee, W.-B.; Yeon, Y.-M.; Jung, S.-B. The joint properties of dissimilar formed Al alloys by friction stir welding according to the fixed location of materials. *Scr. Mater.* **2003**, *49*, 423–428. [[CrossRef](#)]
302. Schmale, J.; Fehrenbacher, A.; Shrivastava, A.; Pfefferkorn, F.E. Calibration of Dynamic Tool–Workpiece Interface Temperature Measurement during Friction Stir Welding. *Measurement* **2016**, *88*, 331–342. [[CrossRef](#)]
303. Simar, A.; Jonckheere, C.; Deplus, K.; Pardoën, T.; de Meester, B. Comparing Similar and Dissimilar Friction Stir Welds of 2017–6005A Aluminium Alloys. *Sci. Technol. Weld. Join.* **2010**, *15*, 254–259. [[CrossRef](#)]
304. Kim, N.K.; Kim, B.C.; An, Y.G.; Jung, B.H.; Song, S.W.; Kang, C.Y. The effect of material arrangement on mechanical properties in Friction Stir Welded dissimilar A5052/A5J32 aluminum alloys. *Met. Mater. Int.* **2009**, *15*, 671–675. [[CrossRef](#)]
305. Donatus, U.; Thompson, G.E.; Zhou, X.; Wang, J.; Beamish, K. Flow Patterns in Friction Stir Welds of AA5083 and AA6082 Alloys. *Mater. Des.* **2015**, *83*, 203–213. [[CrossRef](#)]
306. Park, S.-K.; Hong, S.-T.; Park, J.-H.; Park, K.-Y.; Kwon, Y.-J.; Son, H.-J. Effect of Material Locations on Properties of Friction Stir Welding Joints of Dissimilar Aluminium Alloys. *Sci. Technol. Weld. Join.* **2010**, *15*, 331–336. [[CrossRef](#)]
307. Hong, S.-T. Mixing of materials in FSW of dissimilar aluminum alloys. *Trans. Korean. Soc. Mech. Eng. A* **2009**, *33*, 108–113.
308. Niu, P.; Li, W.; Chen, D. Strain hardening behavior and mechanisms of friction stir welded dissimilar joints of aluminum alloys. *Mater. Lett.* **2018**, *231*, 68–71. [[CrossRef](#)]
309. Niu, P.; Li, W.; Li, N.; Xu, Y.; Chen, D.L. Exfoliation corrosion of friction stir welded dissimilar 2024-to-7075 aluminum alloys. *Mater. Charact.* **2019**, *147*, 93–100. [[CrossRef](#)]

310. Hasan, M.M.; Ishak, M.; Rejab, M.R.M. Effect of pin tool flute radius on the material flow and tensile properties of dissimilar friction stir welded aluminum alloys. *Int. J. Adv. Manuf. Technol.* **2018**, *98*, 2747–2758. [[CrossRef](#)]
311. Kalemba-Rec, I.; Kopyściański, M.; Miara, D.; Krasnowski, K. Effect of process parameters on mechanical properties of friction stir welded dissimilar 7075-T651 and 5083-H111 aluminum alloys. *Int. J. Adv. Manuf. Technol.* **2018**, *97*, 2767–2779. [[CrossRef](#)]
312. Safarwali, B.; Shamanian, M.; Eslami, A. Effect of post-weld heat treatment on joint properties of dissimilar friction stir welded 2024-T4 and 7075-T6 aluminum alloys. *Trans. Nonferrous Met. Soc. China* **2018**, *28*, 1287–1297. [[CrossRef](#)]
313. Palanivel, R.; Laubscher, R.; Vigneshwaran, S.; Dinaharan, I. Prediction and optimization of the mechanical properties of dissimilar friction stir welding of aluminum alloys using design of experiments. *Proc. Inst. Mech. Eng. Part B J. Eng. Manuf.* **2018**, *232*, 1384–1394. [[CrossRef](#)]
314. Hamilton, C.; Dymek, S.; Dryzek, E.; Kopyscianski, M.; Pietras, A.; Węglowska, A.; Wrobel, M. Application of positron lifetime annihilation spectroscopy for characterization of friction stir welded dissimilar aluminum alloys. *Mater. Charact.* **2017**, *132*, 431–436. [[CrossRef](#)]
315. Huang, B.W.; Qin, Q.D.; Zhang, D.H.; Wu, Y.J.; Su, X.D. Microstructure and Mechanical Properties of Dissimilar Joints of Al-Mg₂Si and 5052 Aluminum Alloy by Friction Stir Welding. *J. Mater. Eng. Perform.* **2018**, *27*, 1898–1907. [[CrossRef](#)]
316. Moradi, M.M.; Aval, H.J.; Jamaati, R.; Amirkhanlou, S.; Ji, S. Microstructure and texture evolution of friction stir welded dissimilar aluminum alloys: AA2024 and AA6061. *J. Manuf. Processes.* **2018**, *32*, 1–10. [[CrossRef](#)]
317. Prasanth, R.S.S.; Raj, K.H. Determination of Optimal Process Parameters of Friction Stir Welding to Join Dissimilar Aluminum Alloys Using Artificial Bee Colony Algorithm. *Trans. Indian Inst. Met.* **2017**, *71*, 453–462. [[CrossRef](#)]
318. Azeez, S.; Akinlabi, E. Effect of processing parameters on microhardness and microstructure of a double-sided dissimilar friction stir welded aa6082-t6 and aa7075-t6 aluminum alloy. *Mater. Today Proc.* **2018**, *5*, 18315–18324. [[CrossRef](#)]
319. Peng, G.; Ma, Y.; Hu, J.; Jiang, W.; Huan, Y.; Chen, Z.; Zhang, T. Nanoindentation Hardness Distribution and Strain Field and Fracture Evolution in Dissimilar Friction Stir-Welded AA 6061-AA 5A06 Aluminum Alloy Joints. *Adv. Mater. Sci. Eng.* **2018**, 4873571. [[CrossRef](#)]
320. Das, U.; Toppo, V. Effect of Tool Rotational Speed on Temperature and Impact Strength of Friction Stir Welded Joint of Two Dissimilar Aluminum Alloys. *Mater. Today Proc.* **2018**, *5*, 6170–6175. [[CrossRef](#)]
321. Sarsılmaz, F. Relationship between micro-structure and mechanical properties of dissimilar aluminum alloy plates by friction stir welding. *J. Therm. Sci.* **2018**, *22*, 55–66. [[CrossRef](#)]
322. No, K.; Yoo, J.T.; Yoon, J.H.; Lee, H.S. Effect of Process Parameters on Friction Stir Welds on AA2219-AA2195 Dissimilar Aluminum Alloys. *Korean J. Mater. Res.* **2017**, *27*, 331–338. [[CrossRef](#)]
323. Kopyscianski, M.; Dymek, S.; Hamilton, C.; Węglowska, A.; Pietras, A.; Szczepanek, M.; Wojnarowska, M. Microstructure of Friction Stir Welded Dissimilar Wrought 2017A and Cast AlSi9Mg Aluminum Alloys. *Acta Phys. Pol. A* **2017**, *131*, 1390–1394. [[CrossRef](#)]
324. Ghaffarpour, M.; Kazemi, M.; Mohammadi Sefat, M.J.; Aziz, A.; Dehghani, K. Evaluation of dissimilar joints properties of 5083-H12 and 6061-T6 aluminum alloys produced by tungsten inert gas and friction stir welding. *Proc. Inst. Mech. Eng.* **2015**, *231*, 297–308. [[CrossRef](#)]
325. Bijanrostami, K.; Barenji, R.V.; Hashemipour, M. Effect of Traverse and Rotational Speeds on the Tensile Behavior of the Underwater Dissimilar Friction Stir Welded Aluminum Alloys. *J. Mater. Eng. Perform.* **2017**, *26*, 909–920. [[CrossRef](#)]
326. Kasman, S.; Kahraman, F.; Emiralioglu, A. A Case Study for the Welding of Dissimilar EN AW 6082 and EN AW5083 Aluminum Alloys by Friction Stir Welding. *Metals* **2016**, *7*, 6. [[CrossRef](#)]
327. Doley, J.K.; Kore, S.D. A Study on Friction Stir Welding of Dissimilar Thin Sheets of Aluminum Alloys AA 5052-AA 6061. *J. Manuf. Sci. Eng.* **2016**, *138*, 114502. [[CrossRef](#)]
328. Saravanan, V.; Rajakumar, S.; Nilotpal Banerjee Amuthakkannan, R. Effect of shoulder diameter to pin diameter ratio on microstructure and mechanical properties of dissimilar friction stir welded AA2024-T6 and AA7075-T6 aluminum alloy joints. *Int. J. Adv. Manuf. Technol.* **2016**, *87*, 3637–3645. [[CrossRef](#)]
329. Yan, Z.-J.; Liu, X.-S.; Fang, H.-Y. Fatigue Behavior of Dissimilar Al-Mg-Si/Al-Zn-Mg Aluminum Alloys Friction Stir Welding Joints. *Acta Metall. Sin.* **2016**, *29*, 1161–1168. [[CrossRef](#)]
330. Zapata, J.; Toro, M.; López, D. Residual stresses in friction stir dissimilar welding of aluminum alloys. *J. Mater. Process. Technol.* **2016**, *229*, 121–127. [[CrossRef](#)]
331. Sun, Y.; Tsuji, N.; Fujii, H. Microstructure and Mechanical Properties of Dissimilar Friction Stir Welding between Ultrafine Grained 1050 and 6061-T6 Aluminum Alloys. *Metals* **2016**, *6*, 249. [[CrossRef](#)]
332. Texier, D.; Zedan, Y.; Amoros, T.; Feulvarch, E.; Stinville, J.C.; Bocher, P. Near-surface mechanical heterogeneities in a dissimilar aluminum alloys friction stir welded joint. *Mater. Des.* **2016**, *108*, 217–229. [[CrossRef](#)]
333. Rodriguez, R.I.; Jordon, J.B.; Allison, P.G.; Rushing, T.; Garcia, L. Low-cycle fatigue of dissimilar friction stir welded aluminum alloys. *Mater. Sci. Eng. A* **2016**, *654*, 236–248. [[CrossRef](#)]
334. Rodriguez, R.I.; Jordon, J.B.; Allison, P.G.; Rushing, T.; Garcia, L. Microstructure and mechanical properties of dissimilar friction stir welding of 6061-to-7050 aluminum alloys. *Mater. Des.* **2015**, *83*, 60–65. [[CrossRef](#)]
335. Ilangovan, M.; Boopathy, S.R.; Balasubramanian, V. Effect of tool pin profile on microstructure and tensile properties of friction stir welded dissimilar AA 6061-AA 5086 aluminium alloy joints. *Def. Technol.* **2015**, *11*, 174–184. [[CrossRef](#)]

336. Reza-E-Rabby, M.; Tang, W.; Reynolds, A.P. Effect of tool pin features on process response variables during friction stir welding of dissimilar aluminum alloys. *Sci. Technol. Weld. Join.* **2015**, *20*, 425–432. [[CrossRef](#)]
337. Donatus, U.; Thompson, G.E.; Zhou, X. Anodizing Behavior of Friction StirWelded Dissimilar Aluminum Alloys. *J. Electrochem. Soc.* **2015**, *162*, C657–C665. [[CrossRef](#)]
338. Karam, A.; Mahmoud, T.S.; Zakaria, H.M.; Khalifa, T.A. Friction Stir Welding of Dissimilar A319 and A413 Cast Aluminum Alloys. *Arab. J. Sci. Eng.* **2014**, *39*, 6363–6373. [[CrossRef](#)]
339. Ipekoglu, G.; Çam, G. Effects of Initial Temper Condition and Postweld Heat Treatment on the Properties of Dissimilar Friction-Stir-Welded Joints between AA7075 and AA6061 Aluminum Alloys. *Metall. Mater. Trans. A* **2014**, *45*, 3074–3087. [[CrossRef](#)]
340. Song, Y.; Yang, X.; Cui, L.; Hou, X.; Shen, Z.; Xu, Y. Defect features and mechanical properties of friction stir lap welded dissimilar AA2024–AA7075 aluminum alloy sheets. *Mater. Des.* **2014**, *55*, 9–18. [[CrossRef](#)]
341. Jannet, S.; Mathews, P.K. Effect of Welding Parameters on Mechanical and Microstructural Properties of Dissimilar Aluminum Alloy Joints Produced by Friction Stir Welding. *Appl. Mech. Mater.* **2014**, *592*, 250–254. [[CrossRef](#)]
342. Palanivel, R.; Koshy Mathews, P.; Dinaharan, I.; Murugan, N. Mechanical and metallurgical properties of dissimilar friction stir welded AA5083-H111 and AA6351-T6 aluminum alloys. *Trans. Nonferrous Met. Soc. China* **2014**, *24*, 58–65. [[CrossRef](#)]
343. Palanivel, R.; Mathews, P.K.; Murugan, N. Optimization of process parameters to maximize ultimate tensile strength of friction stir welded dissimilar aluminum alloys using response surface methodology. *J. Cent. South Univ.* **2013**, *20*, 2929–2938. [[CrossRef](#)]
344. Jonckheere, C.; de Meester, B.; Denquin, A.; Simar, A. Torque, temperature and hardening precipitation evolution in dissimilar friction stir welds between 6061-T6 and 2014-T6 aluminum alloys. *J. Mater. Process. Technol.* **2013**, *213*, 826–837. [[CrossRef](#)]
345. Jonckheere, C.; de Meester, B.; Denquin, A.; Simar, A. Dissimilar friction stir welding of 2014 to 6061 aluminum alloys. *Adv. Mater. Res.* **2012**, *409*, 269–274. [[CrossRef](#)]
346. Ghosh, M.; Husain, M.d.M.; Kumar, K.; Kailas, S.V. Friction Stir-Welded Dissimilar Aluminum Alloys: Microstructure, Mechanical Properties, and Physical State. *J. Mater. Eng. Perform.* **2013**, *22*, 3890–3901. [[CrossRef](#)]
347. Ghosh, M.; Kumar, K.; Kailas, S.V.; Ray, A.K. Optimization of friction stir welding parameters for dissimilar aluminum alloys. *Mater. Des.* **2010**, *31*, 3033–3037. [[CrossRef](#)]
348. Koilraj, M.; Sundareswaran, V.; Vijayan, S.; Koteswara Rao, S. Friction stir welding of dissimilar aluminum alloys AA2219 to AA5083—Optimization of process parameters using Taguchi technique. *Mater. Des.* **2012**, *42*, 1–7. [[CrossRef](#)]
349. Dinaharan, I.; Kalaiselvan, K.; Vijay, S.J.; Raja, P. Effect of material location and tool rotational speed on microstructure and tensile strength of dissimilar friction stir welded aluminum alloys. *Arch. Civ. Mech. Eng.* **2012**, *12*, 446–454. [[CrossRef](#)]
350. Palanivel, R.; Koshy Mathews, P.; Murugan, N.; Dinaharan, I. Effect of tool rotational speed and pin profile on microstructure and tensile strength of dissimilar friction stir welded AA5083-H111 and AA6351-T6 aluminum alloys. *Mater. Des.* **2012**, *40*, 7–16. [[CrossRef](#)]
351. Prime, M.B.; Gnäupel-Herold, T.; Baumann, J.A.; Lederich, R.J.; Bowden, D.M.; Sebring, R.J. Residual stress measurements in a thick, dissimilar aluminum alloy friction stir weld. *Acta Mater.* **2006**, *54*, 4013–4021. [[CrossRef](#)]
352. Mroczka, K. Characteristics of AlSi9Mg/2017A Aluminum Alloys Friction Stir Welded with Offset Welding Line and Root-Side Heating. *Arch. Metall. Mater.* **2014**, *59*, 1293–1299. [[CrossRef](#)]
353. Mroczka, K.; Dutkiewicz, J.; Pietras, A. Microstructure of friction stir welded joints of 2017A aluminium alloy sheets. *J. Microsc.* **2010**, *237*, 521–525. [[CrossRef](#)]
354. Yang, M.; Li, C.; Liu, S.; Ye, L.; Tang, J.; Liao, Z. Effect of Artificial Aging on Microstructure and Mechanical Properties of Friction Stir Welded Joint of 7003/7046 Al-alloys. *Chin. J. Mater. Res.* **2020**, *34*, 495–504.
355. Kasman, S.; Ozan, S. Effect of pin offset on the mechanical properties of friction stir welded AA 6013 aluminum alloy plates/Pin-Offset-Einfluss auf die mechanischen Eigenschaften beim Rührreißschweißen von Blechen aus der Aluminiumlegierung AA 6013. *Materialwiss. Werkstofftech* **2019**, *50*, 1511. [[CrossRef](#)]
356. Zhao, Z.; Liang, H.; Zhao, Y.; Yan, K. Effect of Exchanging Advancing and Retreating Side Materials on Mechanical Properties and Electrochemical Corrosion Resistance of Dissimilar 6013-T4 and 7003 Aluminum Alloys FSW Joints. *J. Mater. Eng. Perform.* **2018**, *27*, 1777–1783. [[CrossRef](#)]
357. Yoon, T.J.; Jung, B.H.; Kang, C.Y. The quantitative investigation of mechanical properties and characterization of fractured position for friction stir lap welded A6111/A5023. *Mater. Des.* **2015**, *83*, 377–386. [[CrossRef](#)]
358. Verduzco-Juarez, J.C.; Garcia-Hernandez, R.; Dominguez-Almaraz, G.M.; Villalón-López, J. Effect of Pre and Post Weld Heat Treatment on the Mechanical Properties of Friction Stir Welded AA6061-T6 Joint. *Int. J. Automot. Mech. Eng.* **2020**, *17*, 7882–7889. [[CrossRef](#)]
359. Godhani, P.S.; Patel, V.V.; Vora, J.J.; Chaudhary, N.D.; Banka, R. Effect of Friction Stir Welding of Aluminum Alloys AA6061/AA7075: Temperature Measurement, Microstructure, and Mechanical Properties. In *Innovations in Infrastructure: Proceedings of ICIF 2018*; Springer: Singapore, 2019; pp. 591–598.
360. Chen, Y.; Wang, H.; Li, H.; Wang, X.; Ding, H.; Zhao, J.; Zhang, F. Investigation into the Dissimilar Friction Stir Welding of AA5052 and AA6061 Aluminum Alloys Using Pin-Eccentric Stir Tool. *Metals* **2019**, *9*, 718. [[CrossRef](#)]
361. Zhang, C.; Huang, G.; Yu, C.; Zhu, Y.; Liu, Q. On the microstructure and mechanical properties of similar and dissimilar AA7075 and AA2024 friction stir welding joints: Effect of rotational speed. *J. Manuf. Process.* **2019**, *37*, 470–487. [[CrossRef](#)]
362. Azeez, S.; Akinlabi, E.T.; Kailas, S.V.; Brandi, S.D. Microstructural properties of a dissimilar friction stir welded thick aluminum aa6082-t6 and aa7075-t6 alloy. *Mater. Today Proc.* **2018**, *5*, 18297–18306. [[CrossRef](#)]

363. Hamilton, C.; Kopyściński, M.; Węglowska, A.; Dymek, S.; Pietras, A. A Numerical Simulation for Dissimilar Aluminum Alloys Joined by Friction Stir Welding. *Metall. Mater. Trans. A* **2016**, *47*, 4519–4529. [[CrossRef](#)]
364. Shiva Kumar, G.N.; Rajamurugan, G. Friction stir welding of dissimilar alloy combinations—A Review. *Proc. Inst. Mech. Eng. Part C J. Mech. Eng. Sci.* **2022**, *236*, 6688–6705. [[CrossRef](#)]
365. Kasman, S.; Yenier, Z. Analyzing dissimilar friction stir welding of AA5754/AA7075. *Int. J. Adv. Manuf. Technol.* **2013**, *70*, 145–156. [[CrossRef](#)]
366. Forcellese, A.; Simoncini, M.; Casalino, G. Influence of Process Parameters on the Vertical Forces Generated during Friction Stir Welding of AA6082-T6 and on the Mechanical Properties of the Joints. *Metals* **2017**, *7*, 350. [[CrossRef](#)]
367. Mastanaiah, P.; Sharma, A.; Reddy, G.M. Dissimilar Friction Stir Welds in AA2219-AA5083 Aluminium Alloys: Effect of Process Parameters on Material Inter-Mixing, Defect Formation, and Mechanical Properties. *Trans. Indian Inst. Met.* **2015**, *69*, 1397–1415. [[CrossRef](#)]
368. Saeidi, M.; Babak, M.; Mohammad Kazem, B.G.; Ghader, F. Mathematical modeling and optimization of friction stir welding process parameters in AA5083 and AA7075 aluminum alloy joints. *Proc. Inst. Mech. Eng. Part B J. Eng. Manuf.* **2015**, *230*, 1284–1294. [[CrossRef](#)]
369. Zhu, Z.; Wang, M.; Zhang, H.; Zhang, X.; Yu, T.; Wu, Z. A Finite Element Model to Simulate Defect Formation during Friction Stir Welding. *Metals* **2017**, *7*, 256. [[CrossRef](#)]
370. Prabha, K.A.; Putha, P.K.; Prasad, B.S. Effect of Tool Rotational Speed on Mechanical Properties of Aluminium Alloy 5083 Weldments in Friction Stir Welding. *Mater. Today Proc.* **2018**, *5*, 18535–18543. [[CrossRef](#)]
371. Varunraj, S.; Ruban, M. Investigation of the Microstructure and Mechanical Properties of AA6063 and AA7075 Dissimilar Aluminium Alloys by Friction Stir Welding Process. *Mater. Today Proc.* **2022**, *68*, 1654–1657. [[CrossRef](#)]
372. Amatullah, M.; Jan, M.; Farooq, M.; Zargar, A.S.; Maqbool, A.; Khan, N.Z. Effect of Tool Rotational Speed on the Friction Stir Welded Aluminum Alloys: A Review. *Mater. Today Proc.* **2022**, *62*, 245–250. [[CrossRef](#)]
373. Yan, J.; Sutton, M.A.; Reynolds, A.P. Process–Structure–Property Relationships for Nugget and Heat Affected Zone Regions of AA2524–T351 Friction Stir Welds. *Sci. Technol. Weld. Join.* **2005**, *10*, 725–736. [[CrossRef](#)]
374. Wang, Y.; Ma, H.; Chai, P.; Zhang, Y. GoYal Behavior of AA2A14-T6 Aluminum Alloy Friction Stir Welded Joints. *Weld. World* **2021**, *65*, 1483–1499. [[CrossRef](#)]
375. Goyal, A.; Garg, R.K. Effect of Tool Rotational and Transverse Speed on Mechanical Properties of Friction Stir Welded AA5086-H32 Aluminium Alloy. *Int. J. Microstruct. Mater. Prop.* **2017**, *12*, 79–93. [[CrossRef](#)]
376. Moshwan, R.; Yusof, F.; Hassan, M.A.; Rahmat, S.M. Effect of Tool Rotational Speed on Force Generation, Microstructure and Mechanical Properties of Friction Stir Welded Al–Mg–Cr–Mn (AA 5052-O) Alloy. *Mater. Des.* **2015**, *66*, 118–128. [[CrossRef](#)]
377. Li, Y.; Sun, D.; Gong, W. Effect of Tool Rotational Speed on the Microstructure and Mechanical Properties of Bobbin Tool Friction Stir Welded 6082-T6 Aluminum Alloy. *Metals* **2019**, *9*, 894. [[CrossRef](#)]
378. Rezaei, H.; Mirbeik, M.H.; Bisadi, H. Effect of Rotational Speeds on Microstructure and Mechanical Properties of Friction Stir-Welded 7075-T6 Aluminium Alloy. *Proc. Inst. Mech. Eng. C J. Mech. Eng. Sci.* **2011**, *225*, 1761–1773. [[CrossRef](#)]
379. Laska, A.; Szkodo, M.; Cavaliere, P.; Perrone, A. Influence of the Tool Rotational Speed on Physical and Chemical Properties of Dissimilar Friction-Stir-Welded AA5083/AA6060 Joints. *Metals* **2022**, *12*, 1658. [[CrossRef](#)]
380. Ghaffarpour, M.; Kolahgar, S.; Dariani, B.M.; Dehghani, K. Evaluation of Dissimilar Welds of 5083-H12 and 6061-T6 Produced by Friction Stir Welding. *Metall. Mater. Trans. A* **2013**, *44*, 3697–3707. [[CrossRef](#)]
381. Peel, M.J.; Steuwer, A.; Withers, P.J.; Dickerson, T.; Shi, Q.; Shercliff, H. Dissimilar Friction Stir Welds in AA5083-AA6082. Part I: Process Parameter Effects on Thermal History and Weld Properties. *Metall. Mater. Trans. A* **2006**, *37*, 2183–2193. [[CrossRef](#)]
382. Devaiah, D.; Kishore, K.; Laxminarayana, P. Optimal FSW Process Parameters for Dissimilar Aluminium Alloys (AA5083 and AA6061) Using Taguchi Technique. *Mater. Today Proc.* **2018**, *5*, 4607–4614. [[CrossRef](#)]
383. Gupta, S.K.; Pandey, K.; Kumar, R. Multi-objective optimization of friction stir welding process parameters for joining of dissimilar AA5083/AA6063 aluminium alloys using hybrid approach. *Proc. Inst. Mech. Eng. Part L J. Mater. Des. Appl.* **2016**, *232*, 343–353.
384. Das, U.; Das, R.; Toppo, V. Analysis of Some Mechanical Properties of Friction Stir Welded Joints of AA6101 and AA6351 Aluminium Alloys under T6 Condition. *Mater. Today Proc.* **2021**, *44*, 2700–2704. [[CrossRef](#)]
385. Velotti, C.; Astarita, A.; Squillace, A.; Ciliberto, S.; Villano, M.; Giuliani, M.; Prisco, U.; Montuori, M.; Giorleo, G.; Bellucci, F. On the critical technological issues of friction stir welding lap joints of dissimilar aluminum alloys. *Surf. Interface Anal.* **2013**, *45*, 1643–1648. [[CrossRef](#)]
386. Goriparthi, V.; Nallu, R.; Chebolu, R.; Indupuri, S.; Rudrapati, R. Experimental Studies on Mechanical Behavior of TIG and Friction Stir Welded AA5083 -AA7075 Dissimilar Aluminum Alloys. *Adv. Mater. Sci. Eng.* **2023**, *2023*, 8622525. [[CrossRef](#)]
387. Devaraju, A.; Jeshrun Shalem, M.; Manichandra, B. Effect of Rotation Speed on Tensile Properties & Microhardness of Dissimilar Al Alloys 6061-T6 to 2024 -T6 Welded via Solid State Joining Technique. *Mater. Today Proc.* **2019**, *18*, 3286–3290.
388. Jamshidi Aval, H. Microstructure and Residual Stress Distributions in Friction Stir Welding of Dissimilar Aluminium Alloys. *Mater. Des.* **2015**, *87*, 405–413. [[CrossRef](#)]
389. De Giorgi, M.; Scialpi, A.; Panella, F.W.; De Filippis, L.A.C. Effect of Shoulder Geometry on Residual Stress and Fatigue Properties of AA6082 Fsw Joints. *J. Mech. Sci. Technol.* **2009**, *23*, 26–35. [[CrossRef](#)]
390. Richards, D.G.; Prangnell, P.B.; Withers, P.J.; Williams, S.W.; Nagy, T.; Morgan, S. Efficacy of Active Cooling for Controlling Residual Stresses in Friction Stir Welds. *Sci. Technol. Weld. Join.* **2010**, *15*, 156–165. [[CrossRef](#)]

391. Haribalaji, V.; Boopathi, S.; Mohammed Asif, M. Optimization of Friction Stir Welding Process to Join Dissimilar AA2014 and AA7075 Aluminum Alloys. *Mater. Today Proc.* **2022**, *50*, 2227–2234. [[CrossRef](#)]
392. Zuiko, I.S.; Malopheyev, S.; Mironov, S.; Kaibyshev, R. Dissimilar Friction Stir Welding of AA2519 and AA5182. *Materials* **2022**, *15*, 8776. [[CrossRef](#)]
393. Tarkono, T.; Tenando, F.; Nafrizal, N.; Sukmana, I. The Effect of Rotational Speed on Friction Stir Welding (FSW) Quality of Dissimilar Aluminum Alloy Series AA 1100 and AA 5052. *J. Polimesin* **2023**, *21*, 21–24.
394. Sivaselvan, S.; Natarajan, M.; Devadasan, S.R.; Sivaram, N.M. Influence of Friction Stir Welding Parameters on the Tribological Behavior of Dissimilar Aluminum Alloy Joint. *Ind. Lubr. Tribol.* **2023**, *75*, 197–203.
395. Heramo, W.T.; Workneh, H.Z. Optimization of process parameters in friction stir welding of dissimilar aluminum alloys (AA6061-T6 and AA5052-H32). *Int. J. Adv. Manuf. Technol.* **2023**, *129*, 4473–4489. [[CrossRef](#)]
396. Wang, Z.; Zhu, W.; Zhang, Z.; Wang, B.; Xue, P.; Ni, D.; Liu, F.; Xiao, B.; Ma, Z.; Wang, F.; et al. Dissimilar Friction Stir Welding of, 2.2.1.9.-T.8.; 2195-T8 Aluminum Alloys: Part I—Microstructure Evolution Mechanical Properties. *J. Mater. Sci.* **2023**, *58*, 9737–9754. [[CrossRef](#)]
397. Sivachidambaram, S.; Rajamurugan, G.; Amirtharaj, D. Optimizing the parameters for friction stir welding of dissimilar aluminium alloys AA5383/AA7075. *ARPN J. Eng. Appl. Sci.* **2015**, *10*, 5434–5437.
398. Miles, M.P.; Nelson, T.W.; Melton, D.W. Formability of friction-stir-welded dissimilar-aluminum-alloy sheets. *Metall. Mater. Trans. A* **2005**, *36*, 3335–3342. [[CrossRef](#)]
399. Ouyang, J.H.; Kovacevic, R. Material flow and microstructure in the friction stir butt welds of the same and dissimilar aluminum alloys. *J. Mater. Eng. Perform.* **2002**, *11*, 51–63. [[CrossRef](#)]
400. Ivanov, A.N.; Kalashnikova, T.A.; Zhukov, L.L.; Gurianov, D.A.; Beloborodov, V.A.; Kolubaev, E.A.; Rubtsov, V.E.; Tyurin, A.G.; Bakshaev, V.A.; Nikitin, Y.V. Obtaining of aluminum alloys weld joints with specified strength properties by friction stir welding. *AIP Conf. Proc.* **2022**, *2467*, 020058.
401. Kumar, S.D.; Kumar, S.S. Investigation of mechanical behavior of friction stir welded joints of AA6063 with AA5083 aluminum alloys. *Mech. Mech. Eng.* **2019**, *23*, 59–63. [[CrossRef](#)]
402. Sasikala, G.; Jothiprakash, V.M.; Pant, B.; Subalakshmi, R.; Thirumal Azhagan, M.; Arul, K.; Alonazi, W.B.; Karnan, M.; Kumar, S.P. Optimization of Process Parameters for Friction Stir Welding of Different Aluminum Alloys AA2618 to AA5086 by Taguchi Method. *Adv. Mater. Sci. Eng.* **2022**, *2022*, 3808605. [[CrossRef](#)]
403. Aydin, H.; Tutar, M.; Yigit, K.; Bayram, A. Mechanical Properties of Friction Stir Welded 3003 Aluminum Alloy in Different Welding Conditions. *Int. J. Mech. Prod. Eng.* **2017**, *5*, 92–96.
404. Aydin, H.; Bayram, A.; Yildirim, M.T.; Yigit, K. Influence of Welding Parameters on the Fatigue Behaviours of Friction Stir Welds of 3003-O Aluminum Alloys. *Mater. Sci. (Medzg.)* **2010**, *16*, 311–319.
405. Weglowski, M.S.; Pietras, A.; Weglowska, A. Effect of welding parameters on mechanical and microstructural properties of AL 2024 joints produced by friction stir welding. *J. KONES* **2009**, *16*, 523–532.
406. Nejad, S.G.; Yektapour, M.; Akbarifard, A. Friction stir welding of 2024 aluminum alloy: Study of major parameters and threading feature on probe. *J. Mech. Sci. Technol.* **2017**, *31*, 5435–5445. [[CrossRef](#)]
407. Milčić, M.; Vuherer, T.; Radisavljević, I.; Milčić, D.; Kramberger, J.; Andjelkovic, B. Mechanical behaviour of Al 2024 alloy welded by friction stir welding. In Proceedings of the 10th International Symposium Machine and Industrial Design in Mechanical Engineering, Novi Sad, Serbia, 6–8 June 2018; Volume 393, p. 012107.
408. Lin, S.B.; Zhao, Y.H.; Wu, L. Integral and layered mechanical properties of friction stir welded joints of 2014 aluminium alloy. *Mater. Sci. Technol.* **2006**, *22*, 995–998. [[CrossRef](#)]
409. Ugender, S.; Kumar, A.; Reddy, A.S. Experimental Investigation of Tool Geometry on Mechanical Properties of Friction Stir Welding of AA 2014 Aluminium Alloy. *Procedia Mater. Sci.* **2014**, *5*, 824–831. [[CrossRef](#)]
410. Mroczka, K.; Dutkiewicz, J.; Pietras, A. Structure and Properties of FSW Joints of 2017A Aluminum Alloy Welded at Different Pin-Tool Rate. In *Problems of Modern Techniques in Aspect of Engineering and Education*; University of the National Education Commission: Kraków, Poland, 2006; pp. 267–272.
411. Takhakh, A.M.; Abdullah, A.M. An Experimental Investigation on Fatigue Properties of AA3003-H14 Aluminum alloy Friction Stir Welds. *J. Eng.* **2012**, *17*, 1391–1401. [[CrossRef](#)]
412. Chekalil, I.; Miloudi, A.; Planche, M.P.; Ghazi, A. Prediction of mechanical behavior of friction stir welded joints of AA3003 aluminum alloy. *Frat. Ed Integrità Strutt.* **2020**, *54*, 153–168. [[CrossRef](#)]
413. Kasman, S.; Ozan, S. Characterization of friction stir welded AA 3003-H24 aluminum alloy plates. *Sigma J. Eng. Nat. Sci.* **2022**, *40*, 620–629. [[CrossRef](#)]
414. Xu, A. Properties of Friction Stir Welded 3003-H17 Aluminum Alloy at High Travel Speeds. In Proceedings of the 6th International Conference on Materials, Mechanical Engineering and Automation Technology, Zhuhai, China, 1–3 May 2020; Volume 1676, p. 012114.
415. Goyal, A.; Rohilla, P.K.; Kaushik, A.K. Optimization of Friction Stir Welding Parameters for AA3003 Aluminum Alloy Joints Using Response Surface Methodology. *Int. J. Mech. Solids* **2017**, *12*, 15–26.
416. Janeczek, A.; Tomkow, J.; Fydrych, D. The Influence of Tool Shape and Process Parameters on the Mechanical Properties of AW-3004 Aluminium Alloy Friction Stir Welded Joints. *Materials* **2021**, *14*, 3244. [[CrossRef](#)]

417. Choi, W.H.; Kwon, Y.J.; Yoon, S.; Kang, M.S.; Lim, C.Y.; Seo, J.D.; Hong, S.T.; Park, D.H.; Lee, K.H. Influence of Welding Parameters on Macrostructure and Mechanical Properties of Friction-Stir-Spot-Welded 5454-O Aluminum Alloy Sheets. *J. Weld. Join.* **2011**, *29*, 56–64.
418. Selvarajan, R.; Balasubramanian, V. Multi-Response Optimization of Friction-Stir-Welded AA1100 Aluminum Alloy Joints. *J. Mater. Eng. Perform.* **2011**, *21*, 1–14.
419. Dong, J.; Zhang, D.; Zhang, W.; Zhang, W.; Qiu, C. Microstructure and properties of underwater friction stir-welded 7003-T4/6060-T4 aluminum alloys. *J. Mater. Sci.* **2019**, *54*, 11254–11262. [[CrossRef](#)]
420. Sheikhi, S.; dos Santos, J. Effect of process parameter on mechanical properties of friction stir welded tailored blanks from aluminium alloy 6181-T4. *Sci. Technol. Weld. Join.* **2007**, *12*, 370–375. [[CrossRef](#)]
421. Zhou, Y.; Chen, S.; Wang, J.; Wang, P.; Xia, J. Influences of Pin Shape on a High Rotation Speed Friction Stir Welding Joint of a 6061-T6 Aluminum Alloy Sheet. *Metals* **2018**, *8*, 987. [[CrossRef](#)]
422. Palanivel, R.; Koshy Mathews, P.; Murugan, N. Influences of Tool Pin Profile on the Mechanical and Metallurgical Properties of Friction Stir Welding of Dissimilar Aluminum Alloy. *Int. J. Eng. Sci. Technol.* **2010**, *2*, 2109–2115.
423. Aval, H.J.; Serajzadeh, S.; Kokabi, A.H.; Loureiro, A. Effect of tool geometry on mechanical and microstructural behaviours in dissimilar friction stir welding of AA 5086—AA 6061. *Sci. Technol. Weld. Join.* **2011**, *16*, 597–604. [[CrossRef](#)]
424. Xu, W.; Liu, J.; Zhu, H. Analysis of residual stresses in thick aluminum friction stir welded butt joints. *Mater. Des.* **2011**, *32*, 2000–2005. [[CrossRef](#)]
425. Sinhmar, S.; Dwivedi, D.K. Investigation of mechanical and corrosion behavior of friction stir weld joint of aluminium alloy. *Mater. Proc.* **2019**, *18*, 4542–4548. [[CrossRef](#)]
426. Astarita, A.; Tucci, F.; Silvestri, A.T.; Perrella, M.; Boccarusso, L.; Carlone, P. Dissimilar friction stir lap welding of AA2198 and AA7075 sheets: Forces, microstructure and mechanical properties. *Int. J. Adv. Manuf. Technol.* **2021**, *117*, 1045–1059. [[CrossRef](#)]
427. Tucci, F.; Carlone, P.; Silvestri, A.T.; Parmar, H.; Astarita, A. Dissimilar friction stir lap welding of AA2198-AA6082: Process analysis and joint characterization. *CIRP J. Manuf. Sci. Technol.* **2021**, *35*, 753–764. [[CrossRef](#)]
428. Aydin, H.; Tutar, M.; Durmuş, A.; Bayram, A.; Sayaca, T. Effect of Welding Parameters on Tensile Properties and Fatigue Behavior of Friction Stir Welded 2014-T6 Aluminum Alloy. *Trans. Indian Inst. Met.* **2011**, *65*, 21–30. [[CrossRef](#)]
429. Dewangan, S.K.; Tripathi, M.K.; Manoj, M.K. Effect of Ws on microstructure and mechanical properties of dissimilar friction stir welding of AA7075 and AA5083 alloy. *Mater. Today Proc.* **2019**, *27*, 2713–2717. [[CrossRef](#)]
430. Jia, H.; Wu, K.; Sun, Y.; Hu, F.; Chen, G. Evaluation of Axial Force, Tool Torque and Weld Quality of Friction Stir Welded Dissimilar 6061/5083 Aluminum Alloys. *CIRP J. Manuf. Sci. Technol.* **2022**, *37*, 267–277. [[CrossRef](#)]
431. Anandan, B.; Manikandan, M. Effect of Welding Speeds on the Metallurgical and Mechanical Property Characterization of Friction Stir Welding between Dissimilar Aerospace Grade 7050 T7651-2014A T6 Aluminium Alloys. *Mater. Today Commun.* **2023**, *35*, 106246. [[CrossRef](#)]
432. Dimov, N.; Weisz-Patruil, D.; Tanguy, A.; Sapanathan, T.; Benoist, J.; Charkaluk, E.; Simar, A. Strain and Damage Analysis Using High Resolution Digital Image Correlation in the Stir Zone of an AA6061-AA7075 Dissimilar Friction Stir Weld. *Mater. Today Commun.* **2023**, *34*, 105359. [[CrossRef](#)]
433. Khan, N.Z.; Bajaj, D.; Siddiquee, A.N.; Khan, Z.A.; Abidi, M.H.; Umer, U.; Alkhalefah, H. Investigation on Effect of Strain Rate and Heat Generation on Traverse Force in FSW of Dissimilar Aerospace Grade Aluminium Alloys. *Materials* **2019**, *12*, 1641. [[CrossRef](#)] [[PubMed](#)]
434. Ahmed, M.M.Z.; Ataya, S.; El-Sayed Seleman, M.M.; Ammar, H.R.; Ahmed, E. Friction Stir Welding of Similar and Dissimilar AA7075 and AA5083. *J. Mater. Process. Technol.* **2017**, *242*, 77–91. [[CrossRef](#)]
435. Alemdar, A.S.A.; Jalal, S.R.; Mulapeer, M.M.S. Influence of Friction Stir Welding Process on the Mechanical Characteristics of the Hybrid Joints AA2198-T8 to AA2024-T3. *Adv. Mater. Sci. Eng.* **2022**, *2022*, 7055446. [[CrossRef](#)]
436. Sindhuja, M.; Neelakrishnan, S.; Davidson, B.S. Effect of Welding Parameters on Mechanical Properties of Friction Stir Welding of Dissimilar Metals—A Review. *IOP Conf. Ser. Mater. Sci. Eng.* **2021**, *1185*, 012019. [[CrossRef](#)]
437. Ramamoorthi, R.; Yuvaraj, K.P.; Gokul, C.; Eashwar, S.J.; Arunkumar, N.; Abith Tamil Dheen, S. An Investigation of the Impact of Axial Force on Friction Stir-Welded AA5086/AA6063 on Microstructure and Mechanical Properties Butt Joints. *Mater. Today Proc.* **2021**, *37*, 3159–3163. [[CrossRef](#)]
438. Srinivasan, R.; Ramesh, A.; Athithanambi, A. Effect of Axial Force on Microstructure and Mechanical Properties of Friction Stir Welded Squeeze Cast A413 Aluminium Alloy. *Mater. Today Proc.* **2018**, *5*, 13486–13494. [[CrossRef](#)]
439. Venu, B.; BhavyaSwathi, I.; Raju, L.S.; Santhanam, G. A Review on Friction Stir Welding of Various Metals and Its Variables. *Mater. Today Proc.* **2019**, *18*, 298–302. [[CrossRef](#)]
440. Elangovan, K.; Balasubramanian, V.; Valliappan, M. Influences of Tool Pin Profile and Axial Force on the Formation of Friction Stir Processing Zone in AA6061 Aluminium Alloy. *Int. J. Adv. Manuf. Technol.* **2008**, *38*, 285–295. [[CrossRef](#)]
441. Jayaraman, M.; Sivasubramanian, R.; Balasubramanian, V.; Babu, S. Influences of Process Parameters on Tensile Strength of Friction Stir Welded Cast A319 Aluminium Alloy Joints. *Met. Mater. Int.* **2009**, *15*, 313–320. [[CrossRef](#)]
442. Palanivel, R.; Mathews, P.K.; Balakrishnan, M.; Dinaharan, I.; Murugan, N. Effect of Tool Pin Profile and Axial Force on Tensile Behavior in Friction Stir Welding of Dissimilar Aluminum Alloys. *Adv. Mater. Res.* **2011**, *415–417*, 1140–1146. [[CrossRef](#)]
443. Meyghani, B.; Awang, M. The Influence of the Tool Tilt Angle on the Heat Generation and the Material Behavior in Friction Stir Welding (FSW). *Metals* **2022**, *12*, 1837. [[CrossRef](#)]

444. Dialami, N.; Cervera, M.; Chiumenti, M. Effect of the Tool Tilt Angle on the Heat Generation and the Material Flow in Friction Stir Welding. *Metals* **2018**, *9*, 28. [[CrossRef](#)]
445. Di Bella, G.; Alderucci, T.; Favalaro, F.; Borsellino, C. Effect of Tool Tilt Angle on Mechanical Resistance of AA6082/AA5083 Friction Stir Welded Joints for Marine Applications. In Proceedings of the 16th CIRP Conference on Intelligent Computation in Manufacturing Engineering, CIRP ICME '22, Naples, Italy, 13–15 July 2022.
446. Yuvaraj, K.P.; Ashoka Varthanan, P.; Haribabu, L.; Madhubalan, R.; Boopathiraja, K.P. Optimization of FSW Tool Parameters for Joining Dissimilar AA7075-T651 and AA6061 Aluminium Alloys Using Taguchi Technique. *Mater. Today Proc.* **2021**, *45*, 919–925. [[CrossRef](#)]
447. Kunnathur Periyasamy, Y.; Perumal, A.V.; Kunnathur Periyasamy, B. Influence of Tool Shoulder Concave Angle and Pin Profile on Mechanical Properties and Microstructural Behaviour of Friction Stir Welded AA7075-T651 and AA6061 Dissimilar Joint. *Trans. Indian Inst. Met.* **2019**, *72*, 1087–1109. [[CrossRef](#)]
448. Fuller, C.B. Friction Stir Tooling: Tool Materials and Designs. In *Friction Stir Welding and Processing*; Mishra, R.S., Mahoney, M.W., Eds.; Springer: Cham, Switzerland, 2007.
449. Sunnapu, C.; Kolli, M. Tool Shoulder and Pin Geometry's Effect on Friction Stir Welding: A Study of Literature. *Mater. Today Proc.* **2021**, *39*, 1565–1569. [[CrossRef](#)]
450. Maji, P.; Karmakar, R.; Kanti Nath, R.; Paul, P. An Overview on Friction Stir Welding/Processing Tools. *Mater. Today Proc.* **2022**, *58*, 57–64. [[CrossRef](#)]
451. Muthu Vaidyanathan, R.; Sivaraman, N.; Patel, M.; Woldegiorgis, M.M.; Atiso, T.A. A Review on the Effects of Shoulder Diameter to Pin Diameter (D/d) Ratio on Friction Stir Welded Aluminium Alloys. *Mater. Today Proc.* **2021**, *45*, 4792–4798. [[CrossRef](#)]
452. Chandana, R.; Saraswathamma, K. Impact of Tool Pin Profiles in Friction Stir Welding Process-A Review. *Mater. Today Proc.* **2023**, *76*, 602–606. [[CrossRef](#)]
453. Azmal Hussain, M.; Zaman Khan, N.; Noor Siddiquee, A.; Akhtar Khan, Z. Effect of Different Tool Pin Profiles On The Joint Quality Of Friction Stir Welded AA 6063. *Mater. Today Proc.* **2018**, *5*, 4175–4182.
454. Arora, A.; De, A.; DebRoy, T. Toward Optimum Friction Stir Welding Tool Shoulder Diameter. *Scr. Mater.* **2011**, *64*, 9–12. [[CrossRef](#)]
455. Ramanjaneyulu, K.; Madhusudhan Reddy, G.; Venugopal Rao, A.; Markandeya, R. Structure-Property Correlation of AA2014 Friction Stir Welds: Role of Tool Pin Profile. *J. Mater. Eng. Perform.* **2013**, *22*, 2224–2240. [[CrossRef](#)]
456. Thomas, W.M.; Johnson, K.I.; Wiesner, C.S. Friction Stir Welding—Recent Developments in Tool and Process Technologies. *Adv. Eng. Mater.* **2003**, *5*, 485–490. [[CrossRef](#)]
457. Vijayavel, P.; Balasubramanian, V.; Sundaram, S. Effect of Shoulder Diameter to Pin Diameter (D/d) Ratio on Tensile Strength and Ductility of Friction Stir Processed LM25AA-5% SiCp Metal Matrix Composites. *Mater. Des.* **2014**, *57*, 1–9. [[CrossRef](#)]
458. Sahlot, P.; Jha, K.; Dey, G.K.; Arora, A. Wear-Induced Changes in FSW Tool Pin Profile: Effect of Process Parameters. *Metall. Mater. Trans. A* **2018**, *49*, 2139–2150. [[CrossRef](#)]
459. Goel, P.; Siddiquee, A.N.; Khan, N.Z.; Hussain, M.A.; Khan, Z.A.; Abidi, M.H.; Al-Ahmari, A. Investigation on the Effect of Tool Pin Profiles on Mechanical and Microstructural Properties of Friction Stir Butt and Scarf Welded Aluminium Alloy 6063. *Metals* **2018**, *8*, 74. [[CrossRef](#)]
460. Patel, V.V.; Badheka, V.; Kumar, A. Friction Stir Processing as a Novel Technique to Achieve Superplasticity in Aluminum Alloys: Process Variables, Variants, and Applications. *Metallogr. Microstruct. Anal.* **2016**, *5*, 278–293. [[CrossRef](#)]
461. Patel, V.V.; Badheka, V.; Kumar, A. Effect of polygonal pin profiles on friction stir processed superplasticity of AA7075 alloy. *J. Mater. Process. Technol.* **2017**, *240*, 68–76. [[CrossRef](#)]
462. Patel, V.V.; Badheka, V.J.; Kumar, A. Influence of Pin Profile on the Tool Plunge Stage in Friction Stir Processing of Al–Zn–Mg–Cu Alloy. *Trans. Indian Inst. Met.* **2016**, *70*, 1151–1158. [[CrossRef](#)]
463. Meilinger, Á.; Török, I. The Importance of Friction Stir Welding Tool. *Prod. Process. Syst.* **2013**, *6*, 25–34.
464. Joshi, S.K.; Gandhi, J.D. Influence of Tool Shoulder Geometry on Friction Stir Welding: A Literature Review. In Proceedings of the 2nd International Conference on Multidisciplinary Research & Practice, Gujarat, India, 24 December 2015; pp. 261–264.
465. Verma, S.; Kumar, V. Optimization of Friction Stir Welding Parameters of Dissimilar Aluminium Alloys 6061 and 5083 by Using Response Surface Methodology. *Proc. Inst. Mech. Eng. C J. Mech. Eng. Sci.* **2021**, *235*, 7009–7020. [[CrossRef](#)]
466. Azmi, M.H.; Hasnol, M.Z.; Zaharuddin, M.F.A.; Sharif, S.; Rhee, S. Effect of Tool Pin Profile on Friction Stir Welding of Dissimilar Materials AA5083 and AA7075 Aluminium Alloy. *Arch. Metall. Mater.* **2022**, *67*, 465–470. [[CrossRef](#)]
467. Balamurugan, S.; Jayakumar, K.; Anbarasan, B.; Rajesh, M. Effect of Tool Pin Shapes on Microstructure and Mechanical Behaviour of Friction Stir Welding of Dissimilar Aluminium Alloys. *Mater. Today Proc.* **2023**, *72*, 2181–2185. [[CrossRef](#)]
468. Sambasivam, S.; Gupta, N.; Saeed jassim, A.; Singh, D.P.; Kumar, S.; Mohan Giri, J.; Gupta, M. A Review Paper of FSW on Dissimilar Materials Using Aluminum. *Mater. Today Proc.* **2023**. [[CrossRef](#)]
469. Kumar, K.K.; Kumar Aand Sundar, S. Investigation of Microstructure Characteristics and Work Hardening Behaviour of WaterCooled FSW Dissimilar Aluminium Alloys. *Mater. Today Commun.* **2023**, *35*, 105857. [[CrossRef](#)]
470. Kryukov, I.; Schüddekopf, S.; Böhm, S.; Mund, M.; Kreling, S.; Dilger, K. Non-Destructive Online-Testing Method for Friction Stir Welding Using Infrared Thermography. In Proceedings of the 19th World Conference on Non-Destructive Testing, Munich, Germany, 13–17 June 2016.

471. Shine, K.; Jayakumar, K. Effect of Tool Pin Profile on the Mechanical and Microstructural Properties of Dissimilar Friction Stir Welded AA5083-H111 and AA6061-T6 Aluminium Alloys. *J. Chin. Inst. Eng.* **2022**, *45*, 227–236.
472. Stephen Leon, J.; Essadiqi, E.; Lakshmanan, T.; Ravi, R.; Selvaraj, M. Numerical Modeling of Thermal Field during Friction Stir Welding Using Tool with Polygonal Pin Profile. *J. Phys. Conf. Ser.* **2021**, *2054*, 012006. [\[CrossRef\]](#)
473. Tiwan, Ilman, M.N.; Kusmono; Sehon. Microstructure and Mechanical Performance of Dissimilar Friction Stir Spot Welded AA2024-O/AA6061-T6 Sheets: Effects of Tool Rotation Speed and Pin Geometry. *Int. J. Lightweight Mater. Manuf.* **2023**, *6*, 1–14. [\[CrossRef\]](#)
474. Mehta, K.P.; Badheka, V.J. Effects of Tool Pin Design on Formation of Defects in Dissimilar Friction Stir Welding. *Procedia Technol.* **2016**, *23*, 513–518. [\[CrossRef\]](#)
475. Palani, K.; Elanchezian, C.; Vijaya Ramnath, B.; Bhaskar, G.B.; Naveen, E. Effect of Pin Profile and Rotational Speed on Microstructure and Tensile Strength of Dissimilar AA8011, AA01-T6 Friction Stir Welded Aluminum Alloys. *Mater. Today Proc.* **2018**, *5*, 24515–24524. [\[CrossRef\]](#)
476. Raturi, M.; Garg, A.; Bhattacharya, A. Joint Strength and Failure Studies of Dissimilar AA6061-AA7075 Friction Stir Welds: Effects of Tool Pin, Process Parameters and Preheating. *Eng. Fail. Anal.* **2019**, *96*, 570–588. [\[CrossRef\]](#)
477. Raturi, M.; Bhattacharya, A. Appraising Tool Wear during Secondary Heating Assisted Dissimilar Friction Stir Welding between 6061 and 7075 Aluminium Alloys. *Mater. Trans.* **2023**, *64*, 485–491. [\[CrossRef\]](#)
478. Mehta, M.; Reddy, G.M.; Rao, A.V.; De, A. Numerical Modeling of Friction Stir Welding Using the Tools with Polygonal Pins. *Def. Technol.* **2015**, *11*, 229–236. [\[CrossRef\]](#)
479. Krishna, M.; Udaiyakumar, K.C.; Mohan Kumar, D.K.; Mohammed Ali, H. Analysis on Effect of Using Different Tool Pin Profile and Mechanical Properties by Friction Stir Welding on Dissimilar Aluminium Alloys Al6061 and Al7075. *IOP Conf. Ser. Mater. Sci. Eng.* **2018**, *402*, 012099. [\[CrossRef\]](#)
480. El-Hafez, H.A.; El-Megharbel, A. Friction Stir Welding of Dissimilar Aluminum Alloys. *World J. Eng. Technol.* **2018**, *6*, 408–419. [\[CrossRef\]](#)
481. Abd El-Hafez, H. Mechanical Properties and Welding Power of Friction Stirred AA2024-T35 Joints. *J. Mater. Eng. Perform.* **2011**, *20*, 839–845. [\[CrossRef\]](#)
482. Kumar, N.; Monga, I.; Kumar, M. An Experimental Investigation to Find out the Effect of Different Pin Profile Tools on AA 6061 T6 and AA 2014 T4 with Friction Stir Welding. *Int. J. Technol. Res. Eng.* **2015**, *2*, 1622–1625.
483. Battina, N.M.; Vanthala, V.S.P.; Chirala, H.K. Influence of Tool Pin Profile on Mechanical and Metallurgical Behavior of Friction Stir Welded AA6061-T6 and AA2017-T6 Tailored Blanks. *Eng. Res. Express* **2021**, *3*, 035026. [\[CrossRef\]](#)
484. Jayaprakash, S.; Siva Chandran, S.; Sathish, T.; Gugulothu, B.; Ramesh, R.; Sudhakar, M.; Subbiah, R. Effect of Tool Profile Influence in Dissimilar Friction Stir Welding of Aluminium Alloys (AA5083 and AA7068). *Adv. Mater. Sci. Eng.* **2021**, *2021*, 7387296. [\[CrossRef\]](#)
485. Sun, Y.; Liu, W.; Li, Y.; Gong, W.; Ju, C. The Influence of Tool Shape on Plastic Metal Flow, Microstructure and Properties of Friction Stir Welded 2024 Aluminum Alloy Joints. *Metals* **2022**, *12*, 408. [\[CrossRef\]](#)
486. Khan, N.Z.; Siddiquee, A.N.; Khan, Z.A.; Shihab, S.K. Investigations on tunneling and kissing bond defects in FSW joints for dissimilar aluminum alloys. *J. Alloys Compd.* **2015**, *648*, 360–367. [\[CrossRef\]](#)
487. Patel, V.V.; Li, W.; Vairis, A.; Badheka, V. Recent Development in Friction Stir Processing as a Solid-State Grain Refinement Technique: Microstructural Evolution and Property Enhancement. *Crit. Rev. Solid State Mater. Sci.* **2019**, *44*, 378–426. [\[CrossRef\]](#)
488. Nakamura, T.; Obikawa, T.; Nishizaki, I.; Enomoto, M.; Fang, Z. Friction Stir Welding of Non-Heat-Treatable High-Strength Alloy 5083-O. *Metals* **2018**, *8*, 208. [\[CrossRef\]](#)
489. Patel, V.V.; Badheka, V.; Kumar, A. Influence of Friction Stir Processed Parameters on Superplasticity of Al-Zn-Mg-Cu Alloy. *Mater. Manuf. Process.* **2015**, *31*, 1–10. [\[CrossRef\]](#)
490. Fadaeifard, F.; Matori, K.A.; Abd Aziz, S.; Zolkarnain, L.; Abdul Rahim, M.A.Z.B. Effect of the Welding Speed on the Macrostructure, Microstructure and Mechanical Properties of AA6061-T6 Friction Stir Butt Welds. *Metals* **2017**, *7*, 48. [\[CrossRef\]](#)
491. Niu, P.; Li, W.Y.; Vairis, A.; Chen, D.L. Cyclic deformation behavior of friction-stir-welded dissimilar AA5083-to-AA2024 joints: Effect of microstructure and loading history. *Mater. Sci. Eng. A* **2019**, *744*, 145–153. [\[CrossRef\]](#)
492. Ji, S.D.; Xing, J.; Yue, Y.; Ma, Y.; Zhang, L.; Gao, S. Design of friction stir welding tool for avoiding root flaws. *Materials* **2013**, *6*, 5870–5877. [\[CrossRef\]](#)
493. Wan, L.; Guo, W.; Lv, S.; Feng, J. Mechanical properties and microstructure of 6082-T6 aluminum alloy joints by self-support friction stir welding. *J. Mater. Sci. Technol.* **2014**, *30*, 1243–1250. [\[CrossRef\]](#)
494. Liu, L.; Yang, K.; Yan, D. Refill Friction Stir Spot Welding of Dissimilar 6061/7075 Aluminum Alloy. *High Temp. Mater. Process.* **2019**, *39*, 69–75.
495. Tra, H.M.; Okazaki, M.; Suzuki, K. Fatigue crack propagation behavior in friction stir welding of AA6063-T5: Roles of residual stress and microstructure. *Int. J. Fatigue* **2012**, *43*, 23–29. [\[CrossRef\]](#)
496. Kafali, H.; AY, N. Mechanical Properties of 6013-T6 Aluminium Alloy Friction Stir Welded Plate. In Proceedings of the 13th International Conference on Aerospace Sciences & Aviation Technology, ASAT-13, Cairo, Egypt, 26–28 May 2009; p. ASAT-13-MS-14.
497. Saleh, A.A. Joining of AA2014 and AA5059 dissimilar aluminium alloys by Friction Stir Welding. *J. Achiev. Mater. Manuf. Eng.* **2019**, *91*, 15–20. [\[CrossRef\]](#)

498. Venkateswarlu, D.; Cheepu, M.; Mahapatra, M.M. Analysing the Friction Stir Welded Joints of AA2219 Al-Cu Alloy in Different Heat-Treated-State. In Proceedings of the International Conference on Recent Advances in Materials, Mechanical and Civil Engineering, Hyderabad, India, 1–2 June 2017; Volume 330, p. 012074.
499. Kollapuri, T.; Manoharan, M.; Sadayan, R.B.; Sajja, R.K.R. A Study on the Corrosion Behaviour of Aluminium Alloy 2024 T-3 Friction Stir Welds Using Stress Corrosion Cracking. In Proceedings of the ASME 2015 International Mechanical Engineering Congress and Exposition, Houston, Texas, USA, 13–19 November 2015; Emerging Technologies; Safety Engineering and Risk Analysis; Materials: Genetics to Structures. Volume 14, p. V014T11A004.
500. Tan, Y.B.; Wang, X.M.; Ma, M.; Zhang, J.X.; Liu, W.C.; Fu, R.; Xiang, S. A study on microstructure and mechanical properties of AA 3003 aluminum alloy joints by underwater friction stir welding. *Mater. Charact.* **2017**, *127*, 41–52. [[CrossRef](#)]
501. Deng, Y.L.; Deng, S.H.; Ye, L.Y.; Lin, S.; Sun, L.; Ji, H. Effects of post-weld heat treatment on microstructures and mechanical properties of AA7204-T4 aluminum alloy FSW joint. *J. Mater. Eng.* **2020**, *48*, 131–138.
502. Unfried-Silgado, J.; Rodriguez, J.; Torres, A.; Carrasco, J. Effects of shoulder geometry of tool on microstructure and mechanical properties of friction stir welded joints of AA1100 aluminum alloy. *DYNA* **2017**, *84*, 202–208. [[CrossRef](#)]
503. Guo, J.F.; Chen, H.C.; Sun, C.N.; Bi, G.; Sun, Z.; Wei, J. Friction stir welding of dissimilar materials between AA6061 and AA7075 Al alloys effects of process parameters. *Mater. Des.* **2014**, *56*, 185–192. [[CrossRef](#)]
504. Sato, Y.S.; Kurihara, Y.; Kokawa, H. Microstructural characteristics of dissimilar butt friction stir welds of AA7075 and AA2024. In Proceedings of the 6th Int. FSW Symp., Saint-Sauveur, Quebec, QC, Canada, 10–13 October 2006. TWI, CD-ROM.
505. da Silva, A.A.M.; Arruti, E.; Janeiro, G.; Aldanondo, E.; Alvarez, P.; Echeverria, A. Material flow and mechanical behaviour of dissimilar AA2024-T3 and AA7075-T6 aluminium alloys friction stir welds. *J. Mater. Des.* **2011**, *32*, 2021–2027. [[CrossRef](#)]
506. Khan, N.Z.; Siddiquee, A.N.; Zahid, A.; Khan, Z.A.; Mukhopadhyay, A.K. Mechanical and microstructural behavior of friction stir welded similar and dissimilar sheets of AA2219 and AA7475 aluminium alloys. *J. Alloys Compd.* **2017**, *695*, 2902–2908. [[CrossRef](#)]
507. Abidi, M.H.; Ali, N.; Ibrahim, H.; Anjum, S.; Bajaj, D.; Siddiquee, A.N.; Alkahtani, M.; Rehman, A.U. T-FSW of Dissimilar Aerospace Grade Aluminium Alloys: Influence of Second Pass on Weld Defects. *Metals* **2020**, *10*, 525. [[CrossRef](#)]
508. Albannai, A.I. Review The Common Defects In Friction Stir Welding. *Int. J. Sci. Technol. Res.* **2020**, *9*, 318–329.
509. Yan, J.; Xu, Z.; Li, Z.; Li, L.; Yang, S. Microstructure characteristics and performance of dissimilar welds between magnesium alloy and aluminum formed by friction stirring. *Scr. Mater.* **2005**, *53*, 585–589. [[CrossRef](#)]
510. Esmaeili, A.; Rajani, H.Z.; Sharbati, M.; Givi, M.B.; Shamanian, M. The role of rotation speed on intermetallic compounds formation and mechanical behavior of friction stir welded brass/aluminum 1050 couple. *Intermetallics* **2011**, *19*, 1711–1719. [[CrossRef](#)]
511. Mehta, K.P.; Badheka, V.J. A review on dissimilar friction stir welding of copper to aluminum: Process, properties, and variants. *Mater. Manuf. Process.* **2016**, *31*, 233–254. [[CrossRef](#)]
512. Singh, V.P.; Patel, S.K.; Ranjan, A.; Kuriachen, B. Recent research progress in solid state friction-stir welding of aluminium–magnesium alloys: A critical review. *J. Mater. Res. Technol.* **2020**, *9*, 6217–6256. [[CrossRef](#)]
513. Zhou, N.; Song, D.; Qi, W.; Li, X.; Zou, J.; Attallah, M.M. Influence of the kissing bond on the mechanical properties and fracture behaviour of AA5083- H112 friction stir welds. *Mater. Sci. Eng. A* **2018**, *719*, 12–20. [[CrossRef](#)]
514. Xue, P.; Xiao, B.; Ni, D.; Ma, Z. Enhanced mechanical properties of friction stir welded dissimilar Al–Cu joint by intermetallic compounds. *Mater. Sci. Eng. A* **2010**, *527*, 5723–5727. [[CrossRef](#)]
515. Chitturi, V.; Pedapati, S.; Awang, M. Challenges in dissimilar friction stir welding of aluminum 5052 and 304 stainless steel alloys. *Mater. Werkst.* **2020**, *51*, 811–816. [[CrossRef](#)]
516. Mahto, R.P.; Kumar, R.; Pal, S.K. Characterizations of weld defects, intermetallic compounds and mechanical properties of friction stir lap welded dissimilar alloys. *Mater. Charact.* **2020**, *160*, 110115. [[CrossRef](#)]
517. Galvão, I.; Loureiro, A.; Verdera, D.; Gesto, D.; Rodrigues, D.M. Influence of tool offsetting on the structure and morphology of dissimilar aluminum to copper friction-stir welds. *Metall. Mater. Trans. A* **2012**, *43*, 5096–5105. [[CrossRef](#)]
518. Xue, P.; Ni, D.; Wang, D.; Xiao, B.; Ma, Z. Effect of friction stir welding parameters on the microstructure and mechanical properties of the dissimilar Al–Cu joints. *Mater. Sci. Eng. A* **2011**, *528*, 4683–4689. [[CrossRef](#)]
519. Liu, H.; Zhao, Y.; Su, X.; Yu, L.; Hou, J. Microstructural characteristics and mechanical properties of friction stir spot welded 2A12-T4 aluminum alloy. *Adv. Mater. Sci. Eng.* **2013**, *2013*, 719306. [[CrossRef](#)]
520. Taheri, H.; Kilpatrick, M.; Norvalls, M.; Harper, W.J.; Koester, L.W.; Bigelow, T.; Bond, L.J. Investigation of nondestructive testing methods for friction stir welding. *Metals* **2019**, *9*, 624. [[CrossRef](#)]
521. Morikawa, K.; Kawai, G.; Ochi, H.; Yamamoto, Y.; Suga, Y. Strength of 2017 aluminium alloy stud joints by friction welding. *Weld. Int.* **2013**, *27*, 18–23. [[CrossRef](#)]
522. Dixit, S. Hardness Testing of Friction Stir Welded AA 1200 Aluminium Alloy. *IJMSE* **2017**, *8*, 17–21.
523. Attah, B.I.; Lawal, S.A.; Akinlabi, E.T.; Bala, K.C. Evaluation of mechanical properties of dissimilar aluminium alloys during friction stir welding using tapered tool. *Cogent Eng.* **2021**, *8*, 1909520. [[CrossRef](#)]
524. Jassim, A.K.; Al-Subar, R.K. Studying the Possibility to Weld AA1100 Aluminum Alloy by Friction Stir Spot Welding. *World Acad. Sci. Eng. Technol. Int. J. Mater. Metall. Eng.* **2017**, *11*, 10008041.
525. Senapati, N.P.; Bhoi, R.K. Improving the Strength of Friction-Stir-Welded Joints of AA1100 Alloy. *J. Mater. Eng. Perform.* **2021**, *30*, 510–521. [[CrossRef](#)]

526. Joseph, M.G.; Shaji, J.; Francis, M.J.; Raghavan, A.; Shunmugesh, K. Measurement of Tensile Properties and Hardness of Friction Stir Welded Aluminium Alloy AA1200. *Mater. Today Proc.* **2020**, *24*, 1987–1993. [[CrossRef](#)]
527. Sato, Y.S.; Kurihara, Y.; Park, S.H.C.; Kokawa, H.; Tsuji, N. Friction stir welding of ultrafine grained Al alloy 1100 produced by accumulative roll-bonding. *Scr. Mater.* **2004**, *50*, 57–60. [[CrossRef](#)]
528. Jannet, S.; Mathews, K.; Raja, R. Comparative investigation of friction stir welding and fusion welding of 6061 T6-5083 O aluminum alloy based on mechanical properties and microstructure. *Bull. Pol. Acad. Sci. Tech. Sci.* **2014**, *62*, 791–795. [[CrossRef](#)]
529. Dolatkah, A.; Golbabaei, P.; Besharati Givi, M.K.; Molaiekiya, F. Investigating effects of process parameters on microstructural and mechanical properties of Al5052/SiC metal matrix composite fabricated via friction stir processing. *Mater. Des.* **2012**, *37*, 458–464. [[CrossRef](#)]
530. Bahrami, M.; Dehghani, K.; Givi, M.K.B. A novel approach to develop aluminum matrix nano-composite employing friction stir welding technique. *Mater. Des.* **2014**, *53*, 217–225. [[CrossRef](#)]
531. Pantelis, D.I.; Karakizis, P.N.; Daniolos, N.M.; Charitidis, C.A.; Koumoulos, E.P.; Dragatogiannis, D.A. Microstructural study and mechanical properties of dissimilar friction stir welded AA5083-H111 and AA6082-T6 reinforced with SiC nanoparticles. *Mater. Manuf. Process.* **2016**, *31*, 264–274. [[CrossRef](#)]
532. Dragatogiannis, D.A.; Koumoulos, E.P.; Kartsonakis, I.A.; Pantelis, D.I.; Karakizis, P.N.; Charitidis, C.A. Dissimilar Friction Stir Welding Between 5083 and 6082 Al Alloys Reinforced With TiC Nanoparticles. *Mater. Manuf. Process.* **2016**, *31*, 2101–2114. [[CrossRef](#)]
533. Scudino, S.; Liu, G.; Prashanth, K.G.; Bartusch, B.; Surreddi, K.B.; Murty, B.S.; Eckert, J. Mechanical properties of Al-based metal matrix composites reinforced with Zr-based glassy particles produced by powder metallurgy. *Acta Mater.* **2009**, *57*, 2029–2039. [[CrossRef](#)]
534. Moradi, M.M.; Jamshidi, A.H.; Jamaati, R. Effect of tool pin geometry and weld pass number on microstructural, natural aging and mechanical behaviour of SiC-incorporated dissimilar friction-stir-welded aluminium alloys. *Sadhana-Acad. Proc. Eng. Sci.* **2019**, *44*, 1–9. [[CrossRef](#)]
535. Prabhu, S.; Sri, M.N.S.; Anusha, P.; Saravanan, G.; Kannan, K.; Manickam, S. Improvement of Mechanical Behavior of FSW Dissimilar Aluminum Alloys by Postweld Heat Treatments. In *Advances in Materials Science and Engineering (Hindawi)*; Adam House: London, UK, 2022; p. 3608984.
536. Yang, X.; Meng, T.; Su, Y.; Qi, Z.; Wu, D.; Vairis, A.; Li, W. Study on relieving residual stress of friction stir welded joint of 2219 aluminum alloy using cold spraying. *Mater. Charact.* **2023**, *206*, 113417. [[CrossRef](#)]
537. van der Stelt, A.A.; Bor, T.C.; Geijselaers, H.J.M.; Akkerman, R.; van den Boogaard, A.H. Cladding of Advanced Al Alloys Employing Friction Stir Welding. *Key Eng. Mater.* **2013**, *554–557*, 1014–1021. [[CrossRef](#)]
538. Lacki, P.; Wieckowski, W.; Luty, G.; Wieczorek, P.; Motyka, M. Evaluation of usefulness of AlCrN coatings for increased life of tools used in friction stir welding (FSW) of sheet aluminum alloy. *Materials* **2020**, *13*, 4124. [[CrossRef](#)]
539. Prasad Rao, K.; Janaki Ram, G.D.; Stucker, B.E. Improvement in corrosion resistance of friction stir welded aluminum alloys with micro arc oxidation coatings. *Scr. Mater.* **2008**, *58*, 998–1001. [[CrossRef](#)]
540. Chen, J.; Wang, Y.; Gao, W.; Wang, D.; Chen, S.; Luan, J. A newly designed NiP duplex coating on friction stir welding joint of 6061-T6 aluminum. *Surf. Coat. Technol.* **2022**, *448*, 128940. [[CrossRef](#)]
541. Ehiasarian, A.; Purandare, Y.; Sugumaran, A.; Hovsepian, P.; Hatto, P.; De Backer, J. Improving the Quality of Friction Stir Welds in Aluminium Alloys. *Coatings* **2021**, *11*, 539. [[CrossRef](#)]
542. Kulekci, M.K.; Esme, U.; Er, O.; Kazançoğlu, Y. Modeling and prediction of weld shear strength in friction stir spot welding using design of experiments and neural network. *Mater. Werkst.* **2011**, *42*, 990–995. [[CrossRef](#)]
543. Scotchmer, N.; Chan, K. What's New for Welding Aluminum in the Auto Industry. *Weld. J.* **2012**, *91*, 34–37.
544. Kulekci, M.K. Effects of Process Parameters on Tensile Shear Strength of Friction Stir Spot Welded Aluminium Alloy (EN AW 5005). *Arch. Metal. Mater.* **2014**, *59*, 221–224. [[CrossRef](#)]
545. Hinrichs, J.F.; Smith, C.B.; Orsini, B.F.; DeGeorge, R.J.; Smale, B.J.; Ruehl, P.C. Friction stir welding for the 21st century automotive industry. In Proceedings of the 5th International Symposium on Friction Stir Welding, Metz, France, 14–16 September 2004; The Welding Institute: Metz, France, 2004.
546. Praveen, P.; Yarlagadda, P.K.D.V. Meeting challenges in welding of aluminum alloys through pulse gas metal arc welding. *J. Mater. Process. Technol.* **2005**, *164–165*, 1106–1112. [[CrossRef](#)]
547. Lewise, K.A.S.; Dhas, J.E.R.; Pandiyarajan, R. Optimising aluminium 2024/7075 friction stir welded joints. *Adv. Mater. Process. Technol.* **2022**, *8*, 4579–4597.
548. Borah, M.J.; Rajbongshi, S.K.; Saha, N.; Buddhi, D. Friction stir spot welding process: An innovative approach for transforming from engineering design to production. *Int. J. Interact. Des. Manuf.* **2023**, *17*, 2259–2270. [[CrossRef](#)]
549. Suresh, S.; Elango, N.; Venkatesan, K.; Lim, W.H.; Palanikumar, K.; Rajesh, S. Sustainable friction stir spot welding of 6061-T6 aluminium alloy using improved non-dominated sorting teaching learning algorithm. *J. Mater. Res. Technol.* **2020**, *9*, 11650–11674. [[CrossRef](#)]
550. Zhu, Z.; Li, Y.; Zhang, M.; Hui, C. Effects of stress concentration on the fatigue strength of 7003-T5 aluminum alloy butt joints with weld reinforcement. *Int. J. Mod. Phys. B* **2015**, *29*, 1540023. [[CrossRef](#)]
551. Sangduang, W.; Wattanatham, P.; Eiidhed, K. The Study on welding Effect and Porosity Distribution of 5154 Aluminum Alloys by Gas Metal Arc Welding (GMAW). *Thai Ind. Eng. Netw. J.* **2020**, *6*, 59–67.

552. Ramaswamy, A.; Malarvizhi, S.; Balasubramanian, V. Effect of variants of gas metal arc welding process on tensile properties of AA6061-T6 aluminium alloy joints. *Int. J. Adv. Manuf. Technol.* **2020**, *108*, 2967–2983. [[CrossRef](#)]
553. Mercan, E.; Ayan, Y.; Kahraman, N. Microstructure and Mechanical Properties of Aluminum Alloys AA5754 and AA6013 Joined by GMAW (Gas Metal Arc Welding) Method. *Pamukkale Univ. J. Eng. Sci.* **2020**, *26*, 82–87.
554. Kaushal, C.; Sharma, L. To Determine Effects of Gas Metal Arc Welding (GMAW) Parameters on Mechanical Properties of Aluminium Alloys. *Int. J. Innov. Res. Sci. Eng. Technol.* **2015**, *4*, 4564–4572.
555. Çevik, B. Gas tungsten arc welding of 7075 aluminum alloy: Microstructure properties, impact strength, and weld defects. *Mater. Res. Express.* **2018**, *5*, 066540. [[CrossRef](#)]
556. Jin, L.; Yang, Y.; Yao, P.; Chen, W.; Qian, Z.; Xue, J. Investigation of the Difference in the Pulse Current in the Double Pulsed Gas Metal Arc Welding of Aluminum Alloys. *Materials* **2022**, *15*, 2513. [[CrossRef](#)] [[PubMed](#)]
557. Huang, L.; Hua, X.; Wu, D.; Jiang, Z.; Li, F.; Wang, H.; Shi, S. Microstructural characterization of 5083 aluminum alloy thick plates welded with GMAW and twin wire GMAW processes. *Int. J. Adv. Manuf. Technol.* **2017**, *93*, 1809–1817. [[CrossRef](#)]
558. Kim, C.; Ahn, Y.; Lee, K.-B.; Kim, D. High-deposition-rate position welding of Al 5083 alloy for spherical-type liquefied natural gas tank. *Proc. Inst. Mech. Eng. Part B J. Eng. Manuf.* **2015**, *230*, 818–824. [[CrossRef](#)]
559. Rubino, F.; Tucci, F.; Caruso, S.; Umbrello, D.; Carlone, P. An integrated numerical approach to simulate the filler deposition and the shape distortions in gas metal arc welding. *CIRP J. Manuf. Sci. Technol.* **2023**, *45*, 26–34. [[CrossRef](#)]
560. Arghode, V.; Kumar, A.; Sundarraj, S.; Dutta, P. Computational Modeling of GMAW Process for Joining Dissimilar Aluminum Alloys. *Numer Heat Transf. PT A-APPL* **2008**, *53*, 432–455. [[CrossRef](#)]
561. Guo, H.; Hu, J.; Tsai, H.L. Formation of weld crater in GMAW of aluminum alloys. *Int. J. Heat Mass Transf.* **2009**, *52*, 5533–5546. [[CrossRef](#)]
562. Du, W.; Sun, G.; Li, Y.; Chen, C. Process Optimization, Microstructure and Mechanical Properties of Wire Arc Additive Manufacturing of Aluminum Alloy by Using DP-GMAW Based on Response Surface Method. *Materials* **2023**, *16*, 5716. [[CrossRef](#)]
563. Hernández, M.; Ambriz, R.R.; García, C.; Jaramillo, D. The Thermomechanical Finite Element Analysis of 3003-H14 Plates Joined by the GMAW Process. *Metals* **2020**, *10*, 708. [[CrossRef](#)]
564. Yu, H.; Tong, Y. Magnetic pulse welding of aluminum to steel using uniform pressure electromagnetic actuator. *Int. J. Adv. Manuf. Technol.* **2017**, *91*, 2257–2265. [[CrossRef](#)]
565. Drehmann, R.; Scheffler, C.; Winter, S.; Psyk, V.; Kräusel, V.; Lampke, T. Experimental and Numerical Investigations into Magnetic Pulse Welding of Aluminum Alloy 6016 to Hardened Steel 22MnB5. *J. Manuf. Mater. Process.* **2021**, *5*, 66. [[CrossRef](#)]
566. Khalil, C.; Marya, S.; Racineux, G. Magnetic Pulse Welding and Spot Welding with Improved Coil Efficiency—Application for Dissimilar Welding of Automotive Metal Alloys. *J. Manuf. Mater. Process.* **2020**, *4*, 69. [[CrossRef](#)]
567. Yan, Z.; Xiao, A.; Cui, X.; Guo, Y.; Lin, Y.; Zhang, L.; Zhao, P. Magnetic pulse welding of aluminum to steel tubes using a field-shaper with multiple seams. *J. Manuf. Process.* **2021**, *65*, 214–227. [[CrossRef](#)]
568. Chen, S.; Han, Y.; Gong, W.; Yuan, Y.; Jiang, X. Mechanical properties and joining mechanism of magnetic pulse welding of aluminum and titanium. *Int. J. Adv. Manuf. Technol.* **2022**, *120*, 7115–7126. [[CrossRef](#)]
569. Aizawa, T.; Kashani, M. Magnetic Pulse Welding (MPW) Method for Dissimilar Sheet Metal Joints. In Proceedings of the 57th Ann. Assembly of the Int. Institute of Welding (IIW), Osaka, Japan, 11–16 July 2004.
570. Zhang, Y.; Babu, S.S.; Zhang, P.; Kenik, E.A.; Daehn, G.S. Microstructure characterisation of magnetic pulse welded AA6061-T6 by electron backscattered diffraction. *Sci. Technol. Weld. Join.* **2008**, *13*, 467–471. [[CrossRef](#)]
571. Pereira, D.; Oliveira, J.P.; Pardo, T.; Miranda, R.M.; Santos, T.G. Magnetic pulse welding: Machine optimisation for aluminium tubular joints production. *Sci. Technol. Weld. Join.* **2018**, *23*, 172–179. [[CrossRef](#)]
572. Okagawa, K.; Aizawa, T. Impact seam welding with magnetic pressure for aluminum sheets. *Mater. Sci. Forum* **2004**, *465*, 231–236. [[CrossRef](#)]
573. Raelison, R.N.; Sapanathan, T. Interfacial kinematics and governing mechanisms under the influence of high strain rate impact conditions: Numerical computations of experimental observations. *J. Mech. Phys. Solids* **2016**, *96*, 147–161. [[CrossRef](#)]
574. Liu, B.; Vivek, A.; Daehn, G.S. Use of Vaporizing Foil Actuator for Impact Welding of Aluminum Alloy Sheets with Steel and Magnesium Alloys. In *Light Metals 2015*; Springer: Cham, Switzerland, 2015.
575. Vivek, A. Vaporizing foil actuator: A tool for collision welding. *J. Mater. Process. Technol.* **2013**, *213*, 2304–2311. [[CrossRef](#)]
576. Hahn, M.; Weddeling, C.; Taber, G.; Vivek, A.; Daehn, G.S.; Tekkaya, E.A. Vaporizing foil actuator welding as a competing technology to magnetic pulse welding. *J. Mater. Process. Technol.* **2016**, *230*, 8–20. [[CrossRef](#)]
577. Kapil, A. Aspects of Vaporizing Foil Actuator Welding for Practical Automotive Applications. PhD Thesis, The Ohio State University, Columbus, OH, USA, 2020.
578. Kapil, A.; Lee, T.; Vivek, A.; Bockbrader, J.; Abke, T.; Daehn, G. Benchmarking strength and fatigue properties of spot impact welds. *J. Mater. Process. Technol.* **2018**, *255*, 219–233. [[CrossRef](#)]
579. Nassiri, A.; Kinsey, B. Numerical studies on high-velocity impact welding: Smoothed particle hydrodynamics (SPH) and arbitrary Lagrangian–Eulerian (ALE). *J. Manuf. Process.* **2016**, *24*, 376–381. [[CrossRef](#)]
580. Groche, P.; Becker, M. Process window acquisition for impact welding processes. *Mater. Des.* **2017**, *118*, 286–293. [[CrossRef](#)]
581. Hansen, S.R.; Vivek, A.; Daehn, G.S. Impact Welding of Aluminum Alloys 6061 and 5052 by Vaporizing Foil Actuators: Heat-Affected Zone Size and Peel Strength. *J. Manuf. Sci. Eng.* **2015**, *137*, 051013. [[CrossRef](#)]

582. Hansen, S.R.; Vivek, A.; Daehn, G.S. Control of Velocity, Driving Pressure, and Planarity During Flyer Launch with Vaporizing Foil Actuator. In Proceedings of the 6th International Conference on High Speed Forming, Daejeon, Korea, 27–29 March 2014; pp. 325–334.
583. Meng, Z.; Su, S.; Mao, Y.; Vivek, A.; Huang, S.Y.; Hua, L.; Chen, S.; Daehn, G.S. Welding of 2024-7075 Aluminum Alloys and 5A06 Aluminum to Stainless Steel 321 by Vaporizing Foil Actuator. In Proceedings of the International Conference, Columbus, OH, USA, 14–16 May 2018.
584. Lumley, R.N.; Morton, A.J.; O'Donnell, R.G.; Polmear, I.J. New heat treatments for age-hardenable aluminum alloys. *Heat Treat. Prog.* **2005**, *5*, 23–29.
585. Fujita, T.; Hasegawa, K.; Mitao, S.; Niikura, M.; Koike, T.; Funakawa, M.; Yoshihara, N.; Ohori, K. A new paint-bake-hardenable aluminum alloy for auto body sheet applications. *SAE Trans.* **1995**, *104*, 667–672.
586. Engler, O.; Myhr, O.R. Effect of Natural Ageing on Strength and Anisotropy in Aluminium Alloy AA 6005C. *Mater. Sci. Forum.* **2017**, *877*, 688–694. [[CrossRef](#)]
587. Li, D.; Slater, C.; Cai, H.; Hou, X.; Li, Y.; Wang, Q. Joining Technologies for Aluminium Castings—A Review. *Coatings* **2023**, *13*, 958. [[CrossRef](#)]
588. Li, H.; Liu, X.; Zhang, Y.; Ma, M.; Li, G.Y.; Senkara, J. Current Research and Challenges in Innovative Technology of Joining Dissimilar Materials for Electric Vehicles. In Proceedings of the 4th International Conference on Advanced High Strength Steel and Press Hardening (ICHSU2018), Hefei, China, 20–22 August 2018.
589. Matsukage, T.; Sakurai, S.; Traui, T.; Iyota, M. Mechanical Properties of Resistance-Spot-Welded Joints of Aluminum Castings and Wrought Alloys. *Eng. Proc.* **2023**, *43*, 52. [[CrossRef](#)]
590. Khodir, S.A.; Shibayanagi, T. Friction stir welding of dissimilar AA2024 and AA7075 aluminum alloys. *Mater. Sci. Eng. B* **2008**. [[CrossRef](#)]
591. Dragatogiannis, D.A.; Kollaros, D.; Karakizis, P.; Pantelis, D.; Lin, J.; Charitidis, C. Friction Stir Welding between 6082 and 7075 Aluminum Alloys Thermal Treated for Automotive Applications. *Mater. Perform. Charact.* **2019**, *8*, 571–589. [[CrossRef](#)]
592. Venkateswarlu, D.; Nageswararao, P.; Mahapatra, M.M.; Harsha, S.P.; Mandal, N.R.; Venkateswarlu, D.; Nageswararao, P.; Mahapatra, M.M.; Mandal, N.R. Processing and Optimization of Dissimilar Friction Stir Welding of AA 2219 and AA 7039 Alloys. *J. Mater. Eng. Perform.* **2015**, *24*, 4809–4824. [[CrossRef](#)]
593. Patel, M.M.; Badheka, V.J. A review on friction stir welding (FSW) process for dissimilar aluminium to steel metal systems. *Weld. Int.* **2024**, *38*, 91–115. [[CrossRef](#)]
594. Mehta, K.; Astarita, A.; Carlone, P.; Gatta, R.D.; Vyas, H.; Vilaça, P.; Tucci, F. Investigation of exit-hole repairing on dissimilar aluminum-copper friction stir welded joints. *J. Mater. Res. Technol.* **2021**, *13*, 2180–2193. [[CrossRef](#)]
595. Kvasnová, P.; Novák, D.; Novák, V. Laser Welding of Aluminium Alloys. *Manufac-Turing Technol.* **2017**, *17*, 892–898. [[CrossRef](#)]
596. Pouranvari, M.; Marashi, S.P.H. Critical review of automotive steels spot welding: Process, structure and properties. *Sci. Technol. Weld. Join.* **2013**, *18*, 361–403. [[CrossRef](#)]
597. Sobih, M.; Elseddig, Z. Chapter—Electron Beam Welding of Aluminum Alloys. In *En-Cyclopedia of Aluminum and Its Alloys*, 1st ed.; Totten, G.E., Tiryakioglu, M., Kessler, O., Eds.; Two-Volume Set (Print); CRC Press: Boca Raton, FL, USA, 2018.
598. Armao, F. Aluminum Workshop: Adding Weld Strength with Aging. 20 November 2014. Available online: <https://www.thefabricator.com/thewelder/article/aluminumwelding/aluminum-workshop-adding-weld-strength-with-aging> (accessed on 15 April 2024).

Disclaimer/Publisher's Note: The statements, opinions and data contained in all publications are solely those of the individual author(s) and contributor(s) and not of MDPI and/or the editor(s). MDPI and/or the editor(s) disclaim responsibility for any injury to people or property resulting from any ideas, methods, instructions or products referred to in the content.